

**CONTINUUM MODELING OF ELECTRO-CHEMO-MECHANICAL  
PHENOMENA IN ALL-SOLID-STATE-BATTERIES**

A Dissertation Proposal  
Presented to  
The Academic Faculty

By

Donald Bistri

In Partial Fulfillment  
of the Requirements for the Degree  
Doctor of Philosophy in the  
School of Aerospace Engineering

Georgia Institute of Technology

August 2023

© Donald Bistri 2023

# CONTINUUM MODELING OF ELECTRO-CHEMO-MECHANICAL PHENOMENA IN ALL-SOLID-STATE-BATTERIES

Approved by:

Dr. Claudio Di Leo  
The Daniel Guggenheim School of  
Aerospace Engineering  
*Georgia Institute of Technology*

Dr. Matthew McDowell  
George W. Woodruff School of Mechanical Engineering  
*Georgia Institute of Technology*

Dr. Christos Athanasiou  
The Daniel Guggenheim School of  
Aerospace Engineering  
*Georgia Institute of Technology*

Dr. Ting Zhu  
George W. Woodruff School of Mechanical Engineering  
*Georgia Institute of Technology*

Dr. Julian Rimoli  
The Daniel Guggenheim School of  
Aerospace Engineering  
*Georgia Institute of Technology*

Date approved: August, 2023

Dedicated to my loving family

My parents, Adelina and Bajram, and my precious nephew, Antoine

## ACKNOWLEDGMENTS

First and foremost, I would like to thank Professor Claudio Di Leo for his unwavering support and guidance throughout my PhD studies. Beyond imparting me with great tools for conducting research in the field of computational mechanics and multiphysics modeling, Professor Di Leo has taught me to always conduct research at the highest standards of integrity and quality. I would also like to thank my thesis committee members, Professor Matthew McDowell, Professor Ting Zhu, Professor Julian Rimoli and Professor Christos Athanasiou for their invaluable suggestions and guidance throughout my research. In particular, Professor Matthew McDowell and Professor Thomas Fuller, whose close collaboration throughout my PhD studies has been invaluable in supporting and complementing the theoretical and computational efforts in this thesis. A special thanks and gratitude also extends to Professor David McDowell for his invaluable lessons in continuum and computational mechanics, and Professor Joseph Homer Saleh for his mentorship, support and encouragement throughout my PhD studies. I will dearly miss our academic conversations.

A special thanks and gratitude extends to Deborah Powell, our administrator extraordinaire, who throughout my years at Georgia Tech, has provided all of the necessary support to ensure that I could focus on producing the best research possible.

During my time at Georgia Tech, I have been very fortunate to be surrounded by incredibly talented and supportive friends and colleagues. First and foremost, I am highly indebted to my friend Amir Hossein Salahshoor. Beyond his unconditional support and academic advice, Amir, through his comportment, has taught me the highest standards of conducting quality research. To this day, our conversations are a guiding compass in my academic pursuits. This thesis would not be possible in the slightest without him.

In addition, I am particularly grateful to my invaluable friends Jamshid and Arman, whom my PhD journey started with. This journey would have not been the same without their unconditional support, advice, heated discussions at times, and shared joyful mem-



ories. Many thanks extend to numerous other precious friends and colleagues at Georgia Tech, AaroHi, Mohit, Daniel, Ruthvik, Hernan, Jaechan, Darian, Saba, Satyam, Jiachen, Trevor, Ammar and Rodrigo without whom my graduate life and experience would have been extremely challenging.

Above all, my biggest feeling of gratitude extends to my parents Adelina and Bajram, who always motivated me to strive for excellence and to whom this thesis is dedicated. This thesis would have not been possible in the slightest without their unconditional love, care, support, and trust throughout. Their daily example of humility, sacrifice, discipline, responsibility and companionship is the founding pillar of who I am today. A lifetime is not sufficient to compensate all you have done for me.

Last but not least, to my little nephew Antoine. Your smile is the purest medicine and treasure I have cherished during my PhD. Daja loves you profoundly.

## TABLE OF CONTENTS

<b>Acknowledgments</b> . . . . .	iv
<b>List of Tables</b> . . . . .	x
<b>List of Figures</b> . . . . .	xi
<b>Summary</b> . . . . .	xx
<b>Chapter 1: Introduction</b> . . . . .	1
1.1 Background . . . . .	1
1.1.1 Modeling of the electro-chemo-mechanical behavior of composite electrodes . . . . .	3
1.1.2 Modeling of interphase formation at the electrode-solid electrolyte interface. . . . .	5
1.1.3 Modeling of Li-metal filament growth across solid-state electrolytes . . . . .	8
<b>Chapter 2: A non-linear kinetics interface element for modeling of multi-particle interactions in Li-ion battery electrodes</b> . . . . .	13
2.1 Introduction . . . . .	14
2.2 Theoretical and Numerical Framework . . . . .	19
2.2.1 Continuum Microstructural RVE Description . . . . .	20
2.2.2 Chemo-Mechanical Interfacial Particle Behavior . . . . .	22

2.2.3	Bulk Particle Behavior . . . . .	27
2.3	Numerical Framework Demonstration . . . . .	29
2.4	Multi-particle interactions in double walled a-Si nanotube electrodes . . . .	32
2.4.1	Electrochemical performance and stress generation with varying re- action rate - $k_0$ . . . . .	35
2.4.2	Capacity loss due to mechanical interfacial decohesion . . . . .	40
<b>Chapter 3: On the role of interfacial mechanical damage in composite cathodes for all-Solid-State batteries . . . . .</b>		<b>45</b>
3.1	Model Parameters . . . . .	46
3.1.1	Mechanical Properties of LCO and LGPS . . . . .	46
3.1.2	Chemical Properties of LCO . . . . .	47
3.1.3	Interfacial Properties . . . . .	49
3.2	Effect of varying chemo-mechanical properties on electrochemical perfor- mance of SSB composite cathodes . . . . .	51
3.2.1	Role of SSE stiffness on electrochemical performance and mechan- ical degradation . . . . .	52
3.2.2	Role of active material volumetric change on electrochemical per- formance and mechanical degradation . . . . .	54
3.3	Modeling the effect of particle size distribution and active material volume fraction on interface damage in composite cathodes . . . . .	57
3.3.1	Role of particle size and size distribution on electrochemical per- formance and mechanical degradation. . . . .	57
3.3.2	Role of active material volume fraction on electrochemical perfor- mance and mechanical degradation . . . . .	62
<b>Chapter 4: A continuum electro-chemo-mechanical gradient theory coupled with damage: Application to Li-metal filament growth in all-solid-state batteries . . . . .</b>		<b>70</b>

4.1	Introduction . . . . .	71
4.2	Phase-field formulation and balance equations . . . . .	78
4.2.1	Mass Balance . . . . .	81
4.2.2	Charge Balance . . . . .	82
4.2.3	Electrostatics . . . . .	83
4.3	Kinematics . . . . .	83
4.4	Governing Balance Laws . . . . .	88
4.4.1	Principle of virtual power. Balance of forces . . . . .	89
4.4.2	Balance of energy. Entropy imbalance. Free energy imbalance . . .	91
4.5	Constitutive Theory . . . . .	93
4.5.1	Energetic Constitutive Equations . . . . .	93
4.5.2	Dissipative Constitutive Equations . . . . .	95
4.6	Summary of the general constitutive theory . . . . .	97
4.6.1	Kinematics and Free Energy . . . . .	98
4.6.2	Stress. Force balance . . . . .	99
4.6.3	Electrochemical potential. Flux. Mass Balance . . . . .	99
4.6.4	Reaction driving force. Electrodeposition Kinetics . . . . .	100
4.6.5	Electrostatics . . . . .	100
4.6.6	Damage . . . . .	100
4.7	Specialization of the constitutive equations . . . . .	100
4.7.1	Electrodeposition-Induced Deformation . . . . .	101
4.7.2	Free Energy . . . . .	102
4.7.3	Stress . . . . .	107

4.7.4	Electrochemical Potential. Flux . . . . .	109
4.7.5	Reaction Driving Force. Electrodeposition Kinetics . . . . .	109
4.7.6	Electrostatics . . . . .	114
4.7.7	Damage . . . . .	114
4.8	Governing partial differential equations for the specialized constitutive equations. Boundary conditions . . . . .	115
4.9	Numerical simulations . . . . .	118
4.9.1	Modeling growth of a single Li-metal filament across a LLZO electrolyte. Role of mechanical confinement . . . . .	120
4.9.2	Modeling growth of Li-metal filaments in the presence of microstructure heterogeneity. . . . .	129
4.10	Concluding Remarks . . . . .	135
<b>Chapter 5: Conclusion . . . . .</b>		<b>138</b>
5.1	Summary . . . . .	138
5.2	Outlook . . . . .	141
<b>Appendices . . . . .</b>		<b>145</b>
Appendix A: Details on the numerical implementation of chemo-mechanical surface elements . . . . .		146
Appendix B: Principle of Virtual Work, Macro- and Microforce Balance Law . .		158
<b>References . . . . .</b>		<b>161</b>

## LIST OF TABLES

3.1	Material properties for modeling of coupled chemo- mechanical behavior of a $\text{LiCoO}_2\text{-Li}_{10}\text{GeP}_2\text{S}_{12}$ composite cathode. . . . .	50
4.2	Material properties for modeling of metal filament growth in a $\text{Li-Li}_7\text{La}_3\text{Zr}_2\text{O}_{12}$ system. . . . .	123

## LIST OF FIGURES

1.1	Architecture of an all-solid-state battery including a Li-metal anode, a solid-state electrolyte (SSE), and a composite cathode. Key areas of investigation: (a) behavior of conversion electrodes undergoing sharp interface reactions; (b) evolution of composite cathodes including damage; (c) Li-filament growth within cracks; and (d) formation and evolution of interphases at the SSE/metal interface. Composite figure reproduced with permission from [9, 14, 15, 16, 17, 18, 19, 20]. . . . .	2
1.2	(a) Architecture of a solid-state composite electrode consisting of a conglomerate of active particles, solid-ionic conductor and binders for electronic conduction. Mechanical fracture across constituents of a composite cathode, namely fracture at: (b) active particle bulk; (c) active particle-SSE interface; and (d) solid-state ionic conductor. Composite figure reproduced with permission from [17, 28, 31, 32, 36, 37] . . . . .	4
1.3	(a) Formation of a thermodynamically-unstable interphase at the Li-metal anode-LAGP solid electrolyte interface. (b) Finite element model of the swollen interphase, showing (i) contours of reaction coordinate (left) and (ii) evolution of radial and circumferential stresses across the LAGP pallet, leading to formation of cracks (right). (c) Time sequence of the fracture network induced by sequential volumetric growth of the interphase. (d) Direct correlation between extent of crack propagation and increase in impedance. Reproduced with permission from [18]. . . . .	6
1.4	(a) Formation of voids at the Li-metal anode interface with continuous plating/stripping. Voids formation at the interface induces current constrictions at these sites, facilitating nucleation and subsequent propagation of Li-metal filaments with fracture of the solid-electrolyte. Reproduced with permission from [22]. (b) Transgranular growth of Li-metal filaments across a single-crystal LLZO microstructure. Reproduced with permission from [65]. (c) Preferential deposition of Li-metal along the grain boundaries of a polycrystalline LLZO microstructure. Reproduced with permission from [58]. . . . .	9

2.1	Schematic description of the theoretical and numerical framework employed with a focus on electro-chemistry. (a) Continuum description of the microstructure RVE with $N$ particles and galvanostatic conditions enforced. (b) Particle description showing discretization of current over $M$ elements over each particle surface. (c) Description of the surface element in which non-linear reaction kinetics relate local chemical potential jumps at each node pair to the current density at each element. Reproduced with permission from [17]. . . . .	20
2.2	Example of a two-particle numerical simulation. (a) Total current distribution to both particles as well as the entire simulation domain, illustrating the ability to capture galvanostatic charging conditions. (b - c) Local current densities as a function of the normalized distance ( $s_1, s_2$ ) along the particle surface taken at time $t=t_b$ and $t=t_c$ . (d - e) Contours of maximum in-plane principal stress, $\sigma_1$ over the matrix and normalized concentration, $\bar{c}$ over the particle domain taken at time $t=t_b$ and $t=t_c$ . Also illustrated in white are regions of decohered interface. Reproduced with permission from [17]. . . . .	30
2.3	Multi-particle modeling of hollow double-walled nanotubes. (a) Shows a representative SEM image from the experiment of Wu et al. Reprinted with permission from [116]. (b) Shows a schematic three-dimensional representation of a single tube denoting the simulation domain as a single sliver of the tube in the axial direction. (c) Shows the numerical discretization using finite elements of the a-Si core and the $\text{SiO}_2$ shell, including the discretization of the interface using chemo-mechanical surface elements. Reproduced with permission from [17]. . . . .	33
2.4	Simulation results for a 50-particle system with a statistical distribution in reaction constant $k_0$ . (a) Local (individual nanotube) voltage vs. state-of-charge behavior for three particles spanning the range of $k_0$ values considered. (b) Current vs. time response for the three particles under consideration compared against the total current in the simulation domain. (a) and (b) are for the case of $\text{SD} = 1.0$ . (c) Global (entire simulation domain) voltage vs. state-of-charge behavior for a single particle, simulations with $k_0$ distributions with $\text{SD} = 1.0$ and $\text{SD} = 2.0$ , and the experimentally measured response of Wu et al. [116]. Reproduced with permission from [17]. . . . .	36
2.5	Interfacial normal stress, $\tau_N$ at the a-Si/ $\text{SiO}_2$ interface as a function of local (nanotube) SOC. (a) Results for three representative particles spanning the range of $k_0$ values considered at a C-Rate of 1C. (b-c) Results for a particle with a reaction constant of $k_0 = 3.25 \cdot 10^{-7} \text{ mol}/(\text{m}^2\text{s})$ at three different C-Rates, with (b) mechanical strain-rate sensitivity taken into consideration, and (c) mechanical strain-rate sensitivity neglected. Reproduced with permission from [17]. . . . .	38



2.6	Simulation result of cycling a multi-particle electrode composed of double-walled, hollow nanotubes. Figs. (a) and (b) show the Voltage vs. SOC response of the electrode where (a) compares a simulation with and without damage after the first three conditioning cycles and (b) shows results of the simulation with damage after 9, 12, and 15 cycles. Figs. (c) and (d) show contours of normalized concentration in the a-Si core at the end of the 3rd and 15th cycle. The red arrows highlight those particles which have completely decohered from their shells and are now chemically isolated. Reproduced with permission from [17]. . . . .	42
2.7	Capacity of an ensemble of hollow double-walled nanotubes as a function of cycle number during galvanostatic cycling at various C-rates. Results are shown for a simulation without interfacial damage (blue line) and a simulation with interfacial damage (orange line). Reproduced with permission from [17]. . . . .	43
3.1	(a) SEM image of a $\text{LiCoO}_2\text{-Li}_{10}\text{GeP}_2\text{S}_{12}$ composite cathode microstructure from the work of Zhang et al. Reprinted with permission from [16]. (b) Graphical illustration of the 2D microstructure mimicking SEM images of Zhang et al. [16] used to model the effect of variation in chemo-mechanical properties on electrochemical performance of composite cathode. Reproduced with permission from [17]. . . . .	52
3.2	Composite cathode response with no damage and varying SSE Young's Modulus. (a) Average normal interfacial stress, $\tau_N^{\text{avg}}$ induced at the active-particle/SSE interface vs. SOC. (b) Voltage vs. SOC response of the composite electrode. Reproduced with permission from [17]. . . . .	53
3.3	Effect of variations in SSE stiffness on electrochemical response of a composite cathode with different cohesive strengths $t_N^{\text{cr}}$ and volumetric contractions of the active particles $\bar{\Omega}$ . (a) Simulation results with high cohesive strength $t_N^{\text{cr}} = 250$ MPa and 2% volumetric contraction, $\bar{\Omega} = -2\%$ . (b) Results with reduced cohesive strength $t_N^{\text{cr}} = 150$ MPa. (c) Results with increased 5% volumetric contraction, $\bar{\Omega} = -5\%$ . The range of SSE stiffnesses considered are representative of Sulfides, LGPS, LiPON and Garnets. Reproduced with permission from [17]. . . . .	54
3.4	Simulation results for the particular case with $E_{\text{SSE}} = 20$ GPa and $\bar{\Omega} = -5\%$ . The top-left plot shows the average current density, maximum normal interfacial stress $\tau_N^{\text{max}}$ , and average damage for Particle 1 which is shown in (a). Figs. (a) through (d) show contours of maximum in-plane principal stress $\sigma_1$ in the SSE matrix, while contours of the normalized concentration $\bar{c}$ are shown over the active particles. Note that deformations are scaled by a factor of 10. Reproduced with permission from [17]. . . . .	56

3.5	(a) Single particle representative volume element (RVE) simulation domain. (b) Plot of average normal interfacial stress $\tau_N^{\text{avg}}$ as a function of the geometric factor (i.e volume fraction) $f = R_{\text{ap}}/R_{\text{ins}}$ . Reproduced with permission from [17]. . . . .	58
3.6	Simulated RVEs with a constant active material volume fraction $\phi_{\text{AM}} = 30\%$ . The particle sizes are given a uniform distribution with lower and upper bounds in the range of: i) 2-6 $\mu\text{m}$ ii) 4-5 $\mu\text{m}$ and iii) 6-7 $\mu\text{m}$ . The aspect ratio lower and upper bounds are set to 0.9 and 1.5 respectively for all cases. Reproduced with permission from [17]. . . . .	60
3.7	Simulation results for composite cathode RVEs with constant active material volume fraction $\phi_{\text{AM}} = 30\%$ and varying particle size distribution. (a) Voltage vs. SOC behavior also compared to simulations with no damage. (b) Evolution of average $D_{\text{chem}}$ as a function of time for the first half-cycle. (c) Evolution of Voltage as a function of average $D_{\text{chem}}$ . Reproduced with permission from [17]. . . . .	60
3.8	Simulation results for composite cathode RVEs with constant active material volume fraction $\phi_{\text{AM}} = 30\%$ and varying particle size distribution. Results are shown at the end of the first half-cycle of each simulation domain. Reproduced with permission from [17]. . . . .	62
3.9	Simulated RVEs with a constant particle size distribution and varying active material volume fraction $\phi_{\text{AM}}$ . Reproduced with permission from [17]. . . .	63
3.10	Simulation results for composite cathode RVEs with constant particle size distribution and varying volume fraction $\phi_{\text{AM}}$ . (a) and (b) show Voltage vs. Capacity (defined per unit total mass of the RVE) for simulations with and without interfacial damage respectively. (c) Stable capacity during cycling as a function of $\phi_{\text{AM}}$ for simulations with and without damage and also shows the stable capacity loss due to damage, which is the difference of the two simulation results. (d) Voltage as a function of accumulated chemical damage (i.e. average $D_{\text{chem}}$ in the entire simulation domain) for simulations with varying $\phi_{\text{AM}}$ and interfacial damage. Note the legend in (a) applies equally to (b) and (d). Reproduced with permission from [17]. . . . .	64

3.11	Simulation results for composite cathode RVEs with constant particle size distribution and varying volume fraction $\phi_{AM}$ . Results are shown at (a) Voltage of 4.5 V (top row), (b) Voltage of 4.2 V (middle row), and (c) Voltage of 3.9 V (bottom row). In all results, we show contours of the maximum principal stress, $\sigma_1$ , over the SSE matrix, and contours of normalized concentration $\bar{c}$ over the active particles. Note that the colorbar for $\sigma_1$ is constant over a given Voltage, and the colorbar for $\bar{c}$ is constant for all simulations shown. Deformations are scaled by 10x. Reproduced with permission from [17]. . . . .	66
4.1	(a) Schematic of a metal electrode-solid conductor assembly. (b) Illustrates a pre-existing defect ( $\bar{\xi} = 0, d = 1$ ) at the solid host-metal electrode interface prior to metal deposition inside the crack. (c) Illustrates deposition of metal inside the imperfection ( $\bar{\xi} = 1, d = 1$ ), leading in turn to a build up in normal stresses, $\sigma_n$ , at the crack surfaces. (d) Build-up in normal stresses on the crack surface eventually causes the solid host to damage further ahead of the crack tip, creating a new damage zone ( $\bar{\xi} = 0, d = 1$ ), which can accommodate subsequent deposition of metal inside the solid host. Reproduced with permission from [19]. . . . .	81
4.2	Logistic functions modulating the reaction constant $R_0$ with (a) the function $f_1(\bar{\xi})$ and (b) the function $f_2(d)$ . Reproduced with permission from [19]. . .	113
4.3	Initial configuration of the Li-electrode/solid electrolyte simulation containing a pre-existing defect. Contours of (a) reaction coordinate $\bar{\xi}$ , (b) damage $d$ , (c) normalized concentration $\bar{c}$ , and (d) electric potential $\phi$ (V). Reproduced with permission from [19]. . . . .	121
4.4	Evolution in time for (a) the extent of electrodeposition $\bar{\xi}$ , (b) the normalized concentration $\bar{c}$ , (c) the electric potential $\phi$ (V), (d) damage $d$ , and (e) the horizontal stress component $T_{xx}$ . The simulation is mechanically fully-constrained, with rollers present on the left and right edges. Reproduced with permission from [19]. . . . .	126
4.5	Evolution in time of the isocontours of damage $d$ (black lines) and reaction coordinate $\bar{\xi}$ (red lines) for (a - top row) a laterally constrained simulation, and (b - bottom row) a laterally free simulation. Comparing (a) and (b) demonstrates the critical role of mechanical confinement in dictating the degree to which the electrodeposition-induced crack becomes filled with Li-metal. Reproduced with permission from [19]. . . . .	128
4.6	Schematic of the simulation domain highlighting elements chosen to represent grain boundaries in the LLZO solid-state electrolyte. Reproduced with permission from [19]. . . . .	129

4.7	Contours of reaction coordinate $\bar{\xi}$ (top row) and damage $d$ (bottom row) for (a) a fully-coupled simulation, (b) a stress-coupled only simulation, and (c) a kinetics-coupled only simulation. Reproduced with permission from [19].	131
4.8	Contours of reaction coordinate $\bar{\xi}$ (top row) and damage $d$ (bottom row) with varying grain boundary fracture energies, respectively (a) $\psi_{gb}^* = (1/5) \cdot \psi_{bulk}^*$ , (b) $\psi_{gb}^* = (1/3) \cdot \psi_{bulk}^*$ , and (c) $\psi_{gb}^* = (1/2) \cdot \psi_{bulk}^*$ . Reproduced with permission from [19].	134
A.1	Schematic illustration of the cohesive interface for numerical implementation of galvanostatic charging conditions. Reproduced with permission from [17].	148
A.2	(a) Surface elements integrated at the boundary of electrode particles to capture variations in current density along a particle surface and the associated current distribution across different particles. (b) Mechanism of current distribution at the electrode surface as a function of jump in chemical potential at the particle-electrolyte interface. Reproduced with permission from [17].	152
A.3	Analytical fit of (a) Young's Modulus and (b) Shear Modulus for $Li_xCoO_2$ active material with stoichiometric Li amount - $x$ to experimental data by Wu and Zhang [140]. Reproduced with permission from [17].	154
A.4	Comparison of analytical, seventh-order polynomial fit and the finite-element simulated open circuit potential curve against the experimental data by Mizushima et al. [145]. Reproduced with permission from [17].	155
A.5	Calibration of reaction constant, $k_0$ against experimental data by Zhang et al. [152], demonstrating consistency across analytical, numerical and experimentally obtained Voltage vs SOC curves. Reproduced with permission from [17].	155
A.6	Simulated RVEs with a constant active particle volume fraction $\phi_{AM} = 20\%$ . The particle sizes are given a uniform distribution with lower and upper bounds in the range of: i) 2-6 $\mu m$ ii) 4-5 $\mu m$ and iii) 6-7 $\mu m$ . The aspect ratio lower and upper bounds are set to 0.9 and 1.5 respectively for all cases. Reproduced with permission from [17].	156

A.7	Simulation results for composite cathode RVEs with constant active material volume fraction $\phi_{AM} = 20\%$ and varying particle size distribution. (a) Voltage vs. SOC behavior also compared to simulations with no damage. (b) Evolution of average $D_{chem}$ as a function of time for the first half-cycle. (c) Evolution of Voltage as a function of average $D_{chem}$ . Reproduced with permission from [17]. . . . .	157
-----	---	-----

## SUMMARY

Solid-state-batteries (SSBs) present a promising technology for next-generation batteries due to their superior properties including increased energy density and safer electrolyte design. Traditional SSB architecture features a Li-metal anode, a solid-state composite cathode and a stiff ceramic electrolyte for conduction of ionic species. While an attractive alternative, commercialization of SSBs faces a series of chemo-mechanical issues across its constituents, namely growth-induced fracture of the solid-state electrolyte (SSE) due to Li-metal deposition, interphase formation and associated large volumetric deformations at the anode-SSE interface, in addition to mechanical degradation across the various phases in composite electrodes. Computational modeling of SSBs is still at its infancy and constitutes the central theme of this thesis. We develop here a series of numerical frameworks seeking to elucidate the complex electro-chemo-mechanical processes coupled with mechanical fracture governing the behavior of both composite cathodes and solid-state electrolytes with Li-metal deposition.

Both cathode and anode architectures may consist of a composite of active particles surrounded by a ceramic SSE matrix. During cycling, active particles undergo large volumetric changes against the stiff SSE, which can lead to formation of high mechanical stresses. Developing models for these architectures requires then a coupled electro-chemo-mechanical understanding of three critical constituents, namely active particles, solid-state electrolyte and the shared interface between the two. Key to such understanding is the role of mechanical damage on electrode performance. Towards modeling the role of mechanical damage on performance, we propose a novel coupled chemo-mechanical interface element, analogous to cohesive elements used in fracture mechanics. The framework enables

for modeling galvanostatic charging of composite electrodes and captures the continuous evolution of mechanical stresses, interfacial damage, and non-uniform current distribution across particles in a microstructure. We specialize on a  $\text{Li}_x\text{CoO}_2$  (LCO) -  $\text{Li}_{10}\text{GeP}_2\text{S}_{12}$  (LGPS) composite cathode and study the evolution of interfacial damage under varying material and microstructural properties. Specifically, we model electrolyte compositions with varying SSE stiffness and active particle volumetric change to assess their effect on interfacial stresses, mechanical damage, and overall electrochemical response. Subsequently, we discuss how variations in microstructural composition alter the state of interfacial damage. Both packing effects and particle size distribution are studied to understand how these factors impact integrity of the interface and performance.

Towards modeling the phenomenon of Li-metal filament growth, we formulate a continuum electro-chemo-mechanical gradient theory which couples phase-field damage and electrochemical reactions within the solid-state electrolyte. The proposed framework is fully-coupled with electrodeposition impacting mechanical deformation, stress generation and subsequent SSE fracture. Conversely, electrodeposition kinetics are affected by mechanical stresses through a thermodynamically-consistent driving force that distinguishes chemical, electrical, and mechanical contributions. Importantly, the theory captures the interplay between crack propagation and electrodeposition by tracking the extent of damage and electrodeposition across the SSE via distinct phase-field variables, such that filament growth is preceded by and confined to fractured regions within the SSE. An attractive feature of such approach is its ability to simulate the nucleation, propagation and branching of cracks and Li-filaments in arbitrary orientations.

While the framework is general in nature, a specialization towards modeling the growth of Li-metal filaments in an inorganic  $\text{Li}_7\text{La}_3\text{Zr}_2\text{O}_{12}$  (LLZO) electrolyte is demonstrated. We showcase the capacity to capture intergranular and transgranular crack and Li-filament growth mechanisms, both of which have been experimentally observed. In doing so, we elucidate the manner in which mechanics and fracture of the SSE impact electrodeposition

kinetics and Li-filament morphology. From a manufacturing standpoint, we additionally elucidate the role of mechanical boundary conditions (i.e. mechanical confinement) on the rate of crack propagation across the electrolyte versus electrodeposition of Li-metal within cracks. Under specific mechanical boundary conditions, we demonstrate the capacity of the framework to capture the experimentally observed phenomenon of crack fronts propagating ahead of Li-metal filaments, as cracks traverse the entire electrolyte in advance of Li-deposits.

In conjunction with experimental efforts, the theoretical frameworks proposed in this thesis seek to elucidate the inherent electro-chemo-mechanical processes which govern mechanical integrity and ultimately electrochemical performance of all-solid-state batteries in an effort to expedite their successful commercialization for future energy storage applications.



# CHAPTER 1

## INTRODUCTION

### 1.1 Background

Solid-state-batteries (SSBs) present a promising technology for next-generation batteries. In recent years, commercialization of SSBs has attracted significant research attention owing to their promise of superior performance compared to conventional Lithium-ion batteries (LIBs). Transition to SSBs has significant advantages including enhanced current density, faster charging time, wider electrochemical window, and improved safety. Contrary to conventional LIBs which make use of graphite intercalation anodes, incorporation of Li-metal anode designs enables for a ten-fold increase in volumetric capacity, leading to a significant improvement in energy density (3860 mAh/g) [1, 2, 3]. Owing to their wider electrochemical window (0-5V), SSBs also enable for coupling of Li-metal anode with high-voltage cathode materials as demonstrated by several recent studies [4, 5, 6]. From a safety perspective, replacement of toxic and flammable organic electrolytes with highly conductive ( $\geq 10^{-3}$  S/cm), mechanically superior inorganic solid-state electrolytes (SSEs) can alleviate concerns associated with failure of batteries due to short-circuit or ignition [7, 8]. A particularly attractive SSB architecture with high energy density features a lithium metal anode, a composite solid-state cathode and an inorganic SSE separating the electrodes [9]. Fig. 1.1 highlights these three particular areas of interest in an all-solid-state architecture as well as the mechanical modeling issues which must be addressed in order to understand and commercialize these systems.

Traditionally, SSEs are categorized into two groups, pertaining to organic solid polymers and inorganic solids (oxide or sulfide based). Among other properties, successful integration of SSEs in SSBs requires meeting particular chemical standards, including neg-

ligible electronic conductivity, high ionic conductivity, good electrochemical compatibility as well as several mechanical standards including appropriate stiffness and fracture toughness to preserve mechanical integrity. While liquid electrolytes traditionally have a higher ionic conductivity and allow for excellent wetting of electrode surface, comparable ionic conductivity values have been achieved for several ceramic SSEs as reported in multiple studies [10, 11, 12, 13]. Resolution of sluggish ionic conductivity, while a major improvement in research efforts to integrate SSEs in next-generation battery designs, addresses one of the multiple challenges hindering commercialization of SSBs.

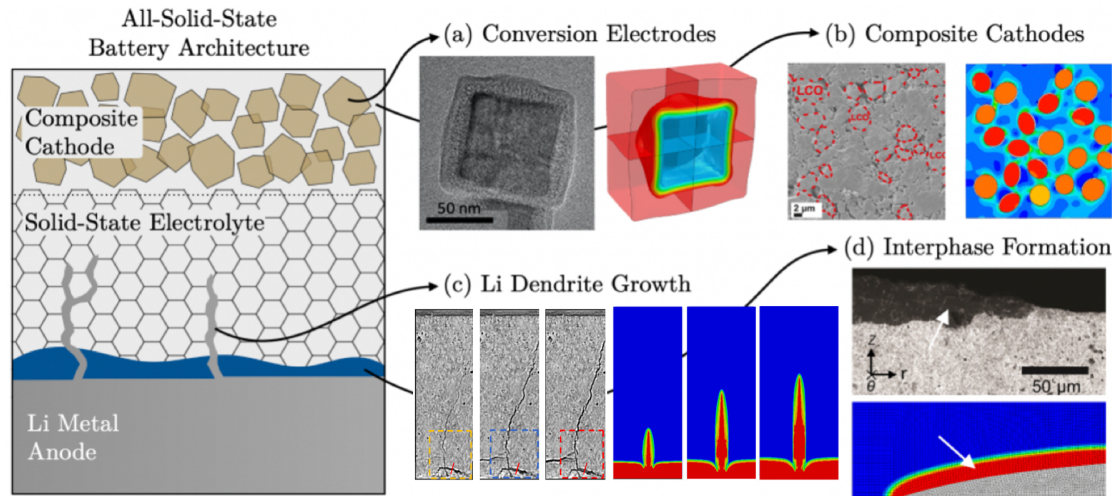


Figure 1.1: Architecture of an all-solid-state battery including a Li-metal anode, a solid-state electrolyte (SSE), and a composite cathode. Key areas of investigation: (a) behavior of conversion electrodes undergoing sharp interface reactions; (b) evolution of composite cathodes including damage; (c) Li-filament growth within cracks; and (d) formation and evolution of interphases at the SSE/metal interface. Composite figure reproduced with permission from [9, 14, 15, 16, 17, 18, 19, 20].

A critical challenge here remains the ability to control chemo-mechanical instabilities and contact loss at the electrode-SSE interface [21, 22]. While research in understanding of solid/liquid interfaces is mature, the community's understanding of solid/solid electrochemical interfaces is still at its infancy. A multi-physics experimentally-guided understanding of the complex nature of solid-solid interfaces and their evolution is thus critical to resolve a series of issues presently hindering commercialization of SSBs and consti-

tutes the central theme of this thesis. In particular, as part of this thesis, we propose a series of novel theoretical frameworks seeking to model and elucidate the complex coupled electro-chemo-mechanical phenomena and associated degradation mechanisms in two primary constituents i) composite electrodes and ii) solid-state electrolyte and its fracture due to Li-filament growth.

#### 1.1.1 Modeling of the electro-chemo-mechanical behavior of composite electrodes

Composite cathodes, as illustrated in Fig. 1.1, present a critical constituent where mechanics plays a key role. By construction, composite cathodes rely on a densely packed architecture of active material, surrounded by a conductive SSE to support ionic transport, in addition to complementary additives for electronic conduction [23, 24, 25]. The active material undergoes volumetric expansion/contraction during insertion/extraction of ionic species, which, due to the confined nature of the all-solid-state architecture, can lead to generation of high stresses [26, 27]. Batteries employing liquid electrolytes traditionally isolate volumetric strains at the active particle level, given the incapacitation of liquid electrolytes to transfer stresses. As a result, in current battery designs, any morphological changes of the active particles do not translate to interfacial delamination at the electrode-electrolyte interface, which continues to support ion transfer.

The confined nature of solid-state electrodes allows for transmission of stresses through the stiff solid framework, resulting in a complex coupled chemo-mechanical behavior, which is prone to damage through failure of the active particles [28, 29, 30], the SSE itself [31], or delamination of the interface between the two [17, 32]. Fig 1.2(b-d) illustrates the different degradation mechanisms across the constituents of a composite cathode for all-solid state battery applications, limiting in turn their electro-chemical performance as also experimentally reported [16, 32, 33].

In addition to the mechanical behavior, there are concurrent electrochemical processes as current (i.e. amount of charge) locally varies between particles in a composite electrode.

From a modeling perspective, there is a need to capture multi-particle interactions—both mechanical and chemical—for these densely packed architectures in order to understand how variations in material properties and microstructure composition affect mechanical degradation and ultimately electrochemical performance. At present, modeling of the concurrent chemical interactions between active particles arising from diffusion of Li-ions through the electrolyte remains largely unexplored, with most frameworks resorting to study of single-particle electrode domains [29, 30, 34, 35]. An inherent obstacle in modeling of chemical interactions between particles is implementation of true galvanostatic conditions. During galvanostatic charging, total current over all particles is held constant, but individual current distribution at each particle surface is unconstrained and depends on the local stress-coupled non-linear reaction kinetics.

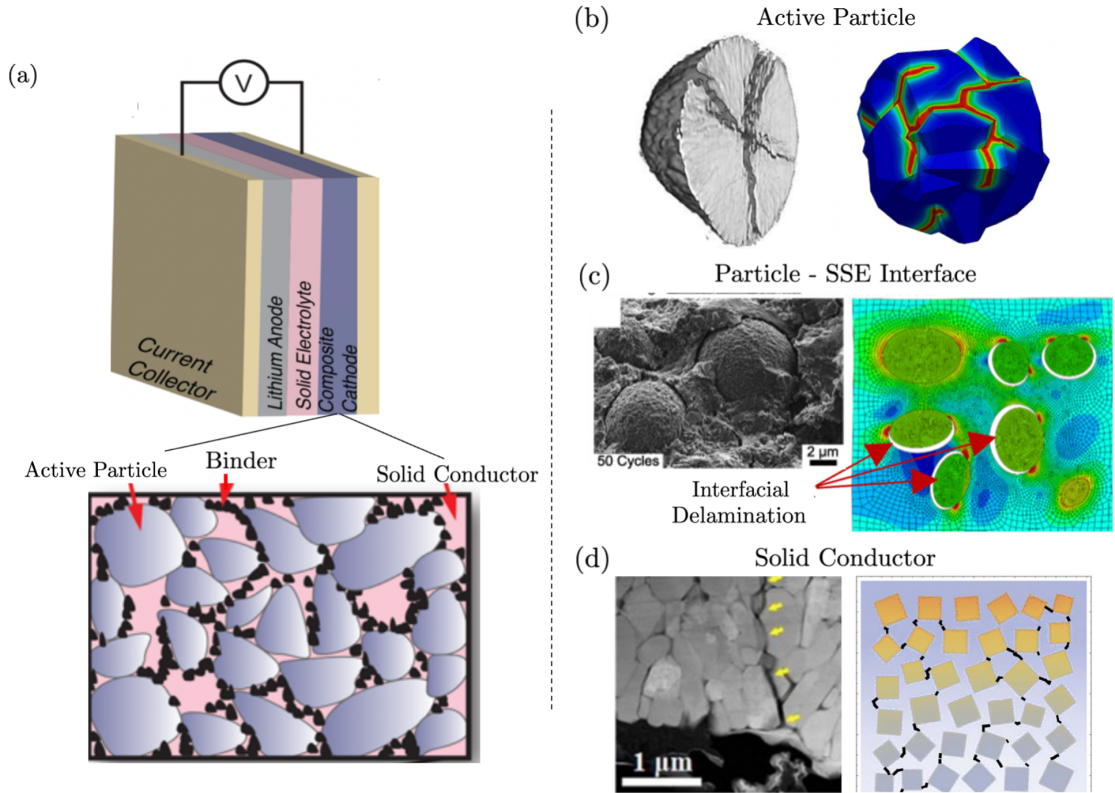


Figure 1.2: (a) Architecture of a solid-state composite electrode consisting of a conglomerate of active particles, solid-ionic conductor and binders for electronic conduction. Mechanical fracture across constituents of a composite cathode, namely fracture at: (b) active particle bulk; (c) active particle-SSE interface; and (d) solid-state ionic conductor. Composite figure reproduced with permission from [17, 28, 31, 32, 36, 37]

To address this limitation, in chapter 2 of this thesis, we formulate and numerically implement a theoretical framework based on application of chemo-mechanical interface elements – analogous in form to conventional cohesive elements used in fracture mechanics – to model the stress-coupled non-linear kinetics of ionic transport at the particle/electrolyte interface. We showcase the capacities of the proposed surface elements to successfully capture galvanostatic charging conditions and cross-particle interactions by first modeling the electro-chemical performance of innovative LIBs electrode designs, in which interactions are purely of chemical nature. Subsequently, we deploy this new element in chapter 3 to model galvanostatic charging of composite electrodes for all-solid-state battery applications and study their electrochemical performance with variation in both chemo-mechanical properties as well as microstructure composition (i.e. active material infill, particle size distribution). From a design standpoint, the proposed framework is particularly utilitarian and can help elucidate manufacturing efforts in terms of optimal microstructure composition to minimize damage and enhance electrochemical performance.

### 1.1.2 Modeling of interphase formation at the electrode-solid electrolyte interface.

Furthermore, unwanted electrochemical reactions between the Li-metal anode and SSEs during cyclic charge/discharge of the battery can produce compounds, which lead to formation of a non-homogeneous interphase layer of low ionic conductivity. This in turn can significantly limit ion transfer kinetics and increase interfacial resistance as reported in several representative SSEs [5, 38, 39, 40]. Simultaneously, formation of non-homogeneous interphase regions is accompanied by volumetric expansion, which in the context of densely packed all-solid-state architectures can induce high stresses, resulting in fracture and degradation of the SSE [18, 41]. Occurring in the confined all-solid-state architecture, this volume expansion introduces internal stresses, leading to possible fracture and degradation of the solid electrolyte.

Tippens et al. [18] have reported the formation of cracks in a  $\text{Li}_{1.4}\text{Al}_{0.4}\text{Ge}_{1.6}(\text{PO}_4)_3$ -

(LAGP) solid-state electrolyte using X-ray tomography, interestingly arguing that it is the presence of these cracks and the subsequent loss of contact that cause high impedance in the battery operation, rather than the transport properties of the interphase itself. Fig. 1.3(a) illustrates the formation of the thermodynamically-unstable interphase at the Li-metal-LAGP interface, while a time sequence of the evolution in fracture of the SSE incurred by volumetric expansion of the interphase is shown in Fig. 1.3(c).

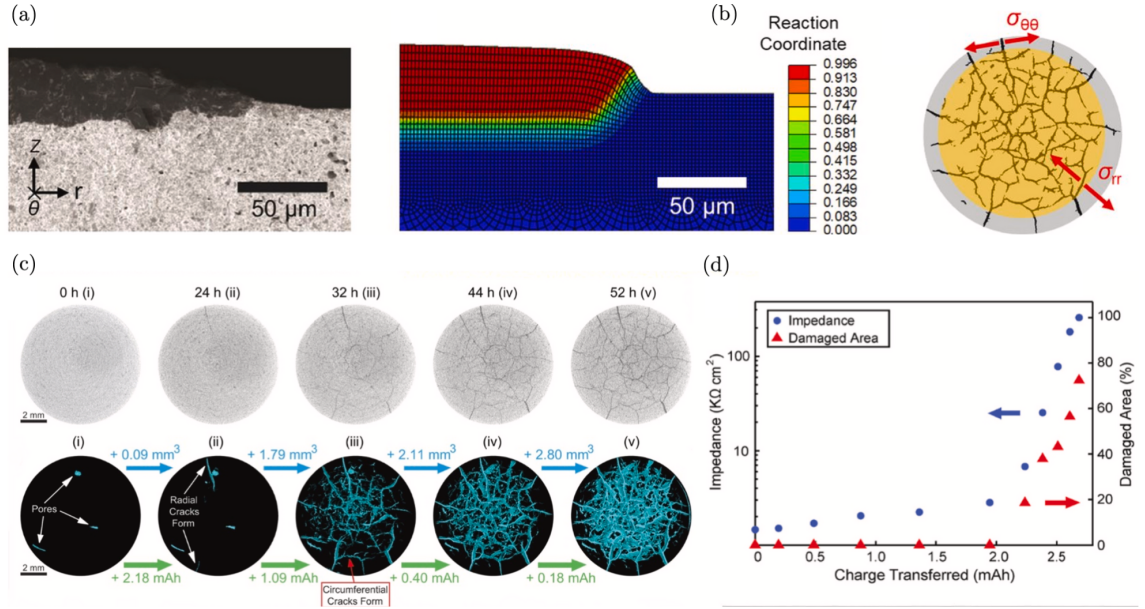


Figure 1.3: (a) Formation of a thermodynamically-unstable interphase at the Li-metal anode-LAGP solid electrolyte interface. (b) Finite element model of the swollen interphase, showing (i) contours of reaction coordinate (left) and (ii) evolution of radial and circumferential stresses across the LAGP pallet, leading to formation of cracks (right). (c) Time sequence of the fracture network induced by sequential volumetric growth of the interphase. (d) Direct correlation between extent of crack propagation and increase in impedance. Reproduced with permission from [18].

From a modeling perspective, the same team also studied the stress distribution in the aforementioned solid state cell using a diffusion-deformation continuum framework by Di Leo et al. [42] as shown in Fig. 1.3(b). It should be noted, however, that the model used to simulate the interphase formation and evolution relied on an ad-hoc description of the interphase, where its position was determined apriori rather than evolved according to the chemo-mechanical physics of the system. Similar volumetric changes incurred by forma-

tion of thermodynamically-unstable interphases at the Li-metal anode in contact with the solid electrolyte have been corroborated by Zhang and co-workers [43]. As reported in their work, the chemically formed interphase strongly affects the mechanical integrity of the LAGP solid electrolyte, pulverizing the LAGP pellet with repeated microcrack formation on the side of the interphase.

While extensively explored experimentally, at present, capturing the phenomenon of interphase formation and its evolution remains one of the challenges for SSE realization from a modeling perspective. Other continuum formulations in chemo-mechanics of solid interphases, such as the one by Rejovitzky et al. [44], are more suitable for modeling the growth of solid interphase in conventional LIBs, as opposed to structural and phase changes associated with interphase formation at the anode-electrolyte interface in SSBs; treatment of growth models in LIBs is fundamentally different from a reaction model relevant to SSBs. There are, however, models in the mechanics community from which useful formulations for interphase growth can be drawn, as they describe physical phenomena similar in nature to interface reactions in SSBs. Particularly, the research conducted on modeling oxidation in thermal barrier coatings [45, 46, 47], and modeling of hydrogen-assisted cracking in metals [48, 49] can serve as potential starting points for building models specific to interface reactions in SSBs. Nevertheless, at present, a diffusion-reaction-deformation theory capable of accommodating chemically-induced phase transformations is currently lacking in the mechanics literature.

A key constituent in development of such frameworks is also the capacity to model the formation and propagation of cracks across the solid conductor induced by large interphase volumetric expansions. Phase-field damage formulations have been extensively reported in the literature with applications across a multitude of problems including active material cracking [36, 50, 51], stress-corrosion cracking [52, 53], hydrogen embrittlement [48, 54], soft-matter [55, 56, 57] etc. These models are easily transferable to modeling of SSE fracture induced by volumetric expansion of the interphase and importantly do not require

prior definition of the crack path. Instead, cracks are free to evolve in any arbitrary direction driven by a thermodynamically-consistent fracture driving force, provided a critical energy condition for damage initiation is met.

### 1.1.3 Modeling of Li-metal filament growth across solid-state electrolytes

Among the numerous degradation mechanisms listed in Fig. 1.1, Li-metal filament growth upon fracture of the solid-state electrolyte constitutes one of the most intricate challenges in SSBs, resorting to the interplay of both mechanical and chemical forces. Contrary to dendrite growth processes in liquid electrolyte systems, growth of metal filaments across SSEs in solid-state architectures depends on a fundamentally different mechanism, hypothesized to be centered on the morphology of the SSE microstructure. Filament protrusions can initiate at perturbations of the interface or microstructural heterogeneities (i.e. pores, cracks, grain boundaries) and subsequently grow through the SSE microstructure by fracturing the latter and creating fresh sites for continuous, non-uniform Li-metal deposition towards the cathode end. Fig. 1.4(a) illustrates the potential formation of surface imperfections in the form of voids at the Li-anode-SSE interface with continuous cycling of the solid-state battery (i.e plating/stripping). Formation of voids at the Li-anode leads to current constrictions at the interface, localizing deposition at these sites. This in turn facilitates nucleation and subsequent propagation of Li-protrusions across the solid electrolyte with fracture of the latter. Eventually, as Li-metal protrusions form a full pathway from the anode towards the cathode, the battery short-circuits [20, 58, 59, 60]. It is thus critical to understand from both an experimental and modeling perspective the interplay between non-uniform electrodeposition at the Li-metal interface and heterogeneity of the SSE microstructure, in particular the size and distribution of surface defects, rate of lithium deposition at the Li/SSE interface, local stress state and the viscoplastic deformation of Li-metal [22, 61, 62, 63, 64].



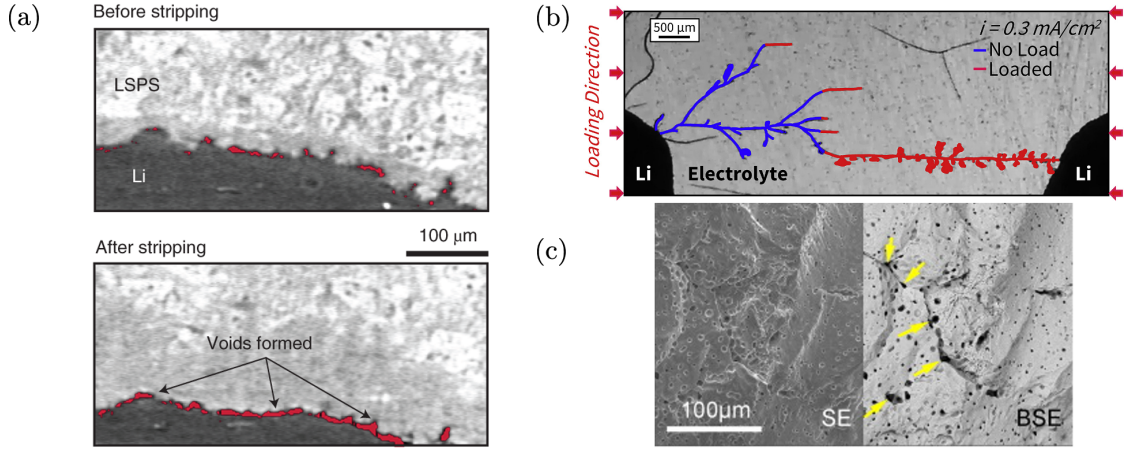


Figure 1.4: (a) Formation of voids at the Li-metal anode interface with continuous plating/stripping. Voids formation at the interface induces current constrictions at these sites, facilitating nucleation and subsequent propagation of Li-metal filaments with fracture of the solid-electrolyte. Reproduced with permission from [22]. (b) Transgranular growth of Li-metal filaments across a single-crystal LLZO microstructure. Reproduced with permission from [65]. (c) Preferential deposition of Li-metal along the grain boundaries of a polycrystalline LLZO microstructure. Reproduced with permission from [58].

From an experimental standpoint, filamentary protrusions across both compliant [20, 66, 67, 68] and stiff oxide-based electrolytes [58, 59, 60, 69, 70, 71] have been extensively reported above a critical current density. These works have nullified the findings of Monroe and Newman that a region of stability for suppression of metal filaments growth exists, provided the shear modulus of the SSE is at least twice larger than that of Li-metal [72]. Advanced characterization techniques including tomographic imaging and spectroscopy have concurrently revealed propagation of Li-metal filaments across SSE microstructures either i) transgranularly, or through cracks typical for single-crystal electrolytes [20, 60, 69, 73] and ii) integranularly or through the grain boundaries, typical for polycrystalline SSEs [58, 59, 66, 74, 75] as shown in Fig. 1.4 (b-c). Recent studies have additionally hypothesized the potential for isolated Li-metal deposits to form within the bulk SSE microstructure due to the favorable SSE electronic properties and presence of trapped electrons. Upon reaction with Li-ions, these trapped electrons may produce isolated Li-metal deposits, seeding subsequent growth of metal filaments across the SSE microstructure [76, 77].

While an understanding of the complex interplay of electro-chemo-mechanical phenomena governing the growth of Li-metal filaments has been extensively explored from an experimental standpoint, development of a microstructure-resolved description of the process of Li-metal filament growth through the SSE microstructure is lacking and necessary, with current frameworks resorting primarily to modeling growth of filaments as pressurized cracks under a linear-elastic fracture mechanics framework [78, 79, 80, 81, 82, 83]. While clearly important, these models are limited to modeling the conditions under which an existing filament might propagate. They can not capture the dynamic evolution of Li-metal filaments.

Only recently, mature continuum frameworks to model the electro-chemo-mechanical processes that govern non-uniform electrodeposition at a Li-metal/SSE interface in the presence of imperfections have been proposed. In [84], Narayan and Anand propose a continuum framework to model non-uniform growth due to uneven deposition at the Li-anode coupled with elastic-viscoplastic behavior of Li-metal. Given the complexity of modeling freshly-deposited Li-layers from a finite element standpoint, the authors propose an analogous mechanical problem of swelling and de-swelling of a thin “interphase layer” at the Li-metal/SSE interface to reproduce the electro-chemical process of plating/stripping. However, the framework is limited in its capacity to directly model the ongoing electrochemical reaction kinetics driving the growth of Li-metal filaments, and can not subsequently predict the morphology and evolution of the resulting Li-filaments. Alternate continuum frameworks, modeling Li-metal protrusions across the SSE as climbing dislocations have been recently proposed by Shishvan et al. [85, 86], importantly showing the capacity to predict the experimentally reported critical current density and growth rate of Li-deposits across SSEs consistent with experiments. However, at present, modeling frameworks accounting for the role of microstructure heterogeneity on both initiation and propagation of Li-metal filaments across SSEs are limited.

Pertaining to initiation, only recently Zhao and co-workers importantly proposed a

phase-field formulation, which enables for modeling the evolution of the metal electrode-SSE interface with the potential for void formation during continuous plating/stripping [87]. Critically, formation of voids at the interface localizes reaction kinetics, leading to formation of current hot spots and potential nucleation of Li-metal filaments at these sites. Consistent with experiments, the authors predict the formation and evolution in void morphology during electrochemical cycling (i.e. plating/stripping) with applied stack pressure, and elucidate the interplay between a series of phenomena including bulk diffusion, Li dissolution/deposition, creep, and the nucleation and annihilation of vacancies. Similar treatments, investigating the formation and evolution of voids at the interface are reported in [88, 89].

Nevertheless, at present, an electro-chemo-mechanical framework which captures: i) the nucleation and evolution of Li-metal filaments, ii) the concurrent fracture of the solid host, and iii) the coupling between mechanical deformation, stress and Li-metal electrodeposition kinetics is missing. Of particular importance in such a framework is also the ability to model the role that heterogeneities in the SSE microstructure (i.e. pores, grain boundaries) play on the coupled fracture behavior of the SSE and concurrent Li-metal filament growth due to electrodeposition.

To address current modeling limitations, in chapter 4 of this thesis, we propose a thermodynamically-consistent, electro-chemo-mechanical gradient theory coupled with damage, which models the phenomenon of Li-metal filament growth inside SSEs. Critically, the proposed framework elucidates the role that heterogeneities in the SSE microstructure (i.e. pores, cracks, grain boundaries) play on the coupled fracture of the SSE and concurrent Li-metal filament growth due to electrodeposition. In particular, through the proposed framework, we demonstrate the capacity to capture intergranular and transgranular growth mechanisms of Li-metal filaments, both of which have been experimentally observed [19]. Altogether, commercialization of next-generation all-solid-state battery architectures relies on development of high-fidelity models across the various components of the cell, capable

of capturing the complex interplay between electro-chemo-mechanical phenomena coupled with fracture. Towards this goal, the research work outlined in this thesis seeks to provide a series of theoretical frameworks – which in conjunction with experimental efforts – can enhance our understanding of the coupled phenomena governing instabilities in all-solid-state architectures in an effort to accelerate their successful commercialization.

The overview on modeling aspects of all-solid-state batteries was adapted with permission from the review work published in:

- Bistri, Donald, Arman Afshar, and Claudio V. Di Leo. "Modeling the chemo-mechanical behavior of all-solid-state batteries: a review." *Meccanica* 56 (2021): 1523-1554.

## **CHAPTER 2**

### **A NON-LINEAR KINETICS INTERFACE ELEMENT FOR MODELING OF MULTI-PARTICLE INTERACTIONS IN LI-ION BATTERY ELECTRODES**

Modeling of chemo-mechanical interactions between active particles in battery electrodes remains a largely unexplored research avenue. Of particular interest from a modeling standpoint is the ability to model the distribution in current (i.e. charge), which may vary across active particles under galvanostatic (i.e. fixed current) charging conditions. This in turn depends on the local stress-coupled electrochemical potential, and may also be affected by mechanical degradation. In this chapter, we formulate and numerically implement a constitutive framework, which captures the complex chemo-mechanical multi-particle interactions in electrode microstructures, including the potential for mechanical degradation. A novel chemo-mechanical surface element is developed to capture the local non-linear reaction kinetics and concurrent potential for mechanical degradation. We specialize the proposed element to model the electrochemical behavior of both (i) a novel anode design for application in LIBs and (ii) a next generation all-solid-state composite cathode, where mechanical interactions are particularly important. In modeling these electrodes, we demonstrate the manner in which the proposed simulation capability may be used to determine optimized electro-chemical and mechanical properties as well as the layout of the electrode microstructure, with a focus on minimizing mechanical degradation and improving electrochemical performance. The work presented in this chapter is adapted with permission from and published in:

- Bistri, Donald, and Claudio V. Di Leo. "Modeling of chemo-mechanical multi-particle interactions in composite electrodes for liquid and solid-state Li-ion batteries." *Journal of The Electrochemical Society* 168.3 (2021): 030515.

## 2.1 Introduction

Lithium-ion batteries (LIBs) have become the dominant energy storage source in a number of areas including consumer electronics and electric vehicles [1]. A number of research avenues exist for the continued improvement of LIBs including improved charging times, increased operational lifespan, expanded capacity, and improved safety [90, 91]. In pursuit of these improvements, research efforts have shifted from conventional liquid LIBs towards next generation all-solid-state battery (SSB) architectures with enhanced current density ( $\approx 3860$  mAh/g), wider electrochemical window (0-5 V), and improved safety [2, 3, 5, 6, 9]. However, battery designs, be it for conventional liquid LIBs or next-generation SSBs, suffer from inherent mechanical degradation across different cell constituents, which in turn limit their electrochemical performance. Upon intercalation/de-intercalation of lithium ions, current electrode designs undergo large inhomogeneous volumetric changes, which give rise to large mechanical stresses and inelastic effects [26, 27, 92, 93]. This in turn can lead to mechanical degradation, which for example may take the form of fracture of the individual constituents or debonding of active particles from their surrounding matrix, as has been reported in the literature [94, 95, 96, 97, 98]. The role of mechanical stresses and mechanical degradation on electrochemical performance is even more critical in all-solid-state architectures owing to the presence of a stiff solid electrolyte. Aside from conventional fracture mechanisms at the electrode level [31, 99, 100], inherent mechanical instabilities associated with: i) metal filament growth [58, 60, 101], and ii) interphase formation and interphase induced fracture of the solid-state electrolyte [18, 41] have hindered commercialization of next generation SSBs as outlined in chapter 1.

Research to date on the coupling between mechanical degradation and electrochemical performance remains mostly limited to study of single-particle systems (cf. [95, 102]). As such, our understanding of the role of mechanical degradation on electrochemical performance, including the effect of mechanics on interfacial kinetics, remains rather limited.

From both an experimental and modeling perspective, it is thus critical to understand the complex interplay of mechanical deformation and chemical processes. This is particularly critical in the context of densely-packed microstructures traditionally employed in design of composite electrodes for commercial batteries.

Conventional composite electrode architectures build upon a compact conglomerate of active particles confined on their exterior by a matrix supporting percolation pathways for ionic conduction in addition to complementary additives for electronic conduction [16, 103, 104]. Owing to their compact nature, composite electrodes experience a complex interplay of chemo-mechanical interactions as Li-ions are inserted/extracted from the active particles, thus leading to emergence of a complex stress field as the particles swell/deswell against the confining matrix. In addition to the mechanical behavior, there are concurrent electrochemical processes as current locally varies between particles in a composite electrode. From a modeling perspective, there is a need to capture multi-particle interactions — both mechanical and chemical — for these densely packed architectures in order to understand how variations in material properties and microstructure composition affect mechanical degradation and ultimately electrochemical performance.

Significant research efforts have been undertaken from a theoretical standpoint to understand the chemo-mechanical behavior of single active particles, cf. Zhao *et al.* [105]. Modeling frameworks have been developed to different levels of complexity for both intercalation electrodes with deformations usually confined within the elastic regime [34, 35, 106, 107, 108, 109], and conversion electrodes undergoing volumetric strains in the order of more than 100% and experiencing large elastic-plastic deformations [14, 42, 110]. Theories coupling large elastic-plastic deformations with large volumetric swelling due to diffusion of Li-ions have been formulated [93, 111, 112, 113] and specialized to capture the chemo-mechanical behavior of single Si-particles [114]. A key constituent is the ability of these frameworks to capture the experimentally measured electrochemical response. Following a combination of experimental measurements and numerical simulations in a

Li-ion half cell, Bucci et al. [115] adopted the theory of Bower et al. [111] to characterize the behavior of amorphous thin film Si-electrodes. The effect of elastic-plastic deformation on electrochemical performance of geometrically complex a-Si anodes experimentally realized by Wu et al. [116] was investigated in the work of Di Leo et al. [42].

While much has been done from a theoretical standpoint to model the chemo-mechanical behavior of single-particle systems, few studies have considered the combined multi-particle behavior of composite electrodes. In modeling the multi-particle behavior of electrodes, one must consider both mechanical and chemical interactions which occur between particles. Mechanical interactions arise from transfer of forces between particles either through direct particle-to-particle contact or through contact with the surrounding matrix. Early modeling efforts aimed at capturing mechanical interactions between active particles in electrodes centered on applications to traditional liquid LIBs. Experimentally, Lee et al. [117] studied mechanical interactions in Si-nanopillars using both in-situ and ex-situ characterization techniques to explore how mechanical interactions among neighboring nanopillars impacted reaction kinetics and their susceptibility to fracture upon lithiation. Numerical finite-element simulations of a 2D porous graphite/binder electrode microstructure were performed by Rahani et al. [118] to model mechanical interactions between active particles and PVDF binders. In a similar effort, Higa and Srinivasan [119] investigated the role of both particle size and binder stiffness on the mechanical stresses induced in active particles, reporting a decrease in stress with decrease in particle size and binder stiffness. Garcia et al. [120] modeled 2D porous electrodes of  $\text{Li}_x\text{Mn}_2\text{O}_4$  spherical particles under a linear-elastic finite-element framework. From a design standpoint, the effect of both packing density and particle size were studied. Microstructure configurations with dense particle aggregates were assessed to be detrimental to electrochemical performance, lowering the utilization of active material and leading to higher mechanical stresses induced in the particles.

Recently, numerical simulations of 3D reconstructed composite electrode microstruc-



tures under a continuum framework have been reported by Zhao and co-workers [103, 104]. The interplay between mechanical stresses and Li-ion diffusion was explored to quantify its role on capacity for two representative microstructures including: i) an NMC cathode undergoing small volumetric changes upon Li insertion, and ii) an SnO anode where volumetric changes upon lithiation are more significant. These simulations were later expanded by the same group to model damage both at the particle level and particle interface in NMC composite cathodes [121, 122]. Efforts of a similar nature are also reported by Hoffman and co-workers [123], where stochastic microstructure models were used for representative graphite anodes.

While these works represent a step towards modeling of complex chemo-mechanical interactions in composite electrodes, development of a general computational framework, along with a suitable numerical implementation, capable of capturing appropriate galvanostatic charging conditions remains at its infancy and is addressed in this chapter. *Of interest here is thus the development of a general computational framework, which captures the role of local variations in chemo-mechanical properties and microstructure composition on the mechanical integrity and electrochemical performance of different electrode microstructures.*

Within the context of all-solid-state batteries, the most notable efforts in modeling of composite electrodes — with a focus on the role of mechanics — are by Bucci and co-workers [31, 99, 100]. In Bucci *et al.* [99], a joint analytical and finite-element framework is reported to model the effect of stresses in Silicon active particles within an SSE composite electrode. A critical Silicon to SSE volume fraction was reported above which mechanical stresses due to multi-particle interactions have a dominant effect on electrochemical performance and one is under-utilizing the added active material from a capacity standpoint. This work was subsequently extended to account for mechanical damage through use of cohesive elements both at the active particle-electrolyte interface [31] and the SSE itself [100]. Interestingly, compliant electrolytes were assessed to be more prone to micro-

cracking. Additionally, fracture initiation at the active particle-SSE interface was reported for most combinations of SSE material properties, provided the active particles undergo 7.5% change in volume upon lithiation. From a design standpoint, the authors assessed initiation of fracture to occur regardless of the size of active particle, claiming that nanostructured electrodes need not perform better from a mechanical standpoint. In the context of all-solid-state batteries, the role of mechanical interactions on transport properties has been recently explored in the work of Behrou and Maute [124]. Here, the effect of damage on mechanical behavior and effective transport properties was studied using a non-local damage model with both mechanical stiffness and diffusivity of active particles penalized with damage evolution. In the same spirit, the role of mechanics on effective transport properties and electrochemical performance of SSBs with increase in active material was also investigated in the work of Al Siraj et al. [125]. A critical active material volume fraction was determined above which electrochemical performance ceases to improve as conduction pathways are significantly decreased.

While research efforts have been devoted to capturing mechanical interactions at the electrode microstructure, modeling of the concurrent *chemical interactions between active particles* arising from diffusion of Li-ions through the electrolyte remains largely unexplored. An inherent obstacle in modeling of chemical interactions between particles is implementation of true galvanostatic conditions. During galvanostatic charging, total current over all particles is held constant, but individual current distribution at each particle surface remains unconstrained and depends on the local stress-coupled non-linear reaction kinetics. This chapter is dedicated to formulating and numerically implementing a novel theoretical framework based on use of a chemo-mechanical interface element – analogous in form to conventional cohesive elements used in fracture mechanics – to model the stress-coupled non-linear kinetics of ionic transport at the particle/electrolyte interface. We deploy this new element to model galvanostatic charging of composite electrodes and study their electrochemical performance. The proposed interface element is introduced at the surface of

active particles within the numerically discretized composite electrode microstructures to capture the non-linear stress-coupled reaction kinetics. Further, mechanical degradation of the interface is concurrently modeled — accounting for a loss in reactivity due to damage — to assess the interplay of mechanical stresses and damage on the behavior of the composite electrode.

We present the theoretical and numerical framework in Sect. 2.2. This section details the continuum description of a representative volume element (RVE) of the microstructure, Sect. 2.2.1, followed by a detailed description of the constitutive modeling and numerical discretization of particles interface in Sect. 2.2.2 and particle bulk in Sect. 2.2.3. Subsequently, we showcase the capabilities of our numerical framework in Sect. 2.3 through a simple demonstration of a two-particle RVE. We then apply our numerical framework to model experimentally relevant electrode microstructures. First, in Sect. 2.4, we investigate a traditional liquid LIB electrode design composed of multiple double-walled hollow nanotubes. Here, only chemical interactions between the multiple nanotubes are considered and we explore the role of material properties and interfacial damage on electrode performance. As later detailed, in chapter 3, we specialize the proposed numerical framework and model a representative solid-state composite cathode where mechanical load transfer through the stiff solid-electrolyte is critical and can significantly affect structural integrity and electrochemical performance of the battery.

## **2.2 Theoretical and Numerical Framework**

We describe the multi-particle behavior of a composite electrode by considering various scales. We consider first a representative volume element (RVE) of the electrode microstructure through a continuum description. Subsequently, we focus on the behavior of individual active particles and finally transition to the behavior of interfaces. This description is shown schematically in Fig. 2.1 with a focus on the treatment of electrochemical behavior of the composite electrode.

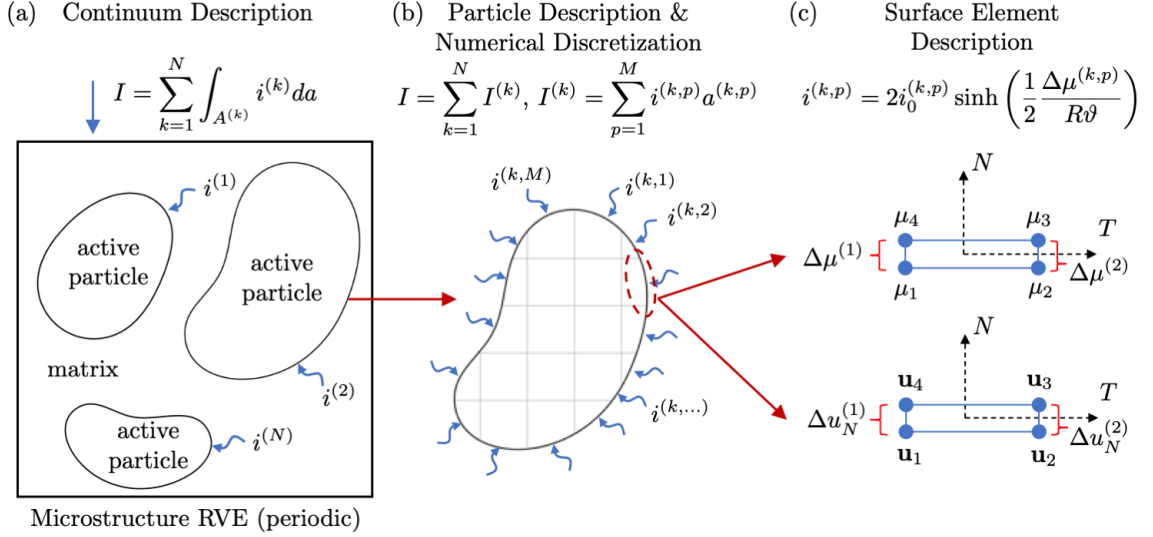


Figure 2.1: Schematic description of the theoretical and numerical framework employed with a focus on electro-chemistry. (a) Continuum description of the microstructure RVE with  $N$  particles and galvanostatic conditions enforced. (b) Particle description showing discretization of current over  $M$  elements over each particle surface. (c) Description of the surface element in which non-linear reaction kinetics relate local chemical potential jumps at each node pair to the current density at each element. Reproduced with permission from [17].

### 2.2.1 Continuum Microstructural RVE Description

We consider first the continuum behavior of a representative volume element (RVE) of the electrode microstructure as shown in Fig. 2.1(a). A critical aspect of capturing the electro-chemo-mechanical behavior of the electrode microstructure is proper implementation of galvanostatic charging conditions. Here, total current  $I$  over the entire domain is held constant, while current density over a particular particle,  $i^{(k)}$ , is free to fluctuate across the particle surface. To ensure galvanostatic charging conditions, we must enforce

$$I = \sum_{k=1}^N I^{(k)}, \quad \text{with} \quad I^{(k)} = \int_{A^{(k)}} i^{(k)} dA \quad (2.2.1)$$

where  $N$  is the number of particles in the RVE. Eqn. (2.2.1) serves as a constraint, which must be numerically enforced over the entire simulation domain. We assume from the onset *that voltage across all particles surface is constant*. We thus restrict ourselves to

physical problems in which transport of ionic species through the matrix is sufficiently fast and variations in electric potential through the electrolyte are negligible. Consistent with this assumption, electric potential across the microstructure RVE is then constant throughout. From a numerical perspective, this has the added benefit that we may exclusively focus on the interfacial kinetics and active particle behavior without having to resolve ion migration and the associated electric field across the conducting matrix. We note that the proposed numerical framework may be extended to remove the constraint that voltage be a constant across all particle surfaces by considering the physics of ion migration through the RVE conducting matrix. The development presented here is a simplification of this more general case, but should serve equally useful in the development of future models, which incorporate this additional physics.

To model non-equilibrium interfacial reaction kinetics, we employ the phenomenological Butler-Volmer equation. At every point on the surface of a particle, current density,  $i$  is related to the overpotential,  $\eta$  through (cf. Bazant [126])

$$i = i_0(\bar{c}) \left( \exp \left( -\frac{\alpha F \eta}{R \vartheta} \right) - \exp \left( \frac{(1 - \alpha) F \eta}{R \vartheta} \right) \right). \quad (2.2.2)$$

Here,  $i_0(\bar{c})$  is the concentration dependent exchange current density,  $R$  - the gas constant,  $\vartheta$  - the absolute temperature,  $F$  - the Faraday constant, and  $\alpha$  - a symmetry factor, representative of the fraction of surface overpotential promoting anodic or cathodic reaction at the electrode interface, such that  $0 < \alpha < 1$ . The exchange current density,  $i_0(\bar{c})$  depends on the species concentration through

$$i_0(\bar{c}) = F k_0 (1 - \bar{c})^\alpha \bar{c}^{(1-\alpha)}, \quad (2.2.3)$$

where  $k_0$  denotes the reaction constant, while  $\bar{c}$  represents the normalized species concentration detailed in Sect. 2.2.3. From thermodynamics, we may relate the overpotential,  $\eta$  to a jump in chemical potential across the particle-electrolyte interface through

$\eta = \Delta\phi - \Delta\phi^{eq} = -\Delta\mu/F$ , with  $\Delta\mu$  the jump in chemical potential of the diffusing species at the reaction site of interest <sup>†</sup>. This definition of  $\eta$ , along with the specialization  $\alpha = 0.5$ , which is typical of elementary single-electron transfer reactions, allows us to write (2.2.2) as

$$i = 2i_0(\bar{c}) \sinh\left(\frac{1}{2} \frac{\Delta\mu}{R\vartheta}\right). \quad (2.2.4)$$

Importantly, this yields a relationship for the local current density at a point on the particle's surface as a function of the chemical potential jump at the same location. Finally, for the microstructure RVE as shown schematically in Fig. 2.1(a), we prescribe periodic boundary conditions.

**Particle description and numerical discretization:** Consider now a single particle discretized with finite elements as shown schematically in Fig. 2.1(b). The behavior of this particle can be described through its interfacial and bulk behavior. For clarity, we discuss these behaviors separately.

### 2.2.2 Chemo-Mechanical Interfacial Particle Behavior

Focusing first on the chemo-mechanical interfacial behavior, the particle is discretized with finite elements resulting in  $M$  elements on the surface of the particle. Galvanostatic conditions are now enforced by writing the constraint (2.2.1) in discretized form as

$$I = \sum_{k=1}^N I^{(k)} \quad \text{with} \quad I^{(k)} = \sum_{p=1}^M i^{(k,p)} a^{(k,p)} \quad (2.2.5)$$

Here,  $I^{(k)}$  is the total current over the  $k$ -th particle, while  $i^{(k,p)}$  and  $a^{(k,p)}$  denote the current density and area of the  $p$ -th surface element of the  $k$ -th particle. It is important to recall that we allow for and expect current density variations throughout the surface of the particles. Hence, we make no assumptions about current density at any point of the particles surface, rather we only enforce the galvanostatic constraint that the total current,  $I$  be a constant.

---

<sup>†</sup>Consistent with [42], we define  $\eta = (1/F)(\mu_{Li} - (\mu_{Li^+} + \mu_{e^-}))$

To enforce the galvanostatic constraint — and motivated by the physical nature of the problem containing non-linear reaction kinetics at the particle/matrix interface — we introduce surface elements to discretize this interface as schematically shown in Fig. 2.1(c). These elements (analogous to traditional cohesive elements in fracture mechanics) are zero-thickness elements, which can be thought of as lines in two-dimensional simulations or surfaces in three-dimensional simulations. Note that the nodes (and hence degrees of freedom) of the bulk continuum elements used to discretize the particle and the nodes on one side of the surface elements are shared.

We enforce the constraint that voltage across all particles be a constant by constraining the chemical potential degree of freedom on the surface element *adjacent to the matrix* to be equal to  $-\bar{V}F$ , with  $\bar{V} \stackrel{\text{def}}{=} (V - V_0)$ ,  $V$  the electrode voltage, and  $V_0$  a reference voltage. That is, in Fig. 2.1(c), if we envision that  $\mu_1$  and  $\mu_2$  are connected to the active particles, and  $\mu_3$  and  $\mu_4$  are connected to the conducting electrolyte matrix, we restrict our surface elements such that  $\mu_3 = \mu_4 = -\bar{V}F$  (c.f. Di Leo et al. [42]).

We may now write the reaction kinetics (2.2.4) for the current density,  $i^{(k,p)}$  at an element on the surface in a discretized form

$$i^{(k,p)} = 2i_0^{(k,p)} \sinh \left( \frac{1}{2} \frac{\Delta\mu^{(k,p)}}{R\vartheta} \right). \quad (2.2.6)$$

with  $\Delta\mu^{(k,p)}$  - the chemical potential jump for the p-th surface element on the k-th particle. Note that the concentration-dependent exchange current density,  $i_0^{(k,p)}(\bar{c})$  is computed at each surface element in order to account for variations in concentration along the particle surface. The chemical potential jump,  $\Delta\mu^{(k,p)}$  is computed using numerical interpolation between the chemical potential jumps  $\Delta\mu^{(1)} = \mu_4 - \mu_1$  and  $\Delta\mu^{(2)} = \mu_3 - \mu_2$ , details of which can be found in Appendix A.2.

The mechanical behavior of the surface elements is also critical as it allows one to capture the manner in which the particle-matrix interface can delaminate due to mechanical

stresses. The mechanical behavior relates displacement jumps,  $\Delta \mathbf{u}$ , across the interface to the associated tractions  $\mathbf{t}$  — in a fashion analogous to how jump in chemical potential,  $\Delta \mu$  relates to the current density,  $i$  across the interface. Broadly, we allow for a finite (yet large) stiffness of the interface, which relates the separation of the surface element nodes to the tractions (stresses) generated at the interface. Damage initiation and evolution criteria are then prescribed to capture interface delamination.

Restricting ourselves to a two-dimensional formulation, the normal  $t_N$ , and tangential  $t_T$ , tractions at the interface prior to damage initiation are computed through,

$$t_N = K_N \Delta u_N, \quad \text{and} \quad t_T = K_T \Delta u_T, \quad (2.2.7)$$

with  $\Delta u_N$  and  $\Delta u_T$  denoting the normal and tangential separations respectively. Note that in Fig. 2.1(c), for brevity, we have only schematically depicted the normal displacement jump (i.e. separation). Following Camanho and Da Vila [127], damage initiation at the interface is modeled following a quadratic traction function of the form,

$$\left( \frac{\langle t_N \rangle}{t_N^{\text{cr}}} \right)^2 + \left( \frac{t_T}{t_T^{\text{cr}}} \right)^2 = 1, \quad (2.2.8)$$

where  $t_N^{\text{cr}}$  and  $t_T^{\text{cr}}$  represent the normal and tangential cohesive strengths (i.e. the peak value these tractions may attain when the deformation is purely normal or purely tangential to the interface), and  $\langle \cdot \rangle$  denotes the Macaulay bracket.

To model the evolution in mechanical damage, a scalar variable,  $D_{\text{mech}}$  is introduced, which denotes the overall state of mechanical damage for an element on the surface of the active particle. As the state of damage at the interface evolves, tractions decay linearly with



mechanical damage and are computed through

$$t_N = \begin{cases} (1 - D_{\text{mech}})K_N\Delta u_N, & \text{if } K_N\Delta u_N \geq 0, \\ K_N\Delta u_N, & \text{otherwise (to avoid surface interpenetration),} \end{cases} \quad (2.2.9)$$

$$t_T = (1 - D_{\text{mech}})K_T\Delta u_T.$$

To model the evolution of damage, it is common to introduce an effective displacement jump,  $\delta_m = (\langle \Delta u_N \rangle^2 + \Delta u_T^2)^{1/2}$ , which concurrently accounts for both normal and tangential opening at the interface. We may then model the linear softening of tractions due to mechanical damage through an evolution equation for  $D_{\text{mech}}$  of the form

$$D_{\text{mech}} = \frac{\delta_m^f(\delta_m^{\text{max}} - \delta_m^0)}{\delta_m^{\text{max}}(\delta_m^f - \delta_m^0)}, \quad D_{\text{mech}} \in [0, 1]. \quad (2.2.10)$$

Here,  $\delta_m^0$  is the effective displacement jump at damage initiation,  $\delta_m^f$  is the effective displacement jump at complete failure, and  $\delta_m^{\text{max}}$  is the maximum value of the effective displacement attained during the loading history, a monotonically increasing quantity. Critically, this enforces that damage processes are irreversible in nature, namely once the particle-electrolyte interface delaminates, it can not heal.

Considering positive normal displacement jumps, the effective displacement jump at damage initiation,  $\delta_m^0$  may be computed as

$$\delta_m^0 = \delta_N^0 \delta_T^0 \sqrt{\frac{1 + \beta^2}{(\delta_T^0)^2 + (\beta \delta_N^0)^2}} = \frac{t_N^{\text{cr}}}{K_N} \frac{t_T^{\text{cr}}}{K_T} \sqrt{(1 + \beta^2) \left( \left( \frac{t_T^{\text{cr}}}{K_T} \right)^2 + \beta^2 \left( \frac{t_N^{\text{cr}}}{K_N} \right)^2 \right)^{-1}}. \quad (2.2.11)$$

In writing (2.2.11), we have made use of the fact that  $\delta_N^0 = t_N^{\text{cr}}/K_N$  and  $\delta_T^0 = t_T^{\text{cr}}/K_T$ . Additionally,  $\beta = \Delta u_T/\Delta u_N$  denotes the mode-mixity parameter, which accounts for the different contributions sourcing from mode I (normal) and mode II (tangential) loading of the active particle-electrolyte interface. Similarly, the effective displacement jump at

complete failure,  $\delta_m^f$  may be computed as

$$\delta_m^f = \frac{2(1 + \beta^2)}{K\delta_m^0} \left[ \left( \frac{1}{G_N} \right) + \left( \frac{\beta^2}{G_T} \right) \right]^{-1} \quad (2.2.12)$$

with  $G_N$  and  $G_T$ , the normal and tangential *fracture energies*. In writing (2.2.12), we further specialize our model such that  $K = K_N = K_T$ .

As shown from (2.2.11) and (2.2.12), the material properties for this model are the stiffnesses, presumed to obey  $K = K_N = K_T$ , the fracture energies  $\{G_N, G_T\}$ , and the critical tractions for damage initiation  $\{t_N^{\text{cr}}, t_T^{\text{cr}}\}$ . Of these parameters,  $K$  may be prescribed arbitrarily provided it is large enough not to introduce artificial compliance in the simulation. The physical material parameters are thus only the critical normal and tangential tractions  $\{t_N^{\text{cr}}, t_T^{\text{cr}}\}$ , and the fracture energies  $\{G_T, G_N\}$ . Note that the mode-mixity parameter,  $\beta = \Delta u_T / \Delta u_N$  depends on the loading path and is not a material property. The limiting case  $\beta \rightarrow 0$  corresponds to pure normal separation, while the limiting case  $\beta \rightarrow \infty$  corresponds to pure shear.

To impart stability to our numerical solver, we employ a viscous regularization scheme to model the evolution of mechanical damage at the interface. Following Hamitouche et al. [128], we introduce a small viscosity,  $\lambda$  (small with respect to the characteristic time increment) and compute the viscous mechanical damage as

$$D_{\text{mech}}^v = D_{\text{mech}} - \lambda \frac{\dot{\delta}_m}{\delta_m}. \quad (2.2.13)$$

Henceforth, when referring to mechanical damage, we are employing the viscous damage definition above. Viscosity values employed in all simulations in this work ranged between 0.1 and 0.3 s.

Finally, to model the effect of mechanical damage on reaction kinetics, current density

across the interface, viz. (2.2.6), is penalized through

$$\dot{i}^{(k,p)} = (1 - D_{\text{chem}}) 2\dot{i}_0^{(k,p)} \sinh\left(\frac{1}{2} \frac{\Delta\mu^{(k,p)}}{R\vartheta}\right), \quad \text{with } D_{\text{chem}} \in [0, 1], \quad (2.2.14)$$

where  $D_{\text{chem}}$  denotes the chemical damage. We specialize the relationship between  $D_{\text{mech}}$  and  $D_{\text{chem}}$  in Sect. 2.4.2 and Sect. 3.1 when we specialize our models to a particular physical system. As captured through (2.2.14), this model allows one to capture the loss of chemical reactivity at a point on the surface of an active particle due to concurring mechanical damage. The effect of this coupling will be studied in detail in the simulation results shown in this thesis.

### 2.2.3 Bulk Particle Behavior

We present here, for completeness, a brief summary of the coupled chemo-mechanical, diffusion-deformation theory for modeling the bulk behavior of active particles. Details of the theoretical framework may be found in Di Leo et al. [42]. This framework models coupling of species diffusion with large elastic-plastic deformations due to volumetric changes caused by the diffusing species. The active particle is treated as a homogeneous mixture of the active material and Li, with the molar concentration of Li per unit reference volume denoted by  $c_{\text{R}}$  and per unit current volume by  $c = J^{-1}c_{\text{R}}$ , with  $J = \det \mathbf{F}$ , and  $\mathbf{F}$  the deformation gradient. We further define a normalized concentration  $\bar{c} = c_{\text{R}}/c_{\text{max}} \in [0, 1]$ . We employ the decomposition  $\mathbf{F} = \mathbf{F}^e \mathbf{F}^p \mathbf{F}^s$  of the deformation gradient into elastic, plastic and swelling parts, where

$$\mathbf{F}^s = (J^s)^{1/3} \mathbf{1}, \quad \text{with } J^s = 1 + \Omega(c_{\text{R}} - c_0), \quad (2.2.15)$$

is the swelling distortion,  $\Omega$  is a constant partial molar volume of the intercalating Li in the host material, and  $c_0$  is the initial concentration of Li. Further, we assume  $J^p = \det \mathbf{F}^p = 1$ ,

such that plastic deformation be volume conserving. The Cauchy stress is given by

$$\mathbf{T} = J^{e-1} \left( 2G(\bar{c})\mathbf{E}_H^e + \left( K(\bar{c}) - \frac{2}{3}G(\bar{c}) \right) (\text{tr} \mathbf{E}_H^e) \mathbf{1} \right), \quad (2.2.16)$$

where  $G(\bar{c})$  and  $K(\bar{c})$  represent the concentration-dependent shear and bulk moduli respectively, while  $\mathbf{E}_H^e$  denotes the spatial logarithmic elastic strain. To complete the mechanical portion of the theory, plastic distortion is taken to evolve according to

$$\dot{\mathbf{F}}^p = \mathbf{D}^p \mathbf{F}^p, \quad \text{with} \quad \mathbf{D}^p = \dot{\bar{\epsilon}}^p \left( \frac{3\mathbf{M}_0^e}{2\bar{\sigma}} \right), \quad \dot{\bar{\epsilon}}^p \geq 0, \quad \mathbf{F}^p(\mathbf{X}, 0) = \mathbf{1}, \quad (2.2.17)$$

where  $\bar{\sigma} \stackrel{\text{def}}{=} \sqrt{3/2} |\mathbf{M}_0^e|$  defines an equivalent tensile stress, and  $\dot{\bar{\epsilon}}^p$  denotes an equivalent tensile plastic strain rate.

Turning attention to diffusion, spatial flux  $\mathbf{j}$ , of the intercalating Li is taken to depend on the spatial gradient  $\text{grad } \mu$ , of the chemical potential through

$$\mathbf{j} = -m \text{grad } \mu, \quad \text{with} \quad m = \frac{D_0}{R\vartheta} c(1 - \bar{c}) \geq 0 \quad \text{the mobility.} \quad (2.2.18)$$

Here,  $D_0$  is a constant diffusion coefficient. The chemical potential of Li in the active particle is given by,

$$\mu = \mu^0 + R\vartheta \ln \left( \gamma \frac{\bar{c}}{1 - \bar{c}} \right) - \Omega \frac{1}{3} \text{tr} \mathbf{M}^e, \quad (2.2.19)$$

where we have defined an activity coefficient  $\gamma$  through  $R\vartheta \ln(\gamma) = \sum_{n=2}^7 a_n \cdot n \cdot \bar{c}^{(n-1)}$ , whose coefficients  $a_n$  are fitted to experimental open circuit potential data. Importantly, the chemical potential, (2.2.19) is *stress-coupled* through the Mandel stress,  $\mathbf{M}^e$  which may be related to the traditional Cauchy stress,  $\mathbf{T}$  through an elastic rotation and elastic volumetric scaling [42].

The above fields are governed by two partial differential equations expressed in the deformed body. As is standard, the mechanical problem (displacement field) is governed by a local force balance,  $\text{div} \mathbf{T} = \mathbf{0}$ , with appropriate boundary conditions requiring that dis-

placement or traction be prescribed at a given point on the exterior of the body. The lithium diffusion problem (chemical potential field) is governed by mass balance,  $\dot{c}_R = -J \operatorname{div} \mathbf{j}$ , where appropriate boundary conditions require one to either prescribe the chemical potential or the spatial flux at a given point on the surface of the body. Finally, we note that current density,  $i$  as described in Sect. 2.2.2 and normal flux of species  $j = \mathbf{j} \cdot \mathbf{n}$ , with  $\mathbf{n}$ , the normal to the surface of an active particle at a point, are related simply through  $j = -i/F$ . Details of the numerical implementation, with a focus on the implementation of the chemo-mechanical surface elements, are presented in Appendix A following the work of Di Leo [129] and Chester et al. [130].

Next, in Sect. 2.3 we illustrate the capability of the proposed framework to (i) model galvanostatic conditions and (ii) capture non-uniform current distribution across particles along with the role of mechanical delamination at the particle surface through a simple demonstration of a two-particle composite electrode RVE.

### 2.3 Numerical Framework Demonstration

To illustrate the capabilities of our numerical framework, we present here a simple simulation of a two particle system. Both particles are embedded in an elastic electrolyte matrix and their surfaces are discretized with the chemo-mechanical surface elements detailed in Sect. 2.2.2 above. As described by (2.2.14), we allow here for mechanical degradation of the interface due to normal stresses leading to a loss in local reactivity. The particles are modeled as chemo-elastic (no plastic deformation) and incur 2% volume decrease when fully lithiated. The specific material parameters are the same as those used in Sect. 3.1 for a LCO-LGPS composite electrode system. For this illustration, we impose galvanostatic charging conditions at a C-Rate of 1C, with the additional aforementioned constraint that voltage over the particles surface be a constant. Mechanically, we impose periodic boundary conditions on the electrode domain, effectively treating it as a representative volume element (RVE). For illustration purposes, we induce significant

variations in current distribution between particles by assigning the left particle a reaction constant,  $k_0 = 9 \cdot 10^{-6} \text{ mol}/(\text{m}^2\text{s})$ , while the right particle has a reaction constant,  $k_0 = 9 \cdot 10^{-7} \text{ mol}/(\text{m}^2\text{s})$ .

Fig. 2.2(a) shows the total current flowing to the left (blue line) and right particle (orange line), as well as into the entire simulation domain (yellow line) as a function of time. We observe that we can successfully maintain galvanostatic charging conditions, while current distribution to the two particles varies in time. Until time  $t = t_a$ , no interfacial damage occurs and the total current is distributed such that more current (i.e. charge) flows to the left particle owing to its faster reaction kinetics.

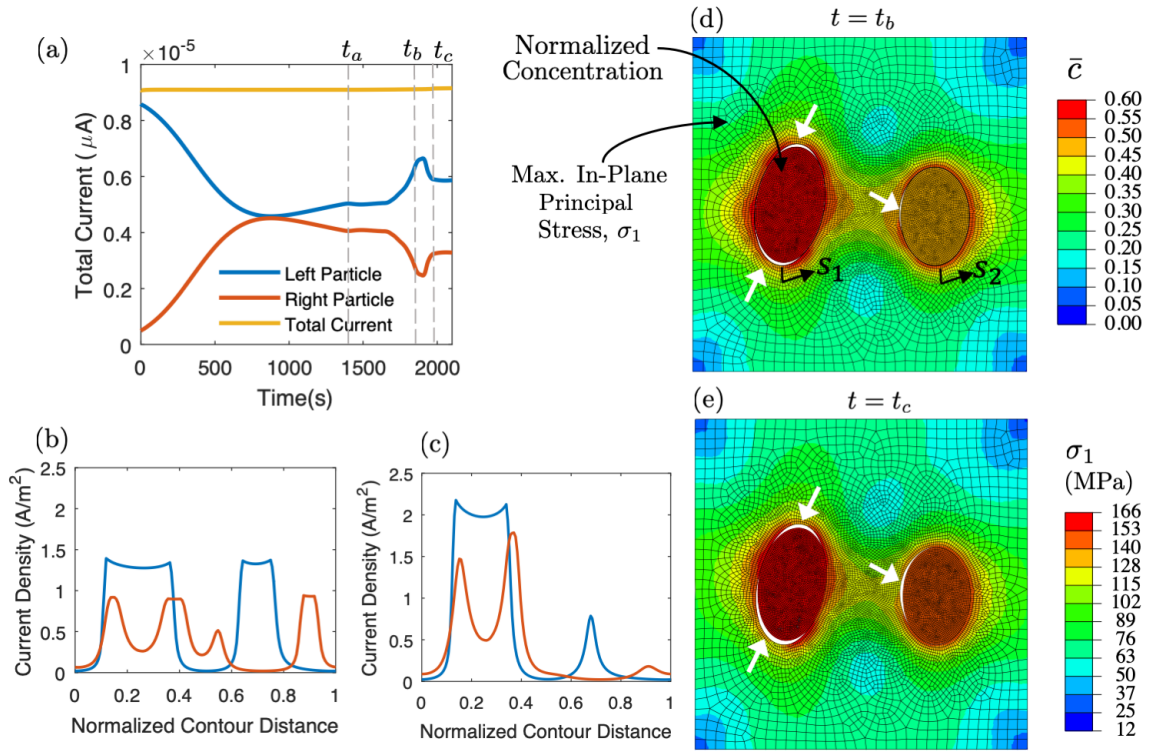


Figure 2.2: Example of a two-particle numerical simulation. (a) Total current distribution to both particles as well as the entire simulation domain, illustrating the ability to capture galvanostatic charging conditions. (b - c) Local current densities as a function of the normalized distance ( $s_1, s_2$ ) along the particle surface taken at time  $t=t_b$  and  $t=t_c$ . (d - e) Contours of maximum in-plane principal stress,  $\sigma_1$  over the matrix and normalized concentration,  $\bar{c}$  over the particle domain taken at time  $t=t_b$  and  $t=t_c$ . Also illustrated in white are regions of decohered interface. Reproduced with permission from [17].

After  $t=t_a$ , interfacial damage occurs over both particles, with mechanical decohesion

starting in the left particle first owing to its higher extent of lithiation (and hence higher mechanical stresses at the interface). Mechanical degradation now causes current to redistribute over both particles, as dictated by the interplay of two mechanisms: i) the variation in reaction constant among particles, and ii) the state of mechanical damage on the particle surface. As interfacial damage across both particles evolves while  $t_a < t < t_b$ , the interplay of these mechanisms first leads to an increase in current flowing to the left particle, while current flowing to the right particle decreases to maintain the galvanostatic charging condition.

Fig. 2.2(b) shows the distribution in current density over each particle as a function of the normalized contour distance (i.e perimeter) of the particle at time  $t=t_b$ . The start of the normalized contour variables is noted in Fig. 2.2(d) as  $s_1$  and  $s_2$ . We can clearly observe the inherent coupling between mechanical degradation and interface kinetics (i.e current density). Here, we observe regions over the particles surface with zero (or near zero) current density. These regions, marked by white arrows in Fig. 2.2(d), represent elements at the surface of both particles which have completely decohered and are now chemically isolated and unable to sustain reaction. In Fig. 2.2(d), we show contours of normalized concentration,  $\bar{c}$ , over the particle simulation domains, and contours of the maximum in-plane principal stress,  $\sigma_1$  over the electrolyte matrix at time  $t = t_b$ .

After time  $t=t_b$ , a significant portion of the surface of the left particle has decohered and can no longer sustain sufficiently large currents. Thus, there is a decrease in current to the left particle as shown in Fig. 2.2(a). In turn, to preserve a state of galvanostatic charging, the right particle sees an increase in total current. Fig. 2.2(c) illustrates the distribution in current density over each particle as a function of the normalized contour distance at time  $t = t_c$ . Across both particles, we observe that most of the interface can no longer carry any significant current (i.e. ability to sustain reaction). In turn, the interface portions which remain intact carry a higher current density when compared to Fig. 2.2(b), since the same amount of total current prescribed to the electrode domain needs to now distribute over a

smaller active area available for reaction. Fig. 2.2(e) shows the corresponding simulation results at  $t = t_c$ , where we can observe significant damage accumulated now over the surface of both particles.

This simple numerical example serves to illustrate the ability of our numerical framework — enabled by the development of chemo-mechanical surface elements — to capture: i) the chemo-mechanical interactions between particles under galvanostatic charging and the associated non-uniform current distribution to different particles, and ii) the non-uniform variation in local current density which develops across each particle.

In Sect. 2.4 to follow, we deploy this numerical framework to study mechanical integrity and electro-chemical performance in composite electrode systems of relevance to liquid LIBs.

## 2.4 Multi-particle interactions in double walled a-Si nanotube electrodes

We consider now a multi-particle electrode composed of hollow double-walled a-Si nanotubes, which are chemically connected, but mechanically isolated, representative of the limiting case of a liquid LIB in which mechanical stress transfer through the electrolyte is negligible. The simulation mimics the experimental research of Wu et al. [116], who manufactured a new anode architecture composed of an ensemble of double-walled a-Si nanotubes with the particular objective of preventing failure of the solid electrolyte interphase (SEI), see Fig. 2.3(a). As has been studied in the literature, volumetric expansions of active particles can induce large mechanical stresses on the SEI layer, causing it to fracture and fail [44, 131, 132]. The double-walled a-Si nanotubes proposed by Wu et al. [116] consist of an a-Si hollow nanotube, whose exterior is oxidized to form a mechanically stiff  $\text{SiO}_2$  layer, thus forming a double-walled structure. Due to the high relative mechanical stiffness of the exterior  $\text{SiO}_2$  layer when compared to the softer a-Si core, volumetric expansions are accommodated primarily through expansion into the hollow internal cavity, and minimal strains and stresses are incurred by the SEI layer forming on the exterior



surface. In our previous research efforts [42], we investigated the chemo-mechanical behavior of a single hollow double-walled nanotube to gain insight on the coupling between mechanics and chemistry in such a confined geometry. However, we did not address the multi-particle nature of the electrode or the potential for mechanical damage.

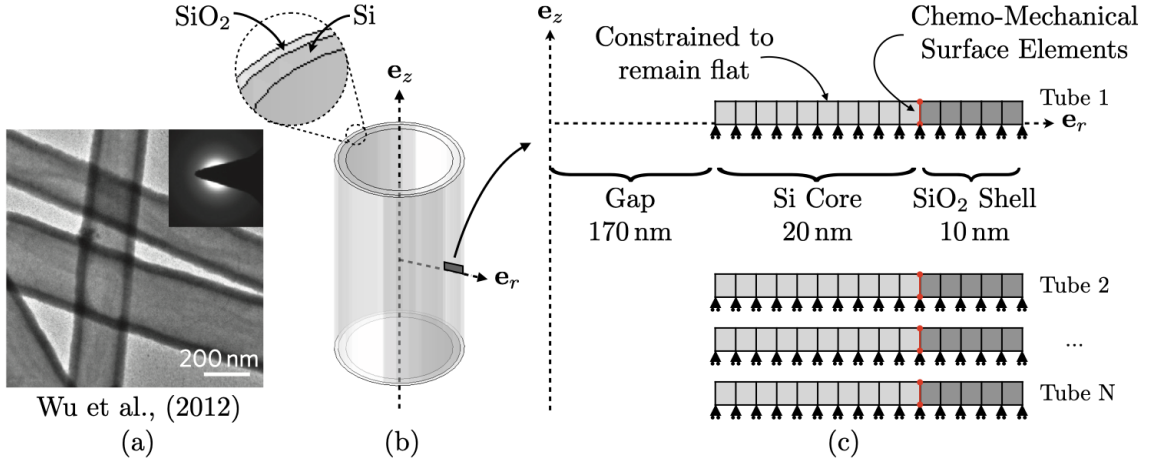


Figure 2.3: Multi-particle modeling of hollow double-walled nanotubes. (a) Shows a representative SEM image from the experiment of Wu et al. Reprinted with permission from [116]. (b) Shows a schematic three-dimensional representation of a single tube denoting the simulation domain as a single sliver of the tube in the axial direction. (c) Shows the numerical discretization using finite elements of the a-Si core and the SiO<sub>2</sub> shell, including the discretization of the interface using chemo-mechanical surface elements. Reproduced with permission from [17].

In this work, each individual tube is modeled through an axisymmetric row of finite elements as shown in Figs. 2.3(b) and (c). Here, we assume the length of the nanotubes to be much larger than their diameter. This effectively enables one to model each nanotube as a row of elements with the flux of Li-ions occurring in the radial direction only. The bottom surface of each row of elements is constrained to have zero displacement in the  $e_z$  direction, while the top surface is constrained to remain flat, but may displace. The simulation domain is broken into two parts, namely an a-Si core and the confining SiO<sub>2</sub> shell, with chemo-mechanical surface elements discretizing the interface between the two domains, see Fig. 2.3(c). The SiO<sub>2</sub> shell is prescribed a purely elastic mechanical behavior and we neglect transport of Li through this layer. The a-Si obeys the chemo-

mechanical framework described in Sect. 2.2.3. Following Di Leo et al. [42], the plastic behavior of the a-Si shell is modeled by introducing a positive-valued, stress-dimensioned, and concentration-dependent yield strength  $Y(\bar{c}) > 0$ , and assuming a no-flow condition of the form  $\bar{\sigma} \leq Y(\bar{c})$ . During plastic flow,  $\dot{\bar{c}}^p > 0$ , and the equivalent tensile stress is taken to be equal to a rate-dependent flow strength,

$$\bar{\sigma} = Y(\bar{c}) + Y_* \left( \frac{\dot{\bar{c}}^p}{\dot{\bar{c}}_0} \right)^{1/m}, \quad \text{with} \quad Y(\bar{c}) = Y_{\text{sat}} + (Y_0 - Y_{\text{sat}}) \exp \left( -\frac{\bar{c}}{\bar{c}_*} \right), \quad (2.4.1)$$

where  $Y_* > 0$  is a positive-valued, stress-dimensioned constant,  $\dot{\bar{c}}_0$  is a reference tensile plastic strain rate, and  $m$  is a measure of the strain-rate sensitivity of the material. All material properties for the a-Si and SiO<sub>2</sub> are adopted from the work of Di Leo et al. [42] and the reader is referred to this reference for numerical values.

The multi-particle behavior is modeled by including  $N$  simulation domains representing  $N$  particles as shown in Fig. 2.3(c). It is important to note that although these particles are mechanically isolated (i.e. that they do not contact each other), they are *chemically connected* through the presence of the chemo-mechanical surface elements. Through these elements, we enforce galvanostatic charging conditions across all particles under the assumption of a constant voltage maintained across the active particle-electrolyte interface.

The numerical framework described above allows us to investigate the interplay of mechanics and chemistry in multi-particle systems and the associated effect on electrochemical performance. First, we investigate the effect of statistical variations in electrochemical properties — namely the reaction constant,  $k_0$  between the active particles and the electrolyte — on current distribution across particles and interfacial mechanical stress build up. Second, we investigate the potential presence and role of interfacial damage on electrochemical performance and capacity fade while cycling. In all of the following studies, we consider  $N = 50$  active particles.

#### 2.4.1 Electrochemical performance and stress generation with varying reaction rate - $k_0$

We consider first the effects that would arise in a multi-particle system from having a distribution of reaction constants,  $k_0$  affecting the reaction kinetics at the interface of the particles and the electrolyte. Such a variation in  $k_0$  may arise experimentally due to a number of mechanisms including poor bonding of the a-Si/SiO<sub>2</sub> interface, failure of the SEI, and pre-existing damage of the active material during manufacturing. The reaction constant,  $k_0$  dictates reaction kinetics at the interface (cf. Eq. (2.2.3)), which is modeled through the chemo-mechanical surface elements, and is prescribed a log-normal distribution. The mean of the distribution is prescribed as the logarithm of the baseline reaction constant,  $k_0 = 3.25 \cdot 10^{-7} \text{ mol}/(\text{m}^2\text{s})$  reported in Di Leo et al. [42]. The standard deviation (SD) is varied in our investigation and we consider values of SD= 1.0 and SD = 2.0. This choice is motivated to produce a significant variation in local current distribution over the simulation domain in order to understand how these local variations affect the overall electrochemical response of the multi-particle system and concurrent stress generation. Consistent with the experiments of Wu et al. [116], the simulation domain is cycled under galvanostatic conditions at a C-Rate of 1C with voltage limits of 0.01 V and 1 V for three half-cycles. We note that in this first set of simulation results, *we do not allow for mechanical interfacial damage*, which will be considered in Sect. 2.4.2.

To understand the effect on electrochemical performance of variations in  $k_0$ , we compute both the local (single nanotube) and global (whole ensemble of nanotubes) voltage vs. state-of-charge (SOC) response during cycling. Recall that Voltage is assumed to be constant throughout the simulation domain and is an unknown which is solved for in the finite element framework in order to ensure the galvanostatic charging constraint is met. In generating the Voltage vs. SOC curves subsequently shown, we ignore the results from the first half-cycle in our simulations.

The simulation results are shown in Fig. 2.4. First, we focus on the individual behavior of three of the 50 nanotube particles from the SD=1.0 simulation, which have been chosen

to represent the lowest, average, and highest reaction constants present in the simulation, and differ in  $k_0$  value by approximately one order of magnitude. An important feature of multi-particle simulations evident in Fig. 2.4(a) is the “smoothing” of the Voltage vs. SOC behavior of the individual particles as cycling is reversed. This feature is enhanced as the reaction constant,  $k_0$  is decreased, as shown in Fig. 2.4(a).

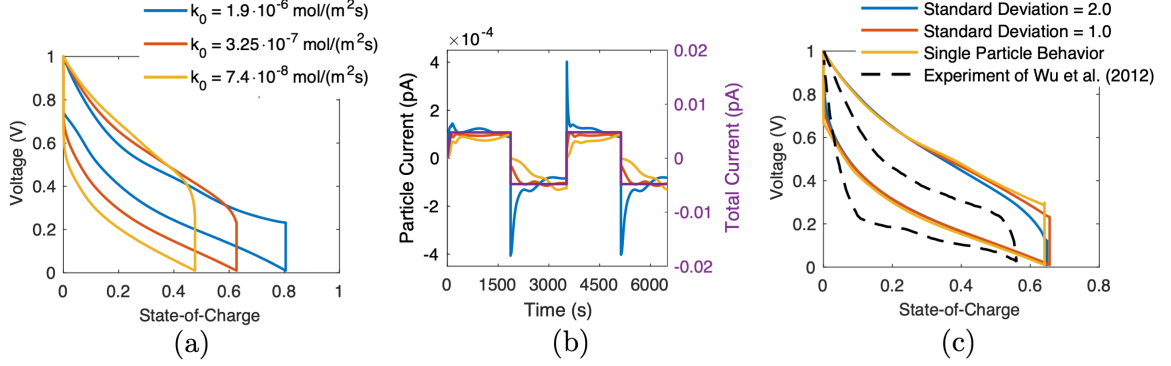


Figure 2.4: Simulation results for a 50-particle system with a statistical distribution in reaction constant  $k_0$ . (a) Local (individual nanotube) voltage vs. state-of-charge behavior for three particles spanning the range of  $k_0$  values considered. (b) Current vs. time response for the three particles under consideration compared against the total current in the simulation domain. (a) and (b) are for the case of SD = 1.0. (c) Global (entire simulation domain) voltage vs. state-of-charge behavior for a single particle, simulations with  $k_0$  distributions with SD = 1.0 and SD = 2.0, and the experimentally measured response of Wu et al. [116]. Reproduced with permission from [17].

This behavior is tied to chemical interactions between particles with varying  $k_0$ , which in turn impact local current distribution to individual particles as shown in Fig. 2.4(b), where we compare the current applied to the entire simulation domain (purple line, right y-axis) with the local current distributed respectively to the three nanotube particles under investigation (left y-axis). While the entire simulation domain experiences a sharp change in total current during cycle reversals (purple line), the individual particles experience a gradual variation in current, which depends on their local reaction kinetics. Particles with sluggish (low) reaction kinetics experience a gradual reversal in current, which in turn affects the contribution of the overpotential to the total Voltage vs. SOC behavior and results in “smoothing” of the Voltage vs. SOC behavior as shown in Fig. 2.4(a).

The global behavior of the system is shown in Fig. 2.4(c). Results are shown for two simulations with log-normal  $k_0$  distributions with a standard deviation of SD=1.0 and SD=2.0, as well as for a single-particle (standard deviation of zero). Also shown is the experimentally measured response of Wu et al. [116]. The “smooth” transition in voltage during cycle reversals can be observed in the experimental results shown and is also captured when a significant variation in  $k_0$  is introduced in the multi-particle simulations developed in this work. As shown in Fig. 2.4(c), this feature cannot be captured when modeling a single particle system, as the jump in current during cycle reversal will always lead to a sharp jump in voltage. This illustrates one of the benefits of developing simulation tools which accurately model galvanostatic charging conditions in multi-particle electrode systems. Further, variation in local current distribution (see Fig. 2.4(b)) also has a significant impact on the generation of stresses and potential for initiation and evolution of mechanical damage as investigated next.

To investigate the interplay between chemical performance and mechanics, we focus on the generation of normal stresses at the a-Si/SiO<sub>2</sub> interface. Here, we demonstrate the manner in which variations in local reaction kinetics of each nanotube — as prescribed through a variation in the reaction constant  $k_0$  — affect the generation of mechanical stresses at these interfaces. Fig. 2.5(a) shows the normal (i.e. radial direction in Fig. 2.3) component of stress  $\sigma_{rr} = \tau_N$  at the a-Si/SiO<sub>2</sub> interface as a function of the local state-of-charge of each particle for the same three particles discussed before. As can be observed, the interfaces develop different levels of normal stress, which are largely correlated to the local state-of-charge of each particle. The local SOC of each particle in turn differs due to variations in reaction constant, which promote a non-uniform state of lithiation across particles during cycling.

This behavior is a direct outcome of the elastic-plastic constitutive behavior used to model the a-Si core and the large deformation kinematics, which result in an increase (either negative or positive) of the normal interfacial stresses as the a-Si core becomes further

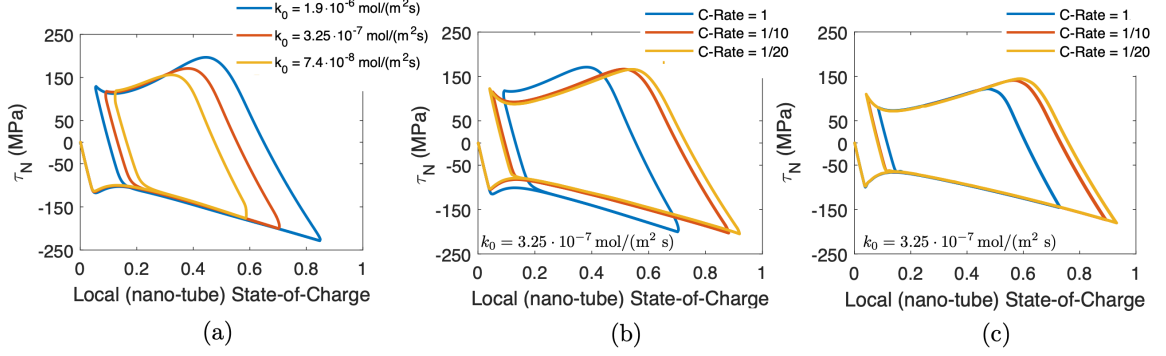


Figure 2.5: Interfacial normal stress,  $\tau_N$  at the a-Si/SiO<sub>2</sub> interface as a function of local (nanotube) SOC. (a) Results for three representative particles spanning the range of  $k_0$  values considered at a C-Rate of 1C. (b-c) Results for a particle with a reaction constant of  $k_0 = 3.25 \cdot 10^{-7} \text{ mol}/(\text{m}^2 \text{ s})$  at three different C-Rates, with (b) mechanical strain-rate sensitivity taken into consideration, and (c) mechanical strain-rate sensitivity neglected. Reproduced with permission from [17].

lithiated. Importantly, differences between these curves *at a given state-of-charge* arise from the *mechanical strain-rate sensitivity* of the material. Since particles experience different currents, they also experience different loading rates, which in turn changes their mechanical response. In summary, the magnitude of normal interfacial stresses is controlled both by the total amount of Lithium reacted into the a-Si core and the rate of lithiation.

From an interfacial mechanical damage perspective (which will be further investigated in the next section), this poses an interesting question, which is to investigate the C-Rate sensitivity of interfacial mechanical stresses. Fig. 2.5(b) shows the normal interfacial stresses as a function of the local SOC for the nanotube with a reaction constant  $k_0 = 3.25 \cdot 10^{-7} \text{ mol}/(\text{m}^2 \text{ s})$ . Three simulations are shown with C-Rates of 1C, 1/10C, and 1/20C. We can observe the *counter-intuitive result* that a decrease in C-Rate does not necessarily lead to a decrease in the maximum (positive or negative) normal interfacial stresses experienced at the a-Si/SiO<sub>2</sub> interface. The rather constant nature of the maximum normal interfacial stresses during cycling shown in Fig. 2.5(b) is due to both the extent of lithiation and the mechanical strain-rate sensitivity of the material. At higher C-Rates, we achieve a lower local SOC for each particle, which would in turn yield lower interfacial stresses. However, mechanical strain-rate sensitivity is amplified at higher C-Rates, which in turn in-

creases interfacial stresses. These two competing mechanisms for the particular case of an a-Si/SiO<sub>2</sub> double-walled nanotube counteract each other to yield a fairly constant normal interfacial stress with varying C-Rates.

To further illustrate this competition, Fig. 2.5(c) shows the same result where the constitutive behavior of the a-Si core has been modified to have *no strain-rate sensitivity* by setting the parameter  $Y_* = 0$  in (2.4.1). As shown in Fig. 2.5(c), normal interfacial stresses are now entirely governed by the local state-of-charge of the particular particle and we can observe that lower C-Rates always lead to higher interfacial stresses.

It is important to note that this behavior — which is counter-intuitive to the usual experience that higher C-Rates are always mechanically detrimental — arises from the fact that here, we focus on the interfacial mechanical stresses at the a-Si/SiO<sub>2</sub> interface, rather than the bulk stresses developed in either the core or the shell. Bulk stresses generally arise due to large gradients in concentration or volumetric expansion under mechanical constraint. However, owing to the nano-metered sized geometry of this particular anode design, concentration gradients are negligible and bulk stresses in this particular geometry arise from the mechanical constraint imposed by the SiO<sub>2</sub> shell on the a-Si core, which is no longer free to expand. An in-depth discussion on the single particle mechanics of this anode geometry can be found in Di Leo et al. [42].

The results shown in this section illustrate the complex nature of multi-particle behavior when taking into consideration potential variations in local reaction kinetics by varying the reaction constant,  $k_0$  through a statistical distribution. The results demonstrate that variation in  $k_0$  can significantly affect local current distribution among the various active particles and in turn influence the global voltage vs. SOC behavior. Further, variation in  $k_0$  can also significantly affect the generation of mechanical stresses with a focus on the development of normal interfacial stresses at the a-Si/SiO<sub>2</sub> interface. These stresses could potentially lead to mechanical damage through decohesion of the interface, which would in turn affect chemical connectivity of the particles to the electrode. In the following section,

we investigate capacity loss in this prototypical liquid LIB electrode due to mechanical damage and loss of connectivity through use of the developed surface elements.

#### 2.4.2 Capacity loss due to mechanical interfacial decohesion

We now shift our attention to modeling capacity loss due to mechanical interfacial decohesion in the electrode under consideration. Unlike the previous section, we consider now a statistical variation in mechanical properties associated with the cohesive strength of the a-Si/SiO<sub>2</sub> interface, while maintaining the reaction rate constant at  $k_0 = 3.25 \cdot 10^{-7} \text{ mol}/(\text{m}^2\text{s})$ . The choice of varying the cohesive strength  $t_N^{\text{cr}}$ , as opposed to the reaction rate  $k_0$ , in this section is made for pragmatic reasons. The material property,  $k_0$  has been previously experimentally determined in [42], while the specific value of  $t_N^{\text{cr}}$ , as will be discussed below, is unclear from the literature and can vary over a significant range depending on manufacturing conditions.

Across the simulation domain containing  $N = 50$  active particles, we prescribe the normal cohesive strength  $t_N^{\text{cr}}$  using a normal distribution with a mean strength of 160 MPa and a standard deviation of 70 MPa. The mean cohesive strength is chosen to approximately match with the average normal stresses at the interface across an ensemble of nanotubes with varying  $k_0$  as determined in Sect. 2.4.1. The standard deviation is such that at least 50% of the particles will incur mechanical damage during cycling at different C-Rates. We consider only normal mechanical damage (i.e.  $\beta = 0$  in Eqns. (2.2.11) and (2.2.12)) with  $t_N^{\text{cr}}$  as defined above, and simply take  $t_T^{\text{cr}}$  in (2.2.8) to be a large number to guarantee no damage initiation due to tangential interfacial stresses. The prescribed variation in cohesive strength is intended to showcase the utility of our modeling framework to study the interplay of chemo-mechanical interactions and role of damage on electrochemical performance and capacity fade through consecutive cycling. The normal stiffness of the interface is taken equal to  $K_N = 6 \cdot 10^{11} \text{ MPa/m}$ , which is sufficiently large not to introduce artificial compliance in the simulation domain. To define damage evolution, we use a baseline



fracture energy of  $G_N = 0.25 \text{ J/m}^2$ . In combination, these material properties define all the necessary parameters for the constitutive behavior summarized in eqns. (2.2.8) to (2.2.10). Finally, for simulations in this section, we consider chemical damage to evolve equal to mechanical damage, that is  $D_{\text{chem}} = D_{\text{mech}}$ .

The simulation domain is cycled under galvanostatic conditions with varying C-Rates and voltage limits of 0.01 and 1 Volts. We simulate 27 cycles of the electrode with a baseline C-Rate of 1/2C and alternating cycles at higher and lower rates. The complete sequence of C-Rates is given by,

$$\text{C-Rate} \in [1/2\text{C}, 2\text{C}, 1/2\text{C}, 4\text{C}, 1/2\text{C}, 1/4\text{C}, 1/2\text{C}, 1/10\text{C}, 1/2\text{C}] \quad (2.4.2)$$

where three cycles are spent at each particular C-Rate. This sequence allows us to assess how damage incurred at higher or lower C-rates — with respect to the baseline 1/2C rate — affects electrochemical performance. By computing the capacity of the electrode at a C-Rate of 1/2C before and after cycling at a different rate, we can understand how damage incurred at a particular rate affects the capacity of the electrode. Following Di Leo et al. [42], a maximum capacity of 3.579 Ah/g for Si is used to convert SOC data to an equivalent capacity.

Simulation results are shown in Fig. 2.6. The top row shows the voltage vs. SOC response for the entire simulation domain, while the bottom row shows the simulation domain, where in the a-Si domain we show contours of the normalized concentration,  $\bar{c}$ . The  $\text{SiO}_2$  shell is shown as a grey region without contours. Fig. 2.6(a) shows the electrochemical response of the electrode at the end of the third conditioning cycle at a C-Rate of 1/2C at which point the battery accrues a significant amount of damage. Fig. 2.6(c) highlights with red arrows the particles which have completely decohered from their  $\text{SiO}_2$  shells during the conditioning cycles and are now chemically isolated from all other particles.

Due to mechanical decohesion, the electrode stabilizes to a new electrochemical win-

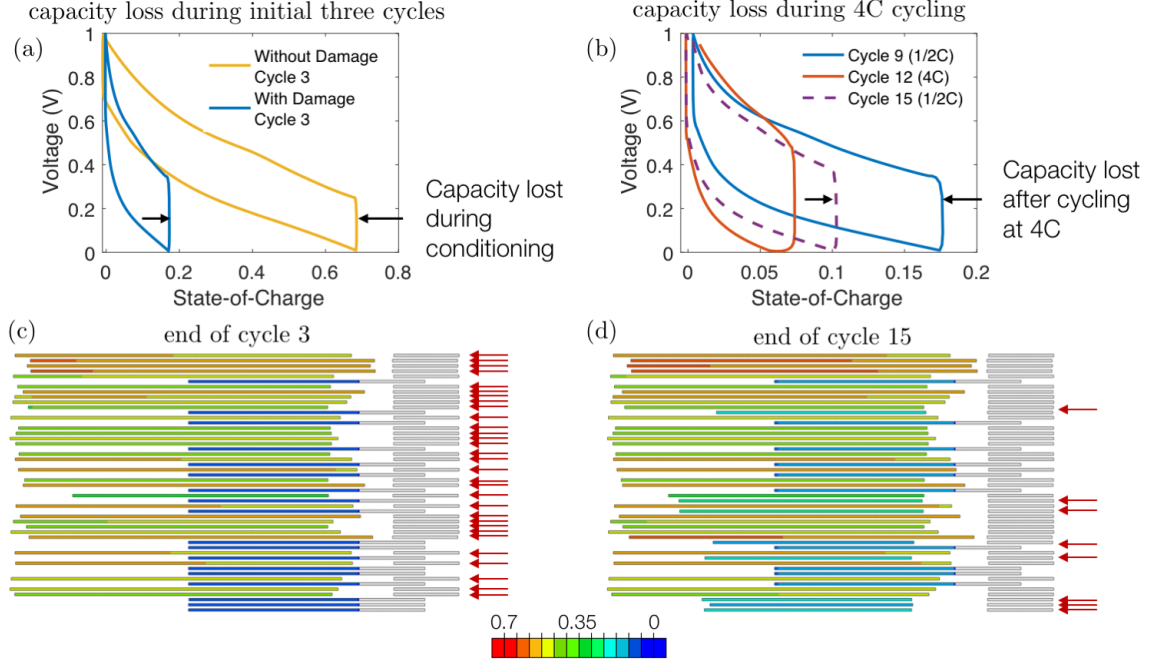


Figure 2.6: Simulation result of cycling a multi-particle electrode composed of double-walled, hollow nanotubes. Figs. (a) and (b) show the Voltage vs. SOC response of the electrode where (a) compares a simulation with and without damage after the first three conditioning cycles and (b) shows results of the simulation with damage after 9, 12, and 15 cycles. Figs. (c) and (d) show contours of normalized concentration in the a-Si core at the end of the 3rd and 15th cycle. The red arrows highlight those particles which have completely decohered from their shells and are now chemically isolated. Reproduced with permission from [17].

dow with a significantly reduced capacity (blue line) compared against a simulation without damage (yellow line). Fig. 2.6(b) shows the voltage vs. SOC response of the a-Si anode at the end of the 9th (blue line), 12th (orange line) and 15th (purple) cycle during which the electrode is intermittently charged at a C-Rate of 4C. By comparing the voltage vs. SOC behavior during cycling at the baseline 1/2C rate before (blue line) and after (purple line) the intermittent 4C cycles, we can visually see the additional loss in capacity as the electrochemical window shrinks. Fig. 2.6(d), highlights with red arrows the additional nanotubes which completely decohere from their  $\text{SiO}_2$  shells during the intermittent 4C cycling.

Capacity loss due to interfacial decohesion is best characterized through a graph of capacity as a function of cycle number as shown in Fig. 2.7. Here, simulation results without (blue line) and with (orange line) damage are displayed. The response of the simulated

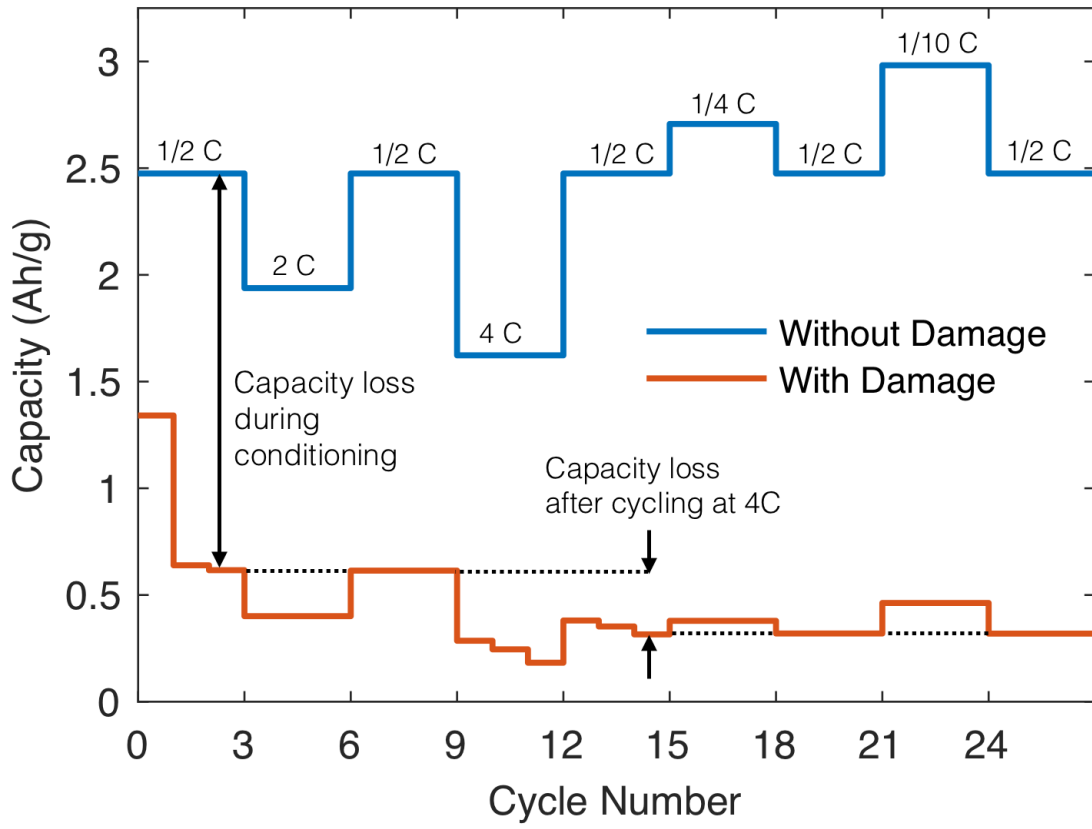


Figure 2.7: Capacity of an ensemble of hollow double-walled nanotubes as a function of cycle number during galvanostatic cycling at various C-rates. Results are shown for a simulation without interfacial damage (blue line) and a simulation with interfacial damage (orange line). Reproduced with permission from [17].

electrode without mechanical damage (blue line) in Fig. 2.7 matches the theoretical expectations for galvanostatic charging within a fixed voltage window, where simulations with higher C-Rates have lower capacity and lower C-rates have higher capacity. It is important to note that the baseline capacity at a C-rate of 1/2C remains unchanged in the absence of mechanical damage and loss of electrochemical contact. The simulated electrode response with mechanical damage (orange line) shown in Fig. 2.7 is markedly different. A large amount, approximately 75%, of the electrodes capacity is lost in the first three conditioning cycles. This correlates with a large number of nanotubes becoming decohered from their  $\text{SiO}_2$  shells as shown in Fig. 2.6(c). During subsequent cycling at 2C, we do not incur additional damage as we can see that the baseline capacity at 1/2C remains unchanged

after cycling at 2C. During cycling at 4C however, the electrode incurs additional damage and we can see another significant drop in the baseline 1/2C capacity of the electrode after cycling at this rate. This is confirmed by the observations in Fig. 2.6(d), where we see visually that additional particles have become decohered. In contrast, no additional damage is incurred in the electrode during cycling at C-Rates of 1/4C and 1/10C, which are below the 1/2C baseline. As shown in Fig. 2.7, the baseline electrode capacity at 1/2C is recovered after intermittent cycling at lower C-Rates.

While use of a different statistical distribution for  $t_N^{cr}$  would clearly impact these results, the qualitative nature of the above study is nevertheless of significant importance and demonstrates: i) the importance of accounting for mechanical damage, which leads to a loss of electrochemical activity at the surface of an active particle, and ii) the manner in which that can be achieved computationally through use of the developed chemo-mechanical surface elements. In combination with further experimental calibration of material properties, the developed modeling technique should serve useful in analyzing the performance of future LIB electrode designs, including chemo-mechanical interactions and role of mechanical damage on electrochemical performance and capacity fade.

### CHAPTER 3

## ON THE ROLE OF INTERFACIAL MECHANICAL DAMAGE IN COMPOSITE CATHODES FOR ALL-SOLID-STATE BATTERIES

We consider now an application of our modeling framework developed in chapter 2 towards composite cathodes for all-solid-state batteries (SSBs), where active particles are connected through a relatively stiff solid-state electrolyte (SSE). This chapter focuses specifically on a relevant engineering problem where active particles interact *both* through chemical connection and direct mechanical load transfer owing to the presence of a stiff solid conductor.

Common design of composite cathodes incorporates a densely packed architecture of active particles, confined on their exterior by a conductive matrix which supports percolation pathways for ionic transport in addition to complementary additives for electronic conduction [16, 24, 133]. The active material undergoes volumetric expansion/contraction during insertion/extraction of the ionic species, which, due to the confined nature of the all-solid-state architecture can lead to generation of high stresses. Delamination of the interface between active particles and the SSE constitutes a critical mechanical degradation mechanism, which can impact electrochemical performance of composite cathodes and SSBs [32, 134]. As a result, efforts aimed at optimizing the performance of composite cathodes for application in SSBs require an understanding of interfacial processes, including damage occurring within the electrode as well as the SSE [31, 99, 100].

In this chapter, we specialize our framework for a system composed of  $\text{LiCoO}_2$  (LCO) active particles and a  $\text{Li}_{10}\text{GeP}_2\text{S}_{12}$  (LGPS) electrolyte, and integrate our chemo-mechanical cohesive element to capture interfacial reaction kinetics and damage. We apply this framework towards studying the manner in which various material and design parameters affect the electrochemical performance of the system. In particular we: i) in Sect. 3.2 investigate the role of variations in chemo-mechanical properties of the active material and SSE

(i.e. volumetric expansion, Young’s modulus), and ii) in Sect. 3.3 investigate the role of variations in microstructural descriptors (i.e. particle size distribution, packing density). Through this modeling, we elucidate the role of both material properties and microstructural composition on the integrity of composite electrodes and overall electrochemical performance of the solid-state battery. The work presented in this chapter was adapted with permission from and published in:

- Bistri, Donald, and Claudio V. Di Leo. ”Modeling of chemo-mechanical multi-particle interactions in composite electrodes for liquid and solid-state Li-ion batteries.” *Journal of The Electrochemical Society* 168.3 (2021): 030515.

### 3.1 Model Parameters

For clarity and completeness, we summarize here all material parameters utilized in our simulation framework for the LCO-LGPS composite cathode under investigation. Where possible, material parameters are taken directly from the literature. The remaining properties have been calibrated to experimental data and a summary of the calibration process is presented. Material properties for our simulation framework are summarized in Table 3.1 along with respective sources. In the following subsections, we briefly detail the manner in which material properties were chosen or calibrated.

#### 3.1.1 Mechanical Properties of LCO and LGPS

The mechanical behavior of LCO active particles is taken as *chemo-elastic* and modeled using the same framework described in Sect. 2.2.3, however here without any plastic deformation. The LGPS electrolyte is treated as a purely elastic solid. Mechanical properties of LCO have been investigated in multiple works [135, 136, 137, 138, 139]. However, past studies and modeling efforts have resorted to an isotropic assumption, thus neglecting variations in mechanical properties of  $\text{Li}_x\text{CoO}_2$  with Li content and crystallographic orientations. Wu and Zhang [140] applied first-principle calculations in addition to ab-initio

tensile tests to study anisotropic and Li concentration-dependent mechanical properties of  $\text{Li}_x\text{CoO}_2$ . Variation in elastic stiffness, shear and bulk modulus with Li content along two axes of anisotropy were reported. While our simulation framework does not account for anisotropic behavior of  $\text{Li}_x\text{CoO}_2$  in a formal continuum treatment, the aforementioned findings of Wu and Zhang are incorporated in the model through a Voigt-Reuss-Hill homogenization scheme, as reported in [141]. Here, a sixth-order polynomial fit is performed to capture the variation of Young's Modulus with Li content from  $E=108.5$  GPa for a pristine, unlithiated state to  $E=252$  GPa for a fully-lithiated state. We employ a constant Poisson ratio of  $\nu = 0.22$  for LCO. This effectively enables us to capture the experimentally reported variation in shear modulus with Li content from  $G=41.71$  GPa for an unlithiated state to  $G=111.38$  GPa for a fully lithiated state. A plot of the polynomial fit for both Young's modulus and Shear modulus against experimental data by Wu and Zhang [140] is reported in Appendix A.3.

The mechanical behavior of the LGPS electrolyte is modeled under a linear-elastic framework. Several studies have investigated the elastic properties of LGPS through first-principle calculations [142, 143]. In Sect. 3.2, we vary the mechanical properties of the SSE to investigate the potential impact of changing the SSE composition on electrochemical performance of the electrode. We use LGPS in our baseline simulations and adopt mechanical properties reported by Wang et al. [142], namely a Young's modulus of  $E = 37.19$  GPa and a Poisson ratio of  $\nu = 0.296$ .

### 3.1.2 Chemical Properties of LCO

Following Di Leo et al. [42], we model the chemo-mechanical behavior of the  $\text{Li}_x\text{CoO}_2$  active particles through the framework summarized in Sect. 2.2.3 above. An important aspect of using this framework is calibrating the activity coefficient,  $\gamma$  through a fitting of the open-circuit behavior of the active material. In the absence of mechanical stresses, using (2.2.19), one can relate the chemical potential of Li atoms at the electrode surface to

a stress-free, open-circuit potential  $U^\theta$ , according to the following relationship (cf. Bucci et al. [115]),

$$U^\theta = -\frac{\mu}{F} = -\frac{\mu^0}{F} - \frac{RT}{F} \ln \left( \gamma \frac{\bar{c}}{1 - \bar{c}} \right) \quad (3.1.1)$$

where  $U_0^\theta = -\mu_0/F$  defines a standard rest potential. Motivated by Verbrugge and Koch [144], the concentration dependent activity coefficient  $\gamma$ , is given by the following polynomial representation

$$RT \ln(\gamma) = \sum_{n=2}^N a_n \cdot n \cdot \bar{c}^{(n-1)}. \quad (3.1.2)$$

Using eqns. (3.1.1) and (3.1.2), a least-square polynomial regression fit is performed to published open-circuit potential data by Mizushima et al. [145] for a  $\text{Li}_x\text{CoO}_2$  compound against a Li-metal reference/counter electrode to determine the polynomial coefficients in (3.1.2). In this work, a seventh order polynomial representation is adopted to determine the  $a_n$  coefficients and  $U_0^\theta$  with the calibrated values summarized in Table 3.1. A plot of the polynomial fit against experimental open-circuit potential data is shown in Appendix A.3.

To model the diffusion process, a Li diffusion coefficient of  $D_0 = 5.387 \cdot 10^{-15} \text{ m}^2/\text{s}$  and a maximum molar concentration of Li in the host material of  $c_{\text{R,max}} = 51555 \text{ mol/m}^3$  are used. These values match with estimates employed in previous modeling efforts for a similar electrode material by Wiedemann et al. [146] and Ramadass et al. [147]. We note that there is a large variation in reported estimates for the diffusion coefficient of Li in  $\text{Li}_x\text{CoO}_2$  electrodes, with values ranging from  $10^{-13}$  to  $10^{-16} \text{ m}^2/\text{s}$  [148, 149, 150]. The volumetric changes experienced with added Li content, that is the partial molar volume  $\Omega$ , is quantified based on the experimental findings of Reimers and Dahn [151]. It is important to note that in contrast to other active materials,  $\text{Li}_x\text{CoO}_2$  experiences a *contraction* upon Li insertion, with an approximately 2% contraction in volume reported upon lithiation to  $\text{Li}_{0.9}\text{CoO}_2$ . Based on these experimental observations, we set the quantity  $\bar{\Omega} = \Omega c_{\text{max}} = -2\%$ , which controls the total volumetric change of active particles due to Li intercalation.

To model interfacial kinetics, we calibrate the reaction constant,  $k_0$ , to experimental



charge-discharge curves for  $\text{Li}_x\text{CoO}_2$  published by Zhang et al. [152]. We do so by adjusting the reaction constant,  $k_0$  so that energy dissipation during a full cycle (evaluated as the area inside the Voltage vs SOC curve) matches with experimental measurements. The calibration procedure is repeated at both a C-Rate of C/7 and C/2.7 to ensure consistency in calibration at different charging rates. The calibrated reaction constant evaluates to  $k_0 = 9 \cdot 10^{-7} \text{ mol}/(\text{m}^2\text{s})$ . A figure of our calibration against the experimental charge-discharge curves by Zhang et. al [152] at a C-Rate of C/2.7 is shown in Appendix A.3.

### 3.1.3 Interfacial Properties

To the authors knowledge, no prior data on interface strength has been reported for a LCO-LPGS composite cathode and in general experimentally measured interface properties within SSBs are scarcely available as pointed out in the review work of Zhang et al. [153]. As such, in the numerical investigations in subsequent sections, we prescribe  $t_N^{\text{cr}}$  values over a certain range to provide a qualitative assessment on the effect of damage on performance of composite cathodes in SSBs.

Further, we note that we consider only *normal* decohesion at the interface (i.e.  $\beta = 0$  in Eqs. (2.2.11) and (2.2.12), and  $t_T^{\text{cr}} \rightarrow \infty$ ), since given the limited experimental data available, it is not necessary at this stage to include a complex, mixed-mode failure mechanism for the interface. In Sect. 3.2 we vary the cohesive strength between  $t_N^{\text{cr}} = 150 \text{ MPa}$  and  $t_N^{\text{cr}} = 250 \text{ MPa}$ . Additionally, in selecting the aforementioned cohesive strengths, an effective Young's Modulus to Cohesive Strength ratio,  $E_{\text{SSE}}/t_N^{\text{cr}} \in [0, 500]$  is maintained, comparable to similar studies in the literature [100]. Fracture energies of  $G_N = 1 \text{ J/m}^2$  and  $G_N = 1.75 \text{ J/m}^2$  are prescribed for the two different cohesive strengths to maintain a similar normal separation at failure. These values are consistent with the recent modeling efforts of Bucci et al. [100]. Stiffness of the interface is prescribed equal to  $K = K_N = 5 \cdot 10^{12} \text{ MPa/m}$ . Choice of a sufficiently high interfacial stiffness is important to preserve the correct mechanical behavior of the microstructure prior to damage initia-

tion, and eliminate the addition of artificial compliance. The stiffness,  $K$  was determined by running multiple simulations with increasing values of  $K$  and analyzing the development of normal stresses at the interface until a sufficiently large stiffness value to match the stress state for a perfectly bonded interface was determined.

Table 3.1: Material properties for modeling of coupled chemo- mechanical behavior of a  $\text{LiCoO}_2\text{-Li}_{10}\text{GeP}_2\text{S}_{12}$  composite cathode.

	Parameter	Value	Source
Chemical	$D_0$	$5.387 \cdot 10^{-15} \text{ m}^2/\text{s}$	Wiedemanan et al. [146]
	$c_{R,\max}$	$51555 \text{ mol/m}^3$	Ramadass et al. [147]
	$\Omega \cdot c_{R,\max}$	-2%	Reimers and Dahn [151]
	$[a_2 - a_7]/F$	$[0.1447, 0.4629, -0.7643, 2.5326, -3.199, 1.2263] \text{ V}$	Fitted to Mizushima et al. [145]
	$U_0^\theta$	4.6 V	Fitted to Mizushima et al. [145]
Reaction	$k_0$	$9 \cdot 10^{-7} \text{ mol}/(\text{m}^2\text{s})$	Fitted to Zhang et al. [152]
Elastic	$E_{\text{LGPS}}$	37.19 GPa	Wang et al. [142]
	$\nu_{\text{LGPS}}$	0.296	Wang et al. [142]
	$E_{\text{Li}_x\text{CoO}_2}$	108.5 - 252 GPa	Wu and Zhang [140]
	$\nu_{\text{Li}_x\text{CoO}_2}$	0.22	Wu and Zhang [140]
Interfacial	$t_N^{\text{cr}}$	[150, 250] MPa	This work
Mechanical	$G_N$	[1, 1.75] J/m <sup>2</sup>	This work
	$K_N$	$5 \cdot 10^{12} \text{ MPa/m}$	This work

Finally, as described in Sect. 2.2.2, current density at a point on the surface of a particle

is damaged through the parameter  $D_{\text{chem}}$ , which is taken to evolve according to

$$D_{\text{chem}} = 1 - \exp(-\kappa \cdot D_{\text{mech}}) \quad (3.1.3)$$

where  $D_{\text{mech}}$  denotes mechanical damage, which evolves according to (2.2.10), and  $\kappa = 30$ . This allows us to prescribe a response for mechanical damage which is relatively ductile, while the response for chemical damage is of a brittle nature. For the value of  $\kappa = 30$  chosen, at 15% mechanical damage,  $D_{\text{mech}} = 0.15$ , we have already achieved 99% loss of chemical conductivity,  $D_{\text{chem}} = 0.99$ . This eases numerical convergence significantly without a loss of the ability to capture sudden losses in chemical conductivity due to mechanical damage.

### **3.2 Effect of varying chemo-mechanical properties on electrochemical performance of SSB composite cathodes**

To study the effect of variations in chemo-mechanical properties on electrochemical response of a composite cathode, we consider a two-dimensional microstructure. SEM images of a  $\text{LiCoO}_2\text{-Li}_{10}\text{GeP}_2\text{S}_{12}$  composite cathode provided in the work of Zhang et al. [16] and shown in Fig. 3.1(a) were used to construct a representative microstructure model as shown in Fig. 3.1(b). We model the electrode particles to be elliptical in shape and prescribe the distribution in particle major and minor axis to match the experimental SEM images. Similar particle dimensions for representative  $\text{LiCoO}_2$  microstructures are also reported in the work of Wilson et al. [154].

Periodic displacement boundary conditions are prescribed, effectively treating the simulated microstructure as a representative volume element (RVE). The surface of each active particle has been discretized with chemo-mechanical surface elements marked by red contour lines in Fig. 3.1(b). The particles are electro-chemically coupled by prescribing that voltage across the active particles surface remains uniform across as described

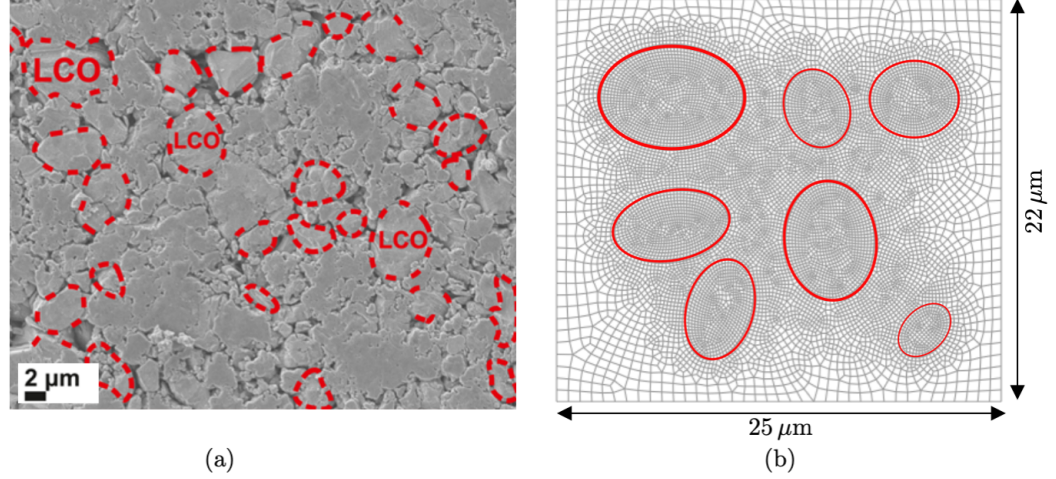


Figure 3.1: (a) SEM image of a  $\text{LiCoO}_2\text{-Li}_{10}\text{GeP}_2\text{S}_{12}$  composite cathode microstructure from the work of Zhang et al. Reprinted with permission from [16]. (b) Graphical illustration of the 2D microstructure mimicking SEM images of Zhang et al. [16] used to model the effect of variation in chemo-mechanical properties on electrochemical performance of composite cathode. Reproduced with permission from [17].

in Sect. 2.2.1. Finally, we note that other complex degradation mechanisms, such as for example the formation of unstable interphases at the active particle/SSE interface can affect both mechanical degradation and interfacial kinetics [18]. Treatment of these phenomena is beyond the scope of this thesis, where we consider the active particle/SSE interface to remain pristine and be affected only by mechanical decohesion.

### 3.2.1 Role of SSE stiffness on electrochemical performance and mechanical degradation

We consider first the role of varying the Young's modulus of the SSE. We vary the elastic modulus between  $E_{\text{SSE}} = 20 \text{ GPa}$  and  $E_{\text{SSE}} = 100 \text{ GPa}$ , representing different families of inorganic electrolytes, namely sulfides, lithium phosphorous oxynitrides, and garnets [31, 153]. The microstructure is cyclically charged-discharged at a C-Rate of 0.5C for five half-cycles between voltage caps of 3.8 - 4.6V.<sup>†</sup>

<sup>†</sup>From an experimental standpoint,  $\text{Li}_x\text{CoO}_2$  is typically charged in the  $0.5 \leq x \leq 1$  stoichiometric range to avoid the detrimental role of phase transitions on battery lifespan. In this work, however, we focus on understanding the role of mechanics and microstructural descriptors on electrochemical performance and neglect the role of phase transitions on capacity fade. As such, in our simulations, lithiation of  $\text{Li}_x\text{CoO}_2$  particles from a pristine state is conducted. Studies employing a similar stoichiometric range are reported in the literature [155, 156, 157]. Additionally, doping techniques for mitigation of phase transitions in  $\text{LiCoO}_2$

First, we establish a baseline behavior by running simulations *without interfacial damage*. The results are shown in Fig. 3.2 where (a) shows the average normal interfacial stress  $\tau_N^{avg}$  experienced in all active particles during charging, while (b) shows the overall Voltage vs. SOC behavior for the composite cathode. As shown in Fig. 3.2(a), there is a significant increase in interfacial normal stresses (and hence also bulk stresses experienced by the active particles) as we increase the stiffness of the SSE. However, this increase in stress is not significant enough to in and of itself cause a significant change in electrochemical behavior of the composite cathode as shown in Fig. 3.2(b). This increase in interfacial stresses can however have a significant impact on electrochemical performance if one is to account for damage and decohesion of the interface as shown next.

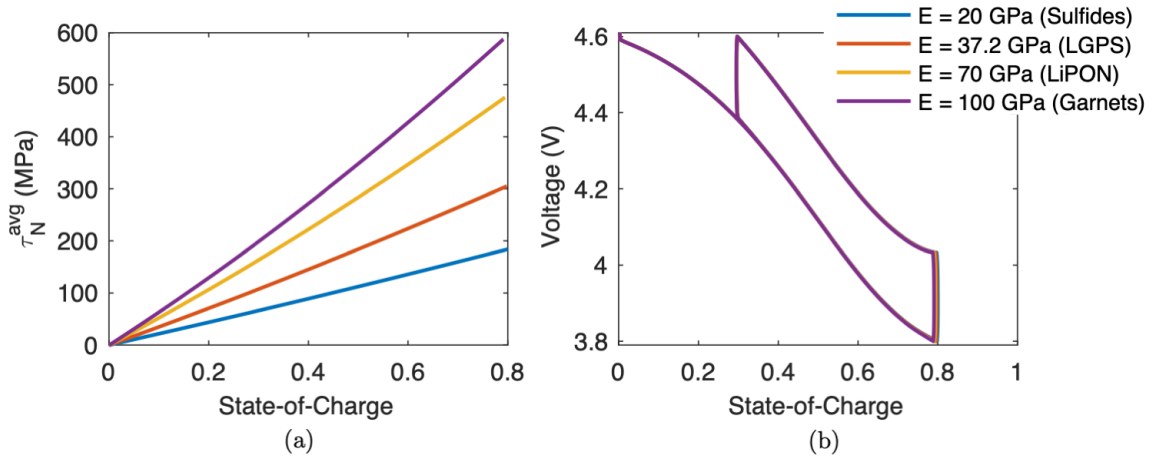


Figure 3.2: Composite cathode response with no damage and varying SSE Young's Modulus. (a) Average normal interfacial stress,  $\tau_N^{avg}$  induced at the active-particle/SSE interface vs. SOC. (b) Voltage vs. SOC response of the composite electrode. Reproduced with permission from [17].

The electrochemical Voltage vs. SOC response of the composite electrode with interfacial damage is shown in Fig. 3.3 with (a)  $t_N^{cr} = 250$  MPa and (b)  $t_N^{cr} = 150$  MPa for the baseline case of  $\bar{\Omega} = -2\%$  volumetric contraction. For the case with higher interfacial strength in Fig. 3.3(a), we see a decrease in electrochemical window (i.e. capacity) for all simulations with a SSE stiffness above 20 GPa. As expected, capacity fade becomes more

---

have been successful [158], enabling for cycling at higher voltages.

pronounced with increase in SSE stiffness owing to the higher interfacial stress generation during deformation of the active particles. As these interfaces become damaged, they lose their charge transfer capacity, which has two consequences. First, under galvanostatic charging, local current densities must increase to maintain a constant total current, leading to an increase in overpotential. Second, some particles may become disconnected from the SSE, making them inaccessible for further ion storage. The effect is further exacerbated at the lower interfacial strength of  $t_N^{\text{cr}} = 150$  MPa shown in Fig. 3.3(b), where we note a significant decrease in electrochemical window for all SSE stiffness values considered. These observations are consistent with previous modeling efforts by Bucci et al. [100], whereby compliant electrolytes are found to perform better at sustaining interfacial integrity.

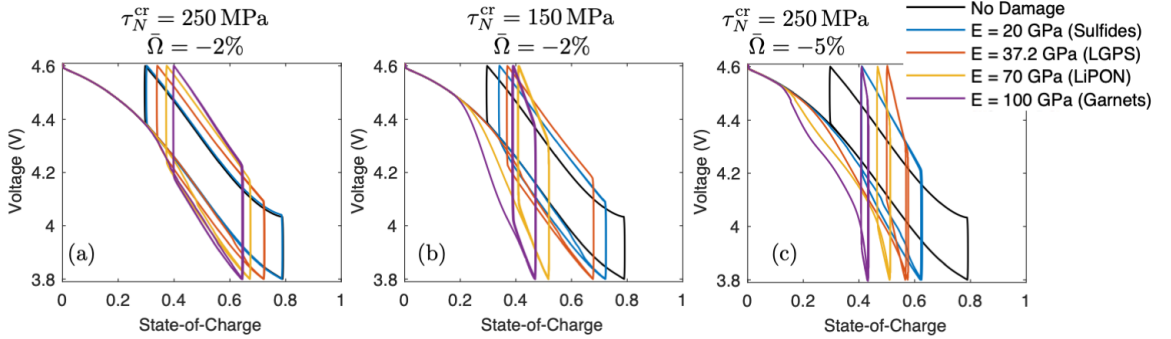


Figure 3.3: Effect of variations in SSE stiffness on electrochemical response of a composite cathode with different cohesive strengths  $t_N^{\text{cr}}$  and volumetric contractions of the active particles  $\bar{\Omega}$ . (a) Simulation results with high cohesive strength  $t_N^{\text{cr}} = 250$  MPa and 2% volumetric contraction,  $\bar{\Omega} = -2\%$ . (b) Results with reduced cohesive strength  $t_N^{\text{cr}} = 150$  MPa. (c) Results with increased 5% volumetric contraction,  $\bar{\Omega} = -5\%$ . The range of SSE stiffnesses considered are representative of Sulfides, LGPS, LiPON and Garnets. Reproduced with permission from [17].

### 3.2.2 Role of active material volumetric change on electrochemical performance and mechanical degradation

We consider next the role of varying the volumetric change incurred by the  $\text{Li}_x\text{CoO}_2$  active particles during lithiation and its effect on electrochemical performance. Here, we fix the normal interfacial strength at  $t_N^{\text{cr}} = 250$  MPa. This mimics studying the potential effect

of changing the composition of active particles to ones with higher capacity and hence higher volumetric changes during lithiation/delithiation. We consider a case with increased volumetric contraction upon lithiation of  $\bar{\Omega} = -5\%$ . The effect on the simulated voltage vs. SOC response is shown by comparing Figs. 3.3 (a) with  $\bar{\Omega} = -2\%$  and (c) with  $\bar{\Omega} = -5\%$ . As observed by contrasting Figs. (a) and (c), increase in volumetric change upon lithiation of active particles has a drastic effect on the loss of electrochemical window due to mechanical interfacial damage. Specifically, in going from a low to a high stiffness SSE, capacity decreases by 56, 84, 90 and 95% when the volumetric contraction is 5%. In the extreme case where the SSE stiffness is  $E_{\text{SSE}} = 100$  GPa and the volumetric contraction upon lithiation is  $\bar{\Omega} = -5\%$ , the composite cathode loses almost its entire energy storing capacity as the majority of the particles in the electrode undergo complete decohesion from the SSE matrix.

The results in Fig. 3.3 show a homogenized view of the composite cathode by describing the voltage vs. SOC behavior of the entire simulation domain. Within the domain, there is a complex coupling in the manner in which mechanical stresses develop, damage occurs, and interfacial currents re-distribute. This coupling is illustrated in Fig. 3.4 for the simulation with  $E_{\text{SSE}} = 20$  GPa and  $\bar{\Omega} = -5\%$ . The top left image of Fig. 3.4 shows the average current density (blue), maximum interfacial normal stress  $\tau_N^{\text{max}}$  (orange), and average damage (yellow) for “particle 1”, which is labeled in Fig. 3.4(a) as the top-left particle in the simulation domain. Figs. 3.4(a)-(d) show two sets of contours. Over the SSE domain we show the maximum in-plane principal stress  $\sigma_1$ , while in the active particles we show contours of normalized concentration  $\bar{c}$ . Note that deformations are scaled by a factor of 10 to better visualize the formation and evolution of interfacial decohesion.

Fig. 3.4(a) shows a snapshot before any damage has occurred over the simulation domain (corresponding to the first dashed line in the top-left plot). At this point we can clearly see the formation of large stresses between particle pairs which are near each other. The remaining three contours shown in Figs. 3.4(b) through (d) show the progression of



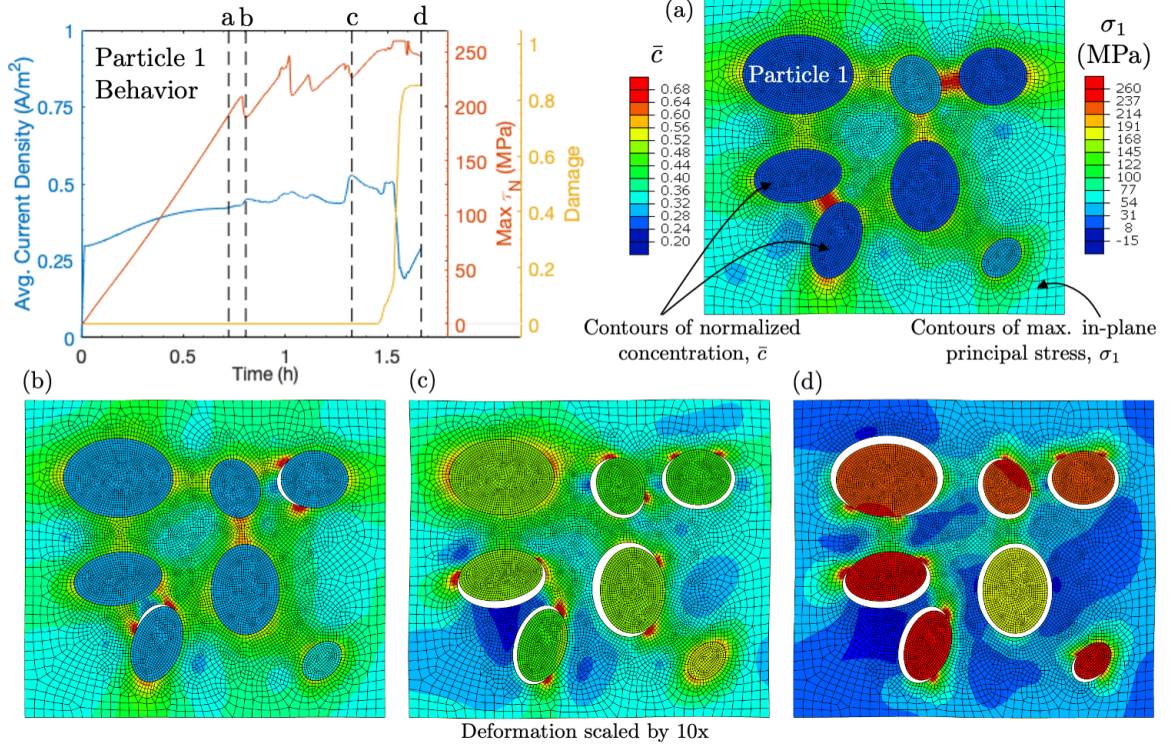


Figure 3.4: Simulation results for the particular case with  $E_{SSE} = 20$  GPa and  $\bar{\Omega} = -5\%$ . The top-left plot shows the average current density, maximum normal interfacial stress  $\tau_N^{max}$ , and average damage for Particle 1 which is shown in (a). Figs. (a) through (d) show contours of maximum in-plane principal stress  $\sigma_1$  in the SSE matrix, while contours of the normalized concentration  $\bar{c}$  are shown over the active particles. Note that deformations are scaled by a factor of 10. Reproduced with permission from [17].

damage as the simulation evolves and the active particles lithiate. Critical to note is the behavior of Particle 1 as shown in the top-left corner. At time (b), we observe that Particle 1 experiences a change in the maximum normal traction it observes as well as the average current density over its surface. This is entirely due to crack formation at *other particles* in the simulation domain. This illustrates the complex mechanical and chemical coupling which occurs in solid-state composite cathodes. Interfacial damage in one particle, and the associated loss in current at the damage site, impacts *the mechanical behavior and interfacial current in all other particles in the domain*. The phenomena is again illustrated in Fig. 3.4(c) where further damage accumulated in the simulation domain — while Particle 1 remains undamaged — affects the interfacial behavior of Particle 1 as shown on the top-left



image. Finally, Fig. 3.4(d) shows the simulation domain at the end of the first half-cycle. Here, Particle 1 has incurred significant damage, but remains partially connected to the SSE matrix.

Interfacial mechanical delamination is shown here to play a significant role in the manner in which the SSE stiffness and choice of active material can affect electrochemical performance of all-solid-state composite electrodes. Even relatively small variations in these material properties can have a significant impact on electrochemical performance. From a design perspective, it is thus critical to map out design guidelines of material property pairs (such as SSE stiffness and active particle expansion/contraction), which will enable for design of solid-state composite cathodes capable of sustaining integrity of the interface. This investigation also points out the critical need for further experiments to characterize the cohesive strength of different active particle/SSE interfaces as this can be critical to modeling the performance of composite electrodes.

### **3.3 Modeling the effect of particle size distribution and active material volume fraction on interface damage in composite cathodes**

We now turn our attention to studying the role of *microstructural descriptors* (e.g particle size distribution, packing density) on electrochemical performance and interfacial integrity of composite cathodes in SSBs. These studies provide insight into important design parameters of consideration for composite cathodes and further illustrate the use of the proposed numerical framework for modeling the chemo-mechanical behavior of SSBs.

#### **3.3.1 Role of particle size and size distribution on electrochemical performance and mechanical degradation.**

We first study the effect of particle size distribution on electrochemical performance and mechanical degradation. As will be shown here, the key factor controlling the role of particle size distribution are *mechanical particle-particle interactions* arising from the presence

of the relatively stiff SSE matrix, rather than the actual size (and size distribution) of the particles themselves. To illustrate this, we first conduct a simple study of a RVE composed of a single circular active particle embedded in a SSE matrix with periodic boundary conditions as shown in Fig. 3.5(a). Note that *we do not allow for interfacial damage* in these single particle simulations and focus only on investigating the build up of mechanical stresses at the interface. Importantly, due to periodic boundary conditions, the simulated domain is a repeated RVE and does not represent a single mechanically isolated particle, but a repeating unit of particle pairs all of the same geometry. Using the simulation domain shown in Fig. 3.5(a), we vary the volume fraction of active material defined through the geometric factor  $f = R_{\text{ap}}/R_{\text{ins}}$ , where  $R_{\text{ap}}$  is the active particle radius and  $R_{\text{ins}}$  is half the length of the simulation domain. The active material volume fraction is varied by changing both the particle size and the domain size through i) varying the active particle radius  $R_{\text{ap}} \in [1, 10] \mu\text{m}$  for a fixed domain size of  $R_{\text{ins}} = 12.5 \mu\text{m}$ , and ii) varying the domain size  $R_{\text{ins}} \in [6, 50] \mu\text{m}$  for a constant active particle radius of  $R_{\text{ap}} = 5 \mu\text{m}$ .

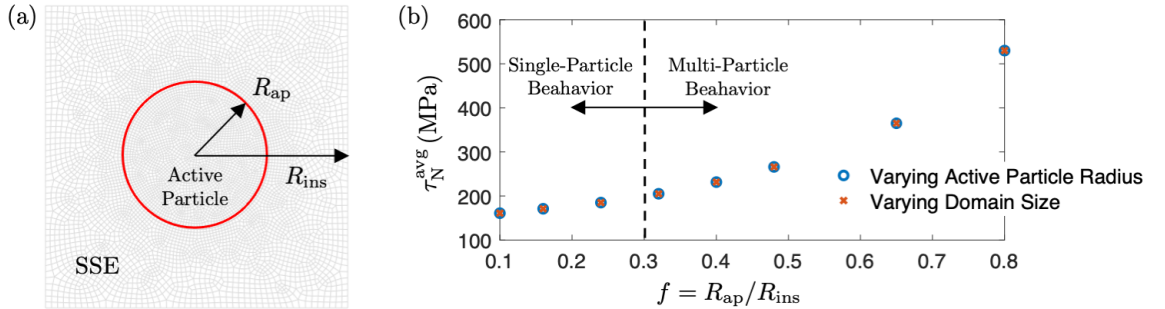


Figure 3.5: (a) Single particle representative volume element (RVE) simulation domain. (b) Plot of average normal interfacial stress  $\tau_N^{\text{avg}}$  as a function of the geometric factor (i.e volume fraction)  $f = R_{\text{ap}}/R_{\text{ins}}$ . Reproduced with permission from [17].

Fig. 3.5(b) shows the average normal interfacial stress  $\tau_N^{\text{avg}}$  induced in the particle at an SOC of 0.8 as a function of the active material volume fraction  $f = R_{\text{ap}}/R_{\text{ins}}$ . Results are shown both for simulations varying the active particle radius  $R_{\text{ap}}$  (circle markers) and simulations varying the domain size  $R_{\text{ins}}$  (x markers). The first critical observation to make is that the two simulation results are identical for a fixed active material volume fraction

$f$ . This demonstrates that active particle size by itself does not control stress generation at the interface, rather it is controlled by the active material volume fraction. In essence, from a design standpoint, generation of interfacial stresses is controlled by the electrode active material volume fraction (i.e. packing density) - through the presence of particle-particle mechanical interactions - and is *independent of the actual size of the active particles*. Similar results are found in the study by Bucci et al. [100].

The second critical observation shown in Fig. 3.5(b) is the importance of particle-particle interactions. At low active material volume fractions, roughly below  $f = 0.3$ , the particle simulated can be considered as “isolated” and we observe that the magnitude of  $\tau_N^{\text{avg}}$  remains relatively constant and low. As volume fraction of active material increases, the particle (through the prescribed periodic boundary conditions) acts in a multi-particle behavior and is affected by particle-particle interactions. In this regime of higher volume fractions of active material, the magnitude of  $\tau_N^{\text{avg}}$  increases rapidly with volume fraction as particle-particle interactions lead to a continuous increase in interfacial stresses with reduction in spacing between particles.

We now expand our study beyond a single particle to investigate the performance of a composite cathode RVE with varying particle size distribution and constant volume fraction of active material. Fig. 3.6 shows the simulated RVE domains, all of which have a constant active material volume fraction of  $\phi_{\text{AM}} = 30\%$ . Particle size and aspect ratio are seeded using a uniform distribution with prescribed lower and upper bounds. We consider active particle size bounds in the range of: i)  $2 - 6 \mu\text{m}$ , ii)  $4 - 5 \mu\text{m}$ , and iii)  $6 - 7 \mu\text{m}$ . This allows us to investigate the response of the electrode for both a uniform distribution with relatively small ( $4-5 \mu\text{m}$ ) and large particles ( $6-7 \mu\text{m}$ ), as well as a distribution with a larger spread in particle sizes ( $2-6 \mu\text{m}$ ).

The RVEs were generated using MicrostructPy [159], an open-source microstructure mesh generator, which allows the user to prescribe the active material volume fraction and lower and upper bounds for the uniform distribution in particle size as an input. The aspect

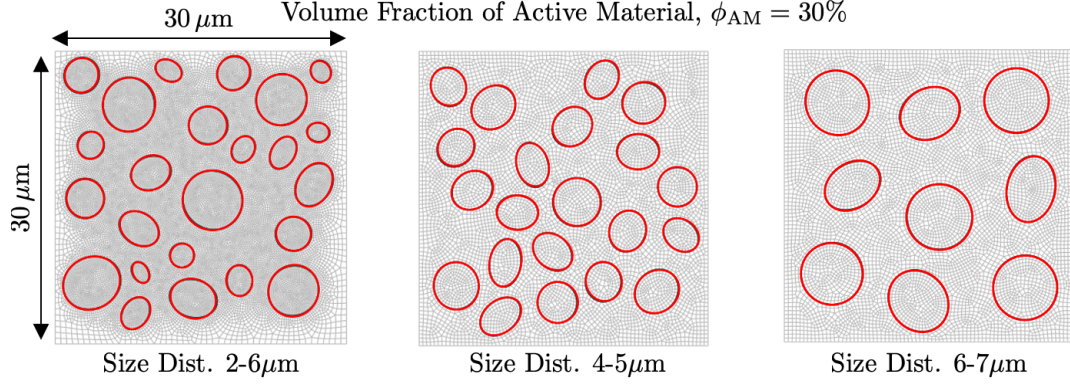


Figure 3.6: Simulated RVEs with a constant active material volume fraction  $\phi_{AM} = 30\%$ . The particle sizes are given a uniform distribution with lower and upper bounds in the range of: i) 2-6  $\mu\text{m}$  ii) 4-5  $\mu\text{m}$  and iii) 6-7  $\mu\text{m}$ . The aspect ratio lower and upper bounds are set to 0.9 and 1.5 respectively for all cases. Reproduced with permission from [17].

ratio lower and upper bounds for the elliptical particles are set to 0.9 and 1.5 respectively for all simulation domains. We cycle the electrode over three half-cycles between 3.8 - 4.6 V voltage caps at a C-Rate of 1/2C *with interfacial damage active*. All material properties are as described in Sect. 3.1, and for the interfacial cohesive strength we use  $t_N^c = 150 \text{ MPa}$ .

The Voltage vs. SOC response of the three RVEs is shown in Fig. 3.7(a) and compared to simulation results with no damage (which are identical for all particle size distributions). As shown in Fig. 3.7(a), electrochemical response of the RVE remains consistent across all

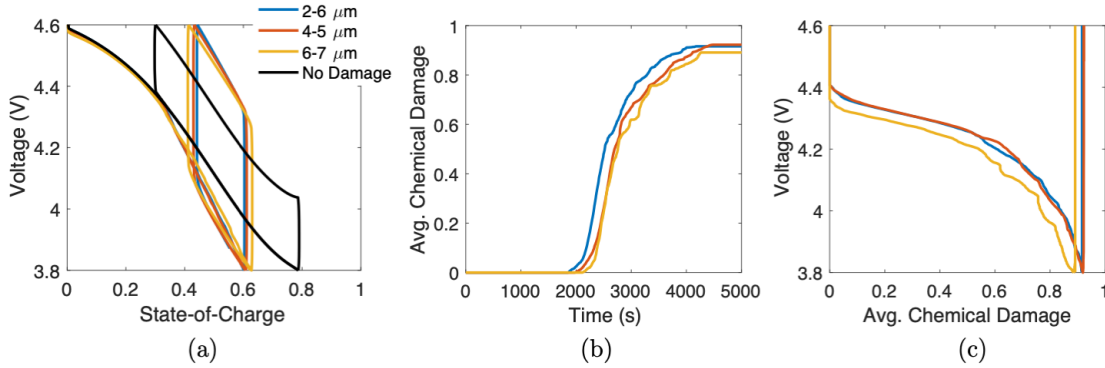


Figure 3.7: Simulation results for composite cathode RVEs with constant active material volume fraction  $\phi_{AM} = 30\%$  and varying particle size distribution. (a) Voltage vs. SOC behavior also compared to simulations with no damage. (b) Evolution of average  $D_{chem}$  as a function of time for the first half-cycle. (c) Evolution of Voltage as a function of average  $D_{chem}$ . Reproduced with permission from [17].

RVEs with a fixed  $\phi_{AM} = 30\%$ , noting again that *particle size distribution is not a critical factor in determining electrochemical performance*.

The evolution of damage is also consistent across the three microstructures as shown in Figs. 3.7(b) and (c). As noted in Sect. 3.1, mechanical damage,  $D_{mech}$  is taken to evolve in a rather ductile manner (so as to avoid numerical convergence issues), while chemical damage  $D_{chem}$ , defined in (3.1.3), is of a brittle nature. Fig. 3.7(b) shows the evolution of average  $D_{chem}$  (i.e average accumulated chemical damage) over the entire simulation domain as a function of time. We note that all damage occurs during the first charging half-cycle of the composite cathode and is fairly consistent across the various RVEs. During the second charging half-cycle, no additional damage occurs in any of the simulations and the electrode behavior stabilizes.

In addition, Fig. 3.7(c) shows the evolution in Voltage as a function of the average  $D_{chem}$ . Plots of this nature are particularly useful in assessing the manner in which adjusting the voltage caps in which we cycle the electrode can have a significant effect on the accumulation of damage. We note again that all RVEs have similar and consistent behaviors. Small differences in behavior of the three RVEs are related to the specific design of the microstructure, where for example, interactions between clusters of particles can lead to a slightly earlier initiation of damage. However, these differences are not significant as compared to changing the volume fraction of active material, as will be discussed in Sect. 3.3.2.

Fig. 3.8 shows the simulation domains at the end of the first half-cycle for the three RVEs, where in the active particles we show contours of the normalized concentration,  $\bar{c}$ , and in the SSE matrix we show contours of the maximum in-plane principal stress,  $\sigma_1$ . Note that deformation is scaled by 10x to best visualize interfacial degradation.

We observe that damage is consistently distributed across all particles, irrespective of particle size, and that we sustain similar levels of stress in the matrix across all simulation domains. Finally, these results also hold for microstructure compositions with other active

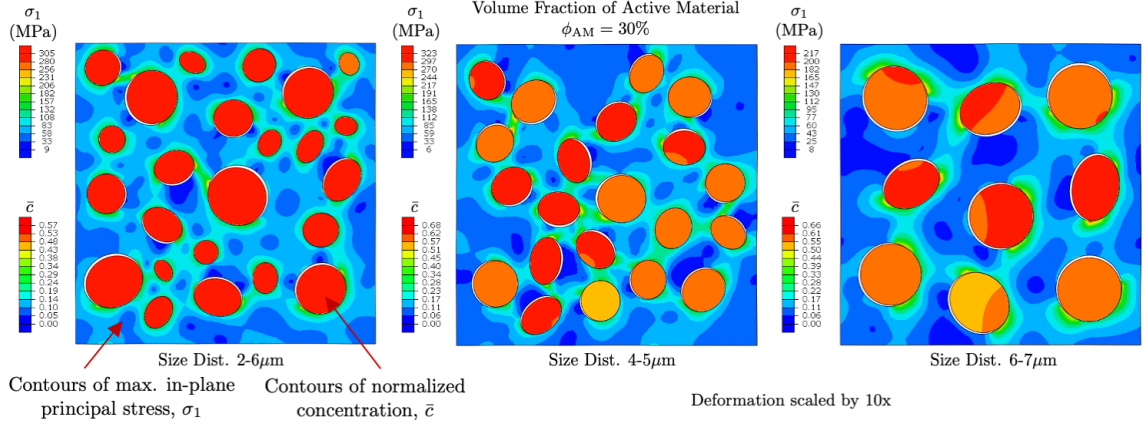


Figure 3.8: Simulation results for composite cathode RVEs with constant active material volume fraction  $\phi_{AM} = 30\%$  and varying particle size distribution. Results are shown at the end of the first half-cycle of each simulation domain. Reproduced with permission from [17].

material volume fractions. We refer the reader to Appendix A.4 for simulation results with an active material infill,  $\phi_{AM} = 20\%$ .

In this Section, we have demonstrated how starting with a fixed composition of active material volume fraction, *variations in particle size and particle size distribution do not play a significant role in the build up of stress, subsequent damage, and ultimately on electrochemical performance*. From a design standpoint, this finding has important implications as it clearly points to the fact that reducing the size of active particles is not an effective mechanism for reducing interfacial stresses and damage. We next discuss the role of varying the active material volume fraction,  $\phi_{AM}$ , which as expected from the discussion surrounding the results shown in Fig. 3.5, can have a significant effect.

### 3.3.2 Role of active material volume fraction on electrochemical performance and mechanical degradation

We consider next the role of varying the *active material volume fraction*,  $\phi_{AM}$  on electrochemical performance of SSB composite cathodes. Increasing the amount of active material in composite cathodes can be viewed as beneficial for it improves the overall volumetric capacity of the electrode. However, as demonstrated here, increasing the active

material infill can also lead to enhanced stress build up at the active particle/SSE interface, which can compromise mechanical integrity. This trade off poses the important question of whether there exists a *critical active material volume fraction* which maximizes volumetric capacity in the presence of mechanical degradation at the active particles interface.

We consider four representative microstructures with active material volume fraction in the range  $\phi_{AM} \in [20\%, 30\%, 40\%, 50\%]$  as shown in Fig. 3.9. Particle size distribution is kept identical for all simulation domains and is prescribed a uniform distribution with particle size lower and upper bounds of 2 and 6  $\mu\text{m}$  respectively. As in Sect. 3.3.1 above, the aspect ratio of active particles is also uniformly distributed with lower and upper bounds set at 0.9 and 1.5 respectively. This size distribution is chosen to match the experimental SEM images in the work of Zhang et al. [16]. As before, periodic boundary conditions are prescribed to the electrode domain and we cycle the composite cathode over three half-cycles between 3.8 - 4.6 V voltage caps at a constant C-Rate of 0.5C. Damage is modeled using the same material parameters described in Sect. 3.3.1 above.

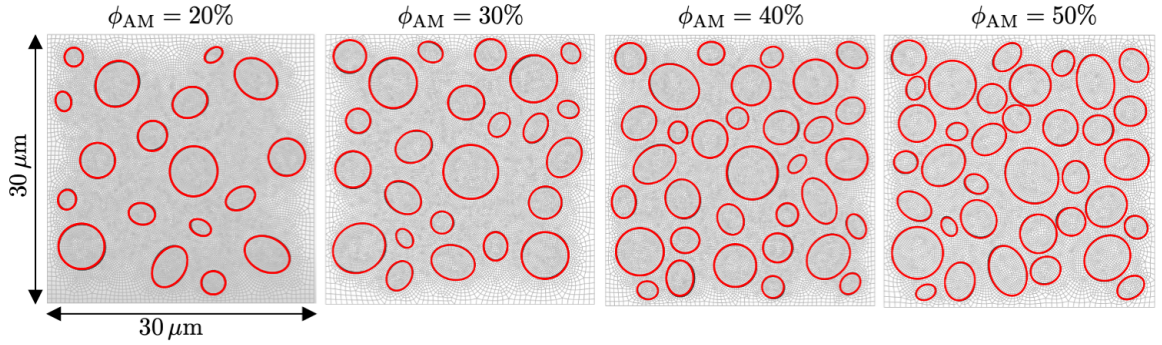


Figure 3.9: Simulated RVEs with a constant particle size distribution and varying active material volume fraction  $\phi_{AM}$ . Reproduced with permission from [17].

In order to account for increase in capacity with added active material, here, we report capacity results normalized by the *total mass* of electrode. That is, capacity is computed as,

$$\text{Capacity} = \frac{\int_{V_{AM}} \bar{c} dV_{AM} \cdot c_{R,\max} \cdot F}{m_{RVE}} \quad (3.3.1)$$

where  $m_{RVE}$  is the total mass of the composite cathode,  $c_{R,\max}$  is the maximum molar con-



centration of the active material given in Table 3.1,  $F$  is the Faraday constant, and  $\bar{c}$  is the normalized concentration integrated over the volume of active material. The mass of the electrode RVE is computed as  $m_{\text{RVE}} = V_{\text{AM}} \cdot \rho_{\text{AM}} + V_{\text{SSE}} \cdot \rho_{\text{SSE}}$ , with  $\rho_{\text{AM}} = 4.79 \text{ g/cm}^3$  for LCO as reported in [139, 160], while we determine the density of the SSE,  $\rho_{\text{SSE}} = 2.1 \text{ g/cm}^3$  from the work of Zhang et al. [16], who reported both volume and mass ratios for various LCO-LGPS microstructure compositions.

Fig. 3.10(a) and (b) show the Voltage vs. Capacity curves for the four simulation domains with and without damage respectively. First, we note as expected, that simula-

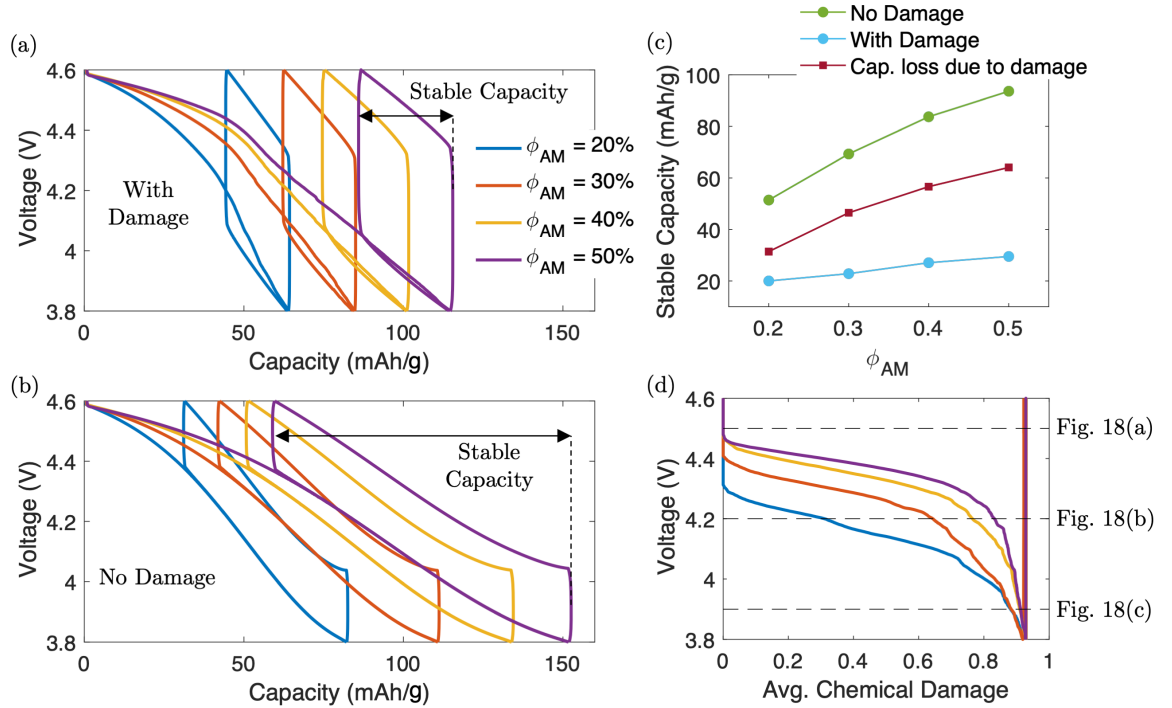


Figure 3.10: Simulation results for composite cathode RVEs with constant particle size distribution and varying volume fraction  $\phi_{\text{AM}}$ . (a) and (b) show Voltage vs. Capacity (defined per unit total mass of the RVE) for simulations with and without interfacial damage respectively. (c) Stable capacity during cycling as a function of  $\phi_{\text{AM}}$  for simulations with and without damage and also shows the stable capacity loss due to damage, which is the difference of the two simulation results. (d) Voltage as a function of accumulated chemical damage (i.e. average  $D_{\text{chem}}$  in the entire simulation domain) for simulations with varying  $\phi_{\text{AM}}$  and interfacial damage. Note the legend in (a) applies equally to (b) and (d). Reproduced with permission from [17].

tions without damage, Fig. 3.10(b), also show variation in Voltage vs. Capacity response,



since capacity is normalized per total mass of the electrode. The effect of damage is clearly visible and we observe a drastic change in electrochemical behavior when comparing Figs. 3.10(a) and (b). In particular, in Fig. 3.10(a), we highlight the stable capacity of electrode as defined by the stable electrochemical window achieved following the first half-cycle. We can clearly observe the significant decrease in capacity when accounting for damage at the interface for a given active material infill.

The stable electrode capacity as a function of the active material volume fraction,  $\phi_{AM}$  is shown in Fig. 3.10(c). Here, we plot the stable electrode capacity for simulations without mechanical damage (green line) and damage at the particle-electrolyte interface active (blue line). In addition, we plot the difference in capacity of the two curves and label the result as the loss in capacity incurred by mechanical delamination of the interface (red line). We observe here the manner in which active material volume fraction plays a critical role in electrochemical performance of the electrode in the presence of interfacial damage. Comparing the undamaged and damaged curves in Fig. 3.10(c), we observe that as active material infill,  $\phi_{AM}$  is varied from 20% to 50%, stable capacity shrinks by 31, 46, 57, and 64 mAh/g. In fact, from Fig. 3.10(c), one can observe that stable capacity remains nearly constant with  $\phi_{AM}$  for simulations with active mechanical damage at the interface. This is attributed to capacity losses due to mechanical damage increasing with  $\phi_{AM}$  almost as rapidly as stable capacity of the undamaged microstructure increases with added active material. That is, *any capacity gains achieved by having a higher active volume fraction,  $\phi_{AM}$  are almost entirely negated by increasing losses due to mechanical degradation.*

From a design perspective, it is also useful to look at the Voltage vs. Accumulated chemical damage behavior of the electrode, as shown in Fig. 3.10(d). Two important trends can be observed here. First, damage *initiates earlier (i.e. at higher voltages)* for microstructures with higher  $\phi_{AM}$ . Second, the *rate of damage evolution* (i.e. the slope of the curve at intermediate accumulated chemical damage values) is also higher for microstructures with higher  $\phi_{AM}$ . From a design standpoint, the data shown in Fig. 3.10(d) is also useful in guid-

ing one to determine where a voltage cutoff could be placed to reduce mechanical damage at interface. For example, at a voltage cutoff of 4.1 V, the microstructure with  $\phi_{AM} = 20\%$  will have only incurred approximately 60% accumulated damage as compared to 90% for microstructures with  $\phi_{AM} = 50\%$ .

The detailed evolution in stress, concentration, and damage across the electrode domain is shown in Fig. 3.11, where we show results at a voltage of (a) 4.5 V (top row), (b) 4.2 V (middle row), and (c) 3.9 V (bottom row). The corresponding voltages are marked in Fig. 3.10(d). In all results, we show contours of the maximum in-plane principal stress,  $\sigma_1$

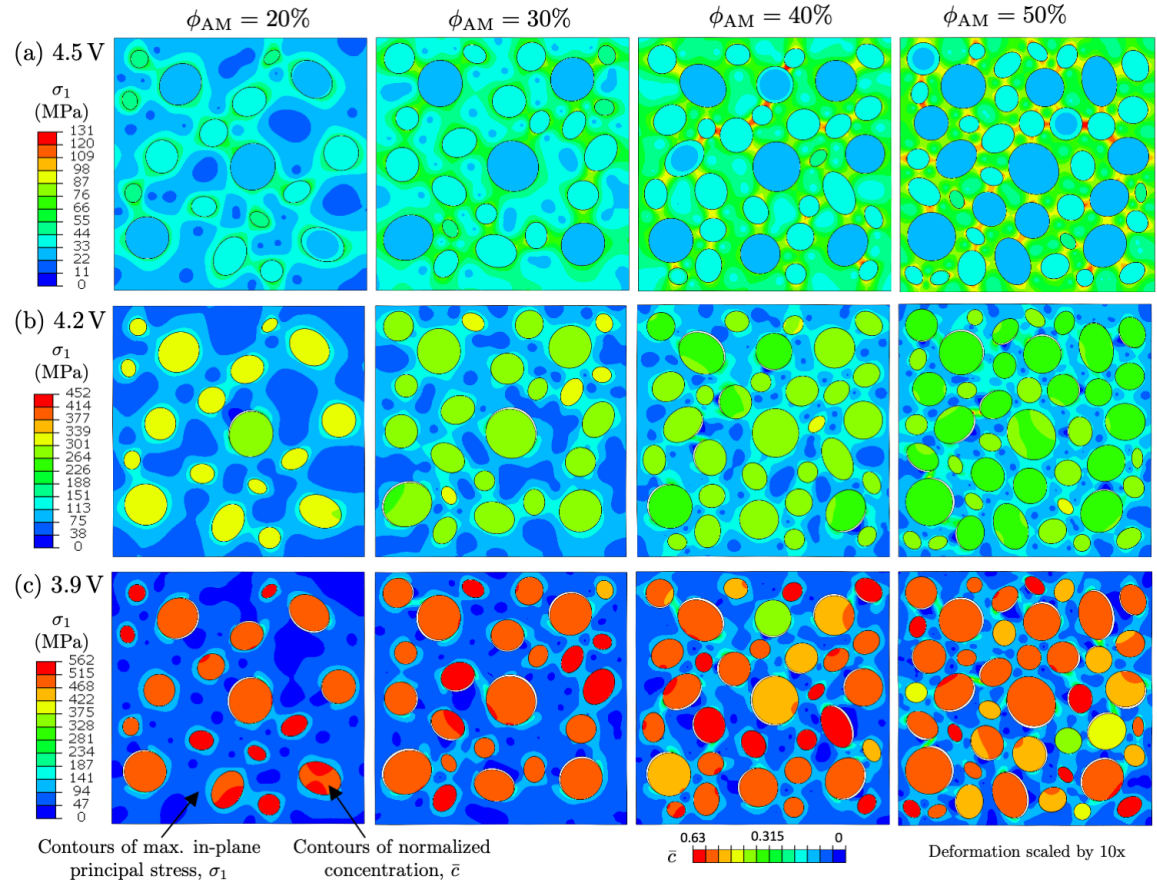


Figure 3.11: Simulation results for composite cathode RVEs with constant particle size distribution and varying volume fraction  $\phi_{AM}$ . Results are shown at (a) Voltage of 4.5 V (top row), (b) Voltage of 4.2 V (middle row), and (c) Voltage of 3.9 V (bottom row). In all results, we show contours of the maximum principal stress,  $\sigma_1$ , over the SSE matrix, and contours of normalized concentration  $\bar{c}$  over the active particles. Note that the colorbar for  $\sigma_1$  is constant over a given Voltage, and the colorbar for  $\bar{c}$  is constant for all simulations shown. Deformations are scaled by 10x. Reproduced with permission from [17].

over the SSE matrix, and contours of normalized concentration,  $\bar{c}$  over the active particles. In Fig. 3.11(a), at 4.5 V, no damage has yet initiated over the domain (see Fig. 3.10(d)) and we can clearly observe the manner in which stresses increase with increase in  $\phi_{AM}$ . We can also clearly observe how  $\sigma_1$  hotspots arise between nearby particles due to mechanical particle-particle interactions. This trend persists at all voltages. In Fig. 3.11(b), at 4.2 V, damage has initiated across all microstructures, with significantly more damage occurring across microstructures of higher active material infill,  $\phi_{AM}$ . A similar response is also observed at 3.9V in Fig. 3.11(c).

Another important observation is with respect to distribution of normalized concentration  $\bar{c}$ . Focusing on the results in Fig. 3.11(c) at 3.9 V, we can clearly observe that *concentration of Li is more uniformly distributed over all particles in microstructures with small active material volume fraction,  $\phi_{AM}$* . In contrast, simulations with high  $\phi_{AM}$  show a broad range of concentrations over the various particles. This phenomena arises from the presence of mechanical interfacial damage. For simulations with high  $\phi_{AM}$ , multiple particles have entirely decohered from the surrounding SSE matrix and thus have chemically isolated. These particles can no longer store Li-ions and contribute to the overall loss of capacity due to mechanical damage experienced by the microstructures with higher active material volume fraction.

In summary, we formulated and numerically implemented a theoretical framework – based on use of a chemo-mechanical surface element – for modeling the stress-coupled chemo-mechanical interactions in complex electrode designs under galvanostatic charging. In particular, the theoretical framework allows one to capture both chemical and mechanical interactions between active particles in battery electrodes. Under galvanostatic charging conditions, the theoretical framework captures chemical interactions between particles whereby current is distributed non-uniformly between active particles based on their local stress-coupled interface reaction kinetics. Mechanically, the proposed surface elements allow one to capture the role of mechanical interfacial damage on electrochemical perfor-

mance by coupling interfacial reaction kinetics (i.e. current) to mechanical damage. This allows one to model how loss of mechanical integrity at the interface limits reaction kinetics and overall electrochemical performance of the electrode. We applied the theoretical framework to investigate the chemo-mechanical behavior — including interfacial degradation — of a LCO-LGPS composite electrode under galvanostatic charging, with a focus on understanding how microstructural features such as local material properties, particle size distribution and packing density impact the overall electrochemical behavior of the composite electrode.

The following important findings were made with respect to this electrode:

- We demonstrated that variations in SSE stiffness and active material contraction during lithiation can have a large impact on electrochemical performance of SSB cathodes in the presence of interfacial delamination. The theoretical framework developed thus provides an important tool for future exploration of design of composite electrodes with different active material-SSE pairs in order to enhance mechanical integrity and concurrently electrochemical performance.
- With respect to microstructural composition, we first demonstrated that particle size does not play a critical role in stress build up at the interface and subsequent mechanical degradation. This was demonstrated both through simple single-particle RVEs and through complex multi-particle RVEs with different particle size distributions.
- The active material volume fraction was demonstrated to be a critical factor in electrochemical performance in the presence of mechanical degradation. This microstructural descriptor largely dictates the build up of interfacial stresses at the active particles, and thus controls the onset and evolution of mechanical interfacial degradation.
- We demonstrated that while increasing the active material volume fraction does naturally increase the capacity of the LCO-LGPS cathode under consideration, these gains can be quickly undermined by the enhanced mechanical interfacial degradation

experienced. The theoretical framework developed provides a quantitative analysis of the manner in which capacity of a given RVE varies with increase in active material in the presence of mechanical interfacial degradation, and can serve as a useful tool for design of complex novel SSB cathode architectures for future applications.

In chapter 4 to follow, we computationally address another critical issue hindering commercialization of all-solid-state batteries, namely the phenomenon of Li-metal filament growth across solid-state electrolytes with fracture of the latter, causing the battery to short-circuit.

**CHAPTER 4**  
**A CONTINUUM ELECTRO-CHEMO-MECHANICAL GRADIENT THEORY**  
**COUPLED WITH DAMAGE: APPLICATION TO LI-METAL FILAMENT**  
**GROWTH IN ALL-SOLID-STATE BATTERIES**

We formulate a thermodynamically-consistent, electro-chemo-mechanical gradient theory which couples electrochemical reactions with mechanical deformation and damage in solids. The framework models both species transport across the solid host due to diffusion/migration mechanisms and concurrent electrochemical reaction at crack surfaces within the solid host where ionic species are reduced to form a new compound. The theory is fully-coupled in nature with electrodeposition impacting mechanical deformation, stress generation and subsequent fracture of the solid host. Conversely, electrodeposition kinetics are affected by mechanical stresses through a thermodynamically-consistent, physically motivated driving force that distinguishes the role of chemical, electrical and mechanical contributions. Critically, the framework captures the interplay between growth-induced fracture of the solid host and electrodeposition of a new material inside cracks by tracking the damage and extent of electrodeposition using separate phase-field variables. Here, the fundamental distinction is made such that material deposition across the solid host can only occur upon preliminary fracture of the solid host to enable for creation of vacant sites which can accommodate the newly deposited compound. An attractive feature of the theory is its ability to model nucleation, propagation and branching of cracks across the solid host in arbitrary orientations driven by a thermodynamically-consistent fracture driving force. Critically, the gradient damage formulation invokes a tension-compression asymmetry to preserve resistance in compression of fractured regions within the solid host.

While the framework is general in nature, we specialize it towards a critical problem of relevance to commercialization of next-generation all-solid-state batteries, namely the

phenomenon of metal filament growth across a solid-state electrolyte, eventually leading to short-circuit. We specialize on a Li-metal -  $\text{Li}_7\text{La}_3\text{Zr}_2\text{O}_{12}$  (LLZO) system and demonstrate the capacity of the framework to capture both intergranular and transgranular crack and Li-filament growth mechanisms, both of which have been experimentally observed. Development of a microstructure-resolved description of the process of metal filament growth through the SSE microstructure is currently lacking and accordingly addressed in this thesis. In modeling this system, we elucidate the manner in which mechanics and fracture of the SSE impact electrodeposition kinetics and Li-filament growth. From a manufacturing standpoint, we additionally elucidate the role of mechanical confinement in solid-state batteries on the rate of crack propagation versus the rate of Li-metal deposition across the LLZO electrolyte. Under specific mechanical boundary conditions, we demonstrate the capacity of the framework to qualitatively reproduce the experimentally observed phenomenon of crack fronts propagating ahead of Li-metal filaments, as partially-filled cracks reach the far electrode end in advance of Li-deposits. Beyond this application, the framework should serve useful in a number of engineering problems of relevance in which electrochemical reactions take place within a damage zone, leading to creation of new material at these locations. The work in this chapter was adopted with permission from:

- Bistri, Donald, and Claudio V. Di Leo. "A continuum electro-chemo-mechanical gradient theory coupled with damage: Application to Li-metal filament growth in all-solid-state batteries." *Journal of the Mechanics and Physics of Solids* 174 (2023).

## 4.1 Introduction

Solid-state batteries (SSBs) present a promising technology for next-generation energy storage systems. In recent years, commercialization of SSBs has attracted significant research attention owing to their promise of superior performance compared to conventional Lithium-ion batteries (LIBs). Among their many advantages, SSB architectures can enable for increased current density ( $\approx 3860 \text{ mAh/g}$ ), improved safety, and a wider electro-

chemical window (0-5V) - in turn enabling for coupling of Li-metal anodes with high voltage cathode materials [3, 4, 5, 7, 161]. From a safety standpoint, use of inorganic solid-state electrolytes (SSEs) immediately alleviates potential hazards associated with ignition of liquid electrolytes commonly used in LIBs. In addition, the solid-state nature of the electrolyte material has the potential to alleviate failure mechanisms associated with dendrite growth. However, successful design and operation of SSBs is hampered by several chemo-mechanical challenges across its constituents [9, 17, 18, 19, 153, 162], the most critical one associated with metal filament growth across the SSE microstructure, eventually leading to short-circuit.

Unlike the process of dendrite growth in liquid electrolyte systems, growth of metal filaments across the SSE in a solid-state architecture depends on fundamentally different mechanics. Owing to the solid-state nature of the electrolyte, the SSE microstructure is hypothesized to play a fundamental role. Li-metal filaments can initiate at imperfections or heterogeneities of the metal/SSE interface such as voids, cracks, and grain boundaries. Once initiated, these filaments propagate through the SSE microstructure by fracturing the latter and creating fresh sites for continuing Li-metal deposition and filament growth. In this view, *mechanical fracture and Li-metal filament growth are intrinsically coupled*. Eventually, metal filaments may pierce through the entire SSE, reaching the cathode and leading to short-circuit of the battery [20, 58, 59, 60]. It is thus critical to understand from both an experimental and modeling perspective the interplay between electrodeposition at the Li-metal interface and the SSE microstructure. In particular, the manner in which defects, rate of Li deposition, local stress state, and mechanical behavior (including fracture) of both Li-metal and SSE couple to govern the onset and evolution of Li-metal filaments in SSB architectures [22, 61, 62, 63, 64, 163].

Filament growth has been experimentally observed to occur above a critical current density in both compliant [20, 66, 67, 68] and stiff oxide-based [58, 59, 60, 69, 70, 71] electrolytes. These experimental observations counter previous modeling predictions [72]



that claimed filament growth could be suppressed - and replaced with stable Li-metal deposition - provided the shear modulus of the SSE is at least twice as large as that of Li-metal. Advanced characterization techniques including tomographic imaging and spectroscopy have revealed propagation of Li-metal filaments across the SSE microstructure to occur either i) transgranularly, in the form of a dominant Li-filament, typical for single-crystal electrolytes [20, 60, 69, 73] or ii) intergranularly, through the grain boundaries, typical for polycrystalline SSEs [58, 59, 66, 74, 75]. Recent studies have additionally hypothesized the potential for isolated Li-metal deposits to form within the bulk SSE microstructure due to the favorable SSE electronic properties and presence of trapped electrons. Upon reaction with Li-ions, these trapped electrons may produce isolated Li-metal deposits, seeding subsequent growth of Li-metal filaments across the SSE microstructure [76, 77].

Aside from experimental observations, several modeling frameworks have been proposed in the literature to address different aspects of the nucleation and propagation of Li-metal filaments in SSEs. Related to nucleation of Li-metal filaments, linear perturbation analysis has been extensively employed in several models [78, 79, 80, 81, 82, 83]. Starting with a sinusoidal interface perturbation, these models have investigated the stability of electrodeposition at the Li-metal/SSE interface with variation in perturbation amplitude, applied current density and state of pre-stress. Consistent with experimental observations, growth of Li-metal filaments (e.g. unstable electrodeposition) was shown to occur irrespective of the SSE stiffness provided the applied current density and perturbation wavelength are sufficiently high. To study the potential for propagation of existing Li-metal filaments, a second class of models, treating metal protrusions as pressurized cracks under a linear elastic fracture mechanics framework was later developed [60, 164, 165, 166, 167, 168]. These works investigated the role that defect size, surface resistance and tip overpotential play on the propensity for Li-metal filaments to fracture the SSE and grow across the solid conductor. While clearly important, the two classes of models discussed above are limited to either modeling the nucleation of Li-filaments or the conditions under which an

existing filament might propagate. They can not capture the dynamic evolution of Li-metal filaments, which is the focus of this work.

Recently, mature continuum chemo-mechanical frameworks have been developed to model the complex electro-chemo-mechanical processes that govern non-uniform electrodeposition at a Li-metal/SSE interface in the presence of imperfections. Narayan and Anand [84] propose a thermodynamically-consistent continuum theory to model non-uniform plating/stripping kinetics at the Li-anode coupled with elastic-viscoplastic deformation of Li-metal. Given the complexity of modeling freshly-deposited Li-layers from a finite element standpoint, the authors propose an analogous mechanical problem of swelling and de-swelling of a thin “interphase layer” at the Li-metal/SSE interface to reproduce the electro-chemical process of plating/stripping. The framework provides important insights on the role that both geometric imperfections and chemical impurities at the metal/SSE interface play on the evolution of Li-metal filaments and concomitant deformation and fracture of the associated metal electrode-solid electrolyte materials. However, the framework is limited in its capacity to model the ongoing electrochemical reaction kinetics driving the growth of Li-metal filaments, and can not subsequently predict the morphology and evolution of the resulting Li-filaments. The work of Shishvan et al. [85, 86] presents one of the first attempts to model the evolution of Li-metal filaments across the SSE beyond the idealization of filaments as pressurized cracks. In [85], the authors propose an alternative mechanism for initiation of metal filaments, treating metal protrusions as thick-edge dislocations and demonstrate the capacity of the framework in [86] to predict the experimentally reported critical current density and growth rate of Li-deposits across SSEs.

Phase-field models have also been extensively developed to capture Li-metal filament growth in both liquid and solid-state battery architectures. Purely electro-chemical non-linear phase-field models have been developed and shown to successfully predict the evolution and morphology of Li dendrites in liquid-electrolyte systems under varying applied electric potentials [169, 170, 171, 172, 173]. Recently, phase-field based models have

been extended to solid-state architectures - including both inorganic and polymer-based electrolytes - to incorporate the role of mechanics and deformation of Li-metal due to the confining SSE on electrodeposition kinetics [77, 174, 175, 176]. These works present the first attempts at capturing the evolution and morphology of Li-metal filaments across a solid conductor, while simultaneously accounting for the presence of microstructural inhomogeneities in the solid-electrolyte [174]. However, these models do not capture the fundamental coupling between fracture of the SSE and electrodeposition. Li-metal filaments growing in solid electrolytes, unlike dendrites in their liquid counterparts, are constrained by a solid continuum and must overcome the associated mechanical resistance by fracturing the solid host. Only upon fracture of the solid conductor, and subsequent creation of an empty deposition site, may Li-metal filaments proceed to grow by plating the newly fractured space. Recent work by Fincher et al. [65] experimentally demonstrates this phenomenon. There, the authors apply an external, experimentally controlled stress field on a solid-state electrolyte through which a Li-filament is growing. By controlling the stress field, Fincher and co-workers change the preferred fracture direction of the underlying SSE and demonstrate that this in turn changes the direction of Li-filament growth correspondingly. This work provides direct experimental evidence for the coupling between SSE fracture and Li-metal filament growth.

As summarized above, there is a need for a fully-coupled, electro-chemo-mechanical framework which captures: i) the nucleation and evolution of Li-metal filaments, ii) the concurrent fracture of the solid host, and iii) the coupling between mechanical deformation, stress and Li-metal electrodeposition kinetics. Of particular importance in such a framework is also the ability to model the role that heterogeneities in the SSE microstructure (i.e. pores, cracks, grain boundaries) play on the coupled fracture behavior of the SSE and concurrent Li-metal filament growth due to electrodeposition. The purpose of this work is to present such a framework.

We develop here a thermodynamically consistent, phase-field electro-chemo-mechanical

framework for modeling concurrent diffusion, reaction, deformation and damage in solids. While the framework is general in nature and can be applied across a number of engineering problems (i.e. electro-chemically active polymers [57, 177, 178, 179], oxidation and corrosion [45, 53, 180, 181, 182], electro-refining [183]), we specialize it towards modeling the onset and evolution of Li-metal filaments in all-solid-state batteries. In particular, our framework includes the following unique features distinguishing it from previous work in the literature:

- The theoretical framework captures concurrent charged species diffusion/migration and reaction, coupled to mechanical deformation and damage of the solid host. Currently, continuum electro-chemo-mechanics theories for energy storage materials in the literature have been largely developed for diffusion of a conserved species across the host (i.e. no chemical reactions) [42, 108, 111, 112, 113], with some recent efforts capturing diffusion-reaction in solids [15, 46, 47]. While rigorous, current diffusion-reaction-deformation frameworks do not consider transport of charged species across the host in the presence of electric field, and thus are limited to modeling chemical rather than electro-chemical reactions. Continuum mechanics formulations for transport of charged species have been developed [87, 177, 178], but in turn do not consider electrochemical reactions and apply only to a conserved diffusing species. This work provides a unified thermodynamically consistent electro-chemo-mechanical framework, which concurrently accounts for diffusion and reactions within the host material with the potential for reaction-induced fracture of the latter.
- The theory captures the coupling between fracture of the solid host and electrodeposition of a new material inside cracks by modeling the evolution of cracks and material deposition using distinct phase-field variables. While numerical frameworks coupling reaction with fracture of the host material have been proposed in the literature (i.e. stress corrosion cracking [52]), the theory importantly presents the first framework coupling a phase-field reaction model for Li-metal filament growth with a

phase-field damage model for electrodeposition-induced fracture of the solid conductor for energy-storage applications. Critically, this enables one to model the manner in which mechanical fracture of the SSE is intrinsically coupled to electrodeposition and growth of Li-metal filaments. We demonstrate how this coupling can arise both through a thermodynamically consistent reaction driving force, and/or through a damage dependent formulation of the reaction kinetics.

- The theoretical framework, and accompanying numerical implementation, allows one to model the role of microstructure heterogeneities (i.e. voids, cracks, grain boundaries) with varying chemo-mechanical properties on concurrent fracture of the SSE and electrochemical growth of Li-filaments. As such, the model may predict the manner in which various microstructural features enhance or suppress Li-filament growth and subsequently guide the development of microstructures for minimizing filament growth-induced degradation.

To demonstrate the relevance and use of the proposed theoretical framework, we specialize it towards modeling the growth of Li-metal filaments in an inorganic Lithium Lanthanum Zirconium Oxide electrolyte, specifically  $\text{Li}_7\text{La}_3\text{Zr}_2\text{O}_{12}$  (LLZO). LLZO is a promising SSE candidate due to its high ionic conductivity, high mechanical stiffness and good stability against Li-metal. We explore the experimentally observed manner in which Li-metal filaments may grow across the LLZO electrolyte either i) transgranularly, as a single dominant Li-metal filament propagating across the conductor [60], and/or ii) intergranularly, across the mechanically weaker grain boundaries [58, 59, 66]. In particular, owing to the coupling between mechanical stresses, fracture and electrodeposition kinetics developed in this framework, we investigate the manner in which mechanically weaker grain boundaries with lower fracture energy dictate the transgranular versus intergranular nature of the resulting Li-metal filaments. Finally, using our framework, we provide insights on the manner in which mechanical confinement and stresses dictate the advancement of cracks versus Li-metal deposits across the solid electrolyte. In particular, whether the crack

front propagates significantly ahead of the Li-metal filaments as has been experimentally observed [20, 66].

The framework is organized as follows. In Sect. 4.2, we introduce mass balance, charge balance and electrostatics equations and define the physically motivated phase-field parameters,  $\bar{\xi}$ , governing the extent of electrodeposition, and  $d$ , governing the extent of damage in the solid host. Kinematics are developed in Sect. 4.3. The remaining governing laws are developed in Sect. 4.4 using the principle of virtual power and the first and second laws of thermodynamics. The constitutive theory is presented in Sect. 4.5 and summarized in its general form in Sect. 4.6. In Sect. 4.7, we present a specialization of the theory towards modeling the growth of Li-metal filaments in a LLZO solid-state electrolyte, and summarize the governing partial differential equations and initial/boundary conditions in Sect. 4.8. Numerical simulations are presented in Sect. 4.9. First, in Sect. 4.9.1, we model the growth of a single Li-metal filament across a LLZO electrolyte. Through this model, we demonstrate the salient features of our theoretical framework and explore the role that mechanical confinement and stress play on the evolution of cracks and Li-metal filament growth across the solid electrolyte. In Sect. 4.9.2, we illustrate the manner in which different microstructural features, in particular grain boundaries, may be incorporated into the modeling framework. Within this model of a LLZO electrolyte with resolved grain boundaries, we elucidate the manner in which mechanical stresses, damage and electrodeposition are coupled and how different coupling mechanisms result in different fracture and Li-filament morphologies. Finally, we demonstrate the manner in which this framework directly couples mechanical properties, such as grain boundary fracture energy, with the resulting Li-filaments growth pattern. We close with concluding remarks in Sect. 4.10.

## 4.2 Phase-field formulation and balance equations

This section details the conservation laws for electrodeposition phenomena within a solid ion-conducting host. The problem is shown schematically in Fig. 4.1(a), where we illus-

trate a solid conductor (SSE) adjacent to an electrode composed of a metallic compound “M”. The solid conductor/metal electrode interface may contain a number of defects (i.e. pores, voids, cracks), which serve as vacant sites for the metallic compound to fill and subsequently deposit inside the solid host (c.f. [60, 164, 165]). Consider now a simple and general electrodeposition reaction. Cations,  $M^{n+}$  conduct across the solid host towards the conductor/metal interface, where they react with electrons,  $e^-$  to deposit M-atoms as follows



The electrodeposition of M-atoms (i.e. metallic compound) is treated in a phase-field sense and taken to occur over a diffuse boundary, with the extent of reaction tracked via a normalized phase-field parameter

$$\bar{\xi} = \xi/\xi^{\max} \in [0, 1]. \quad (4.2.2)$$

Here,  $\xi$  denotes the moles of electrodeposited species per unit reference volume, with  $\xi^{\max}$  the maximum amount of the metallic compound that can be electrodeposited at the reaction site. Physically, a state of  $\bar{\xi} = 0$  denotes the absence of metallic compound or “void”, while a state of  $\bar{\xi} = 1$  denotes the fully deposited metallic compound. Naturally then, intermediate values of  $0 < \bar{\xi} < 1$  represent the reaction zone.

In this physical interpretation of the phase field variable,  $\bar{\xi}$ , we restrict the formulation such that *electrodeposition inside the solid host may occur only within voids* (i.e. cracks, pores), which either form through mechanical loading or exist inherently in the microstructure. This interpretation conforms with experimental observations that for metal deposits to grow through a solid host, they must first overcome mechanical resistance by fracturing the solid to create the necessary vacant space to accommodate plating (c.f. Fincher et al. [65] and Ren et al. [184]).

We now introduce a phase-field damage variable,  $d(\mathbf{X}, t)$  to describe *any state of im-*

*perfections across the solid host, either pre-existing (i.e. pores, voids) or mechanically induced (crack formation)*

$$d(\mathbf{X}, t) \in [0, 1].$$

Here, a state of  $d = 0$  represents the intact material, while a state of  $d = 1$  represents the fully-fractured solid host. Intermediate values,  $0 < d < 1$  naturally denote then a partially fractured material. Additionally, we assume microstructural changes leading to fracture to be irreversible and require damage to grow monotonically such that

$$\dot{d}(\mathbf{X}, t) > 0. \quad (4.2.3)$$

With a focus on the crack/electrodeposition interplay, we restrict ourselves such that *electrodeposition may only occur within damaged regions of the SSE*. That is,

$$\bar{\xi} > 0 \quad \text{only if} \quad d > 0. \quad (4.2.4)$$

This is shown schematically in Fig. 4.1(b-d). Fig. 4.1(b) illustrates a microstructural defect in the form of a void or crack (region of  $d = 1$ ) at the metal/SSE interface, which provides the necessary vacant space for metal to deposit. With continuous deposition, the metallic compound progressively covers the entire area of the crack ( $d = 1, \bar{\xi} = 1$ ), as illustrated in Fig. 4.1(c). This in turn induces a build-up in stresses acting on the crack's surface, large enough to eventually overcome the fracture toughness of the solid conductor and incur further damage on the solid host, Fig. 4.1(d). The newly formed damaged region ( $d = 1, \bar{\xi} = 0$ ) then provides the additional vacant site for the metal to deposit further into the solid electrolyte. This synergistic mechanism sustains the growth of Li-metal filament across the solid host. Eventually, the metallic protrusions fracture and transverse the entire span of the solid conductor, at which point the battery short-circuits.



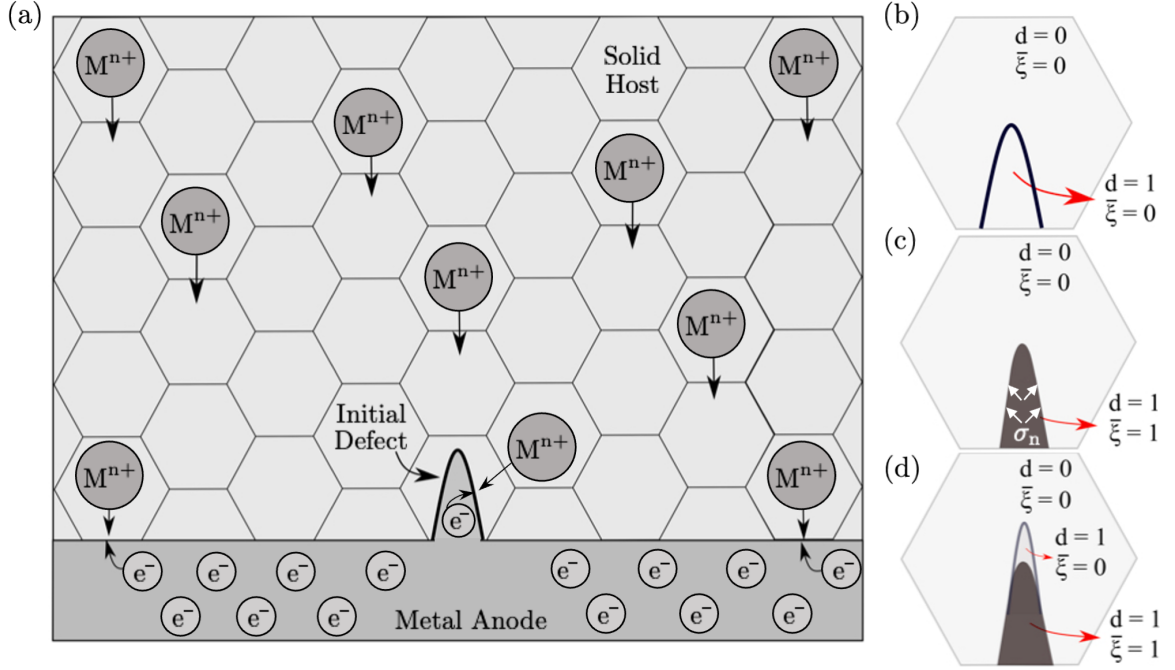


Figure 4.1: (a) Schematic of a metal electrode-solid conductor assembly. (b) Illustrates a pre-existing defect ( $\bar{\xi} = 0, d = 1$ ) at the solid host-metal electrode interface prior to metal deposition inside the crack. (c) Illustrates deposition of metal inside the imperfection ( $\bar{\xi} = 1, d = 1$ ), leading in turn to a build up in normal stresses,  $\sigma_n$ , at the crack surfaces. (d) Build-up in normal stresses on the crack surface eventually causes the solid host to damage further ahead of the crack tip, creating a new damage zone ( $\bar{\xi} = 0, d = 1$ ), which can accommodate subsequent deposition of metal inside the solid host. Reproduced with permission from [19].

#### 4.2.1 Mass Balance

Considering the electrodeposition reaction (4.2.1), conservation of mass for the mobile ionic species transporting across the solid host may then be written as a diffusion-reaction equation of the form

$$\dot{c} = -\text{Div} \mathbf{j}_r - \dot{\xi}. \quad (4.2.5)$$

Here,  $c(\mathbf{X}, t)$  denotes the number of moles of the mobile ionic species per unit reference volume, while  $\xi(\mathbf{X}, t)$  denotes the number of moles of the electrodeposited species per unit reference volume with  $\dot{\xi}$  the electrodeposition rate. Consistent with the discussion in Sect. 4.2, when the extent of reaction  $\bar{\xi} = 1$ , the reaction has led to consumption of  $\xi^{\max}$  moles of the diffusing species. Additionally,  $\mathbf{j}_r(\mathbf{X}, t)$  represents the referential flux of the mobile

ionic species transporting across the solid host, which must be constitutively prescribed. Note here that the reaction-diffusion equation (4.2.5) encapsulates both transport of ionic species across the solid host via the  $\text{Div} \mathbf{j}_R$  term and its subsequent consumption leading to formation of the newly electrodeposited metallic compound via the  $\dot{\xi}$  term.

#### 4.2.2 Charge Balance

The net charge per unit reference volume of the solid conducting host,  $q_R$  is given by (c.f. Narayan and Anand [177] and Li and Monroe. [185])

$$q_R = F(c - c_0), \quad (4.2.6)$$

where  $c_0$  represents the initial (i.e. bulk) concentration per unit reference volume of the mobile ionic species transporting across the solid host, and  $F$  is the Faraday constant. Note here that in writing Eqn. (4.2.6), we restrict our attention to monovalent cationic species and additionally assume negatively charged species in the solid host to be immobile. This restricts the mass flux across the solid host to be carried only by the mobile cations. As a result, any local excess charge density across the solid host can be induced only by a change in concentration of the mobile cationic species from the equilibrium bulk concentration as they transport across the solid conductor.

Defining a referential current density,

$$\mathbf{i}_R \stackrel{\text{def}}{=} F \mathbf{j}_R \quad (4.2.7)$$

taking the time derivative of (4.2.6), and making use of mass balance (4.2.5), one may write for later use

$$\dot{q}_R = -\text{Div} \mathbf{i}_R - F \dot{\xi}. \quad (4.2.8)$$

### 4.2.3 Electrostatics

Under electrostatic conditions, for a polarizable material we require that the two governing Maxwell equations are satisfied. The first equation, Faraday's law, requires the referential electric field,  $\mathbf{e}_R(\mathbf{X}, t)$  to obey the following relationship

$$\text{curl } \mathbf{e}_R = 0. \quad (4.2.9)$$

One can automatically satisfy Eqn. (4.2.9) by representing the electric field,  $\mathbf{e}_R(\mathbf{X}, t)$  as the gradient of an electrostatic potential,  $\phi(\mathbf{X}, t)$  such that

$$\mathbf{e}_R(\mathbf{X}, t) = -\nabla \phi(\mathbf{X}, t). \quad (4.2.10)$$

The second equation of electrostatics is given by Gauss's law, and relates the electric displacement,  $\mathbf{d}_R(\mathbf{X}, t)$  to the net charge per unit reference volume,  $q_R$  as follows

$$\text{Div } \mathbf{d}_R = q_R. \quad (4.2.11)$$

In conjunction, eqs. (4.2.9) and (4.2.11) constitute the governing equations for electrostatics in the solid host.

## 4.3 Kinematics

We introduce here the kinematic formulation for description of a deformation resulting from coupled species transport, distortion due to electrodeposition of a new material inside the solid host, and mechanics. Consider a macroscopically homogeneous body  $\mathcal{B}$  with the region of space it occupies in a fixed reference configuration and let  $\mathbf{X}$  denote an arbitrary material point of  $\mathcal{B}$ . The motion of  $\mathcal{B}$  is then a smooth one-to-one mapping  $\mathbf{x} = \chi(\mathbf{X}, t)$

with deformation gradient, velocity, and velocity gradient given by\*.

$$\mathbf{F} = \nabla \chi, \quad \mathbf{v} = \dot{\chi}, \quad \mathbf{L} = \text{grad } \mathbf{v} = \dot{\mathbf{F}}\mathbf{F}^{-1}. \quad (4.3.1)$$

The theory builds on a multiplicative decomposition of the deformation gradient,

$$\mathbf{F} = \mathbf{F}^{\text{mechanical}} \mathbf{F}^{\text{chemical}} = \mathbf{F}^{\text{m}} \mathbf{F}^{\text{c}}. \quad (4.3.2)$$

Here

- (i)  $\mathbf{F}^{\text{c}}(\mathbf{X})$  represents the concurrent local distortion of the material neighborhood of  $\mathbf{X}$  due to chemical phenomena including: i) species transport across the solid host electrolyte, and ii) distortion due to electrodeposition of a new material inside the solid host at the reaction sites.
- (ii)  $\mathbf{F}^{\text{m}}$  represents the distortion due to macroscopic stresses and may include local irreversible plastic deformation caused by inelastic mechanisms such as dislocation motion, and the subsequent elastic stretching and rotation of the inelastically deformed material neighborhood.

**Remark 1:** In modeling local distortions due to electrodeposition through the tensor  $\mathbf{F}^{\text{c}}$ , the chemical deformation tensor acts as a surrogate for modeling the continuous creation of new material and ensuing distortions, without explicitly accounting for the temporal evolution of the domain. Similar continuum treatments with a focus on growth of electrochemical interphases and growing matter in living systems can be found in the works of Narayan and Anand [84], Tantratian et al. [174] and Kuhl [187].  $\square$

---

\*Notation: We use standard notation of modern continuum mechanics (c.f. Gurtin et al. [186]). Particularly:  $\nabla$  and  $\text{Div}$  denote the gradient and divergence operators with respect to the material point  $\mathbf{X}$  in the reference configuration; while  $\text{grad}$  and  $\text{div}$  operate on the point  $\mathbf{x} = \chi(\mathbf{X}, t)$  in the deformed body; a superposed dot denotes the material time-derivative. Throughout, we write  $\mathbf{F}^{e-1} = (\mathbf{F}^e)^{-1}$ ,  $\mathbf{F}^{e-\top} = (\mathbf{F}^e)^{-\top}$ , etc. We also write  $\text{tr } \mathbf{A}$ ,  $\text{sym } \mathbf{A}$ ,  $\text{skw } \mathbf{A}$ ,  $\mathbf{A}_0$ , and  $\text{sym}_0 \mathbf{A}$  respectively, for the trace, symmetric, skew, deviatoric, and symmetric-deviatoric parts of a tensor  $\mathbf{A}$ . Finally, the inner product of tensors  $\mathbf{A}$  and  $\mathbf{B}$  is denoted by  $\mathbf{A} : \mathbf{B}$ , and the magnitude of  $\mathbf{A}$  by  $|\mathbf{A}| = \sqrt{\mathbf{A} : \mathbf{A}}$ .

We refer to  $\mathbf{F}^m$  and  $\mathbf{F}^c$  as the mechanical and chemical distortions respectively. The volume ratio is given by

$$J \stackrel{\text{def}}{=} \det \mathbf{F} > 0, \quad (4.3.3)$$

and using (4.3.2),

$$J = J^m J^c, \quad \text{with} \quad J^m \stackrel{\text{def}}{=} \det \mathbf{F}^m > 0, \quad \text{and} \quad J^c \stackrel{\text{def}}{=} \det \mathbf{F}^c > 0, \quad (4.3.4)$$

such that  $\mathbf{F}^m$  and  $\mathbf{F}^c$  are invertible. The right and left polar decomposition of  $\mathbf{F}^m$  is given by

$$\mathbf{F}^m = \mathbf{R}^m \mathbf{U}^m = \mathbf{V}^m \mathbf{R}^m, \quad (4.3.5)$$

where  $\mathbf{R}^m$  is a rotation, while  $\mathbf{U}^m$  and  $\mathbf{V}^m$  are symmetric, positive-definite right and left stretch tensors. Consistent with standard notation, the total and the mechanical right Cauchy-Green deformation tensors are given by

$$\mathbf{C} = \mathbf{F}^\top \mathbf{F} \quad \text{and} \quad \mathbf{C}^m = \mathbf{F}^{m\top} \mathbf{F}^m. \quad (4.3.6)$$

Using (4.3.1) and (4.3.2), the velocity gradient may be written as

$$\mathbf{L} = \mathbf{L}^m + \mathbf{F}^m \mathbf{L}^c \mathbf{F}^{m-1} \quad (4.3.7)$$

with

$$\mathbf{L}^m = \dot{\mathbf{F}}^m \mathbf{F}^{m-1}, \quad \mathbf{L}^c = \dot{\mathbf{F}}^c \mathbf{F}^{c-1}. \quad (4.3.8)$$

We define the mechanical and chemical stretching and spin tensors through

$$\left. \begin{aligned} \mathbf{D}^m &= \text{sym} \mathbf{L}^m, & \mathbf{W}^m &= \text{skw} \mathbf{L}^m, \\ \mathbf{D}^c &= \text{sym} \mathbf{L}^c, & \mathbf{W}^c &= \text{skw} \mathbf{L}^c, \end{aligned} \right\} \quad (4.3.9)$$

such that  $\mathbf{L}^m = \mathbf{D}^m + \mathbf{W}^m$  and  $\mathbf{L}^c = \mathbf{D}^c + \mathbf{W}^c$ .

Following Afshar and Di Leo [15], we employ a weighted decomposition of the chemical velocity gradient of the form

$$\mathbf{L}^c = (1 - h(\bar{\xi}))\mathbf{L}^d + h(\bar{\xi})\mathbf{L}^r \quad (4.3.10)$$

with  $h(\bar{\xi})$ , an interpolation function of the reaction coordinate  $\bar{\xi}$ , which satisfies  $h(0) = 0$  and  $h(1) = 1$ . This function is specified in Sect. 4.7 and consistently used for all quantities interpolated by the phase-field parameter  $\bar{\xi}$ .

The weighted decomposition (4.3.10), captures the combined deformation due to species transport across the solid host and distortion due to electrodeposition of a new material at the reaction sites. Here:

- i)  $\mathbf{L}^d$  captures the deformation of a material point due to transport of ionic species across the solid host;
- ii)  $\mathbf{L}^r$  captures the deformation due to electrodeposition of a new material inside the solid host.

Scaling by the interpolation function  $h(\bar{\xi})$  ensures that chemical distortions at material points in the bulk of the solid host, away from the reaction sites (i.e. where  $\bar{\xi} = 0$ ) are only due to transport of ionic species, while in the fully-reacted state (i.e. where  $\bar{\xi} = 1$ ) due to electrodeposition of a new compound.

While the discussion on kinematics is so far presented in its most general form, we specialize our work specifically to modeling *single-ion conductors*. This class of conductors is restricted to a single mobile cationic species transporting across the solid host, while anions remain immobilized in the backbone of the solid conductor. In such a material, both *temporal and spatial concentration gradients are negligible within the bulk of the solid host* (i.e. away from the reaction sites), where deviations from electroneutrality (i.e. equilibrium bulk concentration) are insignificant [188, 189, 190]. Additionally, as detailed in [79, 164,

191, 192], molar volume of Li-ions within the solid host electrolyte vanishes based on the notion that Li-ions lie within a rigid ceramic skeleton of the electrolyte that does not deform upon removal/addition of a Li atom. Henceforth, no deformations are associated with transport of ionic species across this class of solid ionic conductors, and hence  $\mathbf{L}^d = \mathbf{0}$ .

**Remark 2:** The choice to present the kinematic formulation in its most generic form is intended to showcase the versatility of the framework through the kinematic decomposition (4.3.10) to model the phenomena of metal filament growth for the more general class of binary solid-ionic conductors (i.e. polymer solid electrolytes). For this class of solid conductors, chemical deformations may arise due to both a combination of species diffusion across the host and distortion due to electrodeposition of a new material at the reaction sites (c.f. Ganser et al. [193]).  $\square$

Focusing now on single-ion conductors, deformations associated with transport of ionic species across the solid conductor can be neglected, and (4.3.10) simplifies to

$$\mathbf{L}^c = h(\bar{\xi})\mathbf{L}^r. \quad (4.3.11)$$

Further, we make the pragmatic assumption that chemical deformation is irrotational (i.e.  $\mathbf{W}^c = \mathbf{0}$ ) so that

$$\mathbf{D}^c = h(\bar{\xi})\mathbf{D}^r, \quad (4.3.12)$$

with  $\mathbf{D}^r$ , the electrodeposition-induced stretching assumed to depend on the reaction rate,  $\dot{\xi}$  through

$$\mathbf{D}^r = \dot{\xi}\mathbf{N}^r \quad (4.3.13)$$

where  $\mathbf{N}^r$  denotes the direction of electrodeposition-induced deformations.

Finally, the formulation presented so far makes no assumption regarding the nature of  $\mathbf{F}^m$ , which may be further decomposed to model, for example, the elastic-plastic behavior of the underlying solid conductor host and/or of the newly electrodeposited metal. We now

restrict our formulation such that all mechanical deformations are purely elastic in nature and further specialize  $\mathbf{F}^m = \mathbf{F}^e$ , with  $\mathbf{F}^e$  the elastic mechanical distortion. That is, both the solid conductor host and the newly electrodeposited metal will behave elastically.

Finally, using (4.3.1), (4.3.2), (4.3.11) and (4.3.13) we may then rewrite (4.3.7) for future use as

$$(\nabla \dot{\chi})\mathbf{F}^{-1} = \dot{\mathbf{F}}^e \mathbf{F}^{e-1} + h(\bar{\xi})\mathbf{F}^e(\dot{\xi}\mathbf{N}^r)\mathbf{F}^{e-1}. \quad (4.3.14)$$

**Remark 3:** With regards to the solid ionic conductor, the assumption of purely elastic deformations is consistent with their stiff brittle nature. On the other hand, continuous deposition of metallic material (e.g. Li-metal) inside defects induces large compressive stresses, which can cause the metal to flow plastically. As the metal flows plastically, it may extrude from the crack to the electrode, limiting the pressure that can build up inside the crack and in turn the filament growth behavior.

As discussed by Klinsmann et al. [164] and Bucci and Christensen [165], the possibility for the metal to plastically flow out of the crack mouth is impractical for realistic battery designs, suggesting that metal remains confined within the crack. In such a case, pressure will build up in the metal-filled defect until further damage occurs or the reaction is suppressed by mechanical stresses, causing the metal deposition to cease. The nature and relevant importance of Li-metal plastic flow on filament growth through solid-state electrolytes remains a topic of active research. In this thesis, we restrict our theoretical formulation to modeling Li-metal deformations as purely elastic. Owing to the already complex phenomena being modeled in this work, we purposely leave the addition of modeling an elastic-plastic metal phase to a future publication.  $\square$

#### 4.4 Governing Balance Laws

In this section, we develop the governing equations for our theoretical framework, including macroscopic and microscopic force balances and thermodynamic laws. For concise-



ness, we relegate portions of the detailed development to Appendix B, and present here the critical aspects of developing the governing balance laws.

#### 4.4.1 Principle of virtual power. Balance of forces

To develop the remaining balance laws in our theoretical framework, we invoke the virtual-power approach (cf. Gurtin et al. [186]). This results in a macroforce balance and microforce balances for the rate-like kinematical descriptors in our theory. In exploiting the principle of virtual power, we consider a list of generalized virtual velocity fields to be given by

$$\mathcal{V} = (\delta\boldsymbol{\chi}, \delta\mathbf{F}^e, \delta\xi, \nabla\delta\xi, \delta\mathbf{d}, \nabla\delta\mathbf{d}). \quad (4.4.1)$$

In light of (4.3.14), the virtual velocities are not independent and must obey the following kinematic constraint

$$(\nabla\delta\boldsymbol{\chi})\mathbf{F}^{-1} = \delta\mathbf{F}^e\mathbf{F}^{e-1} + h(\bar{\xi})\mathbf{F}^e(\delta\xi\mathbf{N}^T)\mathbf{F}^{e-1} \quad (4.4.2)$$

For any part  $\mathcal{P}$  of the reference body  $\mathcal{B}$ , the internal and external power are formulated in a consistent fashion with the manner in which forces expand power on  $\mathcal{P}$ ,

$$\begin{aligned} \delta W_{\text{ext}}(P, \mathcal{V}) &= \int_{\partial\mathcal{P}} \mathbf{t}_r(\mathbf{n}_r) \cdot \delta\boldsymbol{\chi} \, da_r + \int_{\mathcal{P}} \mathbf{b}_r \cdot \delta\boldsymbol{\chi} \, dv_r + \int_{\partial\mathcal{P}} \eta\delta\xi \, da_r + \int_{\partial\mathcal{P}} \gamma\delta\mathbf{d} \, da_r \\ \delta W_{\text{int}}(P, \mathcal{V}) &= \int_{\mathcal{P}} (\mathbf{S}^e : \delta\mathbf{F}^e + E\delta\xi + \mathbf{G} \cdot \nabla\delta\xi + \varpi\delta\mathbf{d} + \boldsymbol{\zeta} \cdot \nabla\delta\mathbf{d}) \, dv_r \end{aligned} \quad (4.4.3)$$

where we have defined the following macroscopic and microscopic force systems conjugate to the kinematical variables,

- a) A stress  $\mathbf{S}^e$  that expends power over the elastic distortion rate  $\dot{\mathbf{F}}^e$ ;
- b) A traction  $\mathbf{t}_r(\mathbf{n}_r)$  (for each unit vector  $\mathbf{n}_r$ ) that expends power over the velocity  $\dot{\boldsymbol{\chi}}$ ;
- c) A scalar microscopic stress  $E$  that expends power over the rate  $\dot{\xi}$ ;

- d) A vector microscopic stress  $\mathbf{G}$  that expands power over the gradient  $\nabla \dot{\xi}$
- e) A scalar microscopic traction  $\eta(\mathbf{n}_R)$  that expands power over  $\dot{\xi}$  on the boundary of the part;
- f) A scalar microscopic stress  $\varpi$  that expands power over the rate  $\dot{\mathbf{d}}$ ;
- g) A vector microscopic stress  $\boldsymbol{\zeta}$  that expands power over the gradient  $\nabla \dot{\mathbf{d}}$ ; and
- h) A scalar microscopic traction  $\gamma(\mathbf{n}_R)$  that expands power over  $\dot{\mathbf{d}}$  on the boundary of the part.

Note that consistent with the discussion in Sect. 4.3, no deformations are associated with the transport of ionic species in single-ion conductors. As a result, no mechanical power is associated with the concentration variable  $c$ .

The principle of virtual power consists of two basic requirements:

- i) Power balance, which requires that  $\delta W_{\text{ext}}(P, \mathcal{V}) = \delta W_{\text{int}}(P, \mathcal{V})$  for all generalized virtual velocities  $\mathcal{V}$
- ii) Frame-indifference, which requires that  $\delta W_{\text{int}}(P, \mathcal{V})$  is invariant under all changes in frame.

We relegate a detailed development of the derivation of macroforce and microforce balances for the rate-like kinematic descriptors in our theory to Appendix B. Here, we succinctly summarize the macroforce balance for the Piola stress,  $\mathbf{T}_R$  as well as the two corresponding microforce balances for the stresses  $\{E, \mathbf{G}, \boldsymbol{\zeta}, \varpi\}$ . These are given by

$$\left. \begin{aligned} \text{Div } \mathbf{T}_R + \mathbf{b}_R &= 0, \quad \text{with boundary condition} \quad \mathbf{t}_R(\mathbf{n}_R) = \mathbf{T}_R \mathbf{n}_R, \\ E - J^c h(\bar{\xi}) \mathbf{M}^e : \mathbf{N}^r - \text{Div } \mathbf{G} &= 0, \quad \text{with boundary condition} \quad \eta(\mathbf{n}_R) = \mathbf{G} \cdot \mathbf{n}_R, \\ \text{Div } \boldsymbol{\zeta} - \varpi &= 0, \quad \text{with boundary condition} \quad \gamma(\mathbf{n}_R) = \boldsymbol{\zeta} \cdot \mathbf{n}_R. \end{aligned} \right\} \quad (4.4.4)$$

In writing (4.4.4), we have introduced the classical Piola stress  $\mathbf{T}_R = J\mathbf{T}\mathbf{F}^{-\top}$ , with  $\mathbf{T}$  the Cauchy stress. In addition, we define the elastic Mandel stress as

$$\mathbf{M}^e \stackrel{\text{def}}{=} J^e \mathbf{F}^{e\top} \mathbf{T} \mathbf{F}^{e-\top}. \quad (4.4.5)$$

The macro and microforce balances, when supplemented with a set of thermodynamically-consistent constitutive equations, provide the governing mechanical equations for the theory. We note here that a discussion on invariance properties of the fields, consequence of the invariance of internal power under a change in frame, is omitted here for the sake of brevity. We refer the reader to the works of Anand [113] and Afshar and Di Leo [15] for detailed derivations in the context of similar diffusion-reaction-deformation frameworks.

#### 4.4.2 Balance of energy. Entropy imbalance. Free energy imbalance

Our discussion of thermodynamics involves the following fields

- $\varepsilon_R$  the internal energy density per unit reference volume,
- $\eta_R$  the entropy density per unit reference volume,
- $\mathbf{q}_R$  the heat flux per unit reference area,
- $q_R$  the external heat supply per unit reference volume,
- $\vartheta$  the absolute temperature ( $\vartheta > 0$ ),
- $\mu$  the chemical potential,
- $\phi$  the electric potential,

and follows the discussion of Gurtin et al. [186]. Consider a material region  $\mathcal{P}$  and assume inertial effects (i.e. kinetic energy) to be negligible. Under *isothermal conditions*, the two laws of thermodynamics reduce to a single statement requiring that the rate of increase in free energy of any part  $\mathcal{P}$  is less than or equal to the power expended on  $\mathcal{P}$ . Letting  $\psi_R$  denote the free energy per unit reference volume, this requirement takes the form of a

free-energy imbalance,

$$\overline{\int_{\mathcal{P}} \dot{\psi}_{\mathbf{R}} dv_{\mathbf{R}}} \leq \mathcal{W}_{\text{ext}}(\mathbf{P}) - \int_{\partial\mathcal{P}} \mu \mathbf{j}_{\mathbf{R}} \cdot \mathbf{n}_{\mathbf{R}} da_{\mathbf{R}} - \int_{\partial\mathcal{P}} F \phi \mathbf{j}_{\mathbf{R}} \cdot \mathbf{n}_{\mathbf{R}} da_{\mathbf{R}} - \int_{\partial\mathcal{P}} \phi \dot{\mathbf{d}}_{\mathbf{R}} \cdot \mathbf{n}_{\mathbf{R}} da_{\mathbf{R}} \quad (4.4.6)$$

Here, the second term on the right hand side of (4.4.6) represents the flux of energy carried into  $\mathcal{P}$  by the flux,  $\mathbf{j}_{\mathbf{R}}$  of the ionic species transporting across the solid host. Additionally, following Kovetz [194], the power expended on  $\mathcal{P}$  by external charges is represented by an electromagnetic energy flux, which in the electrostatic limit, is given by the last two boundary integral terms on the right hand side of (4.4.6).

Consistent with electrochemical notation, we define

$$\mu^e \stackrel{\text{def}}{=} \mu + F\phi \quad (4.4.7)$$

to denote the electrochemical potential of the mobile ionic species transporting across the solid host, with  $F$  the Faraday constant. Making use of (4.4.7), one can alternatively write the energy imbalance (4.4.6) as

$$\overline{\int_{\mathcal{P}} \dot{\psi}_{\mathbf{R}} dv_{\mathbf{R}}} \leq \mathcal{W}_{\text{ext}}(\mathbf{P}) - \int_{\partial\mathcal{P}} \mu^e \mathbf{j}_{\mathbf{R}} \cdot \mathbf{n}_{\mathbf{R}} da_{\mathbf{R}} - \int_{\partial\mathcal{P}} \phi \dot{\mathbf{d}}_{\mathbf{R}} \cdot \mathbf{n}_{\mathbf{R}} da_{\mathbf{R}}. \quad (4.4.8)$$

Defining the elastic second Piola stress as,

$$\mathbf{T}^e \stackrel{\text{def}}{=} J^e \mathbf{F}^{e-1} \mathbf{T} \mathbf{F}^{e-\top} = \mathbf{C}^{e-1} \mathbf{M}^e \quad (4.4.9)$$

with  $\mathbf{C}^e = \mathbf{F}^{e\top} \mathbf{F}^e$  the elastic right Cauchy-Green tensor, the stress power  $\mathbf{S}^e : \dot{\mathbf{F}}^e$  in (4.4.3) may be written as  $\mathbf{S}^e : \dot{\mathbf{F}}^e = (1/2) J^c \mathbf{T}^e : \dot{\mathbf{C}}^e$ . Equating the external power with the internal power (4.4.3), and applying the divergence theorem to the boundary integral terms, the

energy imbalance (4.4.8) may be written as

$$\int_{\mathcal{P}} \left( \dot{\psi}_{\mathbf{R}} - \frac{1}{2} J^c \mathbf{T}^e : \dot{\mathbf{C}}^e - E \dot{\xi} - \mathbf{G} \cdot \nabla \dot{\xi} - \varpi \dot{\mathbf{d}} - \boldsymbol{\zeta} \cdot \nabla \dot{\mathbf{d}} + \mu^e \text{Div} \mathbf{j}_{\mathbf{R}} + \phi \text{Div} \dot{\mathbf{d}}_{\mathbf{R}} + \nabla \phi \cdot \dot{\mathbf{d}}_{\mathbf{R}} + \mathbf{j}_{\mathbf{R}} \cdot \nabla \mu^e \right) dv_{\mathbf{R}} \leq 0 \quad (4.4.10)$$

Making use of mass balance (4.2.5), charge balance (4.2.6), Gauss's law (4.2.11), along with the definition of electric field (4.2.10) and electrochemical potential (4.4.7), and using the fact that this inequality must hold for all parts  $\mathcal{P}$ , we obtain the local form of the free energy imbalance as

$$\dot{\psi}_{\mathbf{R}} - \frac{1}{2} J^c \mathbf{T}^e : \dot{\mathbf{C}}^e - E \dot{\xi} - \mathbf{G} \cdot \nabla \dot{\xi} - \varpi \dot{\mathbf{d}} - \boldsymbol{\zeta} \cdot \nabla \dot{\mathbf{d}} - \mu \dot{c} - \mu^e \dot{\xi} - \mathbf{e}_{\mathbf{R}} \cdot \dot{\mathbf{d}}_{\mathbf{R}} + \mathbf{j}_{\mathbf{R}} \cdot \nabla \mu^e \leq 0. \quad (4.4.11)$$

For later use, we define the dissipation  $\mathcal{D} \geq 0$  per unit volume per unit time as

$$\mathcal{D} = \frac{1}{2} J^c \mathbf{T}^e : \dot{\mathbf{C}}^e + E \dot{\xi} + \mathbf{G} \cdot \nabla \dot{\xi} + \varpi \dot{\mathbf{d}} + \boldsymbol{\zeta} \cdot \nabla \dot{\mathbf{d}} + \mu \dot{c} + \mu^e \dot{\xi} + \mathbf{e}_{\mathbf{R}} \cdot \dot{\mathbf{d}}_{\mathbf{R}} - \mathbf{j}_{\mathbf{R}} \cdot \nabla \mu^e - \dot{\psi}_{\mathbf{R}} \geq 0. \quad (4.4.12)$$

Finally, we note here that all quantities in the free energy imbalance (4.4.11) and dissipation inequality (4.4.12) are invariant under a change in frame (c.f. Anand [113] and Afshar and Di Leo [15]).

## 4.5 Constitutive Theory

We divide this section into energetic and dissipative constitutive equations.

### 4.5.1 Energetic Constitutive Equations

Guided by the free-energy imbalance (4.4.11), we consider a set of constitutive equations for the free energy  $\psi_{\mathbf{R}}$ , the stress  $\mathbf{T}^e$ , the chemical potential  $\mu$ , the vector microforce  $\boldsymbol{\zeta}$  and

the electric field  $\mathbf{e}_R$  of the form

$$\psi_R = \hat{\psi}_R(\Lambda), \quad \mathbf{T}^e = \hat{\mathbf{T}}^e(\Lambda), \quad \mu = \hat{\mu}(\Lambda), \quad \zeta = \hat{\zeta}(\Lambda), \quad \text{and} \quad \mathbf{e}_R = \hat{\mathbf{e}}_R(\Lambda), \quad (4.5.1)$$

where  $\Lambda$  denotes the list

$$\Lambda = (\mathbf{C}^e, c, \xi, \nabla \xi, \mathbf{d}_R, \mathbf{d}, \nabla \mathbf{d}). \quad (4.5.2)$$

Substituting the constitutive equations (4.5.1) in the free-energy imbalance (4.4.11) yields

$$\begin{aligned} & \left( \frac{\partial \hat{\psi}_R}{\partial \mathbf{C}^e} - \frac{1}{2} J^e \mathbf{T}^e \right) : \dot{\mathbf{C}}^e + \left( \frac{\partial \hat{\psi}_R}{\partial c} - \mu \right) \dot{c} + \left( \frac{\partial \hat{\psi}_R}{\partial \xi} - E - \mu^e \right) \dot{\xi} + \left( \frac{\partial \hat{\psi}_R}{\partial \nabla \xi} - \mathbf{G} \right) \cdot \nabla \dot{\xi} \\ & + \left( \frac{\partial \hat{\psi}_R}{\partial \mathbf{d}} - \varpi_{\text{en}} \right) \dot{\mathbf{d}} + \left( \frac{\partial \hat{\psi}_R}{\partial \nabla \mathbf{d}} - \zeta \right) \cdot \nabla \dot{\mathbf{d}} + \left( \frac{\partial \hat{\psi}_R}{\partial \mathbf{d}_R} - \mathbf{e}_R \right) \cdot \dot{\mathbf{d}}_R - \varpi_{\text{dis}} \dot{\mathbf{d}} + \mathbf{j}_R \cdot \nabla \mu^e \leq 0, \end{aligned} \quad (4.5.3)$$

where we have introduced a decomposition for the scalar damage microstress of the form

$$\varpi = \varpi_{\text{dis}} + \varpi_{\text{en}}. \quad (4.5.4)$$

Motivated by Anand et al. [48], the decomposition (4.5.4) allows for both energetic and dissipative effects associated with temporal changes in  $\mathbf{d}$ , while effects due to the gradient,  $\nabla \mathbf{d}$ , a measure of the inhomogeneity of damage at the microscale, are taken to be entirely energetic.

From an electrochemical standpoint, in (4.5.3), we make the distinction that processes associated with diffusion (governed by  $\dot{c}$ ) and migration (governed by  $\dot{\mathbf{d}}_R$ ) are energetic, while the ones associated with electrodeposition (governed by  $\dot{\xi}$ ) are dissipative. An exception to such choice is the power conjugate to  $\nabla \dot{\xi}$ , which is taken to be entirely energetic (i.e all reaction dissipative processes are already accounted for in the term  $\dot{\xi}$ ).

As the inequality in (4.5.3) is to hold for all values of  $\{\dot{\mathbf{C}}^e, \dot{c}, \nabla \dot{\xi}, \dot{\mathbf{d}}, \nabla \dot{\mathbf{d}}, \dot{\mathbf{d}}_R\}$ , their “coefficients” must vanish, for otherwise they may be chosen to violate (4.5.3). We are

therefore led to the thermodynamic restriction that the free energy determines the stress  $\mathbf{T}^e$ , the chemical potential  $\mu$ , the vector microstress  $\mathbf{G}$ , the scalar microstress  $\varpi_{\text{en}}$ , the vector microstress  $\boldsymbol{\zeta}$  and the electric field  $\mathbf{e}_R$  through the “state relations”

$$\left. \begin{aligned} \mathbf{T}^e &= 2J^{c-1} \frac{\partial \hat{\psi}_R(\Lambda)}{\partial \mathbf{C}^e}, \\ \mu &= \frac{\partial \hat{\psi}_R(\Lambda)}{\partial c}, \\ \mathbf{G} &= \frac{\partial \hat{\psi}_R(\Lambda)}{\partial \nabla \xi}, \\ \varpi_{\text{en}} &= \frac{\partial \hat{\psi}_R(\Lambda)}{\partial \mathbf{d}}, \\ \boldsymbol{\zeta} &= \frac{\partial \hat{\psi}_R(\Lambda)}{\partial \nabla \mathbf{d}}, \\ \mathbf{e}_R &= \frac{\partial \hat{\psi}_R(\Lambda)}{\partial \mathbf{d}_R}. \end{aligned} \right\} \quad (4.5.5)$$

Recalling (4.4.7) and using (4.5.5)<sub>2</sub>, the electrochemical potential of the ionic species transporting across the solid host,  $\mu^e$  is given by

$$\mu^e = \frac{\partial \hat{\psi}_R(\Lambda)}{\partial c} + F\phi. \quad (4.5.6)$$

#### 4.5.2 Dissipative Constitutive Equations

The reduced dissipation inequality is now given by

$$\mathcal{D} = - \left( \frac{\partial \hat{\psi}_R(\Lambda)}{\partial \xi} - E - \mu^e \right) \dot{\xi} + \varpi_{\text{dis}} \dot{\mathbf{d}} - \mathbf{j}_R \cdot \nabla \mu^e \geq 0. \quad (4.5.7)$$

We define the electrochemical potential of the electrodeposited species as

$$\mu^\xi \stackrel{\text{def}}{=} \frac{\partial \hat{\psi}_R(\Lambda)}{\partial \xi} - E. \quad (4.5.8)$$

Then, consistent with the notion of electrochemical reactions, we define the thermodynamic driving force for electrodeposition as a difference in electrochemical potential of the species

participating in the reaction through

$$\mathcal{F} \stackrel{\text{def}}{=} \mu^\xi - \mu^e. \quad (4.5.9)$$

Using (4.5.9) in (4.5.7), the dissipation inequality may be rewritten as,

$$\mathcal{D} = -\mathcal{F}\dot{\xi} + \varpi_{\text{dis}}\dot{\mathbf{d}} + \nabla\mu^e \cdot \mathbf{M}_{\text{mob}}\nabla\mu^e \geq 0, \quad (4.5.10)$$

where guided by the dissipation inequality, we introduce a Fick-type relation for the flux,  $\mathbf{j}_R$  of ionic species across the solid host of the form

$$\mathbf{j}_R = -\mathbf{M}_{\text{mob}}\nabla\mu^e \quad (4.5.11)$$

where as is standard, the flux,  $\mathbf{j}_R$  is linearly proportional to  $\nabla\mu^e$  through the mobility tensor  $\mathbf{M}_{\text{mob}}$ .

Finally, we assume all terms in (4.5.10) to individually satisfy,

$$\begin{aligned} -\mathcal{F}\dot{\xi} &\geq 0, \\ \varpi_{\text{dis}}\dot{\mathbf{d}} &\geq 0, \\ \nabla\mu^e \cdot \mathbf{M}_{\text{mob}}\nabla\mu^e &\geq 0. \end{aligned} \quad (4.5.12)$$

With respect to dissipation due to electrodeposition (4.5.12)<sub>1</sub>, we assume, consistent with electro-kinetics theory, that  $\dot{\xi} > 0$  if and only if  $\mathcal{F} < 0$ , and vice versa  $\dot{\xi} < 0$  if and only if  $\mathcal{F} > 0$  (c.f. Bazant [126], Fuller et al. [189]). Given the constraint (4.2.3) for damage irreversibility such that  $\dot{\mathbf{d}} \geq 0$ , we satisfy (4.5.12)<sub>2</sub> by requiring  $\varpi_{\text{dis}} \geq 0$ . Finally, (4.5.12)<sub>3</sub> leads to the restriction that the mobility tensor  $\mathbf{M}_{\text{mob}}$  is positive semi-definite. Altogether, these restrictions ensure that the dissipation inequality (4.5.10) is not violated.



## 4.6 Summary of the general constitutive theory

In this section, we summarize our general phase-field diffusion-reaction-damage theory.

The theory relates the following fields:

$\mathbf{x} = \chi(\mathbf{X}, t),$	motion;
$\mathbf{F} = \nabla \chi, \quad J = \det \mathbf{F} > 0,$	deformation gradient;
$\mathbf{F} = \mathbf{F}^e \mathbf{F}^c,$	multiplicative decomposition of $\mathbf{F}$ ;
$\mathbf{F}^e, \quad J^e = \det \mathbf{F}^e > 0,$	elastic distortion;
$\mathbf{F}^c, \quad J^c = \det \mathbf{F}^c > 0,$	chemical distortion;
$\mathbf{L} = \dot{\mathbf{F}} \mathbf{F}^{-1} = \mathbf{L}^e + \mathbf{F}^e \mathbf{L}^c \mathbf{F}^{e-1}$	velocity gradient;
$\mathbf{L}^c = \dot{\mathbf{F}}^c \mathbf{F}^{c-1} = \mathbf{D}^c + \mathbf{W}^c \quad \text{with} \quad \mathbf{W}^c = 0$	chemical velocity gradient;
$\mathbf{D}^c = h(\bar{\xi}) \mathbf{D}^r$	chemical stretching;
$\mathbf{D}^r = \dot{\xi} \mathbf{N}^r,$	electrodeposition induced stretching;
$\mathbf{F}^e = \mathbf{R}^e \mathbf{U}^e = \mathbf{V}^e \mathbf{R}^e,$	polar decompositions of $\mathbf{F}^e$ ;
$\mathbf{C}^e = (\mathbf{F}^e)^\top \mathbf{F}^e = (\mathbf{U}^e)^2,$	right Cauchy-Green tensor;
$\mathbf{T} = \mathbf{T}^\top,$	Cauchy stress;
$\mathbf{M}^e = J^e \mathbf{F}^{e\top} \mathbf{T} \mathbf{F}^{e-\top},$	elastic Mandel stress;
$\mathbf{T}_R = J \mathbf{T} \mathbf{F}^{-\top},$	Piola stress;
$\mathbf{T}^e = J^e \mathbf{F}^{e-1} \mathbf{T} \mathbf{F}^{e-\top},$	elastic second Piola stress;
$\psi_R,$	free energy density/unit reference volume;
$c,$	moles of diffusing species/unit reference volume;
$\xi,$	moles of deposited species/unit reference volume;
$\bar{\xi} = \xi / \xi^{\max} \in [0, 1],$	extent of the reaction;
$\nabla \xi,$	gradient of the reacted species concentration;
$\mu^e,$	electrochemical potential of diffusing species;

$\mathbf{j}_R,$	referential species flux vector;
$\mathbf{e}_R,$	referential electric field;
$\phi,$	electric potential;
$\mathbf{d}_R$	referential electric displacement;
$d$	phase-field damage variable;
$\nabla d$	gradient of the damage variable.

#### 4.6.1 Kinematics and Free Energy

The deformation gradient is decomposed as

$$\mathbf{F} = \mathbf{F}^e \mathbf{F}^c, \quad (4.6.1)$$

with  $\mathbf{F}^e$  the elastic distortion, and  $\mathbf{F}^c$  the chemical distortion. Further, the chemical velocity gradient is given by  $\mathbf{L}^c = \dot{\mathbf{F}}^c \mathbf{F}^{c-1} = \mathbf{D}^c$ , with the chemical stretching  $\mathbf{D}^c$  specialized as

$$\mathbf{D}^c = h(\bar{\xi}) \mathbf{D}^r \quad \text{and} \quad \mathbf{D}^r = \dot{\xi} \mathbf{N}^r. \quad (4.6.2)$$

Here,  $\mathbf{D}^r$  is the electrodeposition induced stretching, with  $\dot{\xi}$  the reaction rate,  $\mathbf{N}^r$  the direction of electrodeposition induced deformations, and  $h(\bar{\xi})$ , an interpolation function, which satisfies  $h(0) = 0$  and  $h(1) = 1$ . The free energy is given by

$$\psi = \hat{\psi}(\Lambda) \quad \text{with } \Lambda \text{ the list } \Lambda = (\mathbf{C}^e, c, \xi, \nabla \xi, \mathbf{d}_R, d, \nabla d). \quad (4.6.3)$$

With the direction of electrodeposition induced deformations,  $\mathbf{N}^r$  and the free energy function,  $\hat{\psi}(\Lambda)$  prescribed, the following quantities may be derived.

#### 4.6.2 Stress. Force balance

The second Piola stress is given by (4.5.5)<sub>1</sub>

$$\mathbf{T}^e = 2J^{e-1} \frac{\partial \hat{\psi}_R(\Lambda)}{\partial \mathbf{C}^e} \quad (4.6.4)$$

with the Cauchy stress given by  $\mathbf{T} = J^{e-1} \mathbf{F}^e \mathbf{T}^e \mathbf{F}^{e\top}$ , the elastic Mandel stress by  $\mathbf{M}^e = J^e \mathbf{F}^{e\top} \mathbf{T}^e \mathbf{F}^{e-\top}$ , and the first Piola stress by  $\mathbf{T}_R = J \mathbf{T} \mathbf{F}^{-\top}$ .

The stress is governed by force balance (4.4.4)<sub>1</sub>, viz.

$$\text{Div } \mathbf{T}_R + \mathbf{b}_R = 0, \quad (4.6.5)$$

with Neumann boundary condition (4.4.4)<sub>1</sub>,  $\mathbf{t}_R(\mathbf{n}_R) = \mathbf{T}_R \mathbf{n}_R$ , where  $\mathbf{t}_R$  is a prescribed traction.

#### 4.6.3 Electrochemical potential. Flux. Mass Balance

Using (4.5.5)<sub>2</sub> in (4.4.7) and recalling (4.5.11), the electrochemical potential and referential flux for the mobile ionic species are given by

$$\mu^e = \frac{\partial \hat{\psi}_R(\Lambda)}{\partial c} + F\phi \quad \text{and} \quad \mathbf{j}_R = -\mathbf{M}_{\text{mob}} \nabla \mu^e \quad (4.6.6)$$

with  $\mathbf{M}_{\text{mob}}$ , a positive semi-definite mobility tenor.

The concentration of ionic species transporting across the solid host,  $c$  is governed by mass balance (4.2.5), viz.

$$\dot{c} = -\text{Div } \mathbf{j}_R - \dot{\xi}. \quad (4.6.7)$$

with  $\dot{\xi}$ , the species electrodeposition rate at the reaction site.

#### 4.6.4 Reaction driving force. Electrodeposition Kinetics

Combining (4.5.8), (4.5.9), (4.4.4)<sub>2</sub> and (4.5.5)<sub>3</sub> yields the electrodeposition driving force as

$$\mathcal{F} = \mu^\xi - \mu^e, \quad \text{with} \quad \mu^\xi = \frac{\partial \hat{\psi}(\Lambda)}{\partial \xi} - J^e h(\bar{\xi}) \mathbf{M}^e : \mathbf{N}^r - \text{Div} \left( \frac{\partial \hat{\psi}(\Lambda)}{\partial \nabla \xi} \right). \quad (4.6.8)$$

The reaction kinetics are constrained by the dissipation inequality (4.5.12)<sub>1</sub> to obey  $-\mathcal{F}\dot{\xi} \geq 0$ . Note that due to the phase-field (gradient) nature of the extent of reaction  $\bar{\xi}$ , (4.6.8) constitutes a PDE.

#### 4.6.5 Electrostatics

The electric potential  $\phi$  is governed by Gauss's Law. Combining (4.2.11) with (4.2.6) and (4.5.5)<sub>6</sub> with (4.2.10) yields

$$\text{Div}(\mathbf{d}_r) = F(c - c_0), \quad \text{with} \quad \mathbf{e}_r = \frac{\partial \hat{\psi}(\Lambda)}{\partial \mathbf{d}_r}, \quad \text{and} \quad \mathbf{e}_r = -\nabla \phi(\mathbf{X}, t). \quad (4.6.9)$$

#### 4.6.6 Damage

Combining (4.4.4)<sub>3</sub> with (4.5.5)<sub>4,5</sub> and recalling the decomposition of the microstress  $\varpi = \varpi_{\text{dis}} + \varpi_{\text{en}}$  from (4.5.4) yields the governing equation for the phase-field damage variable as,

$$\text{Div} \left( \frac{\partial \hat{\psi}(\Lambda)}{\partial \nabla \mathbf{d}} \right) - \frac{\partial \hat{\psi}(\Lambda)}{\partial \mathbf{d}} - \varpi_{\text{dis}} = 0, \quad (4.6.10)$$

where the constraint  $\varpi_{\text{dis}} \geq 0$  is required by the dissipation inequality (4.5.12)<sub>2</sub>.

### 4.7 Specialization of the constitutive equations

The theory developed above and summarized in Sect. 4.6 is quite general. We introduce now a set of specialized constitutive equations to elucidate: i) the process of plating and

fracture due to electrodeposition of Li-metal in single-ion conductors, specifically a LLZO inorganic electrolyte, and ii) the inherent coupling of electric, chemical and mechanical effects on electrodeposition kinetics and evolution morphology of Li-metal filaments across the solid-state electrolyte.

The general electrodeposition reaction (4.2.1) is now specialized for Li-metal plating as



#### 4.7.1 Electrodeposition-Induced Deformation

We begin by specifying the manner in which electrodeposition of Li-metal at the reaction sites induces mechanical deformations, specifically the direction tensor  $\mathbf{N}^r$  in (4.3.13). Consistent with Narayan and Anand [84] and Rejovitzky et. al [44], we consider a generic distortion due to electrodeposition such that

$$\dot{\mathbf{F}}^r = \mathbf{D}^r \mathbf{F}^r. \quad (4.7.2)$$

Additionally, we assume the electrodeposition induced stretching tensor  $\mathbf{D}^r$  is anisotropic and specialize it as

$$\mathbf{D}^r = \dot{\epsilon}^r \mathbf{S}^r \quad \text{where} \quad \mathbf{S}^r \stackrel{\text{def}}{=} \mathbf{m}_r \otimes \mathbf{m}_r. \quad (4.7.3)$$

Here, the unit vector,  $\mathbf{m}_r$  represents the direction of electrodeposition induced deformations, while  $\dot{\epsilon}^r = \text{tr}(\mathbf{D}^r)$  denotes the total volumetric strain rate for reaction induced deformations. Consistent with experimental observations [195], we assume deformations due to electrodeposition of Li-metal to occur preferentially in a direction normal to the reaction front (e.g. normal to the conductor/metal interface), and hence specialize  $\mathbf{m}_r$  as

$$\mathbf{m}_r = \nabla \bar{\xi} / |\nabla \bar{\xi}|. \quad (4.7.4)$$

Further, we assume volumetric distortions due to electrodeposition to vary linearly with the extent of reaction (c.f [113, 177]), such that  $J^r = 1 + \Omega\dot{\xi}$ . Then, using the fact that  $\dot{J}^r J^{r-1} = \text{tr}(\mathbf{D}^r)$ , and combining with (4.7.3) yields

$$\mathbf{D}^r = \frac{\Omega\dot{\xi}}{1 + \Omega\dot{\xi}} \mathbf{m}_r \otimes \mathbf{m}_r. \quad (4.7.5)$$

Here,  $\Omega$  denotes the constant partial molar volume associated with formation of Li-metal due to electrodeposition and may be calculated from experiments or ab-initio simulations. Given (4.7.5) and recalling that  $\mathbf{D}^r = \dot{\xi} \mathbf{N}^r$  from (4.3.13), the direction of electrodeposition induced deformations is specialized as

$$\mathbf{N}^r = \frac{\Omega}{1 + \Omega\dot{\xi}} \mathbf{m}_r \otimes \mathbf{m}_r. \quad (4.7.6)$$

#### 4.7.2 Free Energy

Next, we consider a separable free energy per unit volume of the form

$$\begin{aligned} \hat{\psi}_r(\mathbf{C}^e, c, \xi, \nabla\xi, \mathbf{d}_r, \mathbf{d}, \nabla\mathbf{d}) = & \psi_r^m(\mathbf{C}^e, \xi, \mathbf{d}) + \psi_r^c(c) + \psi_r^\xi(\xi) + \psi_r^{\nabla\xi}(|\nabla\xi|) \dots \\ & + \psi_r^e(\mathbf{C}^e, \xi, \mathbf{d}_r) + \psi_r^d(|\nabla\mathbf{d}|) \end{aligned} \quad (4.7.7)$$

All individual functions in (4.7.7) will be specialized as isotropic functions of their arguments. Here:

- (i)  $\psi_r^m(\mathbf{C}^e, \xi, \mathbf{d})$  is the contribution to changes in the free energy density due to elastic deformation of the host material. A consequence of isotropy is that the free energy  $\psi_r^m$  may be expressed as (cf. Anand [113]),

$$\psi_r^m(\mathbf{C}^e, \xi, \mathbf{d}) = \psi_r^m(E_1^e, E_2^e, E_3^e, \xi, \mathbf{d}), \quad (4.7.8)$$

where  $\{E_1^e, E_2^e, E_3^e\}$  denote the principal values of the logarithmic elastic strain de-

defined as

$$\mathbf{E}^e = \ln \mathbf{U}^e = \sum_{i=1}^3 \mathbf{E}_i^e \mathbf{r}_i^e \otimes \mathbf{r}_i^e = \sum_{i=1}^3 \ln \lambda_i^e \mathbf{r}_i^e \otimes \mathbf{r}_i^e. \quad (4.7.9)$$

Further, given (4.7.9) above, straightforward calculations (c.f. Anand and Su [196]) show that the mechanical contribution to Mandel stress<sup>†</sup> is then given by

$$\mathbf{M}^e = J^{e-1} \sum_{i=1}^3 \frac{\partial \psi_{\mathbf{R}}^m(E_1^e, E_2^e, E_3^e, \xi, \mathbf{d})}{\partial \mathbf{E}_i^e} \mathbf{r}_i^e \otimes \mathbf{r}_i^e \quad (4.7.10)$$

We further decompose our free energy formulation due to elastic deformations into a “positive” part,  $\psi_{\mathbf{R}}^{m+}$  due to tension and a “negative” part,  $\psi_{\mathbf{R}}^{m-}$  due to compression (cf. Miehe et al. [197], Klinsmann et al. [51], and Navidtehrani et al. [198]), which yields

$$\psi_{\mathbf{R}}^m(\mathbf{E}^e, \xi, \mathbf{d}) = g(\mathbf{d}) \psi_{\mathbf{R}}^{m+}(\mathbf{E}^e, \xi) + \psi_{\mathbf{R}}^{m-}(\mathbf{E}^e, \xi) \quad (4.7.11)$$

where  $g(\mathbf{d})$  is a degradation function of the damage variable,  $\mathbf{d}$ .

The “positive” and “negative” mechanical parts of the free energy are individually specialized to the classical strain energy function of isotropic linear elasticity to moderately large elastic deformations using the logarithmic strain measure,  $\mathbf{E}^e$  (c.f. Anand [199]). They are given by

$$\left. \begin{aligned} \psi_{\mathbf{R}}^{m+}(\mathbf{E}^e, \xi) &\stackrel{\text{def}}{=} J^e \left[ G(\bar{\xi}) \left( \langle \mathbf{E}_1^e \rangle_+^2 + \langle \mathbf{E}_2^e \rangle_+^2 + \langle \mathbf{E}_3^e \rangle_+^2 \right) + \frac{1}{2} \left( K(\bar{\xi}) - \frac{2}{3} G(\bar{\xi}) \right) \left( \langle \mathbf{E}_1^e + \mathbf{E}_2^e + \mathbf{E}_3^e \rangle_+ \right)^2 \right] \\ \psi_{\mathbf{R}}^{m-}(\mathbf{E}^e, \xi) &\stackrel{\text{def}}{=} J^e \left[ G(\bar{\xi}) \left( \langle \mathbf{E}_1^e \rangle_-^2 + \langle \mathbf{E}_2^e \rangle_-^2 + \langle \mathbf{E}_3^e \rangle_-^2 \right) + \frac{1}{2} \left( K(\bar{\xi}) - \frac{2}{3} G(\bar{\xi}) \right) \left( \langle \mathbf{E}_1^e + \mathbf{E}_2^e + \mathbf{E}_3^e \rangle_- \right)^2 \right] \end{aligned} \right\} \quad (4.7.12)$$

where,  $G(\bar{\xi})$  and  $K(\bar{\xi})$  denote the reaction-dependent shear and bulk moduli respectively. Consistent with (4.7.9),  $\{\mathbf{E}_i^e | i = 1, 2, 3\}$  denote the principal elastic logarithmic

---

<sup>†</sup>We refer to this as the “mechanical” contribution to the Mandel stress as it is based only on the derivative of the mechanical free energy,  $\psi_{\mathbf{R}}^m$ , and not the entire free energy,  $\psi_{\mathbf{R}}$ . As such, it omits certain possible stress contributions, such as the Maxwell stress due to electrostatics. A detailed discussion on the significance of these contributions is presented in Remark 4 below.

mic strains. For notational convenience in (4.7.12), we additionally introduce

$$\langle E_i^e \rangle_+ = \begin{cases} E_i^e & \text{if } E_i^e > 0 \\ 0 & \text{otherwise} \end{cases} \quad \text{and} \quad \langle E_i^e \rangle_- = \begin{cases} E_i^e & \text{if } E_i^e < 0 \\ 0 & \text{otherwise} \end{cases} \quad (4.7.13)$$

We note here that only the “positive” part of the free energy is degraded in (4.7.11), while the “negative” part of the free energy remains undegraded. This in turn prevents damage from occurring under purely compressive stresses. The split in free energy due to elastic deformations is necessary not just to maintain resistance of the material under compression, but to additionally enable damaged regions, which have become electroplated (i.e. regions with  $d = 1$  and  $\bar{\xi} = 1$ ) to develop and sustain compressive stresses.

The degradation function is taken to be a monotonically decreasing function of  $d$ , which concurrently satisfies  $g(0) = 1$  and  $g(1) = 0$ . Consistent with Miehe et al. [197], we adopt

$$g(d) = (1 - d)^2 + \epsilon, \quad (4.7.14)$$

where  $\epsilon \approx 0$  is a small positive-valued constant introduced to prevent ill-conditioning of the model when  $d = 1$ . Finally, the reaction-dependent shear and bulk moduli  $G(\bar{\xi})$  and  $K(\bar{\xi})$  obey

$$\begin{aligned} G(\bar{\xi}) &= (1 - h(\bar{\xi}))G^{\text{SE}} + h(\bar{\xi})G^{\text{M}}, \\ K(\bar{\xi}) &= (1 - h(\bar{\xi}))K^{\text{SE}} + h(\bar{\xi})K^{\text{M}}, \end{aligned} \quad (4.7.15)$$

which, consistent with (4.3.10), are interpolated using the function  $h(\bar{\xi})$ . The specific form of  $h(\bar{\xi})$  is given by

$$h(\bar{\xi}) = \bar{\xi}^3(6\bar{\xi}^2 - 15\bar{\xi} + 10). \quad (4.7.16)$$



This form of the interpolation function (4.7.16) is widely used in the phase-field literature (c.f. Chen et al. [169] and Guyer et al. [200]). Throughout, we invoke the “SE” and “M” superscripts to denote quantities associated with the solid-state electrolyte and the electrodeposited Li-metal respectively.

- (ii)  $\psi_{\text{R}}^c(c)$  is the change in chemical free energy due to mixing of ionic species with the solid host. As a simple continuum approximation to mixing, we take the chemical free energy to be given by a regular solution model (cf. DeHoff [201]) as

$$\psi_{\text{R}}^c(c) = \mu_0 c + R \vartheta c_{\text{max}} \left( \bar{c} \ln \bar{c} + (1 - \bar{c}) \ln(1 - \bar{c}) \right) \quad (4.7.17)$$

Here,  $\bar{c} = c/c_{\text{max}}$  with  $\bar{c} \in [0, 1]$  represents the normalized species concentration in the solid host, while  $c_{\text{max}}$  denotes the maximum species concentration in moles per unit reference volume when all the accommodating sites in the host material are filled. Additionally,  $\mu_0$  denotes the reference chemical potential of the diffusing species,  $R$  the universal gas constant, and  $\vartheta$  the absolute temperature.

- (iii)  $\psi_{\text{R}}^\xi(\xi)$  includes a double-well energy function associated with the energetic barrier across the phases in addition to an electrochemical energetic contribution associated with the standard (reference) chemical state and electrostatic potential of the electrodeposited Li-metal. It is given by

$$\psi_{\text{R}}^\xi(\xi) = \mathcal{W} \bar{\xi}^2 (1 - \bar{\xi})^2 + \xi \mu_0^\xi + \xi F \phi_0. \quad (4.7.18)$$

Consistent with the works of Guyer et al. [200] and Cogswell [202], the first term governed by  $\mathcal{W}$ , sets the height of the energy barrier across the phases in our continuum kinetics formulation. The second term defines the reference chemical potential,  $\mu_0^\xi$  of the electrodeposited species. Finally, the third term represents the energetic contribution associated with the electrostatic potential of the metal,  $\phi_0$  (cf. Chen et

al. [169] and Bucci et al. [203]).

- (iv)  $\psi_{\text{R}}^{\nabla\xi}(|\nabla\xi|)$  is the interfacial free energy, which penalizes sharp interfaces and is simply taken as

$$\psi_{\text{R}}^{\nabla\xi}(|\nabla\xi|) = \frac{1}{2}\lambda_{\xi}|\nabla\xi|^2, \quad (4.7.19)$$

with  $\lambda_{\xi} \geq 0$ , a gradient energy coefficient. This energetic contribution regularizes the problem from a numerical standpoint by defining a finite interface width — controlled by  $\lambda_{\xi}$  — for the phase-field reaction coordinate,  $\bar{\xi}$ .

- (v)  $\psi_{\text{R}}^e(\mathbf{C}^e, \xi, \mathbf{d}_{\text{R}})$  is the electrostatic energy, which is taken as (cf. Narayan et al. [177] and Suo [204])

$$\psi_{\text{R}}^e = J \left( \frac{1}{2\varepsilon} \mathbf{d} \cdot \mathbf{d} \right). \quad (4.7.20)$$

Here,  $\varepsilon(\bar{\xi})$  denotes the reaction-dependent effective electrical permittivity, and  $\mathbf{d}$  is the electric displacement in the current configuration. This function is *isotropic in the deformed body* as it depends only on the magnitude of  $\mathbf{d}$ .

Using  $\mathbf{d} = J^{-1}\mathbf{F}\mathbf{d}_{\text{R}}$ , we may express (4.7.20) in terms of the referential electric displacement as

$$\psi_{\text{R}}^e(\mathbf{C}^e, \mathbf{d}_{\text{R}}, \xi) = J^{-1} \left( \frac{1}{2\varepsilon} \mathbf{d}_{\text{R}} \cdot \mathbf{C}\mathbf{d}_{\text{R}} \right) \quad (4.7.21)$$

The reaction-dependent effective electrical permittivity is expressed as,

$$\varepsilon(\bar{\xi}) = \varepsilon_r(\bar{\xi})\varepsilon_0 \quad (4.7.22)$$

where  $\varepsilon_0 = 8.85 \cdot 10^{-12}$  F/m denotes the electrical permittivity of vacuum and  $\varepsilon_r(\bar{\xi})$  denotes the reaction-dependent relative electrical permittivity of each material phase. Consistent with other interpolations in this theory, we assume

$$\varepsilon_r(\bar{\xi}) = \left(1 - h(\bar{\xi})\right)\varepsilon_r^{\text{SE}} + h(\bar{\xi})\varepsilon_r^{\text{M}}. \quad (4.7.23)$$

(vi)  $\psi_{\text{R}}^{\text{d}}(|\nabla \mathbf{d}|)$  is the free energy contribution associated with gradient effects of damage.

We specialize its form as a quadratic function of the magnitude of the gradients in damage,  $|\nabla \mathbf{d}|$  such that

$$\psi_{\text{R}}^{\text{d}}(|\nabla \mathbf{d}|) = \frac{1}{2} \psi^* \ell^2 |\nabla \mathbf{d}|^2. \quad (4.7.24)$$

Here,  $\psi^* > 0$  is a coefficient with units of energy per cubic volume, while  $\ell > 0$  denotes an internal length scale, which sets the width of the damage zone across which the damage field varies in a diffuse fashion.

Finally, combining (4.7.17) through (4.7.24), the total free energy per unit volume accounting for the combined effects of mixing, reaction, electrostatics, finite elastic deformations and damage is given by

$$\begin{aligned} \psi_{\text{R}}(\mathbf{E}^{\text{e}}, c, \xi, \nabla \xi, \mathbf{d}_{\text{R}}, \mathbf{d}, \nabla \mathbf{d}) &= g(\mathbf{d}) \psi_{\text{R}}^{\text{m}+}(\mathbf{E}^{\text{e}}, \xi) + \psi_{\text{R}}^{\text{m}-}(\mathbf{E}^{\text{e}}, \xi) \\ &+ \mu_0 c + R \vartheta c_{\text{max}} (\bar{c} \ln \bar{c} + (1 - \bar{c}) \ln(1 - \bar{c})) \\ &+ \mathcal{W} \bar{\xi}^2 (1 - \bar{\xi})^2 + \xi \mu_0^{\xi} + \xi F \phi_0 + \frac{1}{2} \lambda_{\xi} |\nabla \xi|^2 \\ &+ J^{-1} \left( \frac{1}{2\varepsilon} \mathbf{d}_{\text{R}} \cdot \mathbf{C} \mathbf{d}_{\text{R}} \right) + \frac{1}{2} \psi^* \ell^2 |\nabla \mathbf{d}|^2 \end{aligned} \quad (4.7.25)$$

with  $\psi_{\text{R}}^{\text{m}+}(\mathbf{E}^{\text{e}}, \xi)$  and  $\psi_{\text{R}}^{\text{m}-}(\mathbf{E}^{\text{e}}, \xi)$  defined in (4.7.12).

### 4.7.3 Stress

Using (4.7.25) in (4.7.10), the Mandel stress is given as

$$\mathbf{M}^{\text{e}} = g(\mathbf{d}) \mathbf{M}^{\text{e}+} + \mathbf{M}^{\text{e}-} \quad (4.7.26)$$

with

$$\begin{aligned}\mathbf{M}^{e+} &= \sum_{i=1}^3 \left[ 2G(\bar{\xi}) \langle \mathbf{E}_i^e \rangle_+ + \left( K(\bar{\xi}) - \frac{2}{3}G(\bar{\xi}) \right) \left( \langle \mathbf{E}_1^e + \mathbf{E}_2^e + \mathbf{E}_3^e \rangle_+ \right) \right] \mathbf{r}_i^e \otimes \mathbf{r}_i^e \\ \mathbf{M}^{e-} &= \sum_{i=1}^3 \left[ 2G(\bar{\xi}) \langle \mathbf{E}_i^e \rangle_- + \left( K(\bar{\xi}) - \frac{2}{3}G(\bar{\xi}) \right) \left( \langle \mathbf{E}_1^e + \mathbf{E}_2^e + \mathbf{E}_3^e \rangle_- \right) \right] \mathbf{r}_i^e \otimes \mathbf{r}_i^e\end{aligned}\quad (4.7.27)$$

and the Cauchy and Piola stress measures related by

$$\mathbf{T} = J^{e-1} \mathbf{R}^e \mathbf{M}^e \mathbf{R}^{e\top} \quad \text{and} \quad \mathbf{T}_R = J^e \left( \mathbf{R}^e \mathbf{M}^e \mathbf{R}^{e\top} \right) \mathbf{F}^{-\top}. \quad (4.7.28)$$

**Remark 4:** We note here that in deriving the stress relations (4.7.26) and (4.7.27), we omit the contribution to stress due to electrostatics (i.e. the Maxwell stress). That is, we neglect the derivative of the electrostatic energy  $\psi_R^e(\mathbf{C}^e, \xi, \mathbf{d}_R)$  with respect to the elastic Cauchy-Green tensor. A detailed derivation of the Maxwell stress due to electrostatics, leading to the classical form  $\mathbf{T}^{\text{es}} = \varepsilon(\mathbf{e} \otimes \mathbf{e} - (1/2)(\mathbf{e} \cdot \mathbf{e})\mathbf{1})$ , with  $\mathbf{e}$  the spatial electric field, may be found in the work of Narayan et al. [177]. For the case of inorganic solid electrolytes, as modeled here, a relative permittivity value  $\varepsilon_r \approx 50$  has been experimentally reported [205]. In light of (4.7.22), the permittivity of the solid host evaluates then to a negligibly small number. As detailed in the works of Natsiavas et al. [82], Shishvan et al. [86] and Narayan et al. [177], the Maxwell stresses due to electrostatics are negligibly small compared to the stresses generated by the deposition of metal filaments inside the solid host, and can be neglected without compromising accuracy. As such, we omit the contribution to mechanics due to electrostatics so as not to obfuscate the more relevant physics discussed next.

#### 4.7.4 Electrochemical Potential. Flux

Using (4.7.25) in (4.6.6)<sub>1</sub>, the electrochemical potential of the ionic species transporting across the solid host is given by

$$\mu^e = \mu_0 + R\vartheta \ln \left( \frac{\bar{c}}{1 - \bar{c}} \right) + F\phi. \quad (4.7.29)$$

We specialize the flux of ionic species across the solid host to be isotropic and write (4.6.6)<sub>2</sub> as

$$\mathbf{j}_R = -m(c, \bar{\xi}) \nabla \mu^e, \quad (4.7.30)$$

with the effective mobility,  $m$  given by

$$m(c, \bar{\xi}) = m_0(\bar{\xi})c(1 - \bar{c}), \quad \text{and} \quad m_0(\bar{\xi}) = \left(1 - h(\bar{\xi})\right)m_0^{\text{SE}} + h(\bar{\xi})m_0^{\text{M}}. \quad (4.7.31)$$

Here,  $m_0^{\text{SE}}$  and  $m_0^{\text{M}}$  are related to the diffusivities of each material phase through the standard relations,

$$m_0^{\text{SE}} = \frac{D_0^{\text{SE}}}{R\vartheta}, \quad \text{and} \quad m_0^{\text{M}} = \frac{D_0^{\text{M}}}{R\vartheta} \quad (4.7.32)$$

with  $D_0^{\text{SE}}$  and  $D_0^{\text{M}}$  denoting the diffusivity of ionic species in the solid host and the electrodeposited Li-metal.

#### 4.7.5 Reaction Driving Force. Electrodeposition Kinetics

Using (4.7.25) in (4.6.8)<sub>2</sub>, the electrochemical potential of the deposited Li-metal is given by

$$\mu^\xi = \mu_0^\xi + \frac{d}{d\xi} \left( \mathcal{W}\bar{\xi}^2(1 - \bar{\xi})^2 \right) + F\phi_0 - J^c h(\bar{\xi}) \mathbf{M}^e : \mathbf{N}^r - \text{Div}(\lambda_\xi \nabla \xi). \quad (4.7.33)$$

We note that in deriving (4.7.33), we neglect the derivatives of  $J^c$  and the reaction-dependent shear,  $G(\xi)$  and bulk modulus  $K(\xi)$ , present in the mechanical free energy,  $\psi_{\text{R}}^{\text{m}}$ , with re-

spect to the reaction coordinate,  $\xi$ . These terms are quadratic in the elastic strains, and expected to be much smaller in magnitude than the other terms in (4.7.33) (c.f. Narayan and Anand [178], Di Leo et al. [42]).

Further, using (4.7.29) and (4.7.33) in (4.6.8)<sub>1</sub>, the thermodynamic driving force,  $\mathcal{F}$  for electrodeposition takes the following form

$$\begin{aligned}
\mathcal{F} &= \mu^\xi - \mu^e \\
&= \underbrace{(\mu_0^\xi - \mu_0)}_{\text{energetic}} - \underbrace{R\vartheta \left( \frac{\bar{c}}{1 - \bar{c}} \right)}_{\text{entropic}} + \underbrace{F(\phi_0 - \phi)}_{\text{electric}} + \underbrace{\frac{d}{d\xi} \left( \mathcal{W}_{\xi^2} (1 - \bar{\xi})^2 \right)}_{\text{energetic barrier}} \dots \\
&\quad - \underbrace{J^c h(\bar{\xi}) \mathbf{M}^e : \mathbf{N}^r}_{\text{mechanical}} - \underbrace{\text{Div}(\lambda_\xi \nabla \xi)}_{\text{numerical regularization}}.
\end{aligned} \tag{4.7.34}$$

Here, the first term denotes the difference in reference chemical potentials between species transporting across the solid host and species in the electrodeposited metallic compound. The second term captures the role of configurational entropy. Critically, enrichment in concentration of ionic species at the reaction sites favors electrodeposition of Li-metal, while depletion in concentration of Li-ions accordingly retards electrodeposition. The third term serves as an electric driving force for electrodeposition, stemming from the difference in electric potential in the electrode and electric potential in the solid conductor at the reaction site. The fourth term introduces a local driving force to the reaction associated with the energy barrier between the phases, which drives the reaction towards the two energy minima. The fifth term captures the effect of mechanical stress on the reaction driving force. In light of the discussion in Sect. 4.7.1, only the stress component normal to the electrode-solid conductor interface affects the driving force for electrodeposition (c.f. Ganser et al. [195] and Deshpande and McMeeking [192]). This coupling is different in form to conventional diffusion-deformation theories employing an isotropic chemical distortion, in which case the reaction driving force couples to mechanics through a pressure term (c.f. [42, 108]). Critically, compressive stresses retard the electrodeposition of metallic compound at the re-

action sites, while tensile stresses accordingly facilitate plating. The final term in (4.7.34) arises from the gradient phase-field nature of the theory and regularizes the interface width, setting a minimum width controlled by  $\lambda_\xi$ .

Having discussed the reaction driving force,  $\mathcal{F}$ , we now specify the reaction kinetics equation. Consistent with electro-kinetics theory, we invoke a Butler-Volmer non-linear reaction kinetics formulation and evolve the extent of electrodeposition,  $\bar{\xi}$  as follows,

$$\dot{\bar{\xi}} = \begin{cases} R_0 \left( \exp \left( \frac{-\alpha \mathcal{F}}{R\vartheta} \right) - \exp \left( \frac{(1-\alpha)\mathcal{F}}{R\vartheta} \right) \right), & \text{if } 0 < \bar{\xi} < 1, \\ 0, & \text{if } \bar{\xi} = 1. \end{cases} \quad (4.7.35)$$

Here,  $\alpha$  denotes a symmetry factor, representative of the fraction of surface overpotential promoting anodic or cathodic reaction at the electrode interface, while  $R_0 > 0$  denotes a positive-valued reaction constant. For elementary single-electron transfer reactions, a value  $\alpha = 0.5$  is typically employed. Note that (4.7.35) satisfies the dissipation inequality (4.5.12)<sub>1</sub>, such that  $-\mathcal{F}\dot{\bar{\xi}} \geq 0$ , where electrodeposition of Li metal,  $\dot{\bar{\xi}} > 0$  proceeds under a negative reaction driving force,  $\mathcal{F} < 0$ , consistent also with electro-kinetics theory.

We emphasize that the focus of this work is on modeling growth of metal filaments across a solid conductor with continuous deposition (i.e.  $\dot{\bar{\xi}} > 0$ ). As a result, *we do not model the reverse “stripping” process (i.e.  $\dot{\bar{\xi}} < 0$ ) and assume perfect contact between the electrode and the solid conductor is maintained at all times.* Models considering the role of electrochemical cycling on the evolution of imperfections at the Li-metal/SSE interface have recently been proposed (cf. Zhao et al. [87]) that complement the proposed framework which focuses on Li-metal filament propagation across the SSE.

#### Restrictions on electrodeposition kinetics

We now introduce two phenomenological restrictions on the electrodeposition kinetics formulation presented above. First, the phase-field reaction formulation presented here

does not explicitly account for the presence of electrons in the electrodeposition reaction (4.7.1), which are necessary for Li-metal plating to occur. Since the solid-state electrolyte is electronically-insulating, we assume that electrons are readily available only at the Li metal/SSE interface. We account for this phenomenon by restricting the electrodeposition reaction (4.7.35) to occur **only** in regions where there is existing Li-metal deposits (and henceforth readily available electrons), modeled as regions with  $\bar{\xi} > 0$ . Phenomenologically, we model this behavior by scaling the reaction rate constant,  $R_0$  with a reaction-dependent logistic function,  $f_1(\bar{\xi})$  of the form

$$f_1(\bar{\xi}) = g_1(\bar{\xi}) - g_1(0), \quad \text{with} \quad g_1(\bar{\xi}) = \left(1 + \exp\left(-\alpha_1(\bar{\xi} - \beta_1)\right)\right)^{-1}. \quad (4.7.36)$$

The logistic function (4.7.36) is guaranteed to satisfy  $f_1(0) = 0$ , such that no Li-metal plating will occur in the solid-state electrolyte bulk where no electrons are present. The parameters  $\alpha_1$  and  $\beta_1$  in (4.7.36) respectively control the steepness of the logistic function and the midpoint location.

Second, as discussed in Sect. 4.2, we model plating to occur only within damaged regions of the solid-state electrolyte, which provide the necessary vacant sites to accommodate Li-metal deposition. The theoretical formulation thus far does not guarantee that  $\dot{\xi} > 0$  only in regions where  $d > 0$ . To phenomenologically enforce this constraint, we once again scale the reaction constant,  $R_0$  by a damage-dependent logistic function of the form

$$f_2(d) = g_2(d) - g_2(0), \quad \text{with} \quad g_2(d) = \left(1 + \exp\left(-\alpha_2(d - \beta_2)\right)\right)^{-1}. \quad (4.7.37)$$

Scaling of the reaction kinetics by the logistic function  $f_2(d)$  shown in (4.7.37) ensures that electrodeposition of Li-metal inside the solid conductor is confined only within regions of the host electrolyte which have incurred some degree of damage.

Given these constraints, the reaction kinetics formulation (4.7.35) is replaced with the



modified form

$$\dot{\bar{\xi}} = \begin{cases} f_1(\bar{\xi})f_2(d)R_0 \left( \exp\left(\frac{-\alpha\mathcal{F}}{R\vartheta}\right) - \exp\left(\frac{(1-\alpha)\mathcal{F}}{R\vartheta}\right) \right), & \text{if } 0 < \bar{\xi} < 1, \\ 0, & \text{if } \bar{\xi} = 1, \end{cases} \quad (4.7.38)$$

with the logistic functions defined in (4.7.36) and (4.7.37).

The specific logistic functions chosen are shown in Fig. 4.2. For both functions, we choose  $\alpha_1 = \alpha_2 = 90$  to ensure a steep transition. For the function  $f_1(\bar{\xi})$ , which phenomenologically models the requirement of electrons being present, we choose a small value of the offset point  $\beta_1 = 0.05$ .

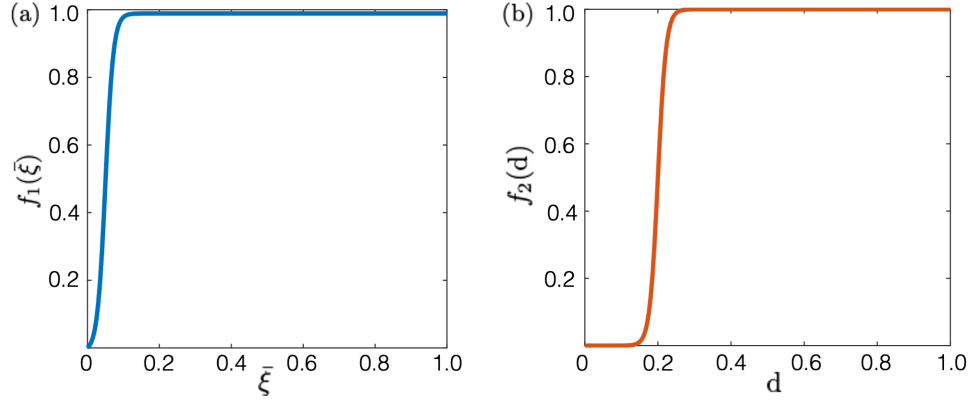


Figure 4.2: Logistic functions modulating the reaction constant  $R_0$  with (a) the function  $f_1(\bar{\xi})$  and (b) the function  $f_2(d)$ . Reproduced with permission from [19].

This suffices to enforce that Li-metal plating occurs in the presence of existing Li-metal deposits (i.e. in the presence of electrons), without altering the reaction kinetics significantly. For the function  $f_2(d)$ , which restricts electrodeposition within damaged regions of the host electrolyte, we specialize  $\beta_2 = 0.2$ . This essentially requires that  $\approx 20\%$  damage is incurred on the solid electrolyte before Li-metal plating can occur. In Sect. 4.9 below, we provide a detailed discussion on the role of the logistic the function,  $f_2(d)$  which couples reaction kinetics and damage.

#### 4.7.6 Electrostatics

Using (4.7.25) in (4.6.9)<sub>2</sub>, the referential electric field is given by

$$\mathbf{e}_R = \frac{1}{\varepsilon} J^{-1} \mathbf{C} \mathbf{d}_R. \quad (4.7.39)$$

Invoking the relations  $\mathbf{e} = \mathbf{F}^{-\top} \mathbf{e}_R$  and  $\mathbf{d} = J^{-1} \mathbf{F} \mathbf{d}_R$ , one may also relate the spatial electric flux density to the spatial electric field as

$$\mathbf{d} = \varepsilon \mathbf{e}. \quad (4.7.40)$$

#### 4.7.7 Damage

The evolution equation for damage is adopted from the works of Anand et al. [48] and Miehe et al. [197]. For brevity, we omit detailed derivations and refer the reader to the aforementioned publications. We note that using (4.7.25) in (4.6.10) and defining the dissipative microstress  $\varpi_{\text{dis}}$  as

$$\varpi_{\text{dis}} = \psi^* + \Gamma \dot{\mathbf{d}}, \quad (4.7.41)$$

the final evolution equation for damage takes the form

$$\Gamma \dot{\mathbf{d}} = 2(1 - \mathbf{d})\mathcal{H} - \psi^* \mathbf{d} + \psi^* \ell^2 \Delta \mathbf{d}. \quad (4.7.42)$$

Here,  $\Gamma > 0$  denotes a small viscous regularization parameter, introduced to impart stability to the numerical solution scheme. Consistent with the derivations in Anand et al. [48], in the rate-independent limit ( $\Gamma = 0$ ), the energy dissipated per unit volume as damage,  $\mathbf{d}$  increases from 0 to 1 evaluates to  $\psi^*$ . Naturally then, in our formulation,  $\psi^*$  represents an energy per unit volume dissipated during the fracture process. As later discussed in Sect. 4.9,  $\psi^*$  can be related to the experimentally reported fracture energy of the material of choice,  $G_c$  through a characteristic length scale parameter,  $\ell$ , which controls the diffuse

fracture zone.

Finally,  $\mathcal{H}$  represents a monotonically increasing history field function, which ensures that the damage irreversibility constraint (4.2.3) holds. It is given by

$$\mathcal{H} = \max_{s \in [0, t]} [\langle \psi_R^{m+}(\mathbf{E}^e, \xi) - \psi^*/2 \rangle]. \quad (4.7.43)$$

Consistent with (4.7.11), only the mechanical energetic contribution associated with tensile strains,  $\psi_R^{m+}$ , contributes to the evolution of damage.

#### 4.8 Governing partial differential equations for the specialized constitutive equations. Boundary conditions

The final set of the governing partial differential equations consists of:

1. Force balance, eq. (4.6.5), viz.

$$\text{Div } \mathbf{T}_R + \mathbf{b}_R = \mathbf{0}, \quad (4.8.1)$$

with the Piola stress  $\mathbf{T}_R$  given by (4.7.28)<sub>2</sub>, and  $\mathbf{b}_R$  the non-inertial body force.

2. The local mass balance for the ionic species (4.6.7), which together with the flux relationship (4.7.30) yields

$$\dot{c} = \text{Div} (m \nabla \mu^e) - \dot{\xi}, \quad (4.8.2)$$

with the mobility,  $m$ , given in (4.7.31), and the electrochemical potential of ionic species,  $\mu^e$ , in (4.7.29). The reaction rate,  $\dot{\xi}$ , is governed by the PDE (4.8.3) below.

3. The reaction kinetics, governed by (4.7.38), which in conjunction with the reaction

driving force (4.7.34), yield the governing PDE for the reaction coordinate

$$\begin{aligned} \dot{\bar{\xi}} &= f_1(\bar{\xi})f_2(\mathbf{d})R_0 \left( \exp \left( \frac{-\alpha\mathcal{F}}{R\vartheta} \right) - \exp \left( \frac{(1-\alpha)\mathcal{F}}{R\vartheta} \right) \right), \quad \text{with} \\ \mathcal{F} &= (\mu_0^\xi - \mu_0) - R\vartheta \left( \frac{\bar{c}}{1-\bar{c}} \right) + F(\phi_0 - \phi) + \frac{d}{d\xi} \left( \mathcal{W}\bar{\xi}^2(1-\bar{\xi})^2 \right) \dots \quad (4.8.3) \\ &\quad - J^e h(\bar{\xi})\mathbf{M}^e : \mathbf{N}^r - \text{Div}(\lambda_\xi \nabla \xi) \end{aligned}$$

Here, eq. (4.8.3) constitutes a PDE due to the presence of the  $\text{Div}(\nabla \xi)$  term in the reaction driving force  $\mathcal{F}$ . Following (4.7.38), the reaction kinetics also obey the restriction  $\dot{\bar{\xi}} = 0$  when  $\bar{\xi} = 1$ , which marks the end of the reaction.

4. Gauss's law, viz. (4.6.9), which along with electric displacement given by (4.7.39), and using  $\mathbf{e}_r = -\nabla \phi$  governs the electric potential,  $\phi$  through

$$\text{Div}(\mathbf{d}_r) = F(c - c_0), \quad \text{with} \quad \mathbf{d}_r = -\varepsilon J \mathbf{C}^{-1} \nabla \phi. \quad (4.8.4)$$

From a computational standpoint, numerically solving for  $\phi$  using (4.8.4) is cumbersome and requires resolution of thin boundary layers in the range of a few nanometers, where deviations from electroneutrality occur [188, 189]. Given the representative dimensions of the domains of interest in this work, this makes the problem computationally non-tractable and expensive.

In practice, granted the regions where concentration gradients occur are small with respect to the domain of interest, an assumption of electroneutrality in the system is often invoked in the literature to numerically solve for  $\phi$ , such that the net charge  $q_r = F(c - c_0) = 0$  (cf. [169, 172, 174, 178, 206]).

We adopt this approach in our numerical implementation. Making use of (4.2.8), we consider the current density,  $\mathbf{i}_r$  to be conserved and described by a Poisson equation including a sink term to represent the charge loss due to electrochemical reactions

(c.f. [169, 172, 174]), yielding a governing equation for  $\phi$  of the form,

$$\text{Div } \mathbf{i}_R = -F\dot{\xi} \quad \text{with} \quad \mathbf{i}_R = -\kappa(\bar{\xi})\nabla\phi \quad (4.8.5)$$

which replaces the use of (4.8.4). Here, consistent with electro-kinetics theory, we introduce the effective conductivity,  $\kappa(\bar{\xi})$ , which interpolates between the conductivity of the electrode,  $\kappa^{SE}$ , and the conductivity of the Li metal,  $\kappa^M$ , through  $\kappa(\bar{\xi}) = (1 - h(\bar{\xi}))\kappa^{SE} + h(\bar{\xi})\kappa^M$ .

5. Damage evolution, governed by eq. (4.7.42), viz.

$$\Gamma\dot{d} = 2(1 - d)\mathcal{H} - \psi^*d + \psi^*\ell^2\Delta d \quad (4.8.6)$$

with  $\mathcal{H}$  a monotonically increasing history function which ensures damage irreversibility (i.e.  $\dot{d} \geq 0$ ) defined in (4.7.43).

Finally, to complete the model, a set of boundary and initial conditions must be supplemented. Let  $\mathcal{S}_1$  and  $\mathcal{S}_2$  be complementary subsurfaces on the boundary  $\partial B$  of the body  $B$ , i.e.  $\partial B = \mathcal{S}_\chi \cup \mathcal{S}_{t_R}$  and  $\mathcal{S}_\chi \cap \mathcal{S}_{t_R} = \emptyset$ . Similarly, let the pairs  $\{\mathcal{S}_3, \mathcal{S}_4\}$ ,  $\{\mathcal{S}_5, \mathcal{S}_6\}$ ,  $\{\mathcal{S}_7, \mathcal{S}_8\}$ , and  $\{\mathcal{S}_9, \mathcal{S}_{10}\}$  be complementary subsurfaces as described above. For the five degrees of freedom  $\{\mathbf{u}, \bar{c}, \phi, \bar{\xi}, d\}$  governed by the PDEs described above, we then respectively consider the boundary conditions

$$\left. \begin{aligned} \mathbf{u} &= \check{\mathbf{u}} \quad \text{on} \quad \mathcal{S}_1, \quad \text{and} \quad \mathbf{T}_R \mathbf{n}_R = \check{\mathbf{t}}_R \quad \text{on} \quad \mathcal{S}_2; \\ \bar{c} &= \check{\bar{c}} \quad \text{on} \quad \mathcal{S}_3, \quad \text{and} \quad -\mathbf{j}_R \cdot \mathbf{n}_R = \check{j} \quad \text{on} \quad \mathcal{S}_4; \\ \phi &= \check{\phi} \quad \text{on} \quad \mathcal{S}_5, \quad \text{and} \quad -\mathbf{d}_R \cdot \mathbf{n}_R = \check{\varpi} \quad \text{on} \quad \mathcal{S}_6; \\ \bar{\xi} &= \check{\bar{\xi}} \quad \text{on} \quad \mathcal{S}_7, \quad \text{and} \quad \lambda_\xi \nabla \bar{\xi} \cdot \mathbf{n}_R = 0 \quad \text{on} \quad \mathcal{S}_8; \\ d &= \check{d} \quad \text{on} \quad \mathcal{S}_9, \quad \text{and} \quad \nabla d \cdot \mathbf{n}_R = 0 \quad \text{on} \quad \mathcal{S}_{10}. \end{aligned} \right\} \quad (4.8.7)$$

Here: i)  $\check{\mathbf{u}}$  is a prescribed displacement and  $\check{\mathbf{t}}_{\text{r}}$  a prescribed traction, ii)  $\check{c}$  is a prescribed normalized concentration and  $\check{j}$  a prescribed flux, iii)  $\check{\phi}$  is a prescribed electric potential and  $\check{\varpi}$  a prescribed surface charge density, iv)  $\check{\xi}$  is a prescribed reaction coordinate, and v)  $\check{d}$  is a prescribed state of damage. Consistently, the initial conditions are also prescribed as

$$\mathbf{u}(\mathbf{X}, 0) = \mathbf{u}_0(\mathbf{X}), \bar{c}(\mathbf{X}, 0) = \bar{c}_0(\mathbf{X}), \phi(\mathbf{X}, 0) = \phi_0(\mathbf{X}), \bar{\xi}(\mathbf{X}, 0) = \bar{\xi}_0(\mathbf{X}), d(\mathbf{X}, 0) = d_0(\mathbf{X}) \quad (4.8.8)$$

The fully coupled set of PDEs (4.8.1) through (4.8.6), along with the boundary conditions (4.8.7) and initial conditions (4.8.8) give then an initial/boundary-value problem for the unknowns of displacement  $\mathbf{u}(\mathbf{X}, t)$ , normalized concentration  $\bar{c}(\mathbf{X}, t)$ , electric potential  $\phi(\mathbf{X}, t)$ , reaction coordinate  $\bar{\xi}(\mathbf{X}, t)$  and state of damage  $d(\mathbf{X}, t)$ .

## 4.9 Numerical simulations

In this section, we detail a set of numerical simulations aimed to highlight the important features of our theory, namely the interplay of electro-chemo-mechanical processes that govern the initiation and propagation of Li-metal filaments in SSEs. While the proposed framework is general in nature, we specialize it towards modeling a problem of engineering relevance to commercialization of next-generation all-solid-state batteries as detailed below.

The theoretical framework specialized in Sect. 4.7 contains five degrees of freedom  $\{\bar{\xi}, \bar{c}, \phi, d, \mathbf{u}\}$  governed by the partial differential equations summarized in Sect. 4.8. The fully-coupled PDEs are solved using the finite element method in Abaqus Standard [207] by developing a custom user-element (UEL) subroutine following the details described in Chester et al. [130]. We note that implementation of the reaction kinetics PDE (4.8.3) is done through the so called “micromorphic” formulation, where an auxiliary variable is introduced to ease numerical convergence [129, 208]. The implementation is akin to that of Afshar and Di Leo [15] and we refer the reader to this work for further details. Importantly,

we note that use of this numerical technique *does not affect* the numerical results, and produces equivalent outputs as would be generated with a direct implementation of (4.8.3).

We specialize our theory for a Li-metal/LLZO solid-state architecture, which has been widely investigated in the literature (c.f [58, 59, 60, 65, 73]). This architecture, using an oxide-based electrolyte, is relevant due to its superior chemo-mechanical properties (i.e. high stiffness and fracture toughness, high ionic conductivity, excellent stability against Li-metal etc.). Growth of Li-metal filaments across a LLZO solid-state electrolyte has been experimentally observed to occur as both a single transgranular branch, as well as through a network of filaments proceeding across the grain boundaries of the SSE [58, 60, 73, 74, 169].

In Sect. 4.9.1, we focus on modeling the growth of a single Li-metal filament traversing from the anode towards the cathode end. For the set of simulations in Sect. 4.9.1, we do not consider the LLZO microstructure composition (i.e. the presence of grain boundaries) and treat the solid host as a homogenized medium. Starting with a small initial imperfection at the electrode interface, we demonstrate the manner in which the coupled electro-chemo-mechanical phenomena govern the growth of Li-metal filaments with continuous fracture of the SSE. Additionally, we elucidate the role that mechanical confinement (i.e. mechanical boundary conditions) plays on the rate of crack propagation versus the rate of Li-metal filament growth. We demonstrate the ability of our theory to qualitatively reproduce the experimentally observed phenomenon of crack fronts propagating ahead of Li-metal filaments, with cracks only partially filled by the electrodeposited Li-metal [20, 69].

In Sect. 4.9.2, we consider the role of the SSE microstructure composition by modeling the presence of grain boundaries through seeding of elements with varying mechanical properties. At present, there is a lack of numerical frameworks, which can incorporate the manner in which microstructural information affects the coupled electro-chemo-mechanical growth of Li-metal filaments through SSEs. We use this set of simulations to elucidate the manner in which damage and mechanical stresses are coupled to electrodepo-

sition kinetics in this theoretical framework. In particular, we investigate how damage can impact electrodeposition through both the thermodynamically-consistent reaction driving force  $\mathcal{F}$  in (4.7.34), and the reaction kinetics restrictions in (4.7.38). Finally, we demonstrate the utility of our theoretical framework by modeling the manner in which the morphology of Li-metal filaments changes for a LLZO microstructure depending on the relative fracture strength of the LLZO grains versus the grain boundaries.

#### 4.9.1 Modeling growth of a single Li-metal filament across a LLZO electrolyte. Role of mechanical confinement

We present here an application of the fully-coupled, electro-chemo-mechanical framework towards modeling the growth of Li-metal filaments across a  $\text{Li}_7\text{La}_3\text{Zr}_2\text{O}_{12}$  (LLZO) electrolyte. Growth of Li-metal filaments across pre-existing defects at the metal electrode interface for single-crystal LLZO microstructures has been extensively reported in the literature (c.f. [60, 73]). We demonstrate the ability of our framework to numerically reproduce the phenomena of Li-metal filament growth as a single branch protruding from the anode towards the cathode, while fracturing the SSE in the process. Through these simulations, we elucidate the interplay of electro-chemo-mechanical processes, which govern electrodeposition of Li-metal across SSEs. In particular, we elucidate the manner in which mechanical confinement of the simulation domain plays a critical role on the resulting fracture and electrodeposition morphology.

We consider a two-dimensional (2D),  $200\ \mu\text{m} \times 200\ \mu\text{m}$  plane-strain simulation domain, meshed with  $350 \times 350$  quadrilateral finite elements. This domain is representative of a half-cell system consisting of a Li-metal anode and a LLZO solid electrolyte, see Fig. 4.3(a). The dimensions of the simulation domain are assigned consistent with works in the literature invoking a similar phase-field treatment [77, 172, 174]. To simulate the Li-metal anode, a  $5\ \mu\text{m}$  thick layer (c.f. [84, 174]) is initialized in an already fully-reacted state at the bottom of the domain, Fig. 4.3(a). We do so by prescribing a reaction co-



ordinate,  $\bar{\xi} = 1$  across this area. To simulate the presence of a Li-filled crack-like defect on the electrolyte's surface [60, 164, 165], an imperfection  $8 \mu\text{m}$  in width and  $2 \mu\text{m}$  in height is seeded on the anode/SSE interface by prescribing a state of damage,  $d = 1$  and reaction coordinate,  $\bar{\xi} = 1$ , see Fig. 4.3(b). The prescribed defect dimensions are comparable to experimental works investigating the role of surface defects on metal growth across inorganic SSEs [60, 209]. This setup, Figs. 4.3(a,b), mimics infiltration of Li-metal in a pre-existing imperfection. As shown later, the Li-filled defect serves to break the symmetry of the model and initiate subsequent growth of Li-metal filaments across the SSE.

A vanishing normalized cation concentration,  $\bar{c} \approx 0$  is prescribed across the anode layer, Fig. 4.3(c), to numerically simulate a state of complete ionic species depletion in the pure Li-metal phase. According to the calculations of Li and Monroe [185], there are 15 available sites for lithium per  $\text{La}_3\text{Zr}_2\text{O}_{12}$  formula unit, 7 of which are occupied at equilibrium, yielding an equilibrium occupancy  $\theta = x/x_{\text{max}} \approx 0.5$  for  $\text{Li}_7\text{La}_3\text{Zr}_2\text{O}_{12}$ . Consistently, we prescribe a normalized bulk cationic concentration,  $\bar{c} = 0.5$  as an initial condition across the solid electrolyte (regions of  $\bar{\xi} = 0$ ), see Fig. 4.3(c). The same normalized concentration,  $\bar{c} = 0.5$ , is additionally prescribed as a Dirichlet boundary condition on the top edge of the simulation domain. As shown in Fig. 4.3(d), we set the anode potential at the bottom of the domain,  $\phi = 0\text{V}$  and prescribe a potential,  $\phi = 0.20\text{V}$  on the top of

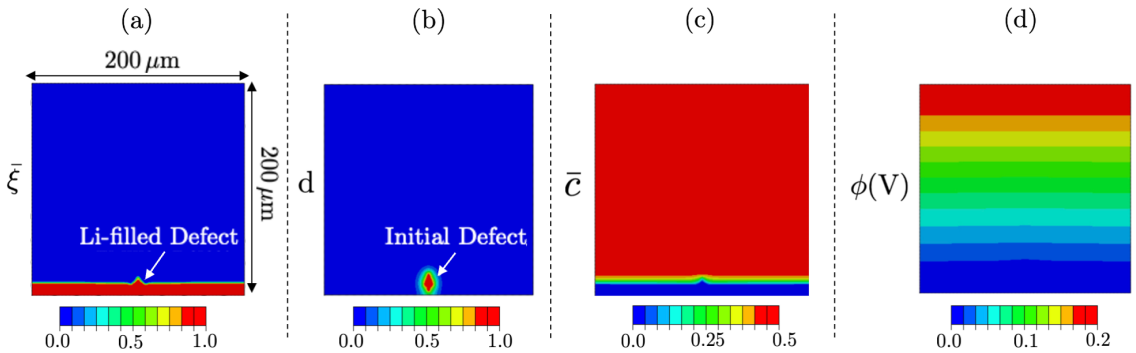


Figure 4.3: Initial configuration of the Li-electrode/solid electrolyte simulation containing a pre-existing defect. Contours of (a) reaction coordinate  $\bar{\xi}$ , (b) damage  $d$ , (c) normalized concentration  $\bar{c}$ , and (d) electric potential  $\phi$  (V). Reproduced with permission from [19].

the domain, consistent with works in the literature [77, 175, 176]. The prescribed electric potential on the top edge of the domain, i.e. the electrolyte surface, serves to drive the system out of equilibrium, enabling for electrodeposition of Li-metal at the electrode-SSE interface. Altogether, Fig. 4.3(a-d) constitute the initial, *stress-free* configuration of the Li-metal electrode-solid electrolyte assembly.

Mechanically, roller boundary conditions are applied at the top edge of the simulation domain, while the bottom edge is pinned. We consider two different boundary conditions for the left and right edges of the simulation domain to illustrate the role of mechanical confinement on electrodeposition kinetics and resulting fracture/electrodeposition morphology. It has been experimentally reported via in-situ X-ray tomography the propensity for Li-metal filaments to sometimes only partially fill cracked regions of SSEs (c.f. [20, 69]). The cited experimental works have demonstrated the potential for electrodeposition-induced cracks to traverse the entire SSE ahead of the Li-deposits, which trail behind. To numerically reproduce this phenomenon, we apply first a roller boundary condition to the sides. Subsequently, we relax this lateral mechanical constraint and consider the sides to be free.

**Remark 5:** Note that the region being modeled as the Li-metal anode shown in Figs. 4.3(a,b) is characterized by a state of  $\bar{\xi} = 1$  and  $d = 0$ , unlike the lithium-filled defect, which is characterized by  $\bar{\xi} = 1$  and  $d = 1$ . As noted in Sect. 4.2, in developing the theoretical framework, we restrict Li-electrodeposition inside the SSE to occur only within damaged regions (i.e.  $\bar{\xi} > 0$  only if  $d > 0$ ). Since the Li-metal anode is initialized before the start of the physical simulation (i.e. in a stress-free configuration), we do not require that  $d > 0$  in this region. The Li-metal anode region is characterized by  $\bar{\xi} = 1$  and  $d = 0$  so as to model a solid Li-metal layer capable of sustaining both tensile and compressive loads, as would be physically present in a Li-metal/LLZO half cell. In addition, we note here that we allow for electrodeposition of Li-metal at the flat horizontal anode/SSE interface, which as discussed above are characterized by a state

of  $\bar{\xi} = 1, d = 0$ . As such, in those regions, *we omit* the logistic function  $f_2(d)$  in the reaction kinetics (4.7.38), such that electroplating on the flat horizontal interfaces may occur.  $\square$

The electro-chemo-mechanical properties for a Li-Metal/LLZO solid-state system are tabulated in Table 4.2. We emphasize that the physics based thermodynamically-consistent

Table 4.2: Material properties for modeling of metal filament growth in a Li-Li<sub>7</sub>La<sub>3</sub>Zr<sub>2</sub>O<sub>12</sub> system.

	Parameter	Value	Source
Electro-Chemical	$\kappa_{\text{LLZO}}$	$4.43 \cdot 10^{-2}$ S/m	Li <i>et al.</i> [210]
	$\kappa_{\text{Li}}$	$1.0 \cdot 10^7$ S/m	Chen <i>et al.</i> [169]
	$D_{\text{LLZO}}$	$1.0 \cdot 10^{-12}$ m <sup>2</sup> /s	Tian <i>et al.</i> [77]
	$D_{\text{Li}}$	$1.0 \cdot 10^{-15}$ m <sup>2</sup> /s	Tian <i>et al.</i> [77]
	$c_{\text{max}}$	$4.22 \cdot 10^4$ mol/m <sup>3</sup>	Tian <i>et al.</i> [77]
Reaction Kinetics	$R_0$	$0.1$ s <sup>-1</sup>	Yuan <i>et al.</i> [206]
	$\Omega_{\text{Li}}$	$1.3 \cdot 10^{-5}$ m <sup>3</sup> /mol	Tantratian <i>et al.</i> [174]
	$\Omega_{\text{Li}} \xi^{\text{max}}$	0.3	This Work
	$\mathcal{W}$	$1.18 \cdot 10^6$ J/m <sup>3</sup>	Tian <i>et al.</i> [77]
	$\lambda_{\xi}$	$8 \cdot 10^4$ pJ $\cdot\mu\text{m}^5/\text{pmol}^2$	Numerical
Mechanical	$E_{\text{LLZO}}$	150 GPa	Narayan and Anand [84]
	$\nu_{\text{LLZO}}$	0.26	Narayan and Anand [84]
	$E_{\text{Li}}$	4.91 GPa	Narayan and Anand [211]
	$\nu_{\text{Li}}$	0.36	Narayan and Anand [211]
Damage	$\Gamma$	0.04 MPa $\cdot$ s	This Work
	$\psi^* \cdot \ell$	6.67 J/m <sup>2</sup>	Narayan and Anand [84]
	$\ell$	5.0 $\mu\text{m}$	Regularization Parameter

formulation *allows virtually all material parameters to be found from the literature, either experimentally or from ab-initio simulations.* That is, the theoretical framework may be

calibrated in a straightforward fashion and as such should prove useful in application to a number of engineering problems of relevance.

As detailed in Sect. 4.7.2, the parameter,  $\psi^*$  represents the dissipated energy per unit volume during the fracture process, while  $\ell$  denotes a length scale to account for the damage gradient effects. As discussed by Narayan and Anand [212] and De Borst and Verhoosel [213], the gradient damage formulation will be mesh-independent, provided the element size,  $h_e$ , is sufficiently small compared to the length scale,  $\ell$ . Typically, an element size  $h_e \leq 0.2 \cdot \ell$  is considered sufficient. Additionally, the product  $\psi^* \cdot \ell$  is related to the macroscopic critical energy release rate,  $G_c$  through  $G_c \approx \psi^* \cdot \ell$  [48, 55, 56]. Provided the length scale parameter,  $\ell$  is chosen in a suitable physically realistic range,  $\ell$  acts as an adjustable regularization parameter in our gradient damage theory. We prescribe a length scale,  $\ell \approx 5 \mu\text{m}$  to obtain a width for the fracture zone comparable in dimensions to published works in the literature [174, 206]. The characteristic element size  $h_e = 570 \text{ nm}$  is then chosen and satisfies the condition  $h_e \leq 0.2 \cdot \ell$  for mesh-independent results. This element size dictates the choice of a  $350 \times 350$  finite-element mesh for the given  $200 \mu\text{m} \times 200 \mu\text{m}$  simulation domain. This ensures the interface is sufficiently narrow, while the number of elements required to resolve the interface does not become computationally intractable. With  $\ell$  fixed, the value of  $\psi^*$  is then chosen such that  $\psi^* \cdot \ell = G_c = 6.67 \text{ J/m}^2$  for LLZO.

Additionally, we note here that choice of the viscous regularization parameter,  $\Gamma$  is done so that it has a negligible effect on the simulation results across the various cases considered in this work, while imparting numerical stability to our solution scheme. The value of the viscous regularization parameter for the framework at hand is also consistent with similar works in the literature (c.f. Narayan and Anand [212] and Miehe et al. [214]).

**Remark 6:** To mitigate the generation of large stresses due to the elastic (rather than elastic-viscoplastic) model employed here for Li-metal, we reduce the overall reaction-induced expansion associated with deposition of Li-metal within cracks. We assume a

30% expansion of Li-metal during electrodeposition in the  $\mathbf{m}_r$  direction. That is, we choose  $\Omega_{\text{Li}}\xi^{\text{max}} = 0.3$  and with  $\Omega_{\text{Li}} = 1.3 \cdot 10^{-5} \text{ m}^3/\text{mol}$  known experimentally (cf. Tantratian *et al.* [174]), we use  $\xi^{\text{max}} = 2.31 \cdot 10^4 \text{ mol/m}^3$  in our simulations. Theoretically, one should choose  $\Omega_{\text{Li}}\xi^{\text{max}} = 1$  (cf. Chen *et al.* [169]). We purposely use a smaller total expansion during electrodeposition to limit stress generation in Li-filaments. The value of  $\Omega_{\text{Li}}\xi^{\text{max}} = 0.3$  was calibrated to reproduce stresses within Li-filaments comparable to theoretical predictions based on linear elastic fracture mechanics models (cf. Klinsmann *et al.* [164]).  $\square$

The onset and evolution of the Li-metal filament with continuous fracture of the LLZO electrolyte is shown in Fig. 4.4. For completeness, we illustrate the evolution of all five fields in time, namely from top to bottom (a) the extent of electrodeposition  $\bar{\xi}$ , (b) the normalized concentration  $\bar{c}$ , (c) the electric potential  $\phi$ , (d) damage  $d$ , and (e) the horizontal stress component,  $\mathbf{T}_{xx}$ . Note that the first column of Fig. 4.4 shows the initial configuration of the Li-metal electrode-SSE assembly, where the domain is stress-free.

Starting with a small imperfection at the anode-electrolyte interface, we can observe the growth in time of the amplitude of the Li-metal filament relative to the flat electrode sides, Fig. 4.4(a). Fig. 4.4(b-c) illustrate the evolution in normalized concentration and electric potential. Critically, concentration of Li-ions remains unchanged in the bulk of the SSE, where the unaffected electrolyte (i.e.  $\bar{c} = \bar{c}_0$  where  $\bar{\xi} = 0$ ) preserves a state of electroneutrality. In contrast, significant concentration gradients arise at the Li-Metal/SSE interface, where Li-ions are continuously consumed to plate fresh layers of Li-metal. Owing to the much higher conductivity of the Li-metal electrode compared to the SSE, the electric potential across the freshly plated regions strictly follows the anode potential. These profiles are consistent with works in the literature invoking a similar phase-field framework to model the growth of Li-metal filaments across SSEs [58, 174].

Growth of a dominant Li-metal filament — in contrast to uniform plating of Li-metal — is attributed to localization of reaction kinetics at the tip of the protrusion, a phenom-

ena governed by both electro-chemical and mechanical forces. From an electro-chemical standpoint, growth of Li-metal filaments is directly related to the concentration of Li-ions and electric potential at the reaction site, as described by the reaction driving force,  $\mathcal{F}$  in

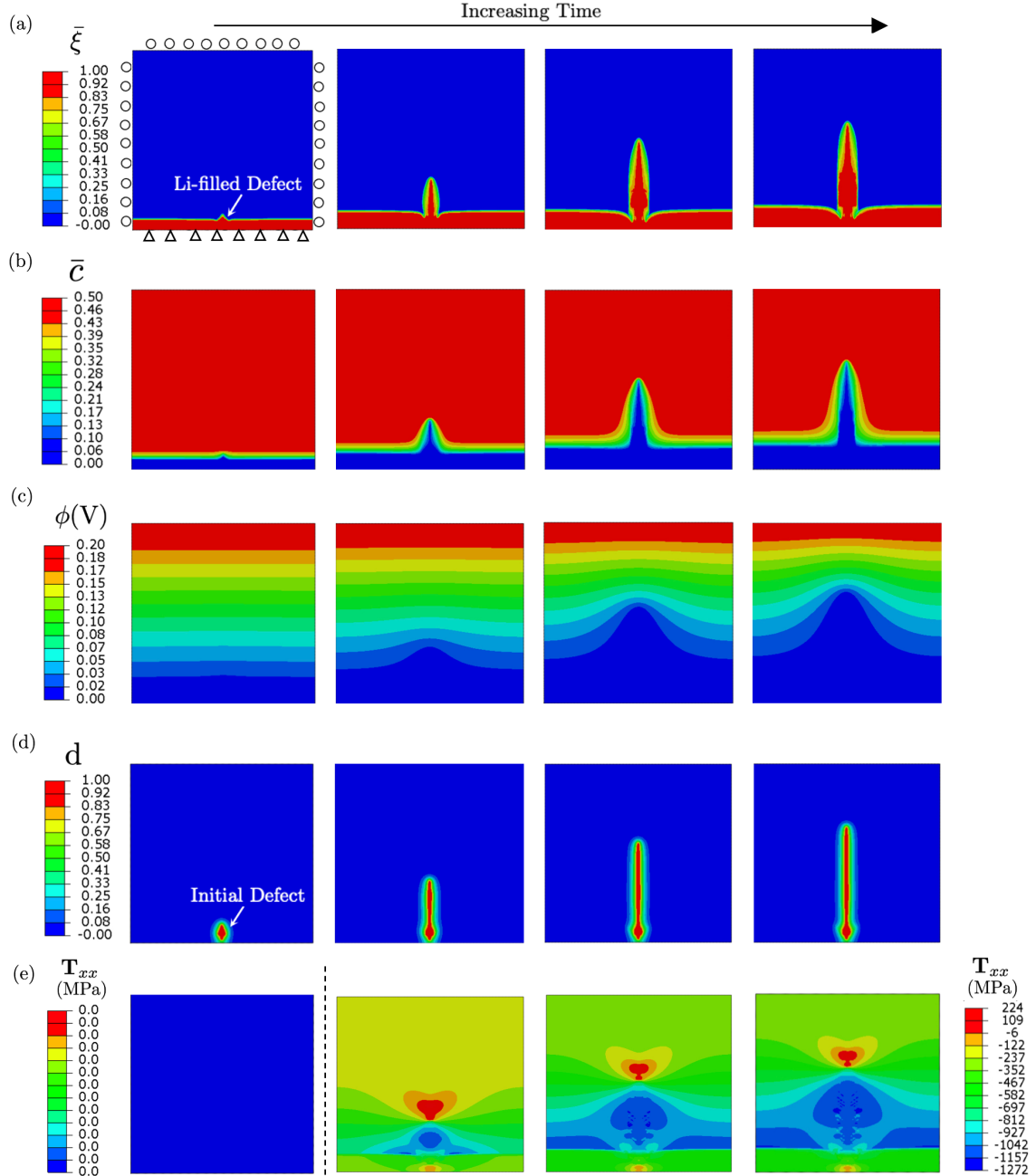


Figure 4.4: Evolution in time for (a) the extent of electrodeposition  $\bar{\xi}$ , (b) the normalized concentration  $\bar{c}$ , (c) the electric potential  $\phi(V)$ , (d) damage  $d$ , and (e) the horizontal stress component  $T_{xx}$ . The simulation is mechanically fully-constrained, with rollers present on the left and right edges. Reproduced with permission from [19].

(4.7.34). Fig. 4.4(b-c) illustrate the localization of larger concentration and electric potential gradients at the tip of the Li-metal filament, as it propagates from the metal anode towards the far electrolyte end. This results in an increase in driving force for electrodeposition, further localizing reaction kinetics and speeding up metal filament growth at these sites.

From a mechanical standpoint, Fig. 4.4(e) illustrates the evolution of the horizontal stress stress,  $\mathbf{T}_{xx}$  across the simulation domain. Li-metal deposition inside the crack induces a large build-up in normal stresses acting on the crack surfaces. Owing to the stiffer nature of the solid electrolyte, Li-metal confined on the crack interior undergoes large compressive stresses, which in turn retard electrodeposition at the crack edges through the mechanically coupled reaction driving force  $\mathcal{F}$  in (4.7.34). The reverse is true at the tip of the crack, where large tensile stresses develop as the crack sides expand to accommodate the deposition of new lithium. *Tensile stresses at the crack tip facilitate electrodeposition of Li-metal, further driving filament formation, and importantly inducing successive damage of the solid-state electrolyte.* As shown in Fig. 4.4(e), this state of stress is sustained as large tensile stresses drive crack propagation and in turn allow for further Li-metal plating inside the cracks, which sustains filament growth.

Finally, Fig. 4.4(d) illustrates the propagation of the electrodeposition-induced crack with simulation time. We emphasize that we do not predefine the crack path in our simulations. Instead, *cracks are free to evolve in any arbitrary orientation, driven by a thermodynamically consistent driving force* (4.7.42). Here, as there are no asymmetries in the simulation domain, the crack and subsequent Li-filament grow in a straight fashion from the anode through the electrolyte. The numerically simulated crack morphology is consistent with experimental observations of crack propagation in single-crystal SSE microstructures [20, 69, 73].

The importance of mechanical stress on the crack-electrodeposition interplay can be demonstrated by varying the degree of mechanical confinement to the solid-state archi-

ture. Fig. 4.5 shows an overlay of the isocontours of the damage field,  $d$  (black lines) and the reaction coordinate,  $\bar{\xi}$  (red lines) for both a simulation with (a - top row) left and right sides of the domain constrained, i.e. "laterally constrained", and (b - bottom row) laterally free sides. The simulation results are shown at three synchronized times denoted  $\{t_1, t_2, t_3\}$ . We note here that the laterally free simulation terminates at  $t_2$  when the crack reaches the top edge of the simulation domain, while the laterally constrained simulation continues.

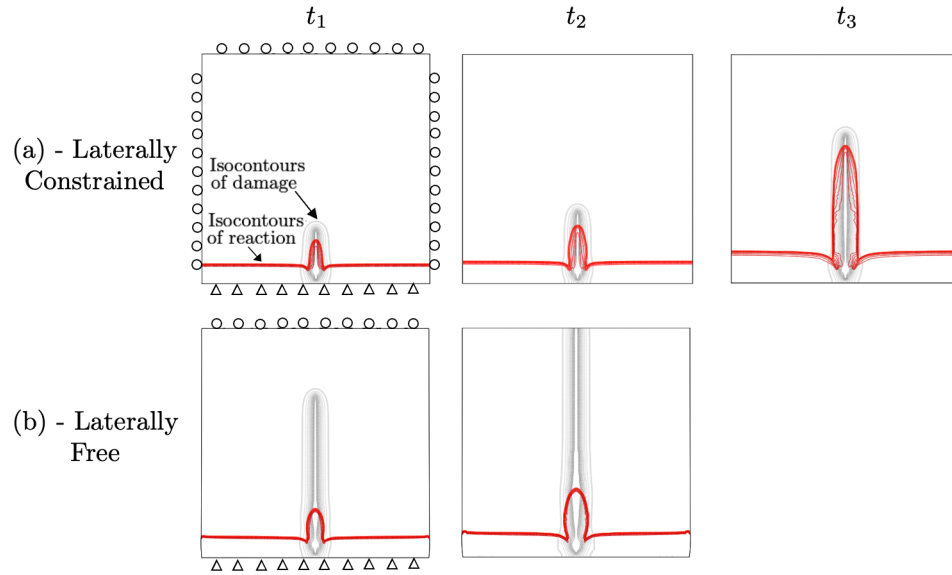


Figure 4.5: Evolution in time of the isocontours of damage  $d$  (black lines) and reaction coordinate  $\bar{\xi}$  (red lines) for (a - top row) a laterally constrained simulation, and (b - bottom row) a laterally free simulation. Comparing (a) and (b) demonstrates the critical role of mechanical confinement in dictating the degree to which the electrodeposition-induced crack becomes filled with Li-metal. Reproduced with permission from [19].

We can clearly observe a significant difference in the extent of the Li-metal plated crack when comparing the laterally constrained, Fig. 4.5(a), and laterally free, Fig. 4.5(b) simulations. In the laterally constrained case, the damage and extent of reaction fields evolve in a one-to-one fashion, with the crack remaining filled with Li-metal throughout. In contrast, *the laterally free simulation predicts that the electrodeposition-induced cracks propagate significantly ahead of the growing Li-metal filament*. In Fig. 4.5(b), we can observe the electrodeposition induced crack traversing the entire solid electrolyte domain,



while the Li-metal filament trails behind. These results are in good qualitative agreement with the experimental observations of Ning et al. [20] and Hao et al. [69], where in-situ X-ray tomography revealed the propensity for Li-metal filaments to sometimes only partially fill cracked regions of the SSE, with cracks traveling at a much faster rate to reach the opposite cathode end plenty in advance of Li-deposits.

Next, in Sect. 4.9.2, we demonstrate the manner in which microstructural features may be incorporated into our framework. Through this modeling, we elucidate the role of mechanics and damage on electrodeposition kinetics and resulting morphology of Li-metal filaments. Additionally, we demonstrate the utility of the framework by modeling the manner in which the morphology of Li-metal filaments changes for a LLZO microstructure depending on the relative fracture strength of the LLZO grains versus the grain boundaries.

#### 4.9.2 Modeling growth of Li-metal filaments in the presence of microstructure heterogeneity.

We present here a set of numerical simulations aimed to illustrate the manner in which grain boundaries may be modeled within the proposed framework. Through these simulations, we elucidate the role of mechanics and damage on electrodeposition kinetics and resulting morphology of Li-metal filaments as they grow across a LLZO electrolyte. In Sect. 4.9.1, we considered only a homogeneous LLZO electrolyte, naturally resulting in the growth of a straight Li-metal filament through the SSE.

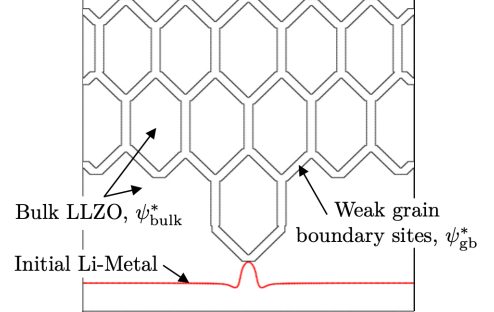


Figure 4.6: Schematic of the simulation domain highlighting elements chosen to represent grain boundaries in the LLZO solid-state electrolyte. Reproduced with permission from [19].

We consider here a simple representation of a polycrystalline LLZO microstructure as schematically illustrated in Fig. 4.6. The hexagonal pattern illustrated in Fig. 4.6 shows the elements within the simulation domain, which represent the grain boundaries. A character-

istic grain size of  $30\text{ }\mu\text{m}$  is chosen for the design, consistent with the experimental reports of Sato et al. [215] and Sharafi et al. [216]. These grain boundary elements represent weaker structural sites characterized by a lower fracture energy,  $\psi_{\text{gb}}^*$ , compared to the bulk SSE, which is characterized by a fracture energy,  $\psi_{\text{bulk}}^*$ . As such, grain boundaries are susceptible to damage and subsequent Li-metal electrodeposition [58]. All other mechanical properties are maintained the same for the entire simulation domain.

From an electro-chemical standpoint, we assume the grain boundaries to have the same electro-chemical properties (i.e. diffusivity, conductivity) as the grain bulk. This assumption is purposely chosen to enable us to investigate *purely the mechanical* effects of grain boundaries on electrodeposition kinetics and resulting Li-metal filaments morphology. As such, any effects sourcing from variation in electro-chemical properties between grain boundaries and the solid electrolyte bulk are neglected, although we note that these effects could also be incorporated in the theoretical framework presented. All material properties remain the same as those in Sect. 4.9.1 and listed in Table 3.1.

Boundary conditions are identical to the fully-constrained simulation described earlier in Sect. 4.9.1 and consistently here, an electrical potential,  $\phi = 0.2\text{ V}$  is applied to drive the system out of equilibrium. We employ a similar configuration for the Li anode-SSE interface and introduce a small Li-filled defect. With Fig. 4.6 in mind, we can observe that as crack and Li-metal filament grow across the SSE, they will eventually intersect with the mechanically weaker grain boundaries. At this point, Li-metal filaments can either propagate: i) intergranularly across the mechanically weaker grain boundaries, ii) transgranularly by fracturing the bulk LLZO and continuing to grow in a straight line, or iii) through a combination of both modes. The growth direction and resulting morphology of Li-filaments is dictated by the thermodynamic reaction driving force (4.7.34), which models the role of chemical, electrical and mechanical driving forces on Li-metal electrodeposition kinetics.

To illustrate the manner in which mechanics couples to electrodeposition kinetics, we perform a series of numerical simulations for the specific case of  $\psi_{\text{gb}}^* = (1/3) \cdot \psi_{\text{bulk}}^*$ .

To distinguish the two ways mechanics couples to electrodeposition, we consider first the reaction kinetics (4.7.38), which may be written as  $\dot{\bar{\xi}} = f_2(d)\hat{F}_1(\bar{\xi}, \mathcal{F})$ . This highlights the first mechanism being the logistic function,  $f_2(d)$  which directly couples the reaction kinetics to mechanical damage. As detailed in Sect. 4.7.5, the function,  $f_2(d)$  is introduced phenomenologically to restrict electrodeposition strictly within damaged regions across the SSE. Second, the electrodeposition driving force  $\mathcal{F}$  from (4.7.34) may be written as  $\mathcal{F} = \hat{F}_2(\bar{c}, \bar{\xi}, \phi) - J^c h(\bar{\xi}) \mathbf{M}^e : \mathbf{N}^r$ , where we now separate the stress-dependent term, which couples the reaction driving force to mechanical stresses.

Fig. 4.7(a) illustrates the fully-coupled simulation, where both mechanisms are active. We can observe the role of mechanically weaker grain boundaries in guiding the crack and subsequent growth of Li-metal filaments across the SSE. As shown in Fig. 4.7(a), Li-metal filaments growth remains almost entirely confined within the damaged grain-boundaries, with a small vertical crack within the first grain appearing, but failing to continue to grow.

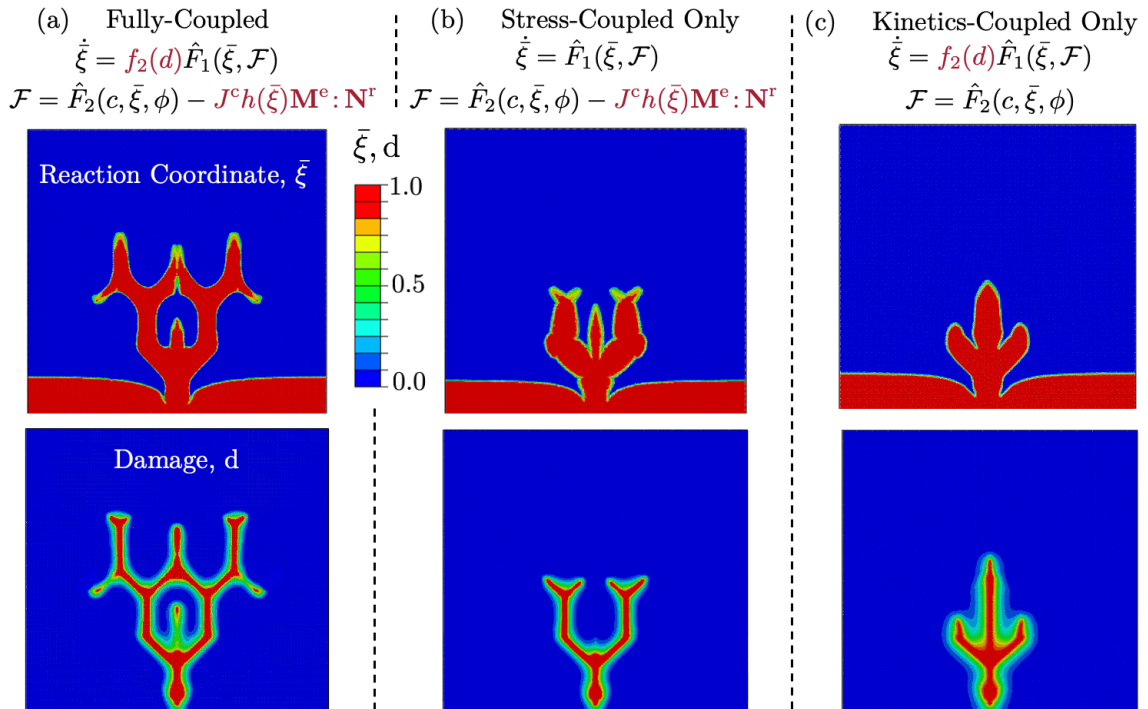


Figure 4.7: Contours of reaction coordinate  $\bar{\xi}$  (top row) and damage  $d$  (bottom row) for (a) a fully-coupled simulation, (b) a stress-coupled only simulation, and (c) a kinetics-coupled only simulation. Reproduced with permission from [19].

Fig. 4.7(b) shows a numerical simulation in which the logistic function,  $f_2(d)$  is removed, and direct coupling of electrodeposition kinetics to damage *is suppressed*. The only coupling between mechanics and electrodeposition is through the stress-coupled reaction driving force  $\mathcal{F}$ . Importantly, we can observe that even in the absence of a restriction preventing plating outside of cracks, *Li-metal filaments propagate primarily in cracked regions due solely to the stress-state within the cracks creating a favorable reaction driving force*. Consistent with the results in Fig. 4.7(a), we observe the tendency for Li-metal to preferentially deposit across the mechanically weaker grain boundaries, even though a concurrent transgranular branch forms in this case. This result illustrates that the presence of the logistic function,  $f_2(d)$  in (4.7.38) does not significantly alter the resultant morphology of Li-metal filaments across the SSE microstructure.

Finally, Fig. 4.7(c) illustrates the reverse coupling, where the stress-coupling of the reaction driving force  $\mathcal{F}$  *is suppressed*, while the reaction kinetics remain coupled to damage through the function  $f_2(d)$ . In Fig. 4.7(c), we observe an entirely different pattern of crack propagation and Li-metal deposition across the SSE. In contrast to simulation results with active stress-coupling, Figs. 4.7(a,b), in which cracks and Li-metal filaments predominantly evolve across the weaker grain boundaries, *the simulation with no stress-coupling predicts cracks and Li-metal filaments to grow primarily in a transgranular fashion*. That is, *in the absence of a stress-coupled reaction driving force  $\mathcal{F}$ , the presence of weak grain boundaries is virtually unseen by the electrodeposition kinetics*. This difference in pattern is expected, granted in the absence of stress-coupling, electrodeposition kinetics is dictated by purely electrochemical forces. As discussed in Sect. 4.9.1, localization of higher concentration and electric potential gradients at the tip of the straight Li-metal branch compared to the slanted grain boundaries favors reaction and speeds up the growth of a dominant vertical Li-metal filament across the SSE.

These results highlight the importance of coupling the electrodeposition driving force,  $\mathcal{F}$  to mechanical stress. Importantly, mechanical stresses in the presence of microstructural

heterogeneities (i.e. grain boundaries, pores etc.) can significantly alter the morphological evolution of cracks and Li-metal filaments across the SSE. Such coupling has also been shown experimentally [58, 59, 217] and is reproduced here through the proposed theoretical framework.

Having discussed the manner in which mechanics couples to electrodeposition kinetics, we now turn our attention to the role of microstructure composition, specifically the role of grain boundaries with varying fracture energy. We consider a range of grain boundary fracture energies,  $\psi_{\text{gb}}^*$ , relative to the bulk solid electrolyte fracture energy,  $\psi_{\text{bulk}}^*$ , to explore the manner in which microstructural features with varying mechanical properties alter the growth morphology of cracks and Li-metal filaments across the SSE.

Fig. 4.8 shows contours of reaction coordinate (top row) and damage (bottom row) for simulations with (a)  $\psi_{\text{gb}}^* = (1/5) \cdot \psi_{\text{bulk}}^*$ , (b)  $\psi_{\text{gb}}^* = (1/3) \cdot \psi_{\text{bulk}}^*$ , and  $\psi_{\text{gb}}^* = (1/2) \cdot \psi_{\text{bulk}}^*$ . Note that all these simulations are fully-coupled, and thus the result in Fig. 4.8(b) is identical to that in Fig. 4.7(a).

For both cases with  $\psi_{\text{gb}}^* = (1/5) \cdot \psi_{\text{bulk}}^*$  and  $\psi_{\text{gb}}^* = (1/3) \cdot \psi_{\text{bulk}}^*$ , Figs. 4.8(a,b), we can observe the role of weaker grain boundaries in guiding Li-metal to preferentially deposit at these sites. Owing to their lower fracture energy, grain boundaries are easier to damage compared to the bulk SSE. This creates a favorable stress-state within the fractured grain boundaries, making it favorable for growth of Li-metal filaments to follow the grain boundary network, suppressing the growth of a vertical transgranular crack and Li-metal branch. These results are consistent with experimental observations, which report Li-metal filaments to preferentially grow along the grain boundaries (i.e. intergranularly) in a polycrystalline LLZO electrolyte [58, 59].

With increase in fracture energy of the grain boundaries relative to the bulk SSE,  $\psi_{\text{gb}}^* = (1/2) \cdot \psi_{\text{bulk}}^*$  in Fig. 4.8(c), we observe a change in the resulting crack and Li-metal filament morphology. We observe now the formation of a distinct vertical transgranular branch propagating through the SSE in advance of concurrent Li-metal growth proceeding

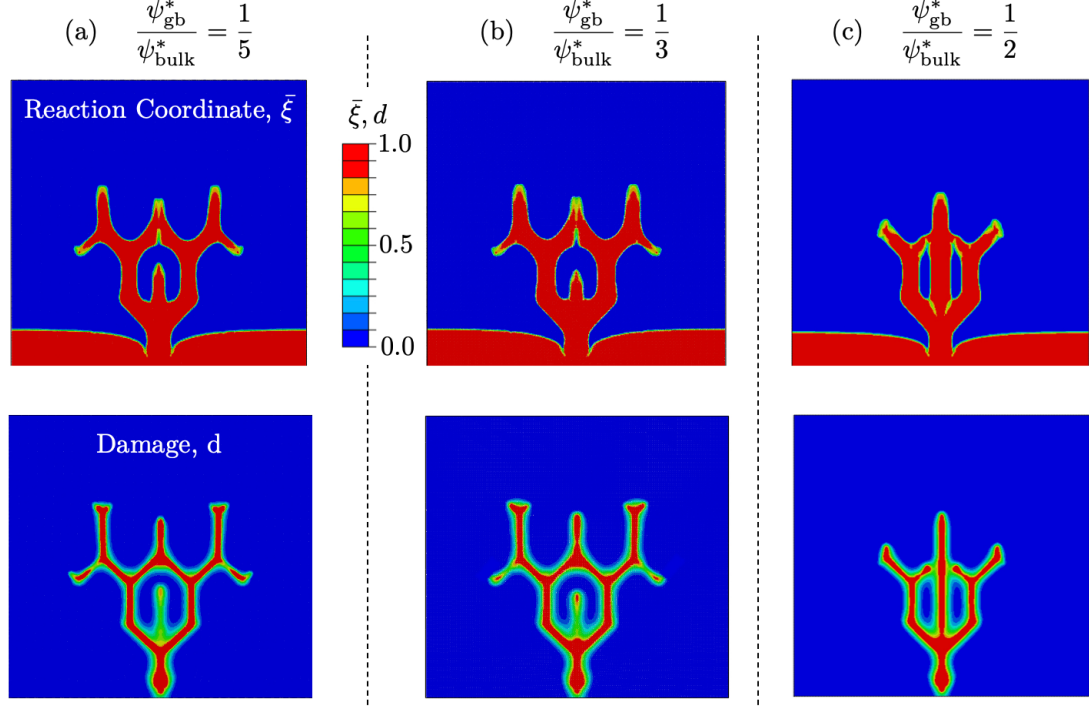


Figure 4.8: Contours of reaction coordinate  $\bar{\xi}$  (top row) and damage  $d$  (bottom row) with varying grain boundary fracture energies, respectively (a)  $\psi_{\text{gb}}^* = (1/5) \cdot \psi_{\text{bulk}}^*$ , (b)  $\psi_{\text{gb}}^* = (1/3) \cdot \psi_{\text{bulk}}^*$ , and (c)  $\psi_{\text{gb}}^* = (1/2) \cdot \psi_{\text{bulk}}^*$ . Reproduced with permission from [19].

across the grain boundaries. As the fracture energy of the grain boundaries increases closer to that of the electrolyte bulk, fracturing these sites becomes more difficult, and transgranular growth becomes preferable. This result suggests there exists a threshold fracture energy ratio, where the electrochemical driving force overcomes the weak grain boundaries and the growth morphology of Li-metal filaments transitions from primarily intergranular to primarily transgranular. Clearly, the limiting case of  $\psi_{\text{gb}}^* = \psi_{\text{bulk}}^*$  is identical to the simulation results shown in Fig. 4.4 and produces a single vertical Li-filament.

At present, a microstructure description of the process of Li-metal filament growth across SSEs is missing and necessary. The theoretical framework summarized and specialized in Sects. 4.6 and 4.7 alongside numerical simulations presented here show the first framework capable of predicting the resulting morphology of Li-metal filaments for a given SSE architecture, including a transition from primarily intergranular to primarily transgranular filament growth.

#### 4.10 Concluding Remarks

We have formulated and numerically implemented a thermodynamically-consistent electro-chemo-mechanical gradient theory, which couples electrochemical reactions with mechanical deformation and damage in solids. The framework models transport of ionic species across the solid host under diffusion/migration mechanisms and concurrent electrochemical reaction at cracks across the solid host, where ionic species are reduced to deposit a new compound. Critically, the theory captures the interplay between growth-induced fracture of the solid host and electrodeposition of a new material inside cracks by tracking the damage and extent of electrodeposition using separate phase-field variables.

While the framework is general in nature, a specialization towards modeling of Li-metal filament growth across SSEs for application in all-solid-state batteries is demonstrated. In particular, we elucidate the coupling of electrical, chemical, and mechanical processes, which govern the growth of Li-metal filaments across SSEs with and without account for microstructure heterogeneity. Consistent with experiments, we demonstrate the ability of the framework to numerically reproduce both transgranular and intergranular growth of metal protrusions across the SSE microstructure.

Major contributions of the proposed framework include:

- The framework enables for modeling concurrent diffusion, reaction, deformation and damage in solids. Importantly, the theory extends the current literature in continuum mechanics to model solids undergoing electrochemical reactions, which are intricately coupled to damage of the underlying solid host.

The interplay between electrodeposition of new material inside damaged (fractured) regions is modeled. Consistent with experiments, electrodeposition is restricted within damaged regions across the solid conductor, which supply the necessary vacant space for accommodating a new material. This feature provides an extension to current electro-chemo-mechanical phase-field formulations in the literature, which

do not model growth-induced fracture of SSE due to Li-deposition and indistinguishably allow for Li-metal plating across the host.

- The thermodynamically-consistent treatment enables for derivation of a physically motivated reaction driving force in which different contributions of energy, configuration entropy, electrostatics, mechanical deformations and damage can be readily identified. Particularly useful then is the fact that material properties driving the electrodeposition kinetics can be calibrated from the literature or experiments.
- The framework elucidates the role of mechanical confinement on the crack vs. electrodeposition morphology. Under specific mechanical boundary conditions, we numerically reproduce the presence of cracks, which are only partially filled with Li-metal.
- Finally, we demonstrate the role of microstructural heterogeneities, in particular grain boundaries, in dictating the morphology of cracks and Li-metal filaments across the SSE microstructure. Both transgranular and intergranular growth mechanisms are numerically reproduced consistent with experiments, elucidating the critical role of mechanics on electrodeposition kinetics and the resulting morphology of Li-metal filaments across the SSE.

Growth of Li-metal filaments across SSEs constitutes a critical degradation mechanism, hindering commercialization of next-generation all-solid-state batteries. It is thus critical, from both an experimental and modeling perspective, to understand the interplay between non-uniform electrodeposition kinetics and the SSE microstructure composition. In particular, the manner in which size and distribution of defects and microstructural heterogeneities ultimately govern the growth of Li-metal filaments. The proposed framework, in conjunction with experiments, enhances our current understanding of the electro-chemo-mechanical processes, which govern the initiation and growth of Li-metal filaments across SSEs. From a design standpoint, the proposed framework provides then a utilitarian numer-



ical tool, which can help elucidate new strategies to mitigate growth of Li-metal filaments and enable for successful commercialization of all-solid-state batteries.

## CHAPTER 5

### CONCLUSION

#### 5.1 Summary

Development of high-fidelity numerical simulations for design and optimization of next-generation all-solid-state batteries (aSSBs) is of critical importance towards their successful commercialization to meet increasing energy demands. While an extensive body of experimental literature, reporting on the numerous degradation mechanisms in solid-state architectures exists, understanding the intricate coupling between electrochemical and mechanical phenomena from a modeling perspective remains a topic of active research. In this thesis, we address this limitation and develop a series of numerical frameworks, which model the governing electro-chemo-mechanical processes coupled with fracture across the different constituents in aSSBs to assess their role on longevity and reliability of aSSBs. In particular, the developed electro-chemo-mechanical frameworks elucidate the degradation mechanisms in two critical constituents of aSSBs, namely (i) composite electrodes and (ii) solid-state electrolyte due to growth of Li-metal filaments. To conclude, we summarize here major contributions associated with each part of the thesis:

**Part I:** Modeling chemo-mechanical multi-particle interactions in composite electrodes for LIBs.

- Formulated and numerically implemented a theoretical framework based on use of chemo-mechanical surface elements for modeling the stress-coupled chemo-mechanical interactions in complex electrode designs under galvanostatic charging. In particular, the theoretical framework allows one to capture both chemical and mechanical interactions between active particles in battery electrodes under galvanostatic charging conditions. Importantly, the developed framework captures chemical interactions

between particles, whereby current is non-uniformly distributed between active particles based on their local stress-coupled interface reaction kinetics.

- Mechanically, the developed surface elements allow one to capture the role of mechanical interfacial damage on electrochemical performance by coupling interfacial reaction kinetics to mechanical damage. This in turn enables for quantifying how loss of mechanical integrity at the interface limits reaction kinetics and overall electrochemical performance of the electrode.
- Using the developed simulation capability, we investigated the chemo-mechanical behavior of novel LIB electrode designs composed of hollow a-Si nanotubes. Electrode capacity loss due to interfacial decohesion (i.e mechanical degradation) was quantified by performing a series of charge/discharge cycles at varying C-rates. In doing so, we demonstrated the manner in which the proposed theoretical framework can be used to capture mechanically induced electrochemical capacity loss over a number of different charging cycles, consistent with experiments.

**Part II:** Modeling of electro-chemo-mechanical behavior coupled with damage of composite electrodes for all-solid-state batteries.

- Leveraging the simulation capability developed in Part I, chemo-mechanical behavior and electrochemical performance of a  $\text{LiCoO}_2\text{-Li}_{10}\text{GeP}_2\text{S}_{12}$  composite cathode for all-solid-state batteries was investigated. A key focus here involved understanding the role of microstructure on the state of mechanics and integrity of interfaces, in turn impacting the overall electrochemical performance. First, we studied the role of variations in chemo-mechanical properties of the composite electrode of choice, with a focus on SSE stiffness and volumetric contraction of active material upon lithiation. Second, we investigated the role of two critical microstructural features: i) the size and size distribution of active particles, and ii) the active material volume fraction (i.e. packing density).

- Variations in SSE stiffness and active material contraction during lithiation were demonstrated to significantly impact the electrochemical performance of SSB cathodes, limiting attainable capacity in the presence of mechanical interfacial delamination. From a design standpoint, the developed theoretical framework thus provides a utilitarian tool for future exploration of manufacturing of composite electrodes with different active material-SSE pairs to enhance mechanical integrity and concurrently electrochemical performance.
- With respect to microstructural composition, particle size distribution was demonstrated to have a negligible effect on the stress build-up and potential for delamination at the active particle-SSE interface. This finding was demonstrated both through simple single-particle RVEs and through complex multi-particle RVEs with different particle size statistics.
- Importantly, active material volume fraction, commensurate with packing density, was shown to dictate the build-up of interfacial stress at the active particles surface, in turn controlling the onset and evolution of mechanical interfacial degradation. While increasing the active material volume fraction naturally increases the capacity of the LCO-LGPS cathode under consideration, these gains can be quickly undermined by the exacerbation in state of interfacial delamination experienced across the electrode microstructure. The proposed theoretical framework can thus serve as a useful tool towards design of complex novel SSB cathode architectures for future applications.

**Part III:** A novel electro-chemo-mechanical framework coupled with fracture for modeling of Li-filament growth in solid-state batteries.

- Formulated a thermodynamically-consistent electro-chemo-mechanical gradient theory, which couples electrochemical reactions with mechanical deformation and damage in solids. The framework models transport of ionic species across the solid host under diffusion/migration mechanisms and concurrent electrochemical reaction at

cracks across the solid host, where ionic species are reduced to deposit a new compound. Critically, the theory captures the interplay between reaction-induced fracture of the solid host and electrodeposition of a new material inside cracks by tracking the damage and extent of electrodeposition using separate phase-field variables.

- The thermodynamically-consistent treatment enables for derivation of a physically motivated reaction driving force in which different contributions of energy, configuration entropy, electrostatics, mechanical deformations and damage can be readily identified. Particularly useful then is the fact that material properties driving the electrodeposition kinetics can be calibrated from the literature or experiments.
- The framework elucidates the role of mechanical confinement on the crack vs. electrodeposition morphology. Under specific mechanical boundary conditions, the capacity of the framework to numerically reproduce propagation of cracks partially filled with Li-metal was demonstrated, consistent with experiments.
- Finally, we demonstrated the role of microstructural heterogeneities, in particular grain boundaries, in dictating the morphology of cracks and Li-metal filaments across the SSE microstructure. Both transgranular and intergranular growth mechanisms were numerically reproduced consistent with experiments, elucidating the critical role of mechanics on electrodeposition kinetics and the resulting morphology of Li-metal filaments across the SSE.

## 5.2 Outlook

While progress has been made in this thesis towards modeling of the coupled electro-chemo-mechanical processes in all-solid-state batteries, much remains to be done. Below, we list potential directions for future work which have not been addressed in this thesis:

Outlook on modeling composite electrodes for all-solid-state batteries

- In its current form, the framework developed in chapter 2 does not account for transport of ionic species across the solid conductor to reach the active material-SSE interface. Instead, an underlying assumption of fast ionic transport across the solid electrolyte is invoked, translated numerically to a uniform constant chemical potential across the nodes at the interface in contact with the solid-electrolyte matrix. With increase in active material (i.e. packing density), aside from an increase in the role of mechanics on integrity of active particle-SSE interface, additional complexities such as blockage of ionic transport pathways arise. Blockage of ionic transport pathways can in turn potentially limit utilization of active material available for reaction, localizing reaction kinetics near the cathode-separator interface. Thus, a fundamental understanding of the coupled role of electrode microstructural stochasticity and the spatio-temporal electrochemical-transport dynamics on the active material utilization is required.
- Owing to the stiff nature of all-solid-state batteries, mechanical integrity of the interface constitutes merely one of three critical mechanisms through which fracture limits performance in composite electrodes. Equally important here is development of an appropriate numerical framework which enables for modeling fracture at the i) bulk of active particles as they undergo swelling/contraction with Li-insertion/extraction and ii) bulk of the solid conductor in response to any chemically induced deformations associated with transport of ionic species or due to deformation of active particles embedded in it. In developing these models, consideration must accordingly be paid to the underlying microstructure of both the active material and solid ionic conductor to numerically resolve the presence of grain boundaries (in the case of polycrystalline active materials or SSE), inherently existing pores etc. At present, a unified cohesive phase-field formulation which concurrently accounts for damage mechanisms at the active material-SSE interface, active particle bulk as well as bulk of the solid ionic conductor is missing. Development of a unified framework

is critical and would enable for elucidating which, if any of the three underlying damage mechanisms, critically dictates electrochemical performance of composite electrodes.

- Towards design optimization of composite electrodes for improved performance, numerical simulation of high-resolution experimentally resolved composite microstructures is critical. Nevertheless, this aspect significantly increases computational requirements and time. Towards this goal, development of deep-learning—AI models, which can connect continuum simulations into a physics-based data-driven multi-scale model are of particular interest and have attracted significant attention as a tool for rapid material design [218]. Through the proposed deep-learning model, data generated in predictive continuum simulations in the form of consecutive images can be used to train a deep neural network, which allows then to make computationally efficient predictions. As an example, use of deep-learning paradigms based on processing of consecutive images as time sequences leveraging ConvLSTM convolutional networks has been demonstrated with great success in predicting i) fracture patterns in crystalline solids from atomistic simulations [218] and ii) complex mechanical stress states in hierarchical composites for material design [219]. Successfully adopting a scalable machine-learning model could enable for fast predictions of microstructure evolution with electro-chemical cycling of more complex electrode architectures composed of hundreds of particles, while bypassing the need for complex, computationally-intensive simulations.

#### Outlook on modeling of growth of Li-metal filament across solid-state electrolytes

- Continuous deposition of Li-metal inside defects induces large compressive stresses, which in turn can cause Li-metal to flow plastically. While the role of plastic flow on propagation of Li-metal filaments across SSEs is a topic of active research, an elastic-viscoplastic extension of the framework is a critical ingredient in modeling

the morphological evolution of voids with continuous plating/stripping for nucleation of Li-metal filaments at the anode-SSE interface. Due to the viscoplastic nature of Li-metal, plastic deformation and creep become relevant at sufficiently high pressures and can act to close the voids, reducing contact loss at the anode-SSE interface. Reducing contact loss could then mitigate the propensity for Li-metal filaments growth.

- In line with the scope of the framework targeting propagation of Li-metal filaments across the solid-state electrolyte, at this stage we purposely specialize the framework to model only forward reaction, i.e. Li-metal deposition. Nevertheless, we emphasize here that the proposed framework, through the employed Butler-Volmer reaction kinetics and the thermodynamically-consistent electrodeposition driving force enables for modeling both plating and stripping processes. Numerically investigating the effect of electrochemical cycling becomes critical during the nucleation stage in modeling the evolution of the Li-metal anode-SSE interface with the potential for void formation, and constitutes an important aspect left to future explorations.
- From a design standpoint, it is important to explore different mechanisms through which one can tailor the solid electrolyte microstructure composition to prevent Li-filament growth. In this context, a natural extension and utilitarian study leveraging the proposed framework includes an understanding of the role of stiff mechanical inclusions as a potential mechanism for hindering Li-filament growth with fracture of the solid electrolyte. Key to investigations of this nature is determination of an optimal inclusion size and percent infill such that one effectively limits dendrite growth, without significantly limiting transport pathways.



# **Appendices**

## APPENDIX A

### DETAILS ON THE NUMERICAL IMPLEMENTATION OF CHEMO-MECHANICAL SURFACE ELEMENTS

We present here details of the numerical implementation of the constitutive model for the chemo-mechanical surface elements described in chapter 2. In Sect. A.1, we first introduce the variational formulation of the surface elements, followed by specialization for a 2D quadrilateral element in Sect. A.2.

#### A.1 Variational Formulation

We present here details on the variational formulation of the proposed surface elements. Note that although our surface elements are *chemo-mechanical* in nature, we present here only the variational formulation for the chemical counterpart of the elements, responsible for modeling of the non-linear reaction kinetics at the interface. The variational formulation for the mechanical portion is standard in the literature, and the reader is referred to the works of Park and Paulino [220] and Camanho and Davila [127] for further details.

We choose the chemical potential,  $\mu$  as the degree of freedom governing mass balance. The strong form of the local species mass balance, supplemented with appropriate boundary conditions is then given by,

$$\text{Mass Balance} = \begin{cases} \dot{c}_R = -J \text{div} \mathbf{j}, & \text{in } \mathcal{B}, \\ \mu = \tilde{\mu}, & \text{on } \mathcal{S}_\mu, \\ -m \text{grad} \mu \cdot \mathbf{n} = \tilde{j}, & \text{on } \mathcal{S}_j, \end{cases} \quad (\text{A.1.1})$$

where  $\mathcal{B}$  denotes the body in the deformed configuration, while  $\mathcal{S}_\mu$  and  $\mathcal{S}_j$  are complementary subsurfaces of the boundary  $\partial\mathcal{B}$  of the body  $\mathcal{B}$  in the sense that  $\partial\mathcal{B} = \mathcal{S}_\mu \cup \mathcal{S}_j$  and

$$\mathcal{S}_\mu \cap \mathcal{S}_j = \emptyset.$$

Let  $w$  be a virtual variation in chemical potential,  $\mu$  such that the variation  $w$  *vanishes* on  $\mathcal{S}_\mu$ . The weak form corresponding to Eqns. (A.1.1) is obtained by multiplying Eqn. (A.1.1)<sub>1</sub> by  $w$  and integrating, which yields

$$\int_{\mathcal{B}} w \dot{c}_R(\mathbf{J}^{-1}) dv - \int_{\mathcal{B}} w \operatorname{div}(m \operatorname{grad} \mu) dv = 0 \quad (\text{A.1.2})$$

where the “grad” and “div” operators are with respect to the current configuration, and in writing (A.1.2) we have used the constitutive equation  $\mathbf{j} = -m \operatorname{grad} \mu$ . Application of the divergence theorem to the second term in (A.1.2) leads to

$$\int_{\mathcal{B}} w \operatorname{div}(m \operatorname{grad} \mu) dv = \int_{\partial \mathcal{B}} w(m \operatorname{grad} \mu) \cdot \mathbf{n} da - \int_{\mathcal{B}} (m \operatorname{grad} \mu) \cdot \operatorname{grad} w dv. \quad (\text{A.1.3})$$

Use of (A.1.3) in (A.1.2), gives

$$\int_{\mathcal{B}} w \dot{c}_R(\mathbf{J}^{-1}) dv + \int_{\mathcal{B}} (m \operatorname{grad} \mu) \cdot \operatorname{grad} w dv - \int_{\partial \mathcal{B}} w(m \operatorname{grad} \mu) \cdot \mathbf{n} da = 0 \quad (\text{A.1.4})$$

We now consider the body  $\mathcal{B}$  to be composed of two sub-domains, namely  $\mathcal{B}^+$  and  $\mathcal{B}^-$ , separated by an interface  $\mathcal{I}$ , as illustrated in Fig. A.1. Application of (A.1.4) individually to  $\mathcal{B}^+$  and  $\mathcal{B}^-$  then yields

$$\int_{\mathcal{B}^+} w \dot{c}_R(\mathbf{J}^{-1}) dv + \int_{\mathcal{B}^+} (m \operatorname{grad} \mu) \cdot \operatorname{grad} w dv - \int_{\partial \mathcal{B}^+} w(m \operatorname{grad} \mu) \cdot \mathbf{n} da - \int_{\mathcal{I}^+} (\mathbf{j}^+ \cdot \mathbf{n}^+) w^+ da = 0 \quad (\text{A.1.5})$$

$$\int_{\mathcal{B}^-} w \dot{c}_R(\mathbf{J}^{-1}) dv + \int_{\mathcal{B}^-} (m \operatorname{grad} \mu) \cdot \operatorname{grad} w dv - \int_{\partial \mathcal{B}^-} w(m \operatorname{grad} \mu) \cdot \mathbf{n} da - \int_{\mathcal{I}^-} (\mathbf{j}^- \cdot \mathbf{n}^-) w^- da = 0 \quad (\text{A.1.6})$$

The unit normal,  $\mathbf{n}^+$  to the surface  $\mathcal{I}^+$  points from  $\mathcal{B}^+$  to  $\mathcal{B}^-$ , while  $\mathbf{n}^-$ , the unit normal to

$\mathcal{I}^-$  points from  $\mathcal{B}^-$  to  $\mathcal{B}^+$ , and for notational convenience we introduce  $\mathbf{n}^- = -\mathbf{n}^+ = \bar{\mathbf{n}}$ . Equivalently, the interface flux  $\mathbf{j}^\pm$  represents species flux across the interface from one side to the other along the  $\mathbf{n}^\pm$  directions.

Making use of  $\mathcal{B} = \mathcal{B}^+ \cup \mathcal{B}^-$ ,  $\partial\mathcal{B} = \partial\mathcal{B}^+ \cup \partial\mathcal{B}^-$ ,  $\mathcal{I}^+ = \mathcal{I}^-$  and the continuity condition,  $\mathbf{j}^+ \cdot \mathbf{n}^+ = -\mathbf{j}^- \cdot \mathbf{n}^- \equiv j_{cz}$  at the interface, we may combine (A.1.5) and (A.1.6) to yield

$$\int_{\mathcal{B}} w \dot{c}_R(\mathbf{J}^{-1}) dv + \int_{\mathcal{B}} (m \text{grad} \mu) \cdot \text{grad} w dv - \int_{\partial\mathcal{B}} w (m \text{grad} \mu) \cdot \mathbf{n} da + \int_{\mathcal{I}} j_{cz} [[w]] da = 0 \quad (\text{A.1.7})$$

where  $[[w]] = w^+ - w^-$  denotes the jump in virtual chemical potential at the interface.

Introducing the boundary condition (A.1.1)<sub>3</sub>, noting that  $w$  vanishes on  $\mathcal{S}_\mu$ , we may finally write (A.1.7) as

$$\int_{\mathcal{B}} w \dot{c}_R(\mathbf{J}^{-1}) dv + \int_{\mathcal{B}} (m \text{grad} \mu) \cdot \text{grad} w dv + \int_{\partial\mathcal{S}_j} w \tilde{j} da + \int_{\mathcal{I}} j_{cz} [[w]] da = 0. \quad (\text{A.1.8})$$

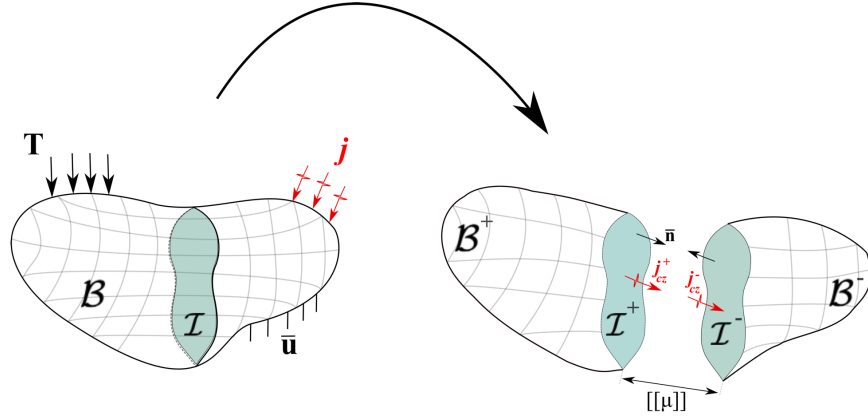


Figure A.1: Schematic illustration of the cohesive interface for numerical implementation of galvanostatic charging conditions. Reproduced with permission from [17].

The terms in (A.1.8) fall under the following categories. The first three terms in (A.1.8) arise from the conventional mass balance across a body  $\mathcal{B}$  without a cohesive interface. In turn, the last term denotes the *contribution from the presence of an interface*. In simulating

a body with an interface such as the one shown in Fig. A.1, the first three terms in (A.1.8) are implemented through traditional continuum elements, which discretize the parts  $\mathcal{B}^+$  and  $\mathcal{B}^-$ , while the last term is implemented through the proposed *surface elements*, which discretize the interface  $\mathcal{I}$ . The implementation of bulk continuum chemo-mechanical elements is discussed in detail in Di Leo et al. [129] and Chester et al. [130]. We thus focus the remainder of our discussion on the last term in (A.1.8), which is implemented through use of surface elements. This entails thus a constitutive law between the flux of chemical species at the interface,  $j_{cz}$  and a jump in the chemical potential  $[[\mu]]$ , modeled under Butler-Volmer interface kinetics as outlined in (A.1.14).

From a finite-element modeling standpoint, evaluation of the consistent residual and tangent stiffness for the chemical counterpart of the theory is then similar to conventional numerical implementation of mechanical cohesive elements reported in [220] and will be briefly summarized here for convenience. We outline the numerical implementation in detail, specializing for a 2D quadrilateral element in Sect. A.2.

In a finite element framework, one can compute the vector of nodal jumps in chemical potential at the interface of surface elements,  $\tilde{\Delta}\boldsymbol{\mu}$  (i.e.  $\tilde{\Delta}\mu^{(1)}, \tilde{\Delta}\mu^{(2)}$  - c.f Fig. A.2) from the vector of nodal chemical potentials,  $\boldsymbol{\mu}$  (c.f Fig. A.2) making use of the following relationship in matrix form

$$\tilde{\Delta}\boldsymbol{\mu} = \mathbf{L}\boldsymbol{\mu} \quad (\text{A.1.9})$$

Analogous to formulation of the mechanical cohesive element, here  $\mathbf{L}$  defines a local separation matrix. It relates the nodal jumps in chemical potential at the interface to nodal chemical potentials of the surface elements [220].

In conjunction with the shape function matrix  $\mathbf{N}$  (c.f (A.2.5)), local jump in chemical potential anywhere along the cohesive interface,  $\Delta\mu$  is interpolated from the nodal chemical potential jumps at the interface of the surface elements,  $\tilde{\Delta}\boldsymbol{\mu}$

$$\Delta\mu = \mathbf{N}\tilde{\Delta}\boldsymbol{\mu} \quad (\text{A.1.10})$$

Combining (A.1.9) and (A.1.10), one obtains the relationship between the jump in chemical potential along the cohesive interface and the nodal chemical potentials of the surface elements,

$$\Delta\mu = \mathbf{B}\boldsymbol{\mu} \quad \text{with} \quad \mathbf{B} = \mathbf{N}\mathbf{L} \quad (\text{A.1.11})$$

Similarly here,  $\mathbf{B}$  defines a matrix analogous to global displacement-separation relation matrix for the conventional mechanical cohesive element [220].

Element level residual,  $\mathbf{R}_\mu^{\text{coh}}$ , and tangent stiffness,  $\mathbf{K}_{\mu\mu}^{\text{coh}}$ , for the surface elements can then be computed as follows,

$$\mathbf{R}_\mu^{\text{coh}} = \int_{\mathcal{I}} \mathbf{B}^T j_{cz} da \quad (\text{A.1.12})$$

$$\mathbf{K}_{\mu\mu}^{\text{coh}} = -\frac{\partial \mathbf{R}_\mu^{\text{coh}}}{\partial \boldsymbol{\mu}} = -\int_{\mathcal{I}} \mathbf{B}^T \frac{\partial j_{cz}}{\partial(\Delta\mu)} \frac{\partial(\Delta\mu)}{\partial \boldsymbol{\mu}} da = -\int_{\mathcal{I}} \mathbf{B}^T \frac{\partial j_{cz}}{\partial(\Delta\mu)} \mathbf{B} da \quad (\text{A.1.13})$$

where flux of ionic species at the interface,  $j_{cz}$  is computed as a function of the jump in chemical potential,  $\Delta\mu$  using Butler-Volmer kinetics

$$j_{cz} = -\frac{i}{F} = -2\frac{i_0}{F} \sinh\left(\frac{1}{2} \frac{\Delta\mu}{R\vartheta}\right) \quad (\text{A.1.14})$$

## A.2 Numerical Solution Methodology

We implement our theory for modeling of multi-particle interactions in composite electrodes and develop a chemo-mechanical surface user-element (UEL) for ABAQUS/Standard finite element package. This section outlines the numerical implementation procedure, specializing on a 2D-quadrilateral element with three degrees of freedom  $(u_1, u_2, \mu)$  active at each node.

At the initiation of each solution step, the user has access to nodal coordinates (COORDS) and updated global degrees of freedom (U), while all specifications regarding nodal connectivity (NODE) and material properties (PROPS) are prescribed via an accompanying input file. As part of the user element subroutine (UEL), the user is required to eval-

uate/update the right-hand side matrix (RHS) and the Jacobian matrix (AMATRX) at the end of each solution step for ABAQUS to access whereby

- The RHS matrix contains the contributions of an element to the right-hand-side vector of the overall system of equations. Specializing for our surface element, RHS is the overall elemental residual which in matrix form is given by

$$\mathbf{R} = [R_{u_1}^1, R_{u_2}^1, R_{\mu}^1, R_{u_1}^2, R_{u_2}^2, R_{\mu}^2 \dots R_{u_1}^n, R_{u_2}^n, R_{\mu}^n]^T$$

with  $n$  denoting the total number of nodes pertaining to an element.

- AMATRX contains the contribution of an element to the stiffness of the overall system of equations. Specializing for our formulation, AMATRX is the global stiffness tangent given by

$$\mathbf{K} = \begin{bmatrix} K_{u_1 u_1}^{11} & K_{u_1 u_2}^{11} & K_{u_1 \mu}^{11} & K_{u_1 u_1}^{12} & K_{u_1 u_2}^{12} & K_{u_1 \mu}^{12} & K_{u_1 u_1}^{1n} & K_{u_1 u_2}^{1n} & K_{u_1 \mu}^{1n} \\ K_{u_2 u_1}^{11} & K_{u_2 u_2}^{11} & K_{u_2 \mu}^{11} & K_{u_2 u_1}^{12} & K_{u_2 u_2}^{12} & K_{u_2 \mu}^{12} & K_{u_2 u_1}^{1n} & K_{u_2 u_2}^{1n} & K_{u_2 \mu}^{1n} \\ K_{\mu u_1}^{11} & K_{\mu u_2}^{11} & K_{\mu \mu}^{11} & K_{\mu u_1}^{12} & K_{\mu u_2}^{12} & K_{\mu \mu}^{12} & K_{\mu u_1}^{1n} & K_{\mu u_2}^{1n} & K_{\mu \mu}^{1n} \\ K_{u_1 u_1}^{21} & K_{u_1 u_2}^{21} & K_{u_1 \mu}^{21} & K_{u_1 u_1}^{22} & K_{u_1 u_2}^{22} & K_{u_1 \mu}^{22} & \dots & K_{u_1 u_1}^{2n} & K_{u_1 u_2}^{2n} & K_{u_1 \mu}^{2n} \\ K_{u_2 u_1}^{21} & K_{u_2 u_2}^{21} & K_{u_2 \mu}^{21} & K_{u_2 u_1}^{22} & K_{u_2 u_2}^{22} & K_{u_2 \mu}^{22} & & K_{u_2 u_1}^{2n} & K_{u_2 u_2}^{2n} & K_{u_2 \mu}^{2n} \\ K_{\mu u_1}^{21} & K_{\mu u_2}^{21} & K_{\mu \mu}^{21} & K_{\mu u_1}^{22} & K_{\mu u_2}^{22} & K_{\mu \mu}^{22} & & K_{\mu u_1}^{2n} & K_{\mu u_2}^{2n} & K_{\mu \mu}^{2n} \\ & & & \vdots & & & \ddots & & \vdots & \\ K_{u_1 u_1}^{n1} & K_{u_1 u_2}^{n1} & K_{u_1 \mu}^{n1} & K_{u_1 u_1}^{n2} & K_{u_1 u_2}^{n2} & K_{u_1 \mu}^{n2} & & K_{u_1 u_1}^{nn} & K_{u_1 u_2}^{nn} & K_{u_1 \mu}^{nn} \\ K_{u_2 u_1}^{n1} & K_{u_2 u_2}^{n1} & K_{u_2 \mu}^{n1} & K_{u_2 u_1}^{n2} & K_{u_2 u_2}^{n2} & K_{u_2 \mu}^{n2} & & K_{u_2 u_1}^{nn} & K_{u_2 u_2}^{nn} & K_{u_2 \mu}^{nn} \\ K_{\mu u_1}^{n1} & K_{\mu u_2}^{n1} & K_{\mu \mu}^{n1} & K_{\mu u_1}^{n2} & K_{\mu u_2}^{n2} & K_{\mu \mu}^{n2} & & K_{\mu u_1}^{nn} & K_{\mu u_2}^{nn} & K_{\mu \mu}^{nn} \end{bmatrix}$$

While the proposed surface element is of chemo-mechanical nature, we detail here the numerical implementation of the chemical counterpart of the theory only. For the interested reader, a more detailed description on the numerical implementation of a mechanical cohesive element under mixed-mode softening can be found in the work of Park and Paulino [220].

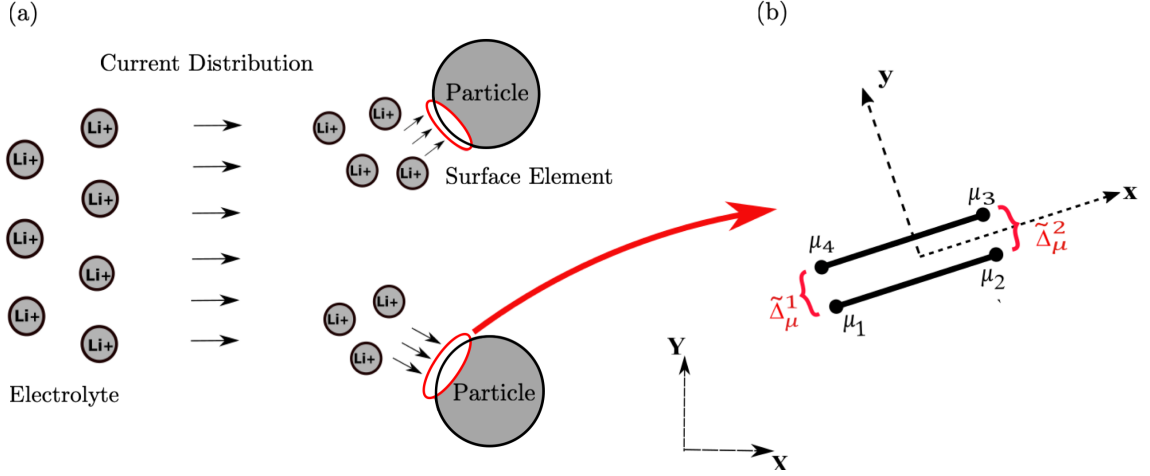


Figure A.2: (a) Surface elements integrated at the boundary of electrode particles to capture variations in current density along a particle surface and the associated current distribution across different particles. (b) Mechanism of current distribution at the electrode surface as a function of jump in chemical potential at the particle-electrolyte interface. Reproduced with permission from [17].

Given the nodal chemical potentials of the surface elements ( $\mu_1, \mu_2, \mu_3, \mu_4$ ) at the initiation of a solution step, nodal jumps in chemical potential ( $\tilde{\Delta}_\mu^{(1)}, \tilde{\Delta}_\mu^{(2)}$ ) at the interface of the surface elements are computed using

$$\tilde{\Delta}_\mu^{(1)} = \mu_4 - \mu_1 \quad \text{and} \quad \tilde{\Delta}_\mu^{(2)} = \mu_3 - \mu_2 \quad (\text{A.2.1})$$

In matrix notation, nodal jumps in chemical potential at the interface of the surface elements,  $\tilde{\Delta}_\mu$  can be obtained from the nodal chemical potentials,  $\mu$  through

$$\tilde{\Delta}_\mu = \mathbf{L}\mu \quad (\text{A.2.2})$$

with

$$\mathbf{L} = \begin{bmatrix} -1 & 0 & 0 & 1 \\ 0 & -1 & 1 & 0 \end{bmatrix} \quad (\text{A.2.3})$$

In conjunction with the shape function matrix  $\mathbf{N}$ , jump in chemical potential,  $\Delta_\mu$  anywhere along the interface is interpolated from the nodal jumps in chemical potential at the inter-



face of the surface elements,  $\tilde{\Delta}\boldsymbol{\mu}$  using,

$$\Delta\mu = \mathbf{N}\tilde{\Delta}\boldsymbol{\mu} \quad (\text{A.2.4})$$

with

$$N_1 = \frac{1 - \xi}{2} \quad \text{and} \quad N_2 = \frac{1 + \xi}{2} \quad (\text{A.2.5})$$

and  $\xi$  denoting a normalized coordinate along the undeformed surface element.

Combining (A.2.2) and (A.2.4), jump in chemical potential along the interface of surface elements,  $\Delta\mu$  can be related to the vector of nodal chemical potentials,  $\boldsymbol{\mu}$  through

$$\Delta\mu = \mathbf{B}\boldsymbol{\mu} \quad \text{where} \quad \mathbf{B} = \mathbf{N}\mathbf{L} = [-N_1 \quad -N_2 \quad N_2 \quad N_1] \quad (\text{A.2.6})$$

One can then numerically compute the element level residual,  $\mathbf{R}_\mu^{\text{coh}}$  and tangent,  $\mathbf{K}_{\mu\mu}^{\text{coh}}$  from Eqns. (A.1.12) and (A.1.13), employing a Gauss-quadrature scheme to evaluate the integral expressions. In our implementation, we use a two-point Gauss-quadrature rule with location of Gauss integration points at  $\xi = \pm 1/3$ .

### A.3 Calibration of electro-chemo-mechanical parameters for modeling solid state cathodes

We present here a brief summary of the calibration of necessary parameters used to model the chemo-mechanical behavior of a  $\text{LiCoO}_2\text{-Li}_{10}\text{GeP}_2\text{S}_{12}$  composite cathode. In particular, we performed calibrations to fit the Young's Modulus, open-circuit voltage, and reaction constant for LCO.

A sixth-order polynomial is used to capture the variation of Young's modulus of  $\text{Li}_x\text{CoO}_2$  with Li content from  $E = 108.5$  GPa for a pristine unlithiated state to  $E = 252$  GPa for a fully-lithiated state as reported in Wu and Zhang [140]. The result of our fitting is given by

$$E(x) = 136.93x^6 - 84.93x^3 + 91.57x + 108.5 \quad (\text{A.3.1})$$

where  $x$  denotes the stoichiometric amount of Li in  $\text{Li}_x\text{CoO}_2$  composition.

Fig. A.3 (a) illustrates in red the analytical fit to the experimental Young's modulus data reported in Wu and Zhang [140]. Also illustrated in Fig. A.3(b) is the variation in shear modulus with stoichiometric Li content employed in our simulations and compared against experimental data by Wu and Zhang [140]. Note that we did not fit for the variation in Shear modulus shown in Fig. A.3(b), rather it is produced from our fit for Young's modulus and use of a constant Poisson's ratio of  $\nu = 0.22$ .

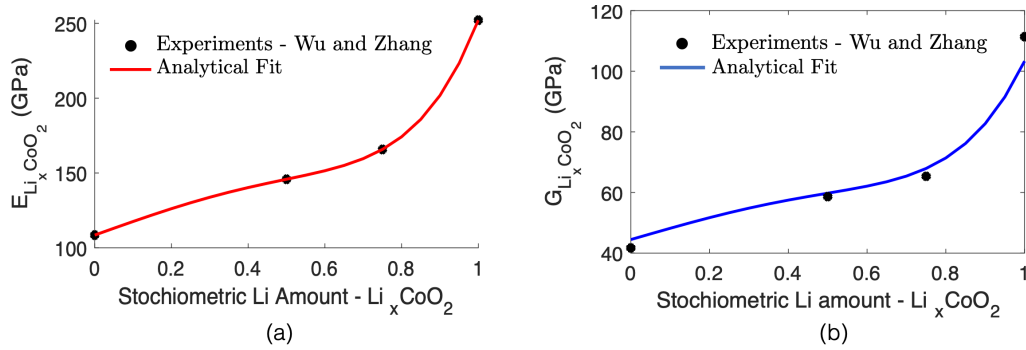


Figure A.3: Analytical fit of (a) Young's Modulus and (b) Shear Modulus for  $\text{Li}_x\text{CoO}_2$  active material with stoichiometric Li amount -  $x$  to experimental data by Wu and Zhang [140]. Reproduced with permission from [17].

The activity coefficient of Li for an  $\text{LiCoO}_2$  electrode is calibrated by fitting a seventh-order polynomial (c.f [115]) to the open-circuit potential data for  $\text{Li}_x\text{CoO}_2$  against a Li reference electrode reported in the work of Mizushima et al. [145]. Fig. A.4 illustrates in red the analytical fit to experimental data. Also illustrated is the finite-element simulated open-circuit potential curve (yellow curve), demonstrating consistent results with experimental data.

The reaction constant,  $k_0$  is calibrated to charge-discharge curves for  $\text{Li}_x\text{CoO}_2$  by Zhang et al. [152]. We adjust  $k_0$  such that energy dissipation during a full cycle (evaluated as the area inside the Voltage vs. SOC curve) matches with the area from experiments. A

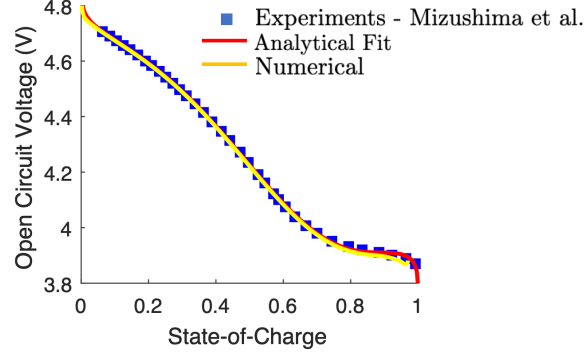


Figure A.4: Comparison of analytical, seventh-order polynomial fit and the finite-element simulated open circuit potential curve against the experimental data by Mizushima et al. [145]. Reproduced with permission from [17].

representative figure of our calibration scheme against the experimental charge-discharge curves by Zhang et al. at a C-Rate of C/2.7 is illustrated in Fig. A.5. Here, analytical, finite-element simulated and experimental Voltage vs. SOC curves are included and illustrate the consistency of our calibration procedure.

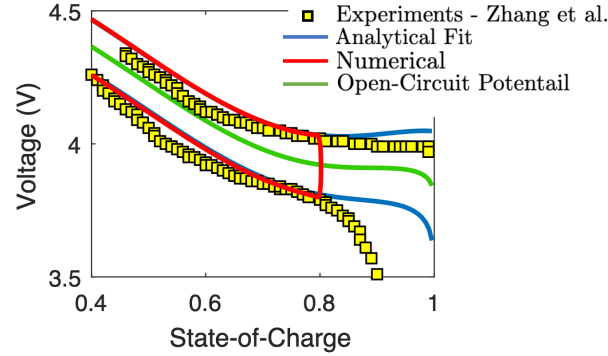


Figure A.5: Calibration of reaction constant,  $k_0$  against experimental data by Zhang et al. [152], demonstrating consistency across analytical, numerical and experimentally obtained Voltage vs SOC curves. Reproduced with permission from [17].

#### A.4 Modeling of interfacial damage in a $\text{LiCoO}_2$ -LGPS composite cathode for an all-Solid-State Battery. Additional simulations.

We include here additional simulation results, which for conciseness, were not included in the main body of the thesis and are presented here for completeness.

Role of particle size and size distribution on electrochemical performance and mechanical degradation.

In addition to the simulations shown in Sect. 3.3 investigating the role of particle size and size distribution at a volume fraction of  $\phi_{AM} = 30\%$ , we performed an additional set of simulations at  $\phi_{AM} = 20\%$ . The generated results are included here for completeness. Fig. A.6 shows the simulation RVEs, all of which have a constant active particle volume fraction of  $\phi_{AM} = 20\%$ , while particle size distribution is allowed to vary. As in the main body of this manuscript, particle size and aspect ratio are seeded using a uniform distribution with prescribed lower and upper bounds.

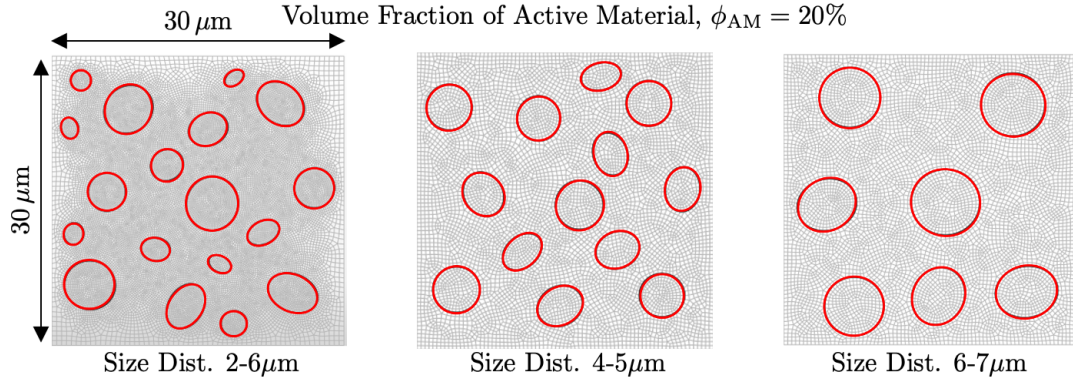


Figure A.6: Simulated RVEs with a constant active particle volume fraction  $\phi_{AM} = 20\%$ . The particle sizes are given a uniform distribution with lower and upper bounds in the range of: i) 2-6  $\mu\text{m}$  ii) 4-5  $\mu\text{m}$  and iii) 6-7  $\mu\text{m}$ . The aspect ratio lower and upper bounds are set to 0.9 and 1.5 respectively for all cases. Reproduced with permission from [17].

The results of these simulations are shown in Fig. A.7, where again we observe consistent results in electrochemical performance and damage evolution across the three simulated RVEs with different particle size distributions and a constant active material volume fraction  $\phi_{AM} = 20\%$ . The results are in agreement with those discussed in Sect. 3.3 in the main body of this thesis.

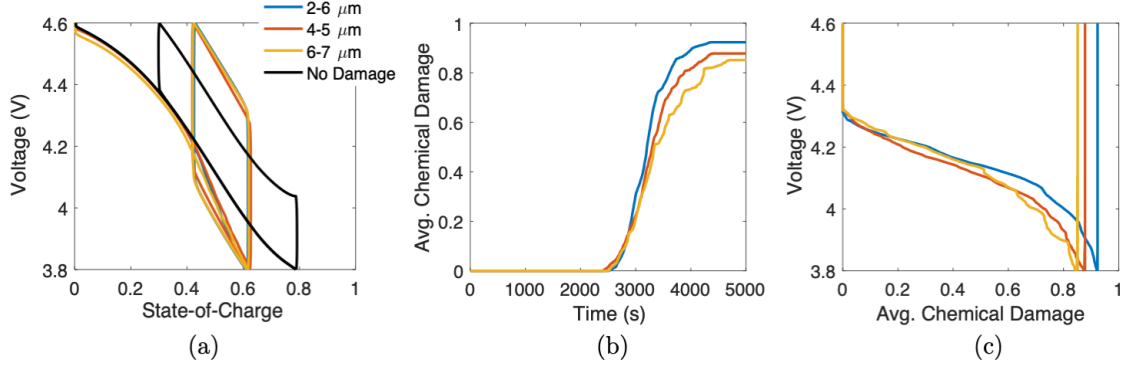


Figure A.7: Simulation results for composite cathode RVEs with constant active material volume fraction  $\phi_{AM} = 20\%$  and varying particle size distribution. (a) Voltage vs. SOC behavior also compared to simulations with no damage. (b) Evolution of average  $D_{chem}$  as a function of time for the first half-cycle. (c) Evolution of Voltage as a function of average  $D_{chem}$ . Reproduced with permission from [17].

## APPENDIX B

### PRINCIPLE OF VIRTUAL WORK, MACRO- AND MICROFORCE BALANCE LAW

We present here a detailed derivation of the macro- and microforce balance laws for the rate-like kinematical descriptors in our theory. We consider a list of generalized virtual velocity fields to be given by  $\mathcal{V} = (\delta\boldsymbol{\chi}, \delta\mathbf{F}^e, \delta\xi, \nabla\delta\xi, \delta\mathbf{d}, \nabla\delta\mathbf{d})$  and constrained through the kinematic relation (4.4.2) presented in Sect. 4.4.1. For any part  $\mathcal{P}$  with outward unit normal  $\mathbf{n}_R$  of the reference body  $\mathcal{B}$ , the internal and external power are given by

$$\begin{aligned}\delta W_{\text{ext}}(P, \mathcal{V}) &= \int_{\partial P} \mathbf{t}_R(\mathbf{n}_R) \cdot \delta\boldsymbol{\chi} \, da_R + \int_P \mathbf{b}_R \cdot \delta\boldsymbol{\chi} \, dv_R + \int_{\partial P} \eta \delta\xi \, da_R + \int_{\partial P} \gamma \delta\mathbf{d} \, da_R \\ \delta W_{\text{int}}(P, \mathcal{V}) &= \int_P (\mathbf{S}^e : \delta\mathbf{F}^e + E \delta\xi + \mathbf{G} \cdot \nabla\delta\xi + \varpi \delta\mathbf{d} + \boldsymbol{\zeta} \cdot \nabla\delta\mathbf{d}) \, dv_R\end{aligned}\tag{A.1}$$

To derive the balance laws, we invoke the power balance requirement (c.f. Sect. 4.4.1) and demand that  $\delta W_{\text{ext}}(P, \mathcal{V}) = \delta W_{\text{int}}(P, \mathcal{V})$  for all generalized virtual velocities  $\mathcal{V}$ .

First, we derive the local macroforce balance. Let  $\delta\xi = 0, \nabla\delta\xi = \mathbf{0}, \delta\mathbf{d} = 0, \nabla\delta\mathbf{d} = \mathbf{0}$  such that the kinematic constraint (4.4.2) yields the relation  $\delta\mathbf{F}^e = (\nabla\delta\boldsymbol{\chi})\mathbf{F}^{-1}\mathbf{F}^e$ . For this choice, the principle of virtual power gives,

$$\int_{\partial P} \mathbf{t}_R(\mathbf{n}_R) \cdot \delta\boldsymbol{\chi} \, da_R + \int_P \mathbf{b}_R \cdot \delta\boldsymbol{\chi} \, dv_R = \int_P \mathbf{S}^e : \delta\mathbf{F}^e \, dv_R = \int_P \mathbf{S}^e \mathbf{F}^{e-\top} : \nabla\delta\boldsymbol{\chi} \, dv_R \tag{A.2}$$

which by defining

$$\mathbf{T}_R \stackrel{\text{def}}{=} \mathbf{S}^e \mathbf{F}^{e-\top} \tag{A.3}$$

and applying the divergence theorem on (A.2) leads to the macroscopic force balance

$$\text{Div } \mathbf{T}_R + \mathbf{b}_R = 0, \quad \text{and the traction boundary condition } \mathbf{t}_R(\mathbf{n}_R) = \mathbf{T}_R \mathbf{n}_R. \tag{A.4}$$

As is standard, the Piola stress  $\mathbf{T}_R$  is related to the symmetric Cauchy stress  $\mathbf{T}$  through

$$\mathbf{T}_R = J\mathbf{T}\mathbf{F}^{-\top}, \quad (\text{A.5})$$

and for future use we may write  $\mathbf{S}^e = J\mathbf{T}\mathbf{F}^{e-\top}$ .

Subsequently, we derive the local microforce balances. The first microforce balance associated with reaction is obtained by letting  $\delta\chi = \mathbf{0}$ ,  $\delta d = 0$ ,  $\nabla\delta d = \mathbf{0}$ , such that (4.4.2) yields,

$$\begin{aligned} \mathbf{S}^e : \delta\mathbf{F}^e &= \mathbf{S}^e : \left( -h(\bar{\xi})\mathbf{F}^e\mathbf{N}^r \right) \delta\xi \\ &= \left( -\mathbf{F}^{e\top}\mathbf{S}^e : (h(\bar{\xi})\mathbf{N}^r) \right) \delta\xi \\ &= \left( - (J\mathbf{F}^{e\top}\mathbf{T}\mathbf{F}^{e-\top}) : (h(\bar{\xi})\mathbf{N}^r) \right) \delta\xi \\ &= \left( -J^c h(\bar{\xi})\mathbf{M}^e : \mathbf{N}^r \right) \delta\xi \end{aligned} \quad (\text{A.6})$$

where we have defined the elastic Mandel stress as,

$$\mathbf{M}^e \stackrel{\text{def}}{=} J^e \mathbf{F}^{e\top} \mathbf{T} \mathbf{F}^{e-\top} \quad (\text{A.7})$$

For this choice, and accounting for (A.6), the virtual power balance then yields

$$\int_{\partial P} \eta \delta\xi da_R = \int_P (-J^c h(\bar{\xi})\mathbf{M}^e : \mathbf{N}^r \delta\xi + E\delta\xi + \mathbf{G} \cdot \nabla\delta\xi) dv_R. \quad (\text{A.8})$$

Applying the divergence theorem leads to

$$\int_P (-J^c h(\bar{\xi})\mathbf{M}^e : \mathbf{N}^r \delta\xi + E\delta\xi - \text{Div}\mathbf{G} \delta\xi) dv_R = \int_{\partial P} (\eta - \mathbf{G} \cdot \mathbf{n}_R) \delta\xi da_R \quad (\text{A.9})$$

Granted this relationship must hold for all  $P$  and all values of  $\delta\xi$ , standard variational

arguments yield the second microforce balance,

$$E - J^c h(\bar{\xi}) \mathbf{M}^e : \mathbf{N}^r - \text{Div} \mathbf{G} = 0 \quad (\text{A.10})$$

along with the corresponding boundary condition

$$\eta(\mathbf{n}_r) = \mathbf{G} \cdot \mathbf{n}_r. \quad (\text{A.11})$$

Lastly, we derive the local microforce balance associated with damage. Let  $\delta \chi = \mathbf{0}$ ,  $\delta \xi = 0$  and  $\nabla \delta \xi = \mathbf{0}$ . In a similar fashion, the virtual power balance statement then yields

$$\int_{\partial \mathcal{P}} \gamma \delta \mathbf{d} \, da_r = \int_{\mathcal{P}} (\varpi \delta \mathbf{d} + \boldsymbol{\zeta} \cdot \nabla \delta \mathbf{d}) \, dv_r \quad (\text{A.12})$$

Applying the divergence theorem on (A.12) gives,

$$\int_{\mathcal{P}} (\text{Div} \boldsymbol{\zeta} - \varpi) \delta \mathbf{d} \, dv_r + \int_{\partial \mathcal{P}} (\gamma - \boldsymbol{\zeta} \cdot \mathbf{n}_r) \delta \mathbf{d} \, da_r = 0 \quad (\text{A.13})$$

which must hold for all  $\mathcal{P}$  and all values of  $\delta \mathbf{d}$ , yielding the second microforce balance

$$\text{Div} \boldsymbol{\zeta} - \varpi = 0 \quad (\text{A.14})$$

along with the corresponding boundary condition

$$\gamma(\mathbf{n}_r) = \boldsymbol{\zeta} \cdot \mathbf{n}_r \quad (\text{A.15})$$

In summary, using the principle of virtual work we have derived one macroforce balance for the Piola stress,  $\mathbf{T}_r$  as well as two corresponding microforce balances for the stresses  $\{E, \mathbf{G}, \boldsymbol{\zeta}, \varpi\}$  as outlined in Sect. 4.4.1.



## REFERENCES

- [1] M. Armand and J.-M. Tarascon, “Building better batteries,” *nature*, vol. 451, no. 7179, pp. 652–657, 2008.
- [2] P. G. Bruce, S. A. Freunberger, L. J. Hardwick, and J.-M. Tarascon, “Li-o 2 and li-s batteries with high energy storage,” *Nature materials*, vol. 11, no. 1, p. 19, 2012.
- [3] X. Yao *et al.*, “High-energy all-solid-state lithium batteries with ultralong cycle life,” *Nano letters*, vol. 16, no. 11, pp. 7148–7154, 2016.
- [4] J. Li, C. Ma, M. Chi, C. Liang, and N. J. Dudney, “Solid electrolyte: The key for high-voltage lithium batteries,” *Advanced Energy Materials*, vol. 5, no. 4, p. 1 401 408, 2015.
- [5] Y. Zhu, X. He, and Y. Mo, “Origin of outstanding stability in the lithium solid electrolyte materials: Insights from thermodynamic analyses based on first-principles calculations,” *ACS applied materials & interfaces*, vol. 7, no. 42, pp. 23 685–23 693, 2015.
- [6] W. D. Richards, L. J. Miara, Y. Wang, J. C. Kim, and G. Ceder, “Interface stability in solid-state batteries,” *Chemistry of Materials*, vol. 28, no. 1, pp. 266–273, 2016.
- [7] C. Yang, K. Fu, Y. Zhang, E. Hitz, and L. Hu, “Protected lithium-metal anodes in batteries: From liquid to solid,” *Advanced materials*, vol. 29, no. 36, p. 1 701 169, 2017.
- [8] W. Zhang, J. Nie, F. Li, Z. L. Wang, and C. Sun, “A durable and safe solid-state lithium battery with a hybrid electrolyte membrane,” *Nano Energy*, vol. 45, pp. 413–419, 2018.
- [9] D. Bistri, A. Afshar, and C. V. Di Leo, “Modeling the chemo-mechanical behavior of all-solid-state batteries: A review,” *Meccanica*, pp. 1–32, 2020.
- [10] A. Hayashi, T. Ohtomo, F. Mizuno, K. Tadanaga, and M. Tatsumisago, “All-solid-state li/s batteries with highly conductive glass–ceramic electrolytes,” *Electrochemistry communications*, vol. 5, no. 8, pp. 701–705, 2003.
- [11] R. Murugan, V. Thangadurai, and W. Weppner, “Fast lithium ion conduction in garnet-type  $\text{Li}_7\text{La}_3\text{Zr}_2\text{O}_{12}$ ,” *Angewandte Chemie International Edition*, vol. 46, no. 41, pp. 7778–7781, 2007.

- [12] J. S. Thokchom, N. Gupta, and B. Kumar, “Superionic conductivity in a lithium aluminum germanium phosphate glass–ceramic,” *Journal of the Electrochemical Society*, vol. 155, no. 12, A915, 2008.
- [13] J. L. Allen, J. Wolfenstine, E. Rangasamy, and J. Sakamoto, “Effect of substitution (ta, al, ga) on the conductivity of  $\text{Li}_7\text{La}_3\text{Zr}_2\text{O}_{12}$ ,” *Journal of Power Sources*, vol. 206, pp. 315–319, 2012.
- [14] M. G. Boebinger *et al.*, “Avoiding fracture in a conversion battery material through reaction with larger ions,” *Joule*, vol. 2, no. 9, pp. 1783–1799, 2018.
- [15] A. Afshar and C. V. Di Leo, “A thermodynamically consistent gradient theory for diffusion–reaction–deformation in solids: Application to conversion-type electrodes,” *Journal of the Mechanics and Physics of Solids*, vol. 151, p. 104 368, 2021.
- [16] W. Zhang *et al.*, “Interfacial processes and influence of composite cathode microstructure controlling the performance of all-solid-state lithium batteries,” *ACS applied materials & interfaces*, vol. 9, no. 21, pp. 17 835–17 845, 2017.
- [17] D. Bistri and C. V. Di Leo, “Modeling of chemo-mechanical multi-particle interactions in composite electrodes for liquid and solid-state li-ion batteries,” *Journal of The Electrochemical Society*, vol. 168, no. 3, p. 030 515, 2021.
- [18] J. Tippens *et al.*, “Visualizing chemomechanical degradation of a solid-state battery electrolyte,” *ACS Energy Letters*, vol. 4, no. 6, pp. 1475–1483, 2019.
- [19] D. Bistri and C. V. Di Leo, “A continuum electro-chemo-mechanical gradient theory coupled with damage: Application to li-metal filament growth in all-solid-state batteries,” *Journal of the Mechanics and Physics of Solids*, vol. 174, p. 105 252, 2023.
- [20] Z. Ning *et al.*, “Visualizing plating-induced cracking in lithium-anode solid-electrolyte cells,” *Nature Materials*, vol. 20, no. 8, pp. 1121–1129, 2021.
- [21] J. Lewis *et al.*, “Accelerated short circuiting in anode-free solid-state batteries driven by local lithium depletion,” 2022.
- [22] J. A. Lewis *et al.*, “Linking void and interphase evolution to electrochemistry in solid-state batteries using operando x-ray tomography,” *Nature Materials*, vol. 20, no. 4, pp. 503–510, 2021.
- [23] J. Zhang *et al.*, “Microstructure engineering of solid-state composite cathode via solvent-assisted processing,” *Joule*, vol. 5, no. 7, pp. 1845–1859, 2021.

- [24] A. Bielefeld, D. A. Weber, and J. Janek, "Microstructural modeling of composite cathodes for all-solid-state batteries," *The Journal of Physical Chemistry C*, vol. 123, no. 3, pp. 1626–1634, 2018.
- [25] J. Zhang *et al.*, "All-solid-state batteries with slurry coated  $\text{LiNi}_{0.8}\text{Co}_{0.1}\text{Mn}_{0.1}\text{O}_2$  composite cathode and  $\text{Li}_6\text{PS}_5\text{Cl}$  electrolyte: Effect of binder content," *Journal of Power Sources*, vol. 391, pp. 73–79, 2018.
- [26] L. Beaulieu, K. Eberman, R. Turner, L. Krause, and J. Dahn, "Colossal reversible volume changes in lithium alloys," *Electrochemical and solid state letters*, vol. 4, no. 9, A137, 2001.
- [27] V. A. Sethuraman, M. J. Chon, M. Shimshak, V. Srinivasan, and P. R. Guduru, "In situ measurements of stress evolution in silicon thin films during electrochemical lithiation and delithiation," *Journal of Power Sources*, vol. 195, no. 15, pp. 5062–5066, 2010.
- [28] H.-H. Ryu, K.-J. Park, C. S. Yoon, and Y.-K. Sun, "Capacity fading of ni-rich  $\text{Li}[\text{Ni}_x\text{Co}_y\text{Mn}_{1-x-y}]\text{O}_2$  (0.6 < x < 0.95) cathodes for high-energy-density lithium-ion batteries: Bulk or surface degradation?" *Chemistry of materials*, vol. 30, no. 3, pp. 1155–1163, 2018.
- [29] S. Rezaei, A. Asheri, and B.-X. Xu, "A consistent framework for chemo-mechanical cohesive fracture and its application in solid-state batteries," *Journal of the Mechanics and Physics of Solids*, vol. 157, p. 104612, 2021.
- [30] A. Singh and S. Pal, "Chemo-mechanical modeling of inter-and intra-granular fracture in heterogeneous cathode with polycrystalline particles for lithium-ion battery," *Journal of the Mechanics and Physics of Solids*, vol. 163, p. 104839, 2022.
- [31] G. Bucci, T. Swamy, Y.-M. Chiang, and W. C. Carter, "Modeling of internal mechanical failure of all-solid-state batteries during electrochemical cycling, and implications for battery design," *Journal of Materials Chemistry A*, vol. 5, no. 36, pp. 19422–19430, 2017.
- [32] R. Koerver *et al.*, "Capacity fade in solid-state batteries: Interphase formation and chemomechanical processes in nickel-rich layered oxide cathodes and lithium thiophosphate solid electrolytes," *Chemistry of Materials*, vol. 29, no. 13, pp. 5574–5582, 2017.
- [33] T. Shi, Y.-Q. Zhang, Q. Tu, Y. Wang, M. Scott, and G. Ceder, "Characterization of mechanical degradation in an all-solid-state battery cathode," *Journal of Materials Chemistry A*, vol. 8, no. 34, pp. 17399–17404, 2020.

- [34] J. Christensen and J. Newman, "Stress generation and fracture in lithium insertion materials," *Journal of Solid State Electrochemistry*, vol. 10, no. 5, pp. 293–319, 2006.
- [35] X. Zhang, W. Shyy, and A. M. Sastry, "Numerical simulation of intercalation-induced stress in li-ion battery electrode particles," *Journal of the Electrochemical Society*, vol. 154, no. 10, A910–A916, 2007.
- [36] C. Miehe, H. Dal, L.-M. Schänzel, and A. Raina, "A phase-field model for chemo-mechanical induced fracture in lithium-ion battery electrode particles," *International Journal for Numerical Methods in Engineering*, vol. 106, no. 9, pp. 683–711, 2016.
- [37] S. Xia *et al.*, "Chemomechanical interplay of layered cathode materials undergoing fast charging in lithium batteries," *Nano energy*, vol. 53, pp. 753–762, 2018.
- [38] T. Kobayashi, A. Yamada, and R. Kanno, "Interfacial reactions at electrode/electrolyte boundary in all solid-state lithium battery using inorganic solid electrolyte, thiolisicon," *Electrochimica Acta*, vol. 53, no. 15, pp. 5045–5050, 2008.
- [39] D. Santhanagopalan *et al.*, "Interface limited lithium transport in solid-state batteries," *The journal of physical chemistry letters*, vol. 5, no. 2, pp. 298–303, 2014.
- [40] A. Sakuda, A. Hayashi, and M. Tatsumisago, "Interfacial observation between li-coo2 electrode and li2s- p2s5 solid electrolytes of all-solid-state lithium secondary batteries using transmission electron microscopy," *Chemistry of Materials*, vol. 22, no. 3, pp. 949–956, 2010.
- [41] J. A. Lewis *et al.*, "Interphase morphology between a solid-state electrolyte and lithium controls cell failure," *ACS Energy Letters*, vol. 4, no. 2, pp. 591–599, 2019.
- [42] C. V. Di Leo, E. Rejovitzky, and L. Anand, "Diffusion–deformation theory for amorphous silicon anodes: The role of plastic deformation on electrochemical performance," *International Journal of Solids and Structures*, vol. 67, pp. 283–296, 2015.
- [43] H. Chung and B. Kang, "Mechanical and thermal failure induced by contact between a li1. 5al0. 5ge1. 5 (po4) 3 solid electrolyte and li metal in an all solid-state li cell," *Chemistry of Materials*, vol. 29, no. 20, pp. 8611–8619, 2017.
- [44] E. Rejovitzky, C. V. Di Leo, and L. Anand, "A theory and a simulation capability for the growth of a solid electrolyte interphase layer at an anode particle in a li-ion battery," *Journal of the Mechanics and Physics of Solids*, vol. 78, pp. 210–230, 2015.

- [45] K. Loeffel and L. Anand, “A chemo-thermo-mechanically coupled theory for elastic–viscoplastic deformation, diffusion, and volumetric swelling due to a chemical reaction,” *International Journal of Plasticity*, vol. 27, no. 9, pp. 1409–1431, 2011.
- [46] K. Loeffel, L. Anand, and Z. M. Gasem, “On modeling the oxidation of high-temperature alloys,” *Acta materialia*, vol. 61, no. 2, pp. 399–424, 2013.
- [47] Y. Zhao, Y. Chen, S. Ai, and D. Fang, “A diffusion, oxidation reaction and large viscoelastic deformation coupled model with applications to sic fiber oxidation,” *International Journal of Plasticity*, vol. 118, pp. 173–189, 2019.
- [48] L. Anand, Y. Mao, and B. Talamini, “On modeling fracture of ferritic steels due to hydrogen embrittlement,” *Journal of the Mechanics and Physics of Solids*, vol. 122, pp. 280–314, 2019.
- [49] A. Salvadori, R. McMeeking, D. Grazioli, and M. Magri, “A coupled model of transport-reaction-mechanics with trapping. part i–small strain analysis,” *Journal of the Mechanics and Physics of Solids*, vol. 114, pp. 1–30, 2018.
- [50] X. Zhang, A. Krischok, and C. Linder, “A variational framework to model diffusion induced large plastic deformation and phase field fracture during initial two-phase lithiation of silicon electrodes,” *Computer methods in applied mechanics and engineering*, vol. 312, pp. 51–77, 2016.
- [51] M. Klinsmann, D. Rosato, M. Kamlah, and R. M. McMeeking, “Modeling crack growth during li insertion in storage particles using a fracture phase field approach,” *Journal of the Mechanics and Physics of Solids*, vol. 92, pp. 313–344, 2016.
- [52] C. Cui, R. Ma, and E. Martinez-Pañeda, “A generalised, multi-phase-field theory for dissolution-driven stress corrosion cracking and hydrogen embrittlement,” *Journal of the Mechanics and Physics of Solids*, vol. 166, p. 104 951, 2022.
- [53] T.-T. Nguyen, J. Réthoré, M.-C. Baietto, J. Bolivar, M. Fregonese, and S. P. Bordas, “Modeling of inter-and transgranular stress corrosion crack propagation in polycrystalline material by using phase field method,” *Journal of the Mechanical Behavior of Materials*, vol. 26, no. 5-6, pp. 181–191, 2017.
- [54] A. Valverde-González, E. Martinez-Pañeda, A. Quintanas-Corominas, J. Reinoso, and M. Paggi, “Computational modelling of hydrogen assisted fracture in polycrystalline materials,” *international journal of hydrogen energy*, vol. 47, no. 75, pp. 32 235–32 251, 2022.
- [55] Y. Mao and L. Anand, “Fracture of elastomeric materials by crosslink failure,” *Journal of Applied Mechanics*, vol. 85, no. 8, 2018.

- [56] B. Talamini, Y. Mao, and L. Anand, “Progressive damage and rupture in polymers,” *Journal of the Mechanics and Physics of Solids*, vol. 111, pp. 434–457, 2018.
- [57] Y. Mao and L. Anand, “A theory for fracture of polymeric gels,” *Journal of the Mechanics and Physics of Solids*, vol. 115, pp. 30–53, 2018.
- [58] Y. Ren, Y. Shen, Y. Lin, and C.-W. Nan, “Direct observation of lithium dendrites inside garnet-type lithium-ion solid electrolyte,” *Electrochemistry Communications*, vol. 57, pp. 27–30, 2015.
- [59] E. J. Cheng, A. Sharafi, and J. Sakamoto, “Intergranular li metal propagation through polycrystalline  $\text{Li}_6\text{Zr}_2\text{S}_{10}\text{Al}_3\text{Zr}_2\text{O}_{12}$  ceramic electrolyte,” *Electrochimica Acta*, vol. 223, pp. 85–91, 2017.
- [60] L. Porz *et al.*, “Mechanism of lithium metal penetration through inorganic solid electrolytes,” *Advanced Energy Materials*, vol. 7, no. 20, p. 1701003, 2017.
- [61] F. Shen, M. B. Dixit, X. Xiao, and K. B. Hatzell, “Effect of pore connectivity on li dendrite propagation within llzo electrolytes observed with synchrotron x-ray tomography,” *ACS Energy Letters*, vol. 3, no. 4, pp. 1056–1061, 2018.
- [62] H. Yan *et al.*, “How does the creep stress regulate void formation at the lithium-solid electrolyte interface during stripping?” *Advanced Energy Materials*, vol. 12, no. 2, p. 2102283, 2022.
- [63] L. Anand and S. Narayan, “An elastic-viscoplastic model for lithium,” *Journal of The Electrochemical Society*, vol. 166, no. 6, A1092, 2019.
- [64] W. S. LePage *et al.*, “Lithium mechanics: Roles of strain rate and temperature and implications for lithium metal batteries,” *Journal of The Electrochemical Society*, vol. 166, no. 2, A89, 2019.
- [65] C. D. Fincher *et al.*, “Controlling dendrite propagation in solid-state batteries with engineered stress,” 2022.
- [66] S. Hao *et al.*, “3d imaging of lithium protrusions in solid-state lithium batteries using x-ray computed tomography,” *Advanced Functional Materials*, vol. 31, no. 10, p. 2007564, 2021.
- [67] J. A. Lewis *et al.*, “Role of areal capacity in determining short circuiting of sulfide-based solid-state batteries,” *ACS applied materials & interfaces*, vol. 14, no. 3, pp. 4051–4060, 2022.
- [68] M. Nagao, A. Hayashi, M. Tatsumisago, T. Kanetsuku, T. Tsuda, and S. Kuwabata, “In situ sem study of a lithium deposition and dissolution mechanism in a bulk-type

solid-state cell with a  $\text{Li}_2\text{S-P}_2\text{S}_5$  solid electrolyte,” *Physical Chemistry Chemical Physics*, vol. 15, no. 42, pp. 18 600–18 606, 2013.

- [69] S. Hao *et al.*, “Tracking lithium penetration in solid electrolytes in 3d by in-situ synchrotron x-ray computed tomography,” *Nano Energy*, vol. 82, p. 105 744, 2021.
- [70] E. Kazyak *et al.*, “Li penetration in ceramic solid electrolytes: Operando microscopy analysis of morphology, propagation, and reversibility,” *Matter*, vol. 2, no. 4, pp. 1025–1048, 2020.
- [71] T. Krauskopf, H. Hartmann, W. G. Zeier, and J. Janek, “Toward a fundamental understanding of the lithium metal anode in solid-state batteries—an electrochemo-mechanical study on the garnet-type solid electrolyte  $\text{Li}_6\text{.25Al}_0\text{.25Li}_3\text{Zr}_2\text{O}_{12}$ ,” *ACS applied materials & interfaces*, vol. 11, no. 15, pp. 14 463–14 477, 2019.
- [72] C. Monroe and J. Newman, “The impact of elastic deformation on deposition kinetics at lithium/polymer interfaces,” *Journal of The Electrochemical Society*, vol. 152, no. 2, A396, 2005.
- [73] T. Swamy *et al.*, “Lithium metal penetration induced by electrodeposition through solid electrolytes: Example in single-crystal  $\text{Li}_6\text{Li}_3\text{Zr}_2\text{O}_{12}$  garnet,” *Journal of The Electrochemical Society*, vol. 165, no. 16, A3648, 2018.
- [74] S. Heo *et al.*, “Short-circuit mechanism induced by crack propagation spurred by inhomogeneous electric field in garnet-based solid electrolyte,” *Journal of Power Sources*, vol. 510, p. 230 389, 2021.
- [75] L. Xu, T. Feng, J. Huang, Y. Hu, L. Zhang, and L. Luo, “Structural heterogeneity induced li dendrite growth in  $\text{Li}_0\text{.33La}_0\text{.56TiO}_3$  solid-state electrolytes,” *ACS Applied Energy Materials*, vol. 5, no. 3, pp. 3741–3747, 2022.
- [76] F. Han *et al.*, “High electronic conductivity as the origin of lithium dendrite formation within solid electrolytes,” *Nature Energy*, vol. 4, no. 3, pp. 187–196, 2019.
- [77] H.-K. Tian, Z. Liu, Y. Ji, L.-Q. Chen, and Y. Qi, “Interfacial electronic properties dictate li dendrite growth in solid electrolytes,” *Chemistry of Materials*, vol. 31, no. 18, pp. 7351–7359, 2019.
- [78] P. Barai, K. Higa, and V. Srinivasan, “Effect of initial state of lithium on the propensity for dendrite formation: A theoretical study,” *Journal of the Electrochemical Society*, vol. 164, no. 2, A180, 2016.
- [79] R. M. McMeeking, M. Ganser, M. Klinsmann, and F. E. Hildebrand, “Metal electrode surfaces can roughen despite the constraint of a stiff electrolyte,” *Journal of The Electrochemical Society*, vol. 166, no. 6, A984, 2019.

- [80] Z. Ahmad and V. Viswanathan, “Stability of electrodeposition at solid-solid interfaces and implications for metal anodes,” *Physical review letters*, vol. 119, no. 5, p. 056 003, 2017.
- [81] P. Barai, K. Higa, and V. Srinivasan, “Impact of external pressure and electrolyte transport properties on lithium dendrite growth,” *Journal of The Electrochemical Society*, vol. 165, no. 11, A2654, 2018.
- [82] P. Natsiavas, K. Weinberg, D. Rosato, and M. Ortiz, “Effect of prestress on the stability of electrode–electrolyte interfaces during charging in lithium batteries,” *Journal of the Mechanics and Physics of Solids*, vol. 95, pp. 92–111, 2016.
- [83] Z. Ahmad and V. Viswanathan, “Role of anisotropy in determining stability of electrodeposition at solid-solid interfaces,” *Physical Review Materials*, vol. 1, no. 5, p. 055 403, 2017.
- [84] S. Narayan and L. Anand, “On modeling the detrimental effects of inhomogeneous plating-and-stripping at a lithium-metal/solid-electrolyte interface in a solid-state-battery,” *Journal of The Electrochemical Society*, vol. 167, no. 4, p. 040 525, 2020.
- [85] S. Shishvan, N. Fleck, R. McMeeking, and V. Deshpande, “Dendrites as climbing dislocations in ceramic electrolytes: Initiation of growth,” *Journal of Power Sources*, vol. 456, p. 227 989, 2020.
- [86] —, “Growth rate of lithium filaments in ceramic electrolytes,” *Acta Materialia*, vol. 196, pp. 444–455, 2020.
- [87] Y. Zhao, R. Wang, and E. Martinez-Pañeda, “A phase field electro-chemo-mechanical formulation for predicting void evolution at the li-electrolyte interface in all-solid-state batteries,” *Journal of the Mechanics and Physics of Solids*, p. 104 999, 2022.
- [88] J. Agier, S. Shishvan, N. Fleck, and V. Deshpande, “Void growth within li electrodes in solid electrolyte cells,” *Acta Materialia*, vol. 240, p. 118 303, 2022.
- [89] U. Roy, N. Fleck, and V. Deshpande, “An assessment of a mechanism for void growth in li anodes,” *Extreme Mechanics Letters*, vol. 46, p. 101 307, 2021.
- [90] B. Scrosati and J. Garche, “Lithium batteries: Status, prospects and future,” *Journal of power sources*, vol. 195, no. 9, pp. 2419–2430, 2010.
- [91] D. L. Wood III, J. Li, and C. Daniel, “Prospects for reducing the processing cost of lithium ion batteries,” *Journal of Power Sources*, vol. 275, pp. 234–242, 2015.



- [92] K. Zhao *et al.*, “Lithium-assisted plastic deformation of silicon electrodes in lithium-ion batteries: A first-principles theoretical study,” *Nano letters*, vol. 11, no. 7, pp. 2962–2967, 2011.
- [93] K. Zhao, M. Pharr, S. Cai, J. J. Vlassak, and Z. Suo, “Large plastic deformation in high-capacity lithium-ion batteries caused by charge and discharge,” *Journal of the American Ceramic Society*, vol. 94, s226–s235, 2011.
- [94] X. H. Liu, L. Zhong, S. Huang, S. X. Mao, T. Zhu, and J. Y. Huang, “Size-dependent fracture of silicon nanoparticles during lithiation,” *ACS nano*, vol. 6, no. 2, pp. 1522–1531, 2012.
- [95] M. T. McDowell, I. Ryu, S. W. Lee, C. Wang, W. D. Nix, and Y. Cui, “Studying the kinetics of crystalline silicon nanoparticle lithiation with in situ transmission electron microscopy,” *Advanced Materials*, vol. 24, no. 45, pp. 6034–6041, 2012.
- [96] M. Ebner, F. Marone, M. Stampanoni, and V. Wood, “Visualization and quantification of electrochemical and mechanical degradation in li ion batteries,” *Science*, vol. 342, no. 6159, pp. 716–720, 2013.
- [97] K. Zhao, M. Pharr, L. Hartle, J. J. Vlassak, and Z. Suo, “Fracture and debonding in lithium-ion batteries with electrodes of hollow core–shell nanostructures,” *Journal of Power Sources*, vol. 218, pp. 6–14, 2012.
- [98] S. W. Lee, M. T. McDowell, L. A. Berla, W. D. Nix, and Y. Cui, “Fracture of crystalline silicon nanopillars during electrochemical lithium insertion,” *Proceedings of the National Academy of Sciences*, vol. 109, no. 11, pp. 4080–4085, 2012.
- [99] G. Bucci, T. Swamy, S. Bishop, B. W. Sheldon, Y.-M. Chiang, and W. C. Carter, “The effect of stress on battery-electrode capacity,” *Journal of The Electrochemical Society*, vol. 164, no. 4, A645–A654, 2017.
- [100] G. Bucci, B. Talamini, A. R. Balakrishna, Y.-M. Chiang, and W. C. Carter, “Mechanical instability of electrode-electrolyte interfaces in solid-state batteries,” *Physical Review Materials*, vol. 2, no. 10, p. 105 407, 2018.
- [101] F. Aguesse *et al.*, “Investigating the dendritic growth during full cell cycling of garnet electrolyte in direct contact with li metal,” *ACS applied materials & interfaces*, vol. 9, no. 4, pp. 3808–3816, 2017.
- [102] H. Yang, W. Liang, X. Guo, C.-M. Wang, and S. Zhang, “Strong kinetics-stress coupling in lithiation of si and ge anodes,” *Extreme Mechanics Letters*, vol. 2, pp. 1–6, 2015.

- [103] R. Xu and K. Zhao, “Mechanical interactions regulated kinetics and morphology of composite electrodes in li-ion batteries,” *Extreme Mechanics Letters*, vol. 8, pp. 13–21, 2016.
- [104] R. Xu, L. S. de Vasconcelos, and K. Zhao, “Computational analysis of chemomechanical behaviors of composite electrodes in li-ion batteries,” *Journal of Materials Research*, vol. 31, no. 18, pp. 2715–2727, 2016.
- [105] Y. Zhao, P. Stein, Y. Bai, M. Al-Siraj, Y. Yang, and B.-X. Xu, “A review on modeling of electro-chemo-mechanics in lithium-ion batteries,” *Journal of Power Sources*, vol. 413, pp. 259–283, 2019.
- [106] J. Christensen and J. Newman, “A mathematical model of stress generation and fracture in lithium manganese oxide,” *Journal of The Electrochemical Society*, vol. 153, no. 6, A1019–A1030, 2006.
- [107] Y.-T. Cheng and M. W. Verbrugge, “The influence of surface mechanics on diffusion induced stresses within spherical nanoparticles,” *Journal of Applied Physics*, vol. 104, no. 8, p. 083 521, 2008.
- [108] C. V. Di Leo, E. Rejovitzky, and L. Anand, “A cahn–hilliard-type phase-field theory for species diffusion coupled with large elastic deformations: Application to phase-separating li-ion electrode materials,” *Journal of the Mechanics and Physics of Solids*, vol. 70, pp. 1–29, 2014.
- [109] R. Purkayastha and R. McMeeking, “Stress due to the intercalation of lithium in cubic-shaped particles: A parameter study,” *Meccanica*, vol. 51, no. 12, pp. 3081–3096, 2016.
- [110] Z. Cui, F. Gao, and J. Qu, “A finite deformation stress-dependent chemical potential and its applications to lithium ion batteries,” *Journal of the Mechanics and Physics of Solids*, vol. 60, no. 7, pp. 1280–1295, 2012.
- [111] A. F. Bower, P. R. Guduru, and V. A. Sethuraman, “A finite strain model of stress, diffusion, plastic flow, and electrochemical reactions in a lithium-ion half-cell,” *Journal of the Mechanics and Physics of Solids*, vol. 59, no. 4, pp. 804–828, 2011.
- [112] A. F. Bower and P. Guduru, “A simple finite element model of diffusion, finite deformation, plasticity and fracture in lithium ion insertion electrode materials,” *Modelling and Simulation in Materials Science and Engineering*, vol. 20, no. 4, p. 045 004, 2012.
- [113] L. Anand, “A cahn–hilliard-type theory for species diffusion coupled with large elastic–plastic deformations,” *Journal of the Mechanics and Physics of Solids*, vol. 60, no. 12, pp. 1983–2002, 2012.

- [114] K. Zhao *et al.*, “Concurrent reaction and plasticity during initial lithiation of crystalline silicon in lithium-ion batteries,” *Journal of The Electrochemical Society*, vol. 159, no. 3, A238, 2011.
- [115] G. Bucci, S. P. Nadimpalli, V. A. Sethuraman, A. F. Bower, and P. R. Guduru, “Measurement and modeling of the mechanical and electrochemical response of amorphous si thin film electrodes during cyclic lithiation,” *Journal of the Mechanics and Physics of Solids*, vol. 62, pp. 276–294, 2014.
- [116] H. Wu *et al.*, “Stable cycling of double-walled silicon nanotube battery anodes through solid–electrolyte interphase control,” *Nature nanotechnology*, vol. 7, no. 5, pp. 310–315, 2012.
- [117] S. W. Lee, H.-W. Lee, I. Ryu, W. D. Nix, H. Gao, and Y. Cui, “Kinetics and fracture resistance of lithiated silicon nanostructure pairs controlled by their mechanical interaction,” *Nature communications*, vol. 6, no. 1, pp. 1–7, 2015.
- [118] E. K. Rahani and V. B. Shenoy, “Role of plastic deformation of binder on stress evolution during charging and discharging in lithium-ion battery negative electrodes,” *Journal of The Electrochemical Society*, vol. 160, no. 8, A1153, 2013.
- [119] K. Higa and V. Srinivasan, “Stress and strain in silicon electrode models,” *Journal of the Electrochemical Society*, vol. 162, no. 6, A1111, 2015.
- [120] E. García, Y. Chiang, W. Carter, P. Limthongkul, and C. Bishop, “Microstructural modeling and design of rechargeable lithium-ion batteries,” *Journal of the Electrochemical Society*, vol. 152, A255–A263, Jan. 2005.
- [121] R. Xu *et al.*, “Heterogeneous damage in li-ion batteries: Experimental analysis and theoretical modeling,” *Journal of the Mechanics and Physics of Solids*, vol. 129, pp. 160–183, 2019.
- [122] R. Xu, L. De Vasconcelos, J. Shi, J. Li, and K. Zhao, “Disintegration of meatball electrodes for lini x mn y co z o 2 cathode materials,” *Experimental mechanics*, vol. 58, no. 4, pp. 549–559, 2018.
- [123] T. Hofmann *et al.*, “Electro-chemo-mechanical simulation for lithium ion batteries across the scales,” *International Journal of Solids and Structures*, vol. 184, pp. 24–39, 2020.
- [124] R. Behrou and K. Maute, “Numerical modeling of damage evolution phenomenon in solid-state lithium-ion batteries,” *Journal of The Electrochemical Society*, vol. 164, no. 12, A2573, 2017.

- [125] M. Al-Siraj, P. Stein, and B.-X. Xu, “The effect of morphology changes and mechanical stresses on the effective diffusivity of solid electrolyte for lithium ion batteries,” *Journal of The Electrochemical Society*, vol. 167, no. 2, p. 020 535, 2020.
- [126] M. Z. Bazant, “Theory of chemical kinetics and charge transfer based on nonequilibrium thermodynamics,” *Accounts of chemical research*, vol. 46, no. 5, pp. 1144–1160, 2013.
- [127] P. P. Camanho, C. G. Davila, and M. De Moura, “Numerical simulation of mixed-mode progressive delamination in composite materials,” *Journal of composite materials*, vol. 37, no. 16, pp. 1415–1438, 2003.
- [128] L. Hamitouche, M. Tarfaoui, and A. Vautrin, “An interface debonding law subject to viscous regularization for avoiding instability: Application to the delamination problems,” *Engineering Fracture Mechanics*, vol. 75, no. 10, pp. 3084–3100, 2008.
- [129] C. V. Di Leo, “Chemo-mechanics of lithium-ion battery electrodes,” Ph.D. dissertation, Massachusetts Institute of Technology, 2015.
- [130] S. A. Chester, C. V. Di Leo, and L. Anand, “A finite element implementation of a coupled diffusion-deformation theory for elastomeric gels,” *International Journal of Solids and Structures*, vol. 52, pp. 1–18, 2015.
- [131] A. Mukhopadhyay, A. Tokranov, X. Xiao, and B. W. Sheldon, “Stress development due to surface processes in graphite electrodes for li-ion batteries: A first report,” *Electrochimica Acta*, vol. 66, pp. 28–37, 2012.
- [132] Y. M. Lee, J. Y. Lee, H.-T. Shim, J. K. Lee, and J.-K. Park, “Sei layer formation on amorphous si thin electrode during precycling,” *Journal of The Electrochemical Society*, vol. 154, no. 6, A515, 2007.
- [133] A. Bielefeld, D. A. Weber, and J. Janek, “Modeling effective ionic conductivity and binder influence in composite cathodes for all-solid-state batteries,” *ACS Applied Materials & Interfaces*, vol. 12, no. 11, pp. 12 821–12 833, 2020.
- [134] W. Zhang *et al.*, “Degradation mechanisms at the  $\text{Li}_{10}\text{GeP}_2\text{S}_{12}/\text{LiCoO}_2$  cathode interface in an all-solid-state lithium-ion battery,” *ACS applied materials & interfaces*, vol. 10, no. 26, pp. 22 226–22 236, 2018.
- [135] F. Hart and J. Bates, “Lattice model calculation of the strain energy density and other properties of crystalline  $\text{LiCoO}_2$ ,” *Journal of Applied Physics*, vol. 83, no. 12, pp. 7560–7566, 1998.
- [136] H. Wang, Y.-I. Jang, B. Huang, D. R. Sadoway, and Y.-M. Chiang, “Tem study of electrochemical cycling-induced damage and disorder in  $\text{LiCoO}_2$  cathodes for

- rechargeable lithium batteries,” *Journal of The Electrochemical Society*, vol. 146, no. 2, pp. 473–480, 1999.
- [137] M. Qu, W. H. Woodford, J. M. Maloney, W. C. Carter, Y.-M. Chiang, and K. J. Van Vliet, “Nanomechanical quantification of elastic, plastic, and fracture properties of  $\text{LiCoO}_2$ ,” *Advanced Energy Materials*, vol. 2, no. 8, pp. 940–944, 2012.
  - [138] Y. Qi, L. G. Hector, C. James, and K. J. Kim, “Lithium concentration dependent elastic properties of battery electrode materials from first principles calculations,” *Journal of The Electrochemical Society*, vol. 161, no. 11, F3010–F3018, 2014.
  - [139] E. J. Cheng, N. J. Taylor, J. Wolfenstine, and J. Sakamoto, “Elastic properties of lithium cobalt oxide ( $\text{LiCoO}_2$ ),” *Journal of Asian Ceramic Societies*, vol. 5, no. 2, pp. 113–117, 2017.
  - [140] L. Wu and J. Zhang, “Ab initio study of anisotropic mechanical properties of  $\text{LiCoO}_2$  during lithium intercalation and deintercalation process,” *Journal of Applied Physics*, vol. 118, no. 22, p. 225 101, 2015.
  - [141] C.-S. Man and M. Huang, “A simple explicit formula for the voigt-reuss-hill average of elastic polycrystals with arbitrary crystal and texture symmetries,” *Journal of Elasticity*, vol. 105, no. 1-2, pp. 29–48, 2011.
  - [142] Z. Wang, M. Wu, G. Liu, X. Lei, B. Xu, and C. Ouyang, “Elastic properties of new solid state electrolyte material  $\text{Li}_{10}\text{GeP}_2\text{S}_{12}$ : A study from first-principles calculations,” *Int. J. Electrochem. Sci*, vol. 9, no. 2, pp. 562–568, 2014.
  - [143] Z. Deng, Z. Wang, I.-H. Chu, J. Luo, and S. P. Ong, “Elastic properties of alkali superionic conductor electrolytes from first principles calculations,” *Journal of The Electrochemical Society*, vol. 163, no. 2, A67–A74, 2016.
  - [144] M. W. Verbrugge and B. J. Koch, “Modeling lithium intercalation of single-fiber carbon microelectrodes,” *Journal of the Electrochemical Society*, vol. 143, no. 2, p. 600, 1996.
  - [145] K. Mizushima, P. Jones, P. Wiseman, and J. B. Goodenough, “ $\text{Li}_x\text{CoO}_2$  ( $0 \leq x \leq 1$ ): A new cathode material for batteries of high energy density,” *Materials Research Bulletin*, vol. 15, no. 6, pp. 783–789, 1980.
  - [146] A. H. Wiedemann, G. M. Goldin, S. A. Barnett, H. Zhu, and R. J. Kee, “Effects of three-dimensional cathode microstructure on the performance of lithium-ion battery cathodes,” *Electrochimica Acta*, vol. 88, pp. 580–588, 2013.

- [147] P. Ramadass, B. Haran, R. White, and B. N. Popov, "Mathematical modeling of the capacity fade of li-ion cells," *Journal of power sources*, vol. 123, no. 2, pp. 230–240, 2003.
- [148] A. Honders, J. Der Kinderen, A. Van Heeren, J. De Wit, and G. Broers, "Bounded diffusion in solid solution electrode powder compacts. part ii. the simultaneous measurement of the chemical diffusion coefficient and the thermodynamic factor in  $\text{LiTiS}_2$  and  $\text{LiCoO}_2$ ," *Solid State Ionics*, vol. 15, no. 4, pp. 265–276, 1985.
- [149] Y.-M. Choi, S.-I. Pyun, J.-S. Bae, and S.-I. Moon, "Effects of lithium content on the electrochemical lithium intercalation reaction into  $\text{LiNiO}_2$  and  $\text{LiCoO}_2$  electrodes," *Journal of power sources*, vol. 56, no. 1, pp. 25–30, 1995.
- [150] Y.-I. Jang, B. J. Neudecker, and N. J. Dudney, "Lithium diffusion in  $\text{Li}_{0.45}\text{Co}_{0.7}\text{O}_2$  intercalation cathodes," *Electrochemical and Solid State Letters*, vol. 4, no. 6, A74, 2001.
- [151] J. N. Reimers and J. Dahn, "Electrochemical and in situ x-ray diffraction studies of lithium intercalation in  $\text{Li}_{0.45}\text{CoO}_2$ ," *Journal of The Electrochemical Society*, vol. 139, no. 8, pp. 2091–2097, 1992.
- [152] Q. Zhang, Q. Guo, and R. E. White, "Semi-empirical modeling of charge and discharge profiles for a  $\text{LiCoO}_2$  electrode," *Journal of power sources*, vol. 165, no. 1, pp. 427–435, 2007.
- [153] F. Zhang *et al.*, "A review of mechanics-related material damages in all-solid-state batteries: Mechanisms, performance impacts and mitigation strategies," *Nano Energy*, p. 104545, 2020.
- [154] J. R. Wilson, J. S. Cronin, S. A. Barnett, and S. J. Harris, "Measurement of three-dimensional microstructure in a  $\text{LiCoO}_2$  positive electrode," *Journal of Power Sources*, vol. 196, no. 7, pp. 3443–3447, 2011.
- [155] Y.-I. Jang, N. J. Dudney, D. A. Blom, and L. F. Allard, "Electrochemical and electron microscopic characterization of thin-film  $\text{LiCoO}_2$  cathodes under high-voltage cycling conditions," *Journal of power sources*, vol. 119, pp. 295–299, 2003.
- [156] H. Xia, S. Y. Meng, L. Lu, and G. Ceder, "Electrochemical behavior and li diffusion study of  $\text{LiCoO}_2$  thin film electrodes prepared by pld," 2007.
- [157] Z. Chen, Z. Lu, and J. Dahn, "Staging phase transitions in  $\text{Li}_{0.45}\text{CoO}_2$ ," *Journal of the Electrochemical Society*, vol. 149, no. 12, A1604, 2002.

- [158] Q. Liu *et al.*, “Approaching the capacity limit of lithium cobalt oxide in lithium ion batteries via lanthanum and aluminium doping,” *Nature Energy*, vol. 3, no. 11, pp. 936–943, 2018.
- [159] K. A. Hart and J. J. Rimoli, “Microstructpy: A statistical microstructure mesh generator in python,” *SoftwareX*, vol. 12, p. 100595, 2020.
- [160] J. Akimoto, Y. Gotoh, and Y. Oosawa, *Synthesis and structure refinement of lithium carbonate single crystals*, 1998.
- [161] E. P. Roth and C. J. Orendorff, “How electrolytes influence battery safety,” *The Electrochemical Society Interface*, vol. 21, no. 2, p. 45, 2012.
- [162] P. Wang, W. Qu, W.-L. Song, H. Chen, R. Chen, and D. Fang, “Electro–chemo–mechanical issues at the interfaces in solid-state lithium metal batteries,” *Advanced Functional Materials*, vol. 29, no. 27, p. 1900950, 2019.
- [163] D. K. Singh *et al.*, “Li<sub>6</sub>PS<sub>5</sub>Cl microstructure and influence on dendrite growth in solid-state batteries with lithium metal anode,” *Cell Reports Physical Science*, vol. 3, no. 9, p. 101043, 2022.
- [164] M. Klinsmann, F. E. Hildebrand, M. Ganser, and R. M. McMeeking, “Dendritic cracking in solid electrolytes driven by lithium insertion,” *Journal of Power Sources*, vol. 442, p. 227226, 2019.
- [165] G. Bucci and J. Christensen, “Modeling of lithium electrodeposition at the lithium/ceramic electrolyte interface: The role of interfacial resistance and surface defects,” *Journal of Power Sources*, vol. 441, p. 227186, 2019.
- [166] R. O. Ansell, “The chemical and electrochemical stability of beta-alumina,” *Journal of materials science*, vol. 21, no. 2, pp. 365–379, 1986.
- [167] R. Armstrong, T. Dickinson, and J. Turner, “The breakdown of  $\beta$ -alumina ceramic electrolyte,” *Electrochimica Acta*, vol. 19, no. 5, pp. 187–192, 1974.
- [168] L. Feldman and L. C. De Jonghe, “Initiation of mode I degradation in sodium-beta alumina electrolytes,” *Journal of Materials Science*, vol. 17, no. 2, pp. 517–524, 1982.
- [169] L. Chen *et al.*, “Modulation of dendritic patterns during electrodeposition: A non-linear phase-field model,” *Journal of Power Sources*, vol. 300, pp. 376–385, 2015.
- [170] Y. Shibuta, Y. Okajima, and T. Suzuki, “Phase-field modeling for electrodeposition process,” *Science and Technology of Advanced Materials*, vol. 8, no. 6, p. 511, 2007.

- [171] D. R. Ely, A. Jana, and R. E. Garcia, "Phase field kinetics of lithium electrode-  
posits," *Journal of Power Sources*, vol. 272, pp. 581–594, 2014.
- [172] Z. Hong and V. Viswanathan, "Phase-field simulations of lithium dendrite growth  
with open-source software," *ACS Energy Letters*, vol. 3, no. 7, pp. 1737–1743,  
2018.
- [173] L. Liang, Y. Qi, F. Xue, S. Bhattacharya, S. J. Harris, and L.-Q. Chen, "Nonlinear  
phase-field model for electrode-electrolyte interface evolution," *Physical Review E*,  
vol. 86, no. 5, p. 051 609, 2012.
- [174] K. Tantratian, H. Yan, K. Ellwood, E. T. Harrison, and L. Chen, "Unraveling the  
li penetration mechanism in polycrystalline solid electrolytes," *Advanced Energy  
Materials*, vol. 11, no. 13, p. 2 003 417, 2021.
- [175] X. Shen, R. Zhang, P. Shi, X. Chen, and Q. Zhang, "How does external pres-  
sure shape li dendrites in li metal batteries?" *Advanced Energy Materials*, vol. 11,  
no. 10, p. 2 003 416, 2021.
- [176] Y. Ren, Y. Zhou, and Y. Cao, "Inhibit of lithium dendrite growth in solid com-  
posite electrolyte by phase-field modeling," *The Journal of Physical Chemistry C*,  
vol. 124, no. 23, pp. 12 195–12 204, 2020.
- [177] S. Narayan, E. M. Stewart, and L. Anand, "Coupled electro-chemo-elasticity: Ap-  
plication to modeling the actuation response of ionic polymer–metal composites,"  
*Journal of the Mechanics and Physics of Solids*, vol. 152, p. 104 394, 2021.
- [178] S. Narayan and L. Anand, "A coupled electro-chemo-mechanical theory for poly-  
electrolyte gels with application to modeling their chemical stimuli-driven swelling  
response," *Journal of the Mechanics and Physics of Solids*, vol. 159, p. 104 734,  
2022.
- [179] Y. Cha and M. Porfiri, "Mechanics and electrochemistry of ionic polymer metal  
composites," *Journal of the Mechanics and Physics of Solids*, vol. 71, pp. 156–178,  
2014.
- [180] S. Konica and T. Sain, "A thermodynamically consistent chemo-mechanically cou-  
pled large deformation model for polymer oxidation," *Journal of the Mechanics  
and Physics of Solids*, vol. 137, p. 103 858, 2020.
- [181] C. Cui, R. Ma, and E. Martinez-Pañeda, "A phase field formulation for dissolution-  
driven stress corrosion cracking," *Journal of the Mechanics and Physics of Solids*,  
vol. 147, p. 104 254, 2021.



- [182] K. Ammar, B. Appolaire, G. Cailletaud, F. Feyel, and S. Forest, “Finite element formulation of a phase field model based on the concept of generalized stresses,” *Computational materials science*, vol. 45, no. 3, pp. 800–805, 2009.
- [183] C. Lin, K. Liu, H. Ruan, and B. Wang, “Mechano-electrochemical phase field modeling for formation and modulation of dendritic pattern: Application to uranium recovery from spent nuclear fuel,” *Materials & Design*, vol. 213, p. 110322, 2022.
- [184] Y. Ren, Y. Shen, Y. Lin, and C.-W. Nan, “Microstructure manipulation for enhancing the resistance of garnet-type solid electrolytes to “short circuit” by li metal anodes,” *ACS applied materials & interfaces*, vol. 11, no. 6, pp. 5928–5937, 2019.
- [185] G. Li and C. W. Monroe, “Dendrite nucleation in lithium-conductive ceramics,” *Physical Chemistry Chemical Physics*, vol. 21, no. 36, pp. 20354–20359, 2019.
- [186] M. E. Gurtin, E. Fried, and L. Anand, *The mechanics and thermodynamics of continua*. Cambridge University Press, 2010.
- [187] E. Kuhl, “Growing matter: A review of growth in living systems,” *Journal of the Mechanical Behavior of Biomedical Materials*, vol. 29, pp. 529–543, 2014.
- [188] E. J. Dickinson, J. G. Limon-Petersen, and R. G. Compton, “The electroneutrality approximation in electrochemistry,” *Journal of Solid State Electrochemistry*, vol. 15, no. 7, pp. 1335–1345, 2011.
- [189] T. F. Fuller and J. N. Harb, *Electrochemical engineering*. John Wiley & Sons, 2018.
- [190] G. Bauer, V. Gravemeier, and W. A. Wall, “A 3d finite element approach for the coupled numerical simulation of electrochemical systems and fluid flow,” *International journal for numerical methods in engineering*, vol. 86, no. 11, pp. 1339–1359, 2011.
- [191] P. Barai, A. T. Ngo, B. Narayanan, K. Higa, L. A. Curtiss, and V. Srinivasan, “The role of local inhomogeneities on dendrite growth in llzo-based solid electrolytes,” *Journal of the Electrochemical Society*, vol. 167, no. 10, p. 100537, 2020.
- [192] V. S. Deshpande and R. M. McMeeking, “Models for the interplay of mechanics, electrochemistry, thermodynamics, and kinetics in lithium-ion batteries,” *Applied Mechanics Reviews*, vol. 75, no. 1, p. 010801, 2023.
- [193] M. Ganser, F. E. Hildebrand, M. Kamlah, and R. M. McMeeking, “A finite strain electro-chemo-mechanical theory for ion transport with application to binary solid electrolytes,” *Journal of the Mechanics and Physics of Solids*, vol. 125, pp. 681–713, 2019.

- [194] A. Kovetz, *Electromagnetic theory*. Oxford University Press Oxford, 2000, vol. 975.
- [195] M. Ganser, F. E. Hildebrand, M. Klinsmann, M. Hanauer, M. Kamlah, and R. M. McMeeking, “An extended formulation of butler-volmer electrochemical reaction kinetics including the influence of mechanics,” *Journal of The Electrochemical Society*, vol. 166, no. 4, H167, 2019.
- [196] L. Anand and C. Su, “A theory for amorphous viscoplastic materials undergoing finite deformations, with application to metallic glasses,” *Journal of the Mechanics and Physics of Solids*, vol. 53, no. 6, pp. 1362–1396, 2005.
- [197] C. Miehe, M. Hofacker, and F. Welschinger, “A phase field model for rate-independent crack propagation: Robust algorithmic implementation based on operator splits,” *Computer Methods in Applied Mechanics and Engineering*, vol. 199, no. 45-48, pp. 2765–2778, 2010.
- [198] Y. Navidtehrani, C. Betegón, and E. Martinez-Pañeda, “A simple and robust abaqus implementation of the phase field fracture method,” *Applications in Engineering Science*, vol. 6, p. 100 050, 2021.
- [199] L. Anand, “On h. hencky’s approximate strain-energy function for moderate deformations,” 1979.
- [200] J. E. Guyer, W. J. Boettinger, J. A. Warren, and G. B. McFadden, “Phase field modeling of electrochemistry. i. equilibrium,” *Physical Review E*, vol. 69, no. 2, p. 021 603, 2004.
- [201] R. DeHoff, *Thermodynamics in materials science*. CRC Press, 2006.
- [202] D. A. Cogswell, “Quantitative phase-field modeling of dendritic electrodeposition,” *Physical Review E*, vol. 92, no. 1, p. 011 301, 2015.
- [203] G. Bucci, Y.-M. Chiang, and W. C. Carter, “Formulation of the coupled electrochemical–mechanical boundary-value problem, with applications to transport of multiple charged species,” *Acta Materialia*, vol. 104, pp. 33–51, 2016.
- [204] Z. Suo, “Theory of dielectric elastomers,” *Acta Mechanica Solida Sinica*, vol. 23, no. 6, pp. 549–578, 2010.
- [205] D. Rettenwander *et al.*, “Synthesis, crystal chemistry, and electrochemical properties of  $\text{Li}_{7-2x}\text{La}_3\text{Zr}_2\text{-xMo}_x\text{O}_{12}$  ( $x=0.1\text{--}0.4$ ): Stabilization of the cubic garnet polymorph via substitution of  $\text{Zr}^{4+}$  by  $\text{Mo}^{6+}$ ,” *Inorganic chemistry*, vol. 54, no. 21, pp. 10 440–10 449, 2015.

- [206] C. Yuan, X. Gao, Y. Jia, W. Zhang, Q. Wu, and J. Xu, “Coupled crack propagation and dendrite growth in solid electrolyte of all-solid-state battery,” *Nano Energy*, vol. 86, p. 106 057, 2021.
- [207] D. Systèmes, “Abaqus 6.10: Analysis user’s manual,” *Providence, RI: Dassault Systèmes Simulia Corp*, 2010.
- [208] S. Forest, “Nonlinear regularization operators as derived from the micromorphic approach to gradient elasticity, viscoplasticity and damage,” *Proceedings of the Royal Society A: Mathematical, Physical and Engineering Sciences*, vol. 472, no. 2188, p. 20 150 755, 2016.
- [209] J. Wolfenstine, J. L. Allen, J. Sakamoto, D. J. Siegel, and H. Choe, “Mechanical behavior of li-ion-conducting crystalline oxide-based solid electrolytes: A brief review,” *Ionics*, vol. 24, no. 5, pp. 1271–1276, 2018.
- [210] H.-Y. Li, B. Huang, Z. Huang, and C.-A. Wang, “Enhanced mechanical strength and ionic conductivity of llzo solid electrolytes by oscillatory pressure sintering,” *Ceramics International*, vol. 45, no. 14, pp. 18 115–18 118, 2019.
- [211] S. Narayan and L. Anand, “A large deformation elastic–viscoplastic model for lithium,” *Extreme Mechanics Letters*, vol. 24, pp. 21–29, 2018.
- [212] —, “A gradient-damage theory for fracture of quasi-brittle materials,” *Journal of the Mechanics and Physics of Solids*, vol. 129, pp. 119–146, 2019.
- [213] R. de Borst and C. V. Verhoosel, “Gradient damage vs phase-field approaches for fracture: Similarities and differences,” *Computer Methods in Applied Mechanics and Engineering*, vol. 312, pp. 78–94, 2016.
- [214] C. Miehe, F. Welschinger, and M. Hofacker, “Thermodynamically consistent phase-field models of fracture: Variational principles and multi-field fe implementations,” *International journal for numerical methods in engineering*, vol. 83, no. 10, pp. 1273–1311, 2010.
- [215] M. Sato, R. Garcia-Mendez, and J. Sakamoto, “Mapping hot-pressed li<sub>6</sub>. 25al<sub>0</sub>. 25la<sub>3</sub>zr<sub>2</sub>o<sub>12</sub> (llzo) grains and grain boundaries through a simple thermal grooving technique,” *Journal of Asian Ceramic Societies*, vol. 8, no. 3, pp. 793–803, 2020.
- [216] A. Sharafi, C. G. Haslam, R. D. Kerns, J. Wolfenstine, and J. Sakamoto, “Controlling and correlating the effect of grain size with the mechanical and electrochemical properties of li<sub>7</sub> la<sub>3</sub> zr<sub>2</sub> o<sub>12</sub> solid-state electrolyte,” *Journal of Materials Chemistry A*, vol. 5, no. 40, pp. 21 491–21 504, 2017.

- [217] S. Yu and D. J. Siegel, “Grain boundary contributions to li-ion transport in the solid electrolyte  $\text{Li}_7\text{La}_3\text{Zr}_2\text{O}_{12}$  (LLZO),” *Chemistry of Materials*, vol. 29, no. 22, pp. 9639–9647, 2017.
- [218] Y.-C. Hsu, C.-H. Yu, and M. J. Buehler, “Using deep learning to predict fracture patterns in crystalline solids,” *Matter*, vol. 3, no. 1, pp. 197–211, 2020.
- [219] Z. Yang, C.-H. Yu, and M. J. Buehler, “Deep learning model to predict complex stress and strain fields in hierarchical composites,” *Science Advances*, vol. 7, no. 15, eabd7416, 2021.
- [220] K. Park and G. H. Paulino, “Computational implementation of the ppr potential-based cohesive model in abaqus: Educational perspective,” *Engineering fracture mechanics*, vol. 93, pp. 239–262, 2012.